rijksuniversiteit groningen

High energy irradiated protoplanetary disks

The X-rays and FUV role in thermo-chemical modelling

Proefschrift

ter verkrijging van het doctoraat in de
Wiskunde en Natuurwetenschappen
aan de Rijksuniversiteit Groningen
op gezag van de
Rector Magnificus, dr. E. Sterken,
in het openbaar te verdedigen op
maandag 10 december 2012
om 9:00 uur

door

Giambattista Aresu
geboren op 23 oktober 1983
te Cagliari, Italië

Promotores:	Prof. dr. I. Kamp
	Prof. dr. M. Spaans
Copromotor:	Dr. R. Meijerink
Beoordelingscommissie:	Prof. dr. C. Dominik
	Prof. dr. M. Guedel
	Prof. dr. I. Pascucci

ISBN: 978-90-367-5951-9
ISBN: 978-90-367-5953-3 (electronic version)

O sant'asinità, sant'ignoranza,
santa stoltezza e pia devozione,
qual sola puoi far l'anime si buone
che umano ingegno e studio non l'avanza.

Giordano Bruno
In Lode dell'Asino

alla bri,
alla mia famiglia,
a sa Terra mia.

Contents

Chapter 1

Introduction

To steal ideas from one person is plagiarism,
to steal from many is research.
Wilson Mizner

Since the dawn of time, men has directed his sight to the sky, addressing there his very first existential questions. Unconsciously, the sky has always been the place where to seek for answers.

Among the fundamental dilemmas, the one that is most closely related to the human kind is: where does life come from? As never before, we might be fully equipped to answer this question. In the last two decades we have indeed been able to collect an enormous amount of information about the scenario where life similar to ours is supposed to sprout: the planets.

Not only we learned the basic steps necessary for life development here on planet Earth, but we also discovered the existence of planets external to our own solar system. The Kepler mission has shown that planets are common: they form efficiently and are spread all over our galaxy around young stars. Are their local conditions suitable for the growth of life as we know it? Addressing this question is the coming challenge for the future of astronomy and astrobiology. The star formation process starts in dark clouds, where gravitational collapse leads to the formation of a circumstellar disk. In the still ongoing infrared (IR) satellites era, we do observe these disks of gas and dust in orbit around pre-main sequence stars (PMS), the so called **protoplanetary disks**: these are the birth places of the planets. The study of newly discovered disks and extrasolar systems provides otherwise inaccessible data on the conditions that probably led to the formation of our own planetary system.

1.1 From the ISM to the planetary system: the Lada classification

The journey starts in the interstellar medium (ISM), where three different phases (cold, warm and hot) coexist in pressure equilibrium (McKee & Ostriker, 1977). Gravity plays a major role in the cold over-dense regions (molecular clouds), and dominates their energy budget over internal pressure and turbulent motion. These clouds eventually undergo gravitational collapse and star formation begins (Shu & Adams, 1987). In Fig. 1.1 we sketch the evolutionary scenario that is described in more details in the following paragraphs.

Quantitatively, this evolution is followed by looking at the spectral energy distribution (SED), where the emitted flux is plotted against the wavelength (or frequency) usually expressed in microns. The excess emission, from the near infra-red (NIR) to the millimeter, with respect to the stellar spectrum is associated with circumstellar matter. The slope between 2 and 24 μm was historically used to classify the evolutionary state of the object (Lada, 1987). But it is the complete modelling of the SED that is widely used to infer many properties of the system (e.g. class, size of the dust disk, dust temperature and composition).

During the first phases of the collapse, the central object is completely embedded in its envelope, thus optically obscured (Class 0, few times 10^4 years, Andre et al., 1993). Its presence is revealed by the far infra-red (FIR) dust emission. At this stage the collapse is approximately spherical, but the pristine angular momentum of the cloud is such that the infalling matter lands mostly at some distance from the star, forming an accretion disk, which facilitates angular momentum redistribution and drives matter toward the *first core* (see Sect. 1.3).

The central object evolves to become a *protostar*, the stellar accretion rate increases and commonly drives powerful jets and outflows that progressively carve cavities throughout the infalling envelope (Class I, 10^5 years, Bachiller, 1996; Evans et al., 2009). Depending on the orientation of the object in the sky, the protostar can be visible, but it will be generally obscured by dust absorption. At this stage the disk keeps accreting mass from the infalling envelope. Matter is delivered from the disk onto the star with episodic accretion bursts, this is also known as the FU Orionis phase (Herbig, 1977; Hartmann & Kenyon, 1985). The disk mass is observed to stay fairly constant during this process. As the protostar acquires enough mass to evolve into a pre-main sequence star (not yet burning hydrogen), the circumstellar matter accretes the residual envelope until the disk is finally formed (Class II, 10^5-10^6 years). In this phase the so called *primordial* disk is very much affected by the radiation coming from the central star (Kenyon & Hartmann, 1987), moreover dust coagulation, the seed process that will eventually lead to planet formation, proceeds faster (Weidenschilling & Ruzmaikina, 1993; Dominik et al., 2007). The star is now visible and the circumstellar disk is detected through its continuum (dust) and line (gas) emission.

This is likely the place where dust growth continues toward kilometer sized bodies (*planetesimals*) which will then interact gravitationally, although the growth from small to big presents several issues theoretically not fully understood (Weidenschilling,

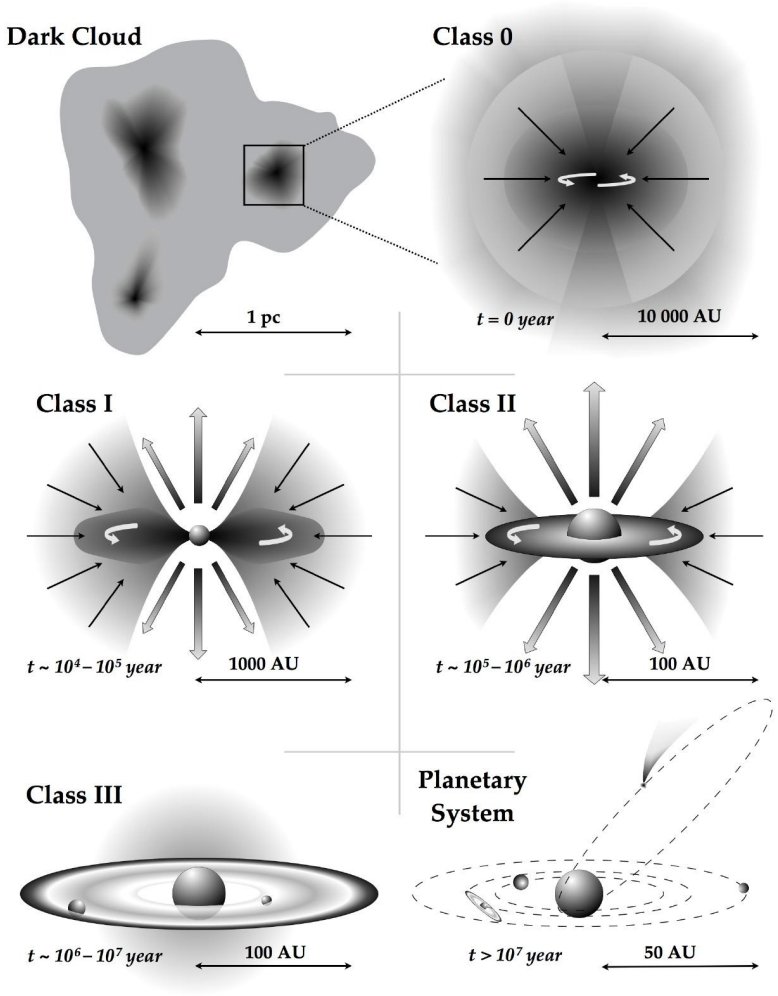

Figure 1.1: Sketch of the stages that lead from the quiescent ISM to the formation of a planetary system. (This figure is shown by kind courtesy of Wilfred Frieswijk.)

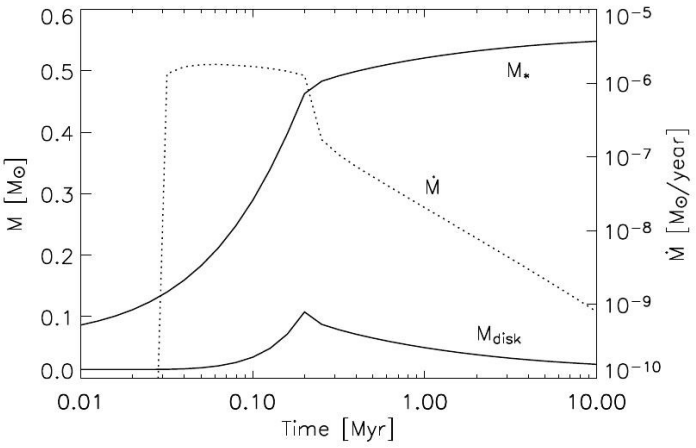

Figure 1.2: Stellar mass, disk mass and mass accretion rate versus age (Dullemond et al., 2007).

1977; Blum & Wurm, 2008; Zsom et al., 2010; Ormel et al., 2010). The clearing of the disk through accretion and/or photo-evaporation from the central star sets the timescale for the formation of such planetesimals in the disk. The system in this stage is referred as *debris disk* (Class III). The interaction between planetesimals causes dynamical ejection of the residual dust, and planets are now assembled via collisions and sticking of these big bodies. The clearing of the debris leaves the planets in their final orbits: the *planetary system* has formed around a hydrogen burning main sequence star. In Fig. (1.2) the stellar mass, disk mass and mass accretion rate behaviour versus age is shown.

Depending on its mass, the central object is referred to as T Tauri Star ($0.3 < M_*(M_\odot) < 1.0$) or Herbig AeB Star ($1.5 < M_*(M_\odot) < 3$). The planetary system evolves on a stellar evolutionary timescale, our own solar system is currently going through this phase. In Table 1.1 the evolutionary scenario described above is summarized for T Tauri stars.

This thesis focuses on the study of the circumstellar disks around T Tauri stars in the Class II stage. It explores the effects of the high energy ultra-violet (UV) and X-ray stellar radiation on the disk structure, chemistry and physics.

1.2 General properties of Class II objects

The disk size, mass and its radial distribution impact the amount of mass available for planet formation at a given radius, and also set the initial condition for disk and planet formation models. These basic parameters have been observed only in the last decade, increasing the understanding of the whole planet formation picture and the prediction capability of such models.

Class	$\dot{M}$ [$M_\odot$ yr^{-1}]	Mass budget	Properties
0	-	$M_{\rm env} > M_* > M_{\rm disk}$	No optical or Near IR emission
I	10^{-6}-10^{-7}	$M_* > M_{\rm env} \sim M_{\rm disk}$	System optically obscured
II	10^{-7}-10^{-10}	$M_{\rm disk} \sim 0.01 M_*$, $M_{\rm env} \sim 0$	Star visible in optical, disk in IR
III	$\ll 10^{-10}$	$M_{\rm disk} \ll 0.01 M_*$, $M_{\rm env} \sim 0$	Possible planetary system, residual accretion

Table 1.1: Typical values for mass accretion rate and mass budget, and observational properties during the evolution of a low mass star (Williams & Cieza, 2011).

Observations of the dust emission at millimeter and sub-millimeter wavelengths provide measurements for the total disk mass in mm sized grains (Beckwith et al., 1990). At these wavelengths most of the disk is optically thin, and the flux received on Earth from a distance d is:

$$F_\nu = \frac{\epsilon_\nu M_{\rm dust}}{d^2} \tag{1.1}$$

where ϵ_ν is the emissivity at the frequency ν. Millimeter radiation traces mostly cold dust (T $\sim$ 20-50 K) in the outer disk. The inner warm dust (T $\sim$ 300 K) emits in the NIR, but soon becomes vertically optically thick, thus impeding observations of the dust stored in the midplane, as the emission is only regulated by the dust temperature there. In its outer regions ($r > 10$ AU), where up to 90% of the mass is stored, the disk is mostly optically thin. Assuming thermal equilibrium, the dust emissivity is related to the opacity through the Kirchhoff law: $\epsilon_\nu = k_\nu B_\nu(T_{\rm dust})$. In the Rayleigh-Jeans regime eq. (1.1) becomes:

$$F_\nu = \frac{2k_B}{c^2} \frac{M_{\rm dust} T_{\rm dust}}{d^2} k_\nu \nu^2 \tag{1.2}$$

The absorption coefficient k_ν in the Rayleigh Jeans limit is usually expressed as $0.1(\nu/10^{12}$ Hz$)^\beta$, in disks $\beta \sim 1$ (Beckwith & Sargent, 1991) and then $k_\nu = 0.03$ cm^2 s^{-1} at 1 mm. The dust temperature is estimated from SED modelling in the infrared. Observations carried out by (Andrews & Williams, 2005, 2007) found a median disk mass of ~ 0.005 $M_\odot$ and a median ratio $M_{\rm disk}/M_* \sim 0.01$. The total disk mass is obtained multiplying the dust mass for the gas to dust mass ratio, typically not known and assumed to be 100. Another important uncertainty within this method, especially at later stages, is the mass hidden in big bodies, which can not be observed with millimeter photometry.

The size of the newly formed circumstellar disk can be estimated analytically by means of the following angular momentum argument. Assuming that the collapsing cloud is a sphere with uniform density, radius of 0.05 pc and angular velocity ω of 10^{-14} s^{-1}, the total angular momentum of the core is $J_{\rm core} \sim 10^{54}$ g cm^2 s^{-1}. The specific angular momentum of such a cloud, that would give birth to a 1 $M_\odot$ star, is: $l_{\rm core} \sim 4 \times 10^{20}$ cm^2 s^{-1}. Since most of the angular momentum will be locked in

the gas motion around the star, it will circularize a particles orbit where the specific Keplerian angular momentum equals $l_{\rm core}$ (Armitage, 2010). This gives $r_{\rm circ} \sim 100$ AU. Observations of disk silhouettes against bright continuum, dust continuum and CO data, suggest similar sizes (Vicente & Alves, 2005; Hughes et al., 2008; Andrews et al., 2010).

Depending on the accretion properties, the class of T Tauri stars is sub–divided into three categories (Walter et al., 1987; Valenti et al., 2000): classical T Tauri stars (CTTS), weak-lined T Tauri stars (WTTS) and naked T Tauri stars (NTTS). CTTS are T Tauri stars surrounded by a disk from which they actively accrete with mass accretion rates between 10^{-7} to 10^{-10} $M_{\odot}$ yr^{-1} (Johns-Krull et al., 2000). They usually show strong emission and widths (EW $>$ 10 Å) in the Hα line, together with other accretion diagnostic (e.g., H_2, C IV lines). WTTS are very weak or non accretors, these are objects that for some reason (later evolutionary stage, quiescence) show very low or no detectable mass accretion rate (EW of the Hα line is less than 10 Å). NTTS are diskless stars, representing either a later evolutionary stage, where the disk has been cleared/accreted or a system in which the natal cloud angular momentum was so low that most of the mass was accreted during its infall (Ingleby et al., 2012), NTTS excess emission is solely due to their photospheric activity. The study of this activity is very important as it yields a benchmark for the comparison with accreting objects.

The disk is generally heated by two sources of energy: the stellar (and interstellar) radiation and the heating due to viscous accretion. Radiation is absorbed in the upper layers while viscous heating is more important in the disk midplane. It is crucial to note that gas and dust couple differently to the radiation depending on its energy. Optical and FUV radiation are mostly absorbed by dust grains, which are heated and emit thermally in the IR. This sets the dust and gas temperature to ∼200 K down to an optical depth of 1, where the gas is mostly neutral and molecular. EUV and X-rays are efficiently absorbed in the upper layers where most of the opacity is in the gas phase. The disk atmosphere ($n_{\langle \rm H \rangle} < 10^8$ cm^3) is almost fully ionized there, and heated to temperatures of few thousand Kelvin, causing the gas to thermally decouple from the dust (Kamp & Dullemond, 2004). The intermediate layers where these two environments meet, show physical and chemical stratification (Section 3.4). Many emission lines are observed from the ionized, atomic and molecular layers. Modelling protoplanetary disks requires a proper treatment of many physical (e.g. heating and cooling) and chemical (e.g. ionization and recombination) processes, provided that the incoming stellar radiation spectrum is well known.

1.2.1 Stellar properties

T Tauri stars are G, K and M type stars. PMS stars are very active in their photospheric and coronal regions, leading to the presence of the so-called UV and X-ray excesses. Another contribution in the UV band comes from the accretion of matter from the disk on the stellar surface (Calvet & Gullbring, 1998).

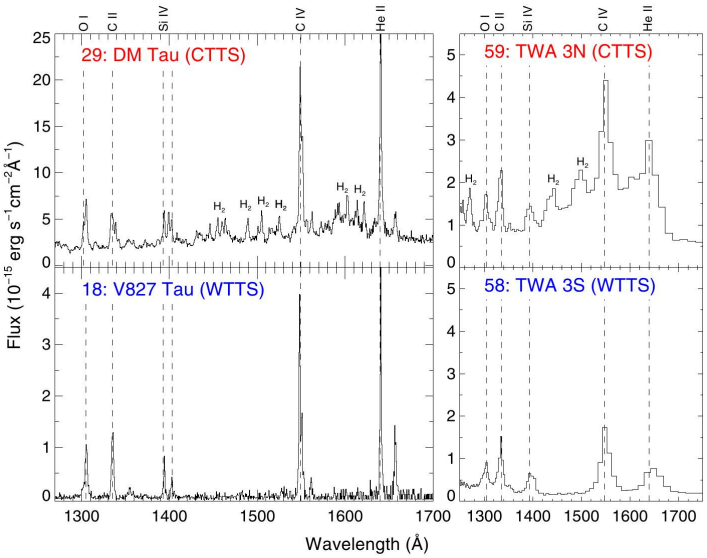

Figure 1.3: Representative FUV spectra (in the range 7-10 eV) for an active CTTS and a WTTS. Note the brightness of the highly ionized lines, the continuum and the presence of H_2 emission in CTTS spectra. Figure taken from Yang et al. (2012).

1.2.2 FUV emission (6-13.6 eV)

In Fig. 1.3 we show the spectra of a CTTS and a WTTS. Both photospheric stellar activity and accretion onto the star cause an excess emission in the FUV band, but the properties of the emitted spectrum are different. Observations in the FUV band suffer from extinction, due to its high absorption cross section. Recent work suggests $L_{\rm FUV}$ between 10^{30} and few times 10^{32} erg s^{-1} (Yang et al., 2012).

- The photospheric regions are characterized by complicated magnetic topology, tangled to the properties of the underlying convective zone. Non radiative transport of energy (e.g. via magnetic fields) provides high degrees of ionization and high temperatures (T $\sim 5000-10000$ K) followed by line cooling (e.g. CaII H & K, C IV and Si IV).

- Accretion onto the stellar surface is accompanied by UV emission: the magnetic field of the star truncates the circumstellar disk at few stellar radii, matter flows from the disk onto the star along the field lines. The release of kinetic energy produces shock heated accretion spots, where about half of the energy is radiated away. Line emission cooling represents up to 90% of the flux. The Lyα emission, one of the brightest FUV lines, pumps molecular hydrogen electronic levels causing fluorescent emission from the directly irradiated disk atmosphere (Herczeg et al., 2002).

While the first process is common to all convective PMS, the second one is accretion dependent and it is used to distinguish between CTTS and NTTS. When comparing the FUV emission between an accreting and non accreting star, several differences stand out. Johns-Krull et al. (2000) identified a number of lines as accretion diagnostics, e.g. the C IV luminosity is ∼40 times brighter for actively accreting CTTS when compared to NTTS. The flux of this, and other lines, is used as a proxy to infer the mass accretion rate and the FUV luminosity (see also Yang et al., 2012).

Lyman α is very important for the disk photo-chemistry: the chemistry of species (e.g. HCN, NH_3 and CH_4) which dissociation cross section includes the Lyα line, is sensitive to the FUV spectrum (Bergin et al., 2003; Fogel et al., 2011)

1.2.3 X-Ray emission (0.1-10 keV)

Similar to what happens to our sun, magnetic field reconnection in the PMS corona produces emission in the X-ray band. Non thermal transport of energy heats the coronal plasma up to temperatures of 10^6 K, and electron temperatures achieve few tens of MK (Feigelson et al., 2007). Such heating is not sustained by conversion of gravitational energy, rather it is the result of magnetic activity as coronal emission is also present in all non-accreting PMS stars. The XEST survey (Güdel et al., 2007), has shown that accretion suppresses the X-ray luminosity, explaining why WTTS are on average a factor 2 brighter than CTTS in the X-ray band. As explained in the previous section, accretion proceeds via flow of matter along the magnetic field lines causing shocks in the photosphere, but when compared to the coronal temperatures this transiting gas is significantly colder, causing a deficit in the overall X-ray luminosity. These colder regions can be diagnosed by looking at their emission in the O VII triplet around 22 Å, which is found in actively accreting CTTS but absent in quiescent objects. The interaction between the stellar magnetic field and the disk might also be responsible for the lower rotation period observed in CTTS, causing a suppression of the dynamo mechanism that ultimately leads to lower X-ray luminosity.

The XMM Taurus survey measured X-ray luminosities between 10^{29} and 10^{31} erg s^{-1}. Episodic flares might enhance the X-ray luminosity; in extreme cases it can be comparable to the bolometric luminosity (Imanishi et al., 2003; Uzawa et al., 2011). Modelled X-ray spectra often use two temperature plasmas (Nomura et al., 2007), Bremsstrahlung (Glassgold et al., 2004) or a double power law peaked at 1-2 keV (Gorti & Hollenbach, 2008). The hardness of the X-ray spectra, i.e. the ratio between the flux in the soft (0.1-1 keV) and hard (1-10 keV) band, impacts the circumstellar disk, as the former is absorbed in the tenuous disk atmosphere while the latter penetrates to deeper layers and might influence the ionization balance there (Schisano et al., 2010).

1.3 Disk Properties

Circumstellar disks evolve viscously: as matter is accreted onto the central star, conservation implies that angular momentum is transported away. In this respect the

disk works as an angular momentum transport machine, which on timescales of a few million years redistributes the original angular momentum of the system, until mass accretion ceases. Matter can be also expelled from the system via photo-evaporation, when high energy irradiation from the central star heats the gas until it can escape the star gravitational field (Hollenbach et al., 1994; Alexander et al., 2006), or via fast ejection into the surrounding medium through jets/outflows (Shu et al., 2000; Konigl & Pudritz, 2000); in either case the angular momentum is expelled from the system. In many Class I and II sources (e.g. T Tau, DG Tau) extended emission is observed in molecular and atomic tracers, with derived velocities that goes from few km/s in slow winds on the disk surface to few 100 km/s in collimated fast bipolar jets, the latter often causes shocks in the material surrounding Class I/II objects. These jets are only observed in sources that also show signs of accretion, for which generally $\dot{M}_{\rm J} \sim 10^{-8} - 10^{-7} {\rm M}_{\odot}$ yr^{-1}.

The long standing problem of how the angular momentum transport works in detail has found its most convincing answer in the magneto-rotational instability (MRI) model (Balbus & Hawley, 1998). This mechanism is linked to the ionization fraction in the disk, the calculation of which requires solving self-consistently the thermal and chemical balance and the disk structure. In this section I will discuss the basic steps necessary to build a disk model and the underlying assumptions that are made.

1.3.1 Disk structure

The equilibrium between gravity and pressure ultimately sets the disk horizontal and vertical structure. The stellar gravitational field is counter balanced by the heating provided by the stellar and interstellar radiation, and by the dissipation of energy due to accretion.

As a first general step it is assumed that the surface density distribution follows a radial power law:

$$\Sigma(r) = \Sigma_0 r^{-\epsilon} \tag{1.3}$$

where Σ_0 is the surface density distribution at 1 AU. In 1981 Hayashi proposed a way to extract this value for the protoplanetary disk that gave birth to our solar system. He considered the mass of each planet spread over an annulus that extends on each side to half of the distance from the previous and the following planet. The light elements abundance is scaled until the augmented composition matches with solar abundances. This way he obtained an exponent of $\epsilon = 1.5$ and an estimate for the minimum mass necessary to form our solar system of 0.01 $M_{\odot}$.

The dusty disk extends at the inside to the sublimation radius for dust (~ 0.01 AU), while gas can exist even further until it is channelled by the magnetic fields of the star at the inner truncation radius (few stellar radii). The exterior size of the disk is generally set by the initial mass available, or by external star encounters which might truncate the disk at few 100 AU, although this last process is rare.

The vertical structure of the disk is found assuming vertical hydrostatic equilibrium between the vertical component of the gravity and the pressure gradient in the

z direction (here $M_{\rm disk} \ll M_*$ is assumed):

$$-\frac{1}{\rho}\frac{\partial P}{\partial z} = \frac{GM_*}{(r^2+z^2)^{\frac{3}{2}}}z \tag{1.4}$$

Given that $P = c_s^2\rho$ and assuming that the disk is thin (z/r $\ll$ 1) and vertically iso-thermal, we can solve for the density and obtain:

$$\rho(r,z) = \rho_0(r)e^{-\frac{z^2}{2H(r)^2}} \tag{1.5}$$

where ρ_0(r) is the density in the midplane, $H(r)$ is the scale height, defined as:

$$H = \sqrt{\frac{r^3 kT(r)}{GM\mu}} = \frac{c_s}{\Omega} \tag{1.6}$$

Assuming that the disk absorbs and re-emit the stellar radiation as a black body:

$$T_{\rm disk} = \left(\frac{\alpha}{2}\right)^{\frac{1}{4}}\left(\frac{R_*}{r}\right)^{\frac{1}{2}}T_* \tag{1.7}$$

Knowing the grazing angle (α) one can estimate the disk radial structure.

Thin disk For a thin disk ($H(r) \ll r$) it can be shown that $\alpha = (4/3\pi)(R/r)$. Inserting this in (1.7) gives $T_{\rm disk} \propto r^{-3/4}$, and ultimately leads to:

$$\frac{H}{r} \propto r^{\frac{1}{8}} \tag{1.8}$$

This result is not self-consistent, as the assumptions for a thin disk in the grazing angle calculation leads to a slightly flaring disk. The grazing angle, the scale height and the temperature radial profile are linked to each other and need to be solved self-consistently, in hydrostatic equilibrium.

Flared disk Given that most of the radiation is absorbed in the disk photosphere, that has a height $H_{\rm p}$, the grazing angle now reads:

$$\alpha \sim 0.4\frac{R}{r} + r\frac{d}{dr}\left(\frac{H_p}{r}\right) \tag{1.9}$$

This equation, together with eq. (1.7) and eq. (1.6) are to be solved simultaneously, leading to the following relations at large radii:

$$\begin{array}{rcll} T_{\rm disk} & \propto & r^{-\frac{1}{2}} & \text{(large radii)} \\ \dfrac{H}{r} & \propto & r^{\frac{2}{7}} & \end{array}$$

The temperature profile is shallower as the disk absorbs more radiation in the outer part compared with the flat disk case (Kenyon & Hartmann, 1987; Chiang & Goldreich, 1997).

These analytical approximations are very useful to understand the basic disk structure and its dependency on physical parameters. Nevertheless, the assumptions made here need to be relaxed in a thorough modelling: the temperature is expected to vary in the vertical direction and to be dependent on the local chemistry. Models need also to include dust radiative transfer as the optical radiation is only able to penetrate the disk to a certain depth and absorption and scattering processes affect the dust temperature, which is set locally by assumption of radiative equilibrium. This is nowadays done in computational codes developed by many groups (D'Alessio et al., 1998; Dullemond et al., 2002; Dullemond & Dominik, 2004; Pinte et al., 2006; Min et al., 2009).

Details between models can vary when dust properties change: composition, size distribution power law, settling, dust to gas mass ratio etc. All these parameters are usually tuned to get a proper match with the observed SED for a given source, and provide then a good starting point for the calculation of the gas lines (Gorti & Hollenbach, 2004; Glassgold et al., 2004; Nomura & Millar, 2005; Ercolano et al., 2008; Semenov et al., 2008; Woods & Willacy, 2009; Woitke et al., 2009). The general accepted picture is sketched in Fig. (1.4), and described in the next section. This result is achieved qualitatively by all disk models.

1.3.2 Chemistry in disks

The disk hosts an extreme range of densities and temperatures: from $n_{<\mathrm{H}>} \sim 10^{14}$ cm^{-3} and 20 K in the midplane to $n_{<\mathrm{H}>} \sim 10^{5}$ cm^{-3} and few thousand Kelvin in the upper layers. This large range of physical condition is very challenging for astrophysical chemical networks. Moreover the interplay between chemistry and thermal processes has to be solved iteratively, in order to find a set of local abundances and temperature that satisfies the thermo-chemical equilibrium.

For a given set of n_{i} species (i=1,N_{sp}) linked by N_{R} reaction, the net formation rate reads:

$$\begin{aligned} \frac{dn_i}{dt} &= \sum_{jkl} R_{jk\rightarrow il}(T_{\mathrm{g}}) n_j n_k + \sum_{jl} \left(R^{\mathrm{ph}}_{j\rightarrow il} + R^{\mathrm{cr}}_{j\rightarrow il} \right) n_j \\ &- n_i \left(\sum_{jkl} R_{il\rightarrow jk}(T_g) + \sum_{jk} \left(R^{\mathrm{ph}}_{i\rightarrow jk} + R^{\mathrm{cr}}_{i\rightarrow jk} \right) \right) \end{aligned} \tag{1.10}$$

ehere the terms involved are:

- $R_{jk\rightarrow il}(T_{\mathrm{g}})$ is the temperature dependent rate for a two body reaction where species i and l are formed out of species j and k.
- $R^{\mathrm{ph}}_{i\rightarrow jk}$ is a photo-reaction rate that depends on the local strength of the UV radiation field
- $R^{\mathrm{cr}}_{i\rightarrow jk}$ designates a reaction that depends on the cosmic ray ionization rate.

Assuming kinetic equilibrium $\left(\frac{dn}{dt} = 0\right)$, we obtain i=1,$N_{\rm sp}$ non-linear equations for the k=1,$N_{\rm sp}$ unknown particle densities.

$$F_i(n_k) = 0 \tag{1.11}$$

Chemical rates are usually read from chemical databases as UMIST (Woodall et al., 2007). In the last decade chemical networks started to include not only gas phase reaction but also reactions involving third particles/bodies: molecule formation on grains, freeze out on grains, interactions with PAHs.

The chemistry in the disk can be summarized by looking at Fig. (1.4). The upper layers are directly exposed to high energy photons such as EUV and X-rays, consequently the energy deposition rates are high (X-ray chemistry is described in details in Sect. 1.3.5). Atoms are ionized and molecules are photo-dissociated, the electron fraction ($x_{\rm el} = n_{el}/n_{\langle H \rangle}$) can be as high as $10^{-1} - 10^{-3}$. Electrons from X-ray/EUV ionization carry the surplus photon energy and cause the temperature of the gas to rise up to a few thousand Kelvin. Chemistry here is dominated by photo-ionization and charge exchange reactions, the latter are faster than electronic recombination at the low densities ($n_{\rm gas} \sim 10^{4-6}$ cm^{-3}) of these surface layers.

Deeper in the disk the density increases (eq. 1.5), hence the optical depth is higher and the gas becomes atomic, although due to X-ray and FUV heating, the electron fraction is sustained at a level of 10^{-4}. Temperatures and densities are such that the transition between the atomic and molecular phase is accompanied by ion-molecular chemistry, the electron fraction is still relatively high ($x_{\rm el} \sim 10^{-4}$-10^{-6}) driving the production of molecules such as OH^+ and NH^+. The transition is approximately located between the H/H_2 transition and the C^+/CO transition. Further down, in the molecular layer, the temperature drops to about 50-100 K. Neutral reactions dominate here, and an active molecular chemistry leads to the formation of complex molecular species (e.g. H_2CO, HCO^+). Deeper in the disk, toward the midplane, where the density reaches 10^{13-14} cm^{-3} and the temperature drops below 50 K, molecules can freeze out onto the dust grains. CO (below ∼24 K) and H_2O (below ∼90 K) ice mantles become the sink for O and C atoms. In these regions only interstellar cosmic rays and radioactive decay provide some energy deposition. Scattering by dust grains can transport some energy, but the stellar radiation is believed to be mostly shielded, due to the very high radial and vertical optical depths ($\tau \sim 10^6$), this is the so called "dead zone", where the electron fraction is so low ($x_{\rm el} \sim 10^{-13}$, Latter & Balbus 2012) that the region is magnetically inactive, and MRI cannot proceed.

1.3.3 Dust: composition and size

Dust modelling has to be informed by observations and laboratory experiments to draw the evolutionary picture that leads from the ISM to planet formation. The dust in the ISM is mainly composed of silicate and carbonaceous material, and represents 1% of the total ISM mass. Shattering due to turbulent motions, shock waves and interaction with energetic ions or photons lead to the typical power law size distribution of the dust:

$$f(a) \propto a^{-3.5} \tag{1.12}$$

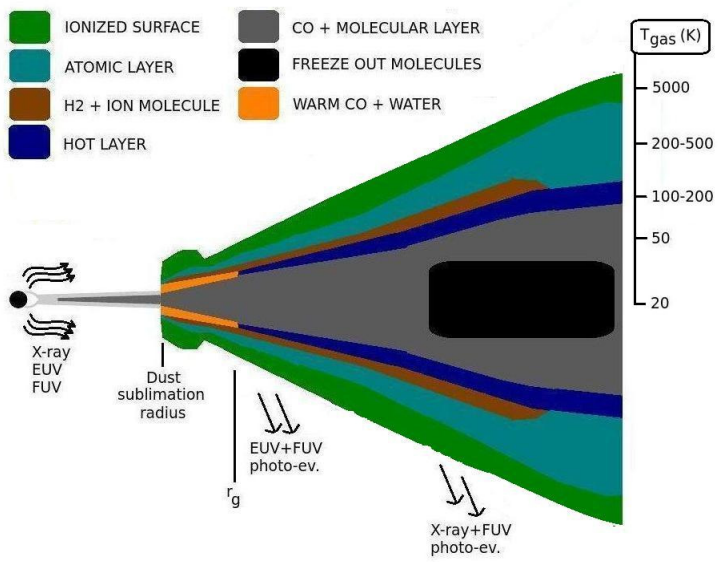

Figure 1.4: Sketch for the gaseous stratification in protoplanetary disks.

where $f(a)$ is the number of dust particles with size a. The exponent was found by fitting extinction, scattering and polarization properties in the MRN model (Mathis et al., 1977). The dust is ultimately used as a building block for the planets, although its properties undergo significant changes from the quiescent ISM through the stages that lead to the disk formation. During the protostellar collapse the dust moves through shocks or high temperature regions, causing a different fate for its volatile and refractory compounds, altering the final elemental abundances with respect to the original nebula (Davis et al., 2005). Even outer disk material (e.g. cometary coma material), which was believed to have existed only in low temperature environments, shows altered composition. This proves that most of the material in our solar system formed, or was processed at some point, in high temperature regions or events. Reconstructing the dust history in external system is a difficult task and indirect evidences on dust composition are made through SED modelling or study of the characteristic emission of silicate crystals (Apai et al., 2005; Dullemond & Dominik, 2004; Mulders et al., 2011).

Disk formation not only changes the dust composition but also impacts its size distribution and percentage of the total mass. Coagulation processes lead to dust growth, shifting the power law distribution to a shallower exponent. Bigger grains decouple dynamically from the vertical motions that mix material in the upper disk layer. They start to settle toward the midplane, thereby changing the dust to gas mass ratio. The extreme low temperatures in the disk also causes the grain to have icy mantles (e.g. H_2O and CO). All these parameters ultimately impact the opacity in the disk, affecting its thermal and chemical properties. The dust is also an important chemical catalyst for the formation of molecules (e.g. H_2, Cazaux & Tielens, 2004),

and it has a crucial role in the thermal balance, being a source of heating through the photo-electric effect and H_2 formation heating.

1.3.4 UV heating

Here we introduce the most important heating and cooling processes that compete to set the temperature in upper layers of the disk. FUV radiation is mostly absorbed by dust and PAHs. When the impinging photon overcomes a given threshold (few eV, depending on the dust material and composition) the photoelectric effect takes place: an electron is ejected with a kinetic energy equal to E_{phot}-E_{ion}, which is then collisionally dissipated in the gas.

Dust grains For small dust grains the efficiency of the process reads (Tielens, 2005):

$$\epsilon_{\rm grains} = Y\left(\frac{h\nu - W - \phi_c}{h\nu}\right) \tag{1.13}$$

Where Y is the yield, measuring the probability that the photon escapes the grain, ϕ_c is the electrostatic grain potential, which becomes important when grains are charged. W is the work function of the grain. This equation does not take into account energy losses due to electron collisions inside the grain.

PAHs For PAH molecules the ionization potential is again given by the sum of the work function W and the Coulomb potential when the PAH is charged. The former is dominant for large PAHs ($N_{\rm C} > 60$), while the latter is more important as smaller PAHs are considered. Eventually, the ionization potential for a small charged PAH, overcomes 13.6 eV.

Theoretical work has been done to summarize the contribution of photoelectric heating in the ISM, this fit formula has been calculated for the efficiency for a size distribution of PAHs and small grains, and takes into account the effect of the UV radiation field (G_0), the local temperature and the electron density through the parameter γ:

$$\epsilon_{\rm PE} = \frac{4.87\times10^{-2}}{1+4\times10^{-3}\gamma^{0.73}} + \frac{3.65\times10^{-2}(T/10^4)^{0.7}}{1+2\times10^{-4}\gamma} \tag{1.14}$$

where $\gamma = G_0 T^{1/2}/n_{\rm el}$. Although this treatment can be used in protoplanetary disks, the situation might be different, as small PAHs are believed to not survive typical physical condition in disk atmospheres and dust grain should coagulate in Myr timescales to bigger sizes (see 1.3.3). Photoelectric heating can be approached separately for dust and PAHs. For the latter, often only one variety of PAH (with $N_{\rm C} \sim 50$) is considered, and the heating rate is calculated consistently with the charge balance of the PAH.

Carbon Ionization Neutral carbon has lower ionization threshold ($\sim$ 11.2 eV) when compared to other abundant elements ($\sim$ 13.6 for H and O), and it can be a major electron donor in disk surfaces. FUV photons between 11.2 and 13.6 eV ionize carbon and cause the outgoing electron to deposit $\sim$ 1 eV in the gas at a rate given by (Black, 1987):

$$\Gamma_{\rm C} = 1.602\times10^{-12} R_{\rm C}^{\rm ph} n_{\rm C} \tag{1.15}$$

where $R_{\rm C}$ is the carbon ionization rate and $n_{\rm C}$ the carbon density.

1.3.5 X-ray Heating and chemistry

X-ray photons ($0.1 < \mathrm{E\,(keV)} < 10$) ionize and photo-dissociate all the species in the gas phase. The cross section are smaller than the grain absorption cross section, but the X-ray heating efficiency can be of the order of 50%, becoming a competitive, if not dominant, heating process in protoplanetary disks atmospheres. X-rays energies are $\sim$ 10-100 times higher than most of the ionization thresholds, the outgoing electron has approximately all the photon energy and it is released in the gas phase with a much higher kinetic energy than the local gas temperature.

The cross section for X-ray absorption is higher for inner electron shells (K, L and M). When one of these electron is ejected, the inner gap will eventually be filled by outer electrons leading to consequent energy emission, which can again be of the order of few hundreds eV. This energy is directly transferred to the outer electrons causing their ejection and leaving the species in a highly ionized state (3+ or more). Charge exchange reactions (mainly with neutral hydrogen) are extremely fast when compared to the typical chemical rates in protoplanetary disks (Glassgold et al., 2004). It is then generally assumed that at most a given species can persist in a double ionized state.

For every X-ray ionization, one or two fast electrons are released in the gas phase. They can potentially cause secondary ionization via collisions or increase the temperature of the gas transferring their energy to the thermal electrons via Coulomb interactions.

The balance between these two processes is regulated by the local ionization fraction in the gas phase (Maloney et al., 1996). When the gas is mostly neutral the heating efficiencies are low and the energy of the fast electrons is mainly channelled toward secondary ionization. If the ionization fraction is high, most of the energy will be exchanged with the thermal electrons. The competition between these two processes, ultimately set the thermal and chemical equilibrium in the X-ray dominated regions of protoplanetary disks. Even though it is not treated here, collisions with fast electrons can also lead to excitation and dissociation of the gas species (Meijerink & Spaans, 2005).

The primary ionization rate for the i-th species is:

$$\zeta_i^1 = \int_{E_i}^{\infty} \sigma_i(E) \frac{F(E)}{E} dE \tag{1.16}$$

where E_i is the ionization threshold for the i-th species, σ_i is the cross section for the absorption of a X-ray photon and $F(E)$ is the flux of the X-ray radiation field per unit of energy interval.

To calculate the secondary ionization rate and the heating rate it is necessary to know the local X-ray energy deposition rate, and the chemical status of the gas, in terms of H, H_2 and electron fraction. The X-ray energy deposition rate is the energy deposited per unit of time per unit of hydrogen nuclei. Given a typical X-ray radiation field between 0.1 and 10 keV, H_{X} is calculated as:

$$H_{\mathrm{X}} = \int_{0.1\mathrm{keV}}^{10\mathrm{keV}} \sum_i \sigma_i(E) \frac{n_i}{n_{\langle \mathrm{H} \rangle}} F(E) dE \tag{1.17}$$

The sum runs over all the species. The fraction of $H_{\rm X}$ that goes into secondary ionization of atomic hydrogen is:

$$\zeta_2^H = \frac{H_{\rm X} n_{\langle {\rm H} \rangle}}{W_{\rm H} n_{\rm H}} \tag{1.18}$$

where $W_{\rm H}$ is the mean energy per ion, the energy needed to collisionally ionize the hydrogen atom in an ionized gas mixture of H, H_2 and He. From theoretical studies the following fit formula was calculated (Dalgarno et al., 1999), with a helium abundance equal to 0.1 $n_{\langle {\rm H} \rangle}$, the total hydrogen nuclei number density.

$$W_{\rm H} = W_0 \left(1 + a \frac{n_{\rm H_2}}{n_{\rm H}}\right) (1 + b x_{\rm el}^{\alpha}) \tag{1.19}$$

where W_0 is the hydrogen collisional ionization energy ($\sim$ 40 eV), $x_{\rm el}$ the electron fraction and a and b are fit parameters. $W_{\rm H}$ increases as the gas becomes molecular or ionized.

For all the other atomic elements (excluding helium) the previous rate is scaled as follows:

$$\zeta_2^i = s_i \frac{H_{\rm X} n_{\langle {\rm H} \rangle}}{W_{\rm H} n_{\rm H}} \tag{1.20}$$

where s_i is $\sigma_i^{\rm coll}/\sigma_H^{\rm coll}$, the ratio between the collisional cross section for the element i and hydrogen (Lennon et al., 1988). The secondary ionization rate for molecular hydrogen reads:

$$\zeta_2^{H_2} = \frac{H_{\rm X} n_{\langle {\rm H} \rangle}}{W_{\rm H_2} n_{\rm H_2}} \tag{1.21}$$

where now $W_{\rm H_2}$ is:

$$W_{\rm H_2} = W_0 \left(1 + c \frac{n_{\rm H}}{n_{\rm H_2}}\right) \left(1 + d y_{\rm el}^{\beta}\right) \tag{1.22}$$

where c, d and β are fit parameters, $W_0 \sim 42$ eV, $y_{\rm el}$ is the electron fraction in a H_2/He gas mixture, and is given by $1.83 x_{\rm el}/(1 + 0.83) x_{\rm el}$. Similarly the helium mean energy per ion is:

$$W_{\rm He} = W_0 \left(1 + b y_{\rm el}^{\alpha}\right) \tag{1.23}$$

and $W_0 \sim 490$ eV. The key parameter is the ionization fraction, regardless of the chemical state of the gas: if the gas is neutral, mean energies are constant, when $x_{\rm el}$ is high, the mean energies per ion increase and secondary ionization rates decrease. The energy of the primary fast electron is now going to be transferred to the thermal electrons in the gas. The heating rate due to the X-ray primary ionization is:

$$\Gamma_X = \eta H_X n_{\langle {\rm H} \rangle} \tag{1.24}$$

where η is the heating efficiency for an ionized gas mixture, defined as:

$$\eta = \frac{10 r \eta_{\rm H_2 He} + \eta_{\rm HeH}}{10 r + 1} \tag{1.25}$$

where r is the ratio between molecular and atomic hydrogen density. When the gas is molecular the first term dominates, otherwise for an atomic gas the second efficiency is considered, both of them are parametrized as follows:

$$\eta' = 1 + \frac{(\eta_0 - 1)}{1 + c w_{\rm el}^{\alpha}} \tag{1.26}$$

where $w_{\rm el}$ is $x_{\rm el}$ for $\eta_{\rm HeH}$ and $y_{\rm el}$ for $\eta_{\rm H_2He}$. The electron fraction, consistent with the expressions for the mean energies per ion, ultimately regulates the heating efficiency.

X-ray radiation thus causes high ionization ($x_{\rm el}$ $\sim$0.1) and high temperatures ($\sim$5000 K) in protoplanetary disks surfaces, thereby contributing to the thermal balance and the chemistry (Glassgold et al., 2007; Gorti & Hollenbach, 2008; Ercolano et al., 2008; Aresu et al., 2011).

1.4 Diagnostics

Disk modelling has become a challenging field of interest, guided by the enormous computational resources and observational data nowadays available with respect to the past: the Spitzer and Herschel satellites gave a crucial contribution to the IR study of protoplanetary disks. Dust emission is modelled through SED fitting, but also many gas lines are detected toward star forming region such as Taurus, Trapezium and Hydra. Gas line interpretation needs thorough modelling, as the line is connected to the thermochemical condition either in the disk, or in the surrounding media when the emission is extended.

Many input data is needed to model correctly the thermal and chemical properties of an accretion disk (reaction rates, thermal processes, stellar spectra), affecting the quality of a thermo-chemical solution. Moreover, the calculation of the gas temperature regulates the predicted photoevaporation rates, impacting the disk evolution modelling. In this section, I list a small sample of detected transitions and their diagnostic power.

Oxygen Detected in the IR fine-structure lines at 63.3 and 145 micron (Pinte et al., 2010) and in the optical forbidden line at 6300 Å. The line comes from the disk atmosphere from a region between 20 and 200 AU, depending on the stellar luminosity. It is optically thick and in LTE, and traces temperatures of the order of 200-300 K in the atomic layer of gas rich disks (Meijerink et al., 2008; Woitke et al., 2009). This line in some sources is associated with extended emission, likely arising from outflow or jet activity (Podio et al., 2012). In such cases the disk contribution to the total flux might be marginal. The 145 micron line traces a slightly deeper region of the disk of similar radial extent. The optical 6300 Å line probes a small region of the inner disk atomic layer, heated to temperatures higher than 3000 K (Woitke et al., 2011).

Ionized Carbon C^+ at 157 micron fine-structure transition is of uncertain origin (Bruderer et al., 2012). Although models predict bright C^+ emission, this line is seen with a low detection rate. The line is predicted to trace the low density upper layers in the outer disk.

Ionized Neon Thi species is detected in the 12.8 micron fine-structure transition originally with Spitzer, then ground based follow-up (Pascucci et al., 2007; Najita et al., 2009). The origin is ubiquitous and not unique as it is often associated to jets, slow outflows and EUV/X-ray irradiated static disk atmospheres due to the high excitation temperature of the line ($\sim$ 1000-2000) (Lahuis et al., 2007; Pascucci et al., 2007; Güdel et al., 2010; Sacco et al., 2012).

Carbon monoxide CO (and the isotope ^{13}CO) is chemically very stable as it is expected to survive a broad range of temperatures in the disk (from $\sim$20 K to 4000 K). It is detected in its ro-vibrational transitions, tracing the warm inner disk (T $\sim$ 2000 K, e.g. Najita et al., 2003), and in its low rotational transition in the outer disk (Dutrey et al., 1997), where T $\sim$ 50 K. In some cases it traces lower temperatures than its sublimation temperature ($\sim$ 20 K) suggesting the presence of vertical mixing (Dartois et al., 2003; Aikawa, 2007). The line, or upper limits on the line, can be used to estimate the gas mass available for giant planet production (Pascucci et al., 2006).

Water H_2O is detected through its high rotational transitions ($\sim 12\,\mu$m and 63 μm) in the inner disk (Pontoppidan et al., 2010; Riviere-Marichalar et al., 2012), the line is optically thick and traces thermal conditions there. Hogerheijde et al. (2011) detected HIFI water lines ($\lambda = 538$ and 269 μm for ortho and para water respectively) toward TW Hya: modelling suggests the presence of a considerable reservoir of water ice in the surrounding protoplanetary disk.

Molecular hydrogen H_2 is observed in FUV emission arising from the inner disk, where Lyα emission from the central object pumps H_2 fluorescence (Herczeg et al., 2006; Ingleby et al., 2012). Colder transitions in the IR (e.g. 2 μm) are consistent with emission in the warm ($\sim$2000 K) atmosphere beyond 10 AU, possibly heated by X-rays (Carmona et al., 2011).

Other molecules Many other molecular species such as HCO^+, CN, HCN, C_2H_2 and some deuterated species are detected toward protoplanetary disks, tracing different thermal and chemical conditions, see Bergin (2009) for a recent review.

1.5 Disk Evolution

Observations in the NIR suggests that most of the disks lose their gas in a few million years (Fig. 1.5). Many processes compete for the gas and dust removal in protoplanetary disks. The most efficient are accretion on the star and photoevaporation of the disk by stellar radiation.

Accretion During the star and disk evolution the mass accretion rate decreases with time, proving that the disk is efficiently accreting mass onto the star (Hartmann et al., 1998). Accretion is thought to proceed because of viscous interactions within the disk, although the details of the viscosity are still under debate. Modelling approaches the problem by hiding the physical cause of the viscosity (ν) in the famous alpha parametrization (Shakura & Sunyaev, 1973):

$$\nu = \alpha c_s H \tag{1.27}$$

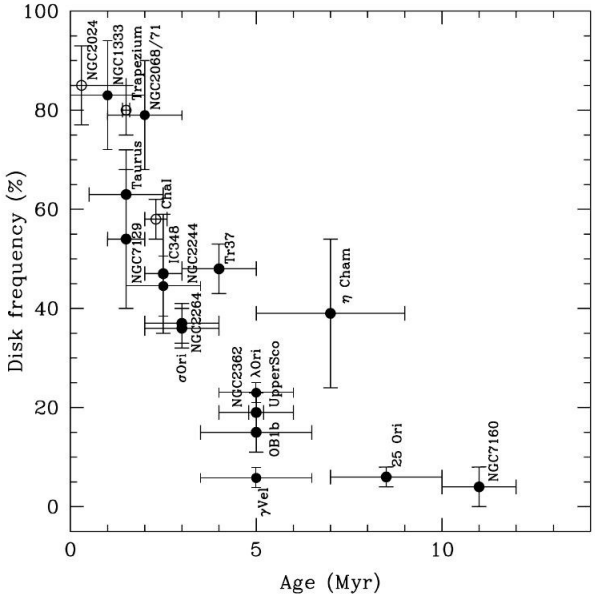

Figure 1.5: Disk frequency in a given stellar cluster versus its age. Measurements are based on NIR observations (Hernández et al., 2008).

where c_s is the sound speed and H the scale height of the disk (eq. 1.6). α is a parameter that contains the physics of the viscous stresses. As mentioned before, the MRI model is currently the best explanation for the accretion process in protoplanetary disks. The magnetic field in the disk together with the differential angular motion produce an instability which causes turbulence, allowing the radial drift of matter inside and outside a given radius. For this to happen, the disk needs to sustain a minimum level of ionization in its deeper layers ($x_{\rm el} \sim 10^{-12}$). With the observed mass accretion rates, accretion can get rid of the disk on a timescale of 10^7 years, which is longer than the observed disk lifetime.

Photoevaporation The surface temperature in the disk due to FUV, EUV and X-rays absorption causes the gas to heat up and thus escape the gravitational field of the star. This removal mechanism starts impacting the disk evolution when accretion rates are comparable to photoevaporation mass loss rates (10^{-10} $M_\odot$ yr^{-1}), the detailed calculation of the mass loss rate depends on the luminosity (Alexander et al., 2006; Gorti et al., 2009; Owen et al., 2010).

EUV are very efficient in the inner disk, due to their high ionizing power they can only penetrate low column densities ($N_{\rm H} \sim 10^{19}$ cm^{-2}), hardly reaching the outer disk. They are capable of heating a thin inner gas layer to a temperature of 10000 K and cause an inner gap in the disk after a few 10^6 years. FUV radiation penetrates more, causing the disk to flare in the first place. Then it contributes to the EUV mass removal in the inner disk, speeding up the whole process, but the major impact

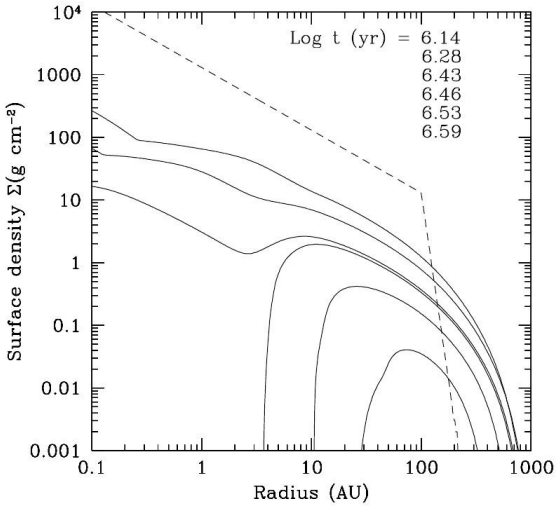

Figure 1.6: Surface density profile versus radius for an EUV, FUV and X-ray illuminated protoplanetary disk (Gorti et al., 2009). Time increases from top to bottom, after a gap is opened at ∼2 AU, the disk survives for a few million years.

of FUV radiation is on the outer disk (R ∼ 100 AU), which is photoevaporated in a few million years. Along with this mass removal, the disk viscosity keeps working, constantly flattening the disk surface density and hence replenishing the inner and outer disk. X-rays alone do not sustain enough photoevaporation to have an important contribution on the disk removal timescale. In the presence of also FUV radiation, X-rays enhance the mass removal rate in the outer disk by a factor 2-3. After a few million years, the disk should be devoid of most of its mass (Fig. 1.6). The residual gas and dust is involved in the dynamical interaction between what potentially is left after major mass removal: the planets.

1.5.1 Last stages

Throughout the disk clearing phase, the planetesimals continue to grow and start to interact gravitationally. The terrestrial planet and the giant planet cores are formed through planetesimal impacts. In the outer disk subsequent core accretion or gravitational instabilities cause the formation of giant gaseous and icy planets. In the 10-1000 Myr that follows the dark cloud collapse, these components undergo frequent collisions until the final setup, the planetary system, is reached. In this environment, around a planet in the terrestrial zone (∼1 AU), life might manifest itself in its primordial beginning. To understand our origin, it is then necessary to identify and examine all the steps that from a quiescent dark cloud lead to the assembly of rocky planets.

Thesis outline

In this thesis, I focus on one fundamental step of star and planet formation: the primordial disk. I investigate on the the role that high energy radiation emitted from the star (X-ray and FUV) plays in protoplanetary disks from a modelling point of view. I modified and used the thermo-chemical code ProDiMo (PRotoplanetary DIsk MOdel, Woitke et al., 2009) to model a fiducial disk around a T Tauri star with solar mass and radius.

In chapter 2, I study the X-ray impact on the chemistry and thermal balance of the disk. In these models the X-ray luminosity is varied from 0 to 10^{29}, 10^{30}, 10^{31} and 10^{32} erg/s. This is the first work in which I included the X-ray chemistry and heating into ProDiMo.

In chapter 3, motivated by the results of the previous work, I investigate the impact of a broader set of parameters on the same disk, developing a grid of models where X-ray luminosity, FUV luminosity, surface density distribution power law, dust minimum grain size and grain size distribution power law are varied. This work analyses the dependency of the physical structure of the disk on the local heating and cooling rates and on the chemistry of the most relevant species.

In chapter 4, I describe the results of the application of line radiative transfer to the above models. The diagnostic power of [O I] 63 μm, [C II] 157 μm, [Ne II] 12.8 μm, [Ar II] 6.9 μm and rotational water lines at 23, 63 and 179 μm is analysed. I study the sensitivity of the fluxes and widths of these lines against the varying parameters, and make predictions for their observation for different disk inclinations.

In chapter 5 the predictions for the neutral oxygen fine structure line fluxes are compared with observation taken with the PACS instrument on board of the Herschel Space Observatory. The models are used to reproduce the line flux dependency on X-ray and FUV luminosity, with the aim of understanding the heating processes that drive [O I] emission in protoplanetary disks.

Chapter 6 summarizes the main results and conclusions. Based on the models results, I suggest possible future research guide lines.

Chapter 2

X-ray impact on the protoplanetary disks around T Tauri stars

G. Aresu, I. Kamp, R. Meijerink, P. Woitke, W.-F. Thi, M. Spaans
Astronomy & Astrophysics, 2011, 526, A163

Abstract

T Taursi stars have X-ray luminosities ranging from $L_{\rm X} = 10^{28} - 10^{32}\,{\rm erg\,s^{-1}}$. These luminosities are similar to UV luminosities ($L_{\rm UV} \sim 10^{30} - 10^{31}{\rm erg\,s^{-1}}$) and therefore X-rays are expected to affect the physics and chemistry of the upper layers of their surrounding protoplanetary disks. The effects and importance of X-rays on the chemical and hydrostatic structure of protoplanetary disks are investigated, species tracing X-ray irradiation (for $L_{\rm X} \geq 10^{29}{\rm erg\,s^{-1}}$) are identified and predictions for [O I], [C II] and [N II] fine structure line fluxes are provided. We have implemented X-ray physics and chemistry into the chemo-physical disk code ProDiMo. We include Coulomb heating and H_2 ionization as heating processes and primary and secondary ionization due to X-rays in the chemistry. X-rays heat up the gas causing it to expand in the optically thin surface layers. Neutral molecular species are not much affected in their abundance and spatial distribution, but charged species such as N^+, OH^+, H_2O^+ and H_3O^+ show enhanced abundances in the disk surface. Coulomb heating by X-rays changes the vertical structure of the disk, yielding temperatures of $\sim 8\,000$ K out to distances of 50 AU. The chemical structure is altered by the high electron abundance in the gas in the disk surface, causing an efficient ion-molecule chemistry. The products of this, OH^+, H_2O^+ and H_3O^+, are of great interest for observations of low-mass young stellar objects with the Herschel Space Observatory. [O I] (at 63 and 145 μm) and [C II] (at 158 μm) fine structure emission are only affected for $L_{\rm X} > 10^{30}$ erg s^{-1}.

2.1 Introduction

Young stellar objects emit X-ray radiation (Koyama et al., 1994), which is associated with magnetic coronal processes (Flaccomio et al., 2005; Wolk et al., 2005; Imanishi et al., 2001), jets (Pravdo et al., 2001) mostly producing soft X-rays (Güdel et al., 2007), or outflows launched in the region between the star and the disk as predicted in the X-wind model (Shu et al., 2000). Non-accreting weak-line T Tauri stars (WTTS) are found to be more X-ray luminous than classical accreting T Tauri stars (CTTS) (Stelzer & Neuhäuser, 2001; Flaccomio et al., 2003,2005), because CTTS absorb part of the X-rays in the accretion column (Gregory et al., 2007).

The effects of stellar X-rays on protoplanetary disks around T Tauri stars have been studied by many groups: Glassgold et al. (2004, 2007) found X-rays to be important in heating the surface layers of the disk and estimated the strength of the fine-structure emission lines of [Ne II] and [Ne III], which arise from the warm disk atmosphere exposed to X-ray radiation. Nomura et al. (2007) focused on H_2 level populations and line emission, finding X-rays to control H_2 level population pumping together with UV. Following work of Meijerink et al. (2008), Ercolano et al. (2008) and Glassgold et al. (2009) studied atomic-line diagnostics of the inner regions of protoplanetary disks and formation of water in the warm disk atmosphere, respectively. Ercolano et al. (2008) and subsequent work focused on the X-ray role in causing photoevaporation of the surface layers of the disk. Gorti & Hollenbach (2004, 2008) include X-rays to predict [Ar II, [Ne II], [Fe I], [S I], [Fe II] and [Si II] as good indicators of gas physics in the disk. Woods & Willacy (2009) studied carbon isotope fractionation using the same method as Gorti & Hollenbach (2004) to calculate X-ray ionization rates. Recent work of Henning et al. (2010) studied the role of UV and X-rays on C_2H column densities and excitation conditions in disks around T Tauri stars.

The scope of this paper is to take a step back and first perform a study of the impact of X-rays on the 2D disk structure, on molecular ionized species and on observational diagnostics such as [O I], [C II] and [N II]. These molecular species were not studied in the above listed previous papers, but are of fundamental interest in the light of their recent detections with the Herschel satellite (Benz et al., 2010; Bruderer et al., 2010). We undertake an exploratory study in this letter of the relative effects of UV and X-rays on the protoplanetary disks hydrostatic, thermal and chemical structure using a series of X-ray models with different L_X (X-ray luminosity).

2.2 Model

The chemo-physical disk modeling code ProDiMo (Woitke et al., 2009; Kamp et al., 2010) has been updated with X-ray physics and chemistry.

2.2.1 Input spectrum

The incident stellar spectrum used in Woitke et al. (2009) is composed of a solar model with $T_{\rm eff} = 5\,800$ K and the cromospheric fluxes of HD 129 333 (Dorren & Guinan, 1994). The UV luminosity between 91.2 and 205 nm is $L_{\rm UV} \sim 4 \cdot 10^{31}$ erg

Table 2.1: Examples of molecular dissociation and cross section calculation: CO dissociation can end up in three different channels which are summed up to give the total CO cross section, CH is assumed to follow only one path.

Molecule	Product 1	Product 2	Cross Section
CO	C^{2+}	O	$\sigma_{CO} = 1/3\sigma_C +$
	C^+	O^+	$1/3(0.5\sigma_C + 0.5\sigma_O) +$
	C	O^{2+}	$1/3\sigma_O$
CH	C^{2+}	H	$\sigma_{CH} = \sigma_C$

Molecules included: H_2, CH, NH, OH, CN, CO, N_2, SiH, NO, O_2, SiO, CH_2, NH_2, H_2O, HCN, CO_2

Table 2.2: Parameters used in the models: the X-ray luminosity values correspond to `Models` from `1` to `5`.

Quantity	Symbol	Value
Stellar mass	M_*	1 $M_\odot$
Stellar luminosity	L_*	1 $L_\odot$
Disk mass	$M_{\rm disk}$	0.01 $M_\odot$
X-ray luminosity (0.1-50 keV)	$L_{\rm X}$	$0, 10^{29}, 10^{30}$ $10^{31}, 10^{32}$
Inner disk radius	$R_{\rm in}$	0.5 AU
Outer disk radius	$R_{\rm out}$	500 AU
Surface density power law index	ϵ	1.5
Min. dust particle size	$a_{\rm min}$	0.1 μm
Max. dust particle size	$a_{\rm max}$	10 μm
Dust size distribution power index	$a_{\rm pow}$	2.5

s^{-1}. Different models for the X-ray input spectrum are adopted in the literature: Nomura et al. (2007) use a two temperature thin thermal plasma model to fit the observed TW Hydrae spectrum; Ercolano et al. (2008) built synthetic coronal spectra using line and continuum emissivities from the CHIANTI compilation of atomic data; Gorti & Hollenbach (2008) use a thermal blackbody. We place the X-ray source on the star and follow Glassgold et al. (1997), Igea & Glassgold (1999) in using an analytic input spectrum to describe the Bremsstrahlung emission from an isothermal plasma: $F(E) \propto 1/E \cdot \exp(-E/kT_{\rm X})$ where E is the photon energy between 0.1 and 100 keV, $kT_{\rm X} = 1\,{\rm keV}$, and $T_{\rm X}$ is the plasma temperature. The X-ray input spectrum is added to the input spectrum shown in Fig. 2 in Woitke et al. (2009).

2.2.2 X-Ray chemistry

The following paragraphs describe the implementation of primary and secondary ionization in the code. 41 primary ionization reactions and 16 secondary ionization

reactions were added in the chemical network.

Primary Ionization

The primary rates for X-ray absorption are calculated following Meijerink & Spaans (2005) (Appendix D.3.1). The cross sections are taken from Verner & Yakovlev (1995). Since X-rays are likely absorbed in the K-shells, we assume that every X-ray absorption leads to a single ionization for H, He, Si, Cl and a double ionization for C, N, O, S and Fe (Meijerink & Spaans, 2005). We take into account molecular X-ray absorption, which leads always to dissociation, of the species. Table A.12 lists two examples of how the total dissociation rates are calculated. When the difference in weight of the elements that form the molecule is large (e.g. CH, OH, H_2O etc.), we use the cross section of the heavier element, when the weight is comparable (e.g. CO, CN, NO etc.) we combine the cross sections of the single elements.

Secondary Ionization

The fast electrons generated by the X-ray absorption can further ionize the gas. The rates are computed as shown in Meijerink & Spaans (2005, Appendix D.3.2) using experimental data from Lennon et al. (1988). The volumetric rates are a function of the local chemistry, i.e. they depend on the species densities $n_{\rm H}$, $n_{\rm H_2}$, $n_{<\rm H>}$ and $n_{\rm e}$ (where $n_{\rm H}$ is the hydrogen atom density and $n_{<\rm H>}$ is the hydrogen nuclei density). This has to be taken into account when solving the chemical equilibrium. The additional entries in the chemical Jacobian that come from the X-ray secondary ionization reactions are implemented following Sect. 5.6 in Woitke et al. (2009).

2.2.3 X-Ray heating

We added Coulomb heating (Dalgarno et al., 1999) and H_2 ionization heating (Meijerink & Spaans, 2005, Appendix B.1) to the heating processes listed in Woitke et al. (2009). The Maloney et al. (1996) heating rate only holds for gas with low x_e, while Dalgarno et al. (1999) present the more general case for different high and low ionization gases (atomic/molecular). The heating efficiency increases by a factor 7-8 in a highly ionized atomic gas and a factor 2 in a highly ionized molecular gas (Shull & van Steenberg, 1985).

2.2.4 Parameter space

We computed five different models with increasing $L_{\rm X}$ to compare the results with the UV only case (`Model 1`) for a disk surrounding a T Tauri star (Table 2.2).
In `Model 1` X-rays are switched off. This is the model as presented in Woitke et al. (2009). For more details, we refer to the original paper. X-ray models (`Model 2 – 5`) have the same parameters as `Model 1`, but include stellar X–rays ($L_{\rm X} = 10^{29} - 10^{32}\,{\rm erg\,s^{-1}}$). We added Cl, Cl^+ and double ionized species (C^{2+}, N^{2+}, O^{2+}, S^{2+}, Fe^{2+}) to the chemical network. The X-ray emission is treated as a point source at the location of the star.

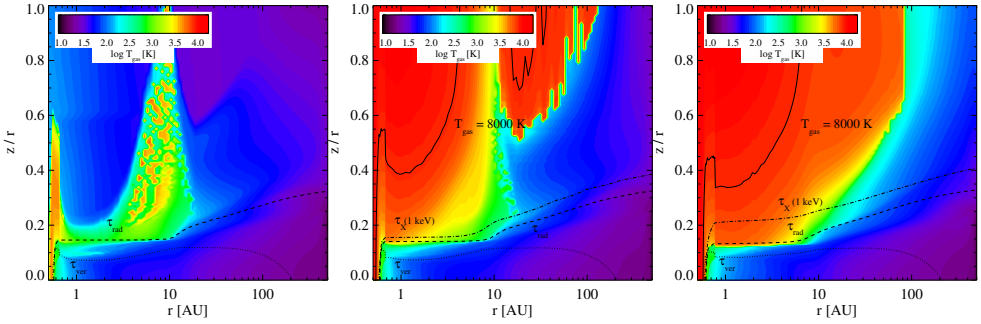

Figure 2.1: Gas temperature distribution: `Model 1` (UV only) in the left panel, X-ray models with $L_{\rm X} = 10^{30}{\rm erg\,s^{-1}}$ (`Model 3`), $L_{\rm X} = 10^{32}{\rm erg\,s^{-1}}$ (`Model 5`) in the middle and right panel respectively. Contour lines are over-plotted for $\tau_{\rm rad} = 1$ (radial dust optical depth at 550 nm, dashed line), $\tau_{\rm ver} = 1$ (vertical dust optical depth at 550 nm, dotted line) and X-ray optical depth of one at 1 keV (dot-dashed line). The relative position of these two depth depend strongly on the assumed dust properties (see Table 2.2). The solid line corresponds to $T_{\rm gas} = 8\,000$ K.

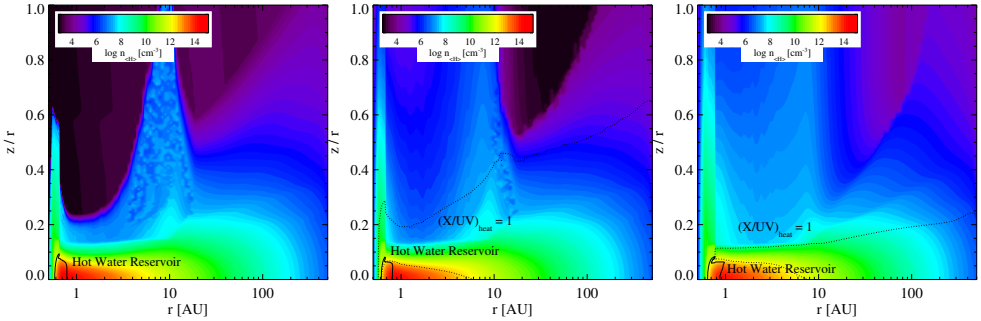

Figure 2.2: Total hydrogen nuclei density $n_{<{\rm H}>}$ distribution: `Model 1` (UV only) in the left panel, X-ray models with $L_{\rm X} = 10^{30}{\rm erg\,s^{-1}}$ (`Model 3`), $L_{\rm X} = 10^{32}{\rm erg\,s^{-1}}$ (`Model 5`) in the middle and right panel respectively. The dotted contour line shows where the ratio between Coulomb heating and photo-electric plus PAH heating equals 1. The solid line circles the hot water reservoir ($T_{\rm H_2O} > 200$ K).

2.3 Results

We analyze the results obtained from the five models described above. We first present the thermal and hydrostatic structure of the various models. Then we describe the impact of X-rays on the chemistry and fine structure line emission, focusing on the main differences between the UV only model and the combined UV+X-ray models.

Temperature and density structure

The low density ($n_{<H>} < 10^8\,\mathrm{cm}^{-3}$) surface layers directly exposed to X-ray radiation are heated efficiently via Coulomb heating: in all X-ray models temperatures reach up to ∼8 000 K (Fig. 2.1). The extension of this high temperature region increases with L_X: it reaches 2 AU in `Model 2` and 100 AU in `Model 3` and `Model 4`. In `Model 5` the temperature is slightly lower for $r > 50$ AU but the whole disk is warmer (Fig. 2.1). X-rays dominate the thermal balance only in the upper layers down to $(X/UV)_{heat} = 1$. Beyond $(X/UV)_{heat} = 1$, UV heating takes over and becomes the main heating process. Deeper in the midplane, both X-ray and UV heating are negligible, but their ratio is inverted again and harder X-rays ($E > 10$ keV) deposit more energy than UV radiation (Fig. 2.2).

The inner wall of the disk is always directly illuminated by the stellar radiation causing the inner rim (0.5 AU $< r <$ 0.7 AU) to have a large scale height and hence vertical extent. In the UV model the shadowed disk atmosphere beyond the inner rim has a lower vertical scale height since radiation cannot penetrate efficiently and sustain high gas temperature. Only radiation that impinges the disk at higher angles ($z/r > 0.6$) and scattered radiation reach the outer disk causing the temperature to increase and consequently the second bump at ∼ 9 AU. When X-rays are switched on, the temperature increase in the surface layers affects directly the vertical density distribution there since we keep the radial surface density profile fixed. The inner rim of the disk ($r < 1$ AU and $z/r > 0.1$) is more puffed up (Fig. 2.2). The second bump at ∼ 9 AU is more vertically extended as well; in `Model 5` it even "merges" with the inner rim and flares as a whole (Fig. 2.2, third panel).

Chemistry

The abundances of neutral molecules such as CO and OH and H_2O generally change by less than an order of magnitude over the entire modeling space. On the other hand, the ion chemistry in the disk surface is strongly changed: the electron abundance in the upper layers increases by a factor 10^4. This leads to an enhancement of OH^+, H_2O^+, H_3O^+ and N^+ abundances. Secondary ionization of H_2 increases the H_2^+ abundances. H_2^+ collisions with H_2 produce H_3^+. Subsequent collisions of H_3^+ with O, OH and H_2O lead to the production respectively of OH^+, H_2O^+ and H_3O^+. Fig. 2.4 shows how the vertical column densities of these species change with L_X for three different disk radii: 3, 10 and 100 AU. OH^+ and H_2O^+ respond more efficiently than H_3O^+ to the X-ray radiation as the total mass ratio $M(OH^+)/M(H_2O^+)$ is only doubled from `Model 1` to `Model 5`, while $M(OH^+)/M(H_3O^+)$ increases by more than a factor 5.

OH^+: OH^+ formation is enhanced approximately proportional to the X-ray luminosity. Its total mass increases from $8 \times 10^{-15}\,M_\odot$ in `Model 1` by a factor 3.6 in `Model 3` and about 500 times in `Model 5` (Table 2.4).

As the X-ray luminosity increases, OH^+ formation is enhanced and pushed outwards, where the disk is colder. The column density of OH^+ increases substantially beyond $r > 10$ AU in all models. It reaches ∼ 100 times its initial value (`Model 1`) in

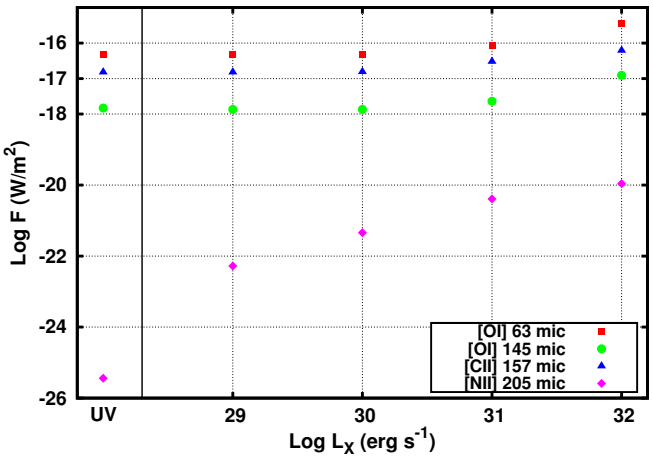

Figure 2.3: Oxygen line flux emission at 63 and 157 μm, ionized carbon line flux emission at 157 μm and ionized nitrogen line flux emission at 205 μm as a function of the X-ray luminosity. All fluxes are compiled for a distance of 140 pc. The correlation between N II and L_X is clear, while O I and C II show no correlation for $L_X < 10^{30}$ erg s^{-1}.

`Model 3` at 100 AU (Fig. 2.4).

H_2O^+: The H_2O^+ mass increases by 3 times (factor of 100) between `Model 1` and `Model 3` (`Model 5`). The column density again increases toward the outer part of the disk. `Model 3` has $\sim$ 10 times higher column density than `Model 1` at 10 and 100 AU. As in the case of OH^+, H_2O^+ is pushed toward the outer part of the disk with increasing X-ray luminosity.

H_3O^+: The H_3O^+ mass is slightly less affected by X-rays: it is 2 times higher than in the UV case in `model 3` and 10 times in `model 4` . In `model 3`, `model 4` and `model 5`, H_3O^+ is also clearly pushed to larger radii and lower temperatures.

N^+: We find the most extreme mass increase for N^+ in all X-ray models (Table 2.4) and at all radii: in `model 3` it is 1 000 times higher than in the UV only case.

In `models 4` and `5`, the N^+ mass increases over-proportionally in the outer part of the disk (Fig. 2.4, right lower panel). Figure 2.5 shows the column density ratio of the X-ray dominated N^+ to the UV dominated C^+. With increasing L_X, the N^+ column density is enhanced by two (outer disk) to six (inner disk) orders of magnitude.

Line Predictions

In table 2.3 we list the flux prediction of [O I] 63 μm, [O I] 145 μm, [C II] 157 μm and [N II] 205 μm for all the models. Fig. 2.3 shows their values as a function of the X-ray luminosity. The [N II] line flux shows the strongest correlation with the X-ray

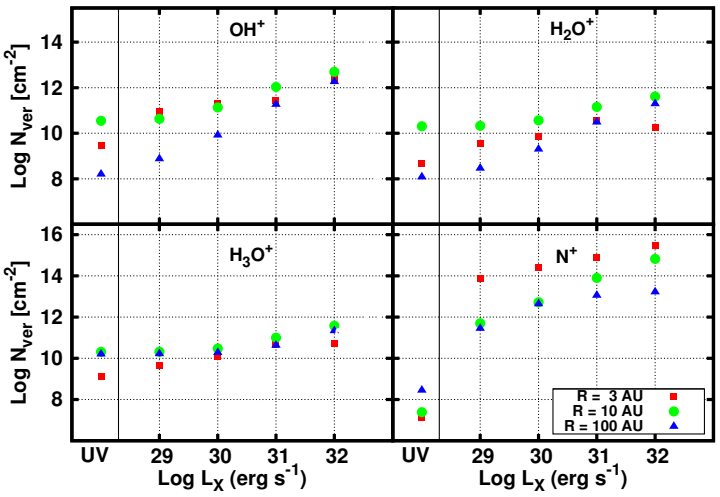

Figure 2.4: Column density of OH^+ (upper left panel), H_2O^+ (upper right panel), H_3O^+ (lower left panel) and N^+ (lower right panel) at three different radii (3, 10, 100 AU) versus X-ray luminosity. In each panel the UV only model is indicated with the "UV" label on the x-axis.

flux, increasing by 5 orders of magnitude from `model 1` to `model 3`. The oxygen fine structure line fluxes and the [C II] line flux are constant from `model 1` to `3` (Fig. 2.3), due to the fact that they originate in the UV heated layer. Only in `model 4` and `5` the line fluxes increase with L_X.

Table 2.3: Predicted line fluxes of [O I] at 63 μm, [C II] at 157 μm and [N II] at 205 μm for all the models expressed in W/m^2. All fluxes are computed for a distance of 140 pc.

Line	`Model 1`	`Model 2`	`Model 3`	`Model 4`	`Model 5`
[O I] 63 μm	4.8(-17)	4.6(-17)	4.8(-17)	8.3(-17)	3.6(-16)
[O I] 145 μm	1.5(-18)	1.3(-18)	1.4(-18)	2.3(-18)	1.2(-17)
[C II] 157 μm	1.5(-17)	1.5(-17)	1.7(-17)	3.0(-17)	6.1(-17)
[N II] 205 μm	3.6(-26)	5.2(-23)	4.6(-22)	4.1(-21)	1.1(-20)

2.4 Discussions and conclusions

We find that X-rays mainly impact the surface layers of protoplanetary disks. The hydrostatic structure of these layers is significantly changed: X-ray radiation is mostly absorbed in the tenuous layers ($z/r \geq 0.2\,\mathrm{cm}^{-3}$) increasing the temperature up to

Table 2.4: Species masses given in units of solar mass in all the models. Luminosities are expressed in erg/s.

Species	UV Only	$L = 10^{29}$	$L = 10^{30}$	$L = 10^{31}$	$L = 10^{32}$
H	5.0(−05)	5.0(−05)	5.2(−05)	7.1(−05)	1.4(−04)
H_2	7.6(−03)	7.6(−03)	7.6(−03)	7.6(−03)	7.5(−03)
C	3.0(−07)	3.0(−07)	3.1(−07)	3.4(−07)	4.8(−07)
C+	1.3(−07)	1.3(−07)	1.3(−07)	1.4(−07)	1.8(−07)
O	1.4(−05)	1.4(−05)	1.4(−05)	1.4(−05)	1.4(−05)
CO	9.5(−06)	9.4(−06)	9.3(−06)	9.0(−06)	9.0(−06)
OH	3.4(−11)	3.4(−11)	3.7(−11)	7.0(−11)	2.8(−10)
H_2O	7.7(−07)	4.7(−08)	3.6(−08)	2.7(−08)	3.3(−08)
OH^+	7.9(−15)	1.1(−14)	2.9(−14)	4.1(−13)	4.6(−12)
H_2O^+	1.9(−15)	2.1(−15)	5.3(−15)	6.2(−14)	4.2(−13)
H_3O^+	3.4(−15)	3.7(−15)	7.3(−15)	4.8(−14)	3.5(−13)
N^+	2.9(−15)	8.7(−13)	3.9(−12)	9.9(−12)	3.6(−11)

$\sim 8\,000$ K; at those temperatures cooling by [O I], Fe II and Lyα balance the X-ray heating. This causes the density structure to flare stronger than in the UV only case (Fig. 2.2).

The general results from Nomura et al. (2007) and Glassgold et al. (2004) are qualitatively confirmed, showing that the inner rim and the surface layers are dominated by X-rays. In addition we find that more distant parts, up to 100 AU, are affected as well (Fig. 2.4). We find that the size of the high temperature X-ray driven region increases with L_X. This is due both to the fact that our model uses the Dalgarno et al. (1999) prescription for the X-ray heating and to our choice of the input spectrum. The Dalgarno et al. (1999) heating efficiencies lead to $\sim 7 - 8$ times higher rates in regions with high electron fraction, compared to Maloney et al. (1996). Furthermore our input spectrum has higher photon flux in the range 0.1-0.3 keV compared with, e.g., Gorti & Hollenbach (2008) and Nomura et al. (2007). These soft X-ray photons are absorbed at low vertical column densities causing high e^- densities there and thus are more efficient in heating the upper layers. This effect was also noted in Gorti et al. (2009).

Gorti & Hollenbach (2008) found X-rays to be the dominant heating process in slightly deeper layers than we do. This is most likely due to the fact that we include UV scattering from dust, which leads to a larger vertical penetration of FUV radiation in the disk. Nomura et al. (2007) also show that FUV penetrates deeper than X-rays, because FUV scattering is more efficient than X-ray Compton scattering at 1 keV, which is not included in our model. Gorti & Hollenbach (2008) also consider a less steep surface density distribution which yields less mass at 1 AU, where most of the X-ray radiation is absorbed in our model.

The X-ray energy deposition does not affect neutral oxygen fine structure emission at 63 and 145 μm (Table 2.3), unless the X-ray luminosity is pushed to $L_X > 10^{30}\,\mathrm{erg\,s^{-1}}$, where X-ray heating dominates in the regions where the emission takes place. Ionized carbon emission at 157 μm is only slightly affected by the

X-rays in all the models, as the line emission is dominated by material at R > 200 AU (Woitke et al., 2009; Kamp et al., 2010), where the X-ray contribution to the chemistry and thermal balance is negligible. Our values are in good agreement with Meijerink et al. (2008) and Ercolano et al. (2008) for $L_X \sim 10^{30}$ erg s^{-1}. However the correlation of the oxygen line fluxes with L_X, found in the Meijerink et al. (2008) model is due to the lack of UV radiation in their model. In our model at low L_X, the UV heating provides the gas temperature to sustain a constant level of [O I] emission.

We find H_2, CO and OH properties in the X-ray models largely unvaried with respect to `Model 1`. The largest change occurs for water which mass diminishes by a factor 20 in the highest L_X model compared with the UV only model. The X-rays enhance the electron abundance in the surface layers, where we find $x_e \sim 0.1$ for $z/r \sim 0.9$ out to 100 AU. Ionized species abundances are enhanced, such as OH^+, H_2O^+, H_3O^+ and N^+. The molecular ionized species formation is pushed outwards as L_X increases. High abundances of OH^+ and H_2O^+ are a characteristic signature of an X-ray dominated region as recently discussed by van der Werf et al. (2010) after the detection with Herschel/SPIRE in the ultra-luminous galaxy Mrk 231. Furthermore this is extremely interesting in the context of the recent detection of these species in a massive YSO by Herschel (Benz et al., 2010). The column densities that we find from our X-ray irradiated disks are of the same order of magnitude as those derived in Benz et al. (2010). This suggests that a disk could in principle bring a substantial contribution to the line fluxes emitted from these molecules, making our result extremely relevant for future Herschel studies of low mass YSOs.

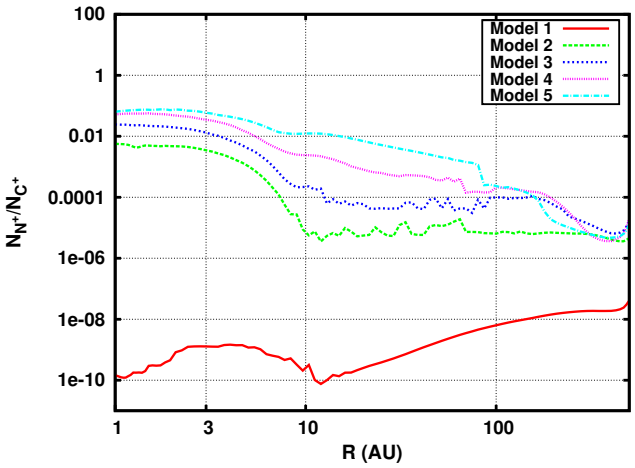

Figure 2.5: Column density ratio between the X-ray dominated N^+ and the UV dominated C^+. The latter does not change in the X-ray models with respect to the UV model

The abundance of these ions increases especially at larger radii ($r > 10$ AU), while the N^+ abundance rises considerably at all radii. The latter is not observed in the UV model due to the high ionization potential of N(I.P.) = 14.5 eV. We find that the N^+ flux emitted at 205 μm in `model 3` is $\sim 5 \times 10^{-22}$ W/m^2, coming for

90% from the upper layers beyond 10 AU. This is much smaller than the current Herschel sensitivity limit of $5 \times 10^{-18}\,\mathrm{W/m^2}$ (HIFI, $5\,\sigma$ in 1 hour) and even below current sensitivity estimates for SPICA/SAFARI (10^{-19} W/m^2, $5\,\sigma$ in 1 hour). We only consider X-ray ionization, but the flux is unlikely to change if EUV is present. Additional ionization occurs only at smaller radii, because of the low penetration depth of EUV radiation (Hollenbach & Gorti, 2009). The molecular ionized species formation is pushed toward the outer disk as L_X increases.

2.5 Outlook

The predicted N^+ line fluxes are too low to be observed with current instruments. In contrast, the [O I] 63 μm and [C II] 157 μm lines are observable in the presence of UV luminosities of $\sim 10^{31}$ erg s^{-1} and/or strong X-rays ($L_X > 10^{30}$ erg s^{-1}). In the context of the current Herschel observatory, the OH^+, H_2O^+ and H_3O^+ lines are extremely interesting as they are likely observable with the HIFI, PACS and SPIRE instruments. These hydride ions and the already observed [Ne II] and [Ar II] line fluxes, will be addressed in the subsequent paper. We will also investigate a larger parameter space and the effect of the change in disk structure - especially the higher inner rim and increased flaring - on the overall SED.

Chapter 3

FUV and X-ray irradiated protoplanetary disks: a grid of models - I. The disk structure

R. Meijerink, G. Aresu, I. Kamp, M. Spaans, W.-F. Thi, P. Woitke
Astronomy & Astrophysics, 2012, 547, A68

Abstract

Planets are thought to eventually form from the mostly gaseous ($\sim 99\%$ of the mass) disks around young stars. The density structure and chemical composition of protoplanetary disks are affected by the incident radiation field at optical, far-ultraviolet (FUV), and X-ray wavelengths, as well as by the dust properties. The effect of FUV and X-rays on the disk structure and the gas chemical composition are investigated. This work forms the basis of a second paper, which discusses the impact on diagnostic lines of, e.g., C^+, O, H_2O, and Ne^+ observed with facilities such as Spitzer and Herschel. A grid of 240 models is computed in which the X-ray and FUV luminosity, minimum grain size, dust size distribution, and surface density distribution are varied in a systematic way. The hydrostatic structure and the thermo-chemical structure are calculated using Protoplanetary Disk Model (ProDiMo), with the recent addition of X-rays. The abundance structure of neutral oxygen is very stable to changes in the X-ray and FUV luminosity, and the emission lines will thus be useful tracers of the disk mass and temperature. The C^+ abundance distribution is sensitive to both X-rays and FUV. The radial column density profile shows two peaks, one at the inner rim and a second one at a radius $r = 5-10$ AU. The minimum is caused by shadowing from the inner rim. The fluctuations in value of the column density as a function of radius are smoothed out when FUV and X-ray luminosities increase. Ne^+ and other

heavy elements with an ionization potential higher than $IP > 13.6$ eV have a very strong response to X-rays, and the column density in the inner disk increases by two orders of magnitude from the lowest ($L_{\rm X} = 10^{29}$ erg s^{-1}) to the highest considered X-ray flux ($L_{\rm X} = 10^{32}$ erg s^{-1}). FUV confines the Ne^+ ionized region to areas closer to the star at low X-ray luminosities ($L_X = 10^{29}$ erg s^{-1}). This is indirectly caused by changes in the disk structure. The radial column densities of Ne^+ are higher than 10^{12} cm^{-1} out to radii $r > 100$ AU (at $L_{\rm FUV} \geq 10^{31}$ erg s^{-1}), whereas the column density already drops below this value at radii $r > 20$ AU at $L_{\rm FUV} = 10^{32}$ erg s^{-1}. H_2O abundances are enhanced by X-rays due to higher temperatures in the inner disk than in the FUV only case, thus leading to a more efficient neutral-neutral formation channel. Also, the higher ionization fraction provides an ion-molecule route in the outer disk. The line fluxes and profiles are affected by the effects on these species, thus providing diagnostic value in the study of FUV and X-ray irradiated disks around T Tauri stars.

3.1 Introduction

New observing facilities in the past decade pushed our understanding of protoplanetary disks from a rough picture of a vertically layered structure to a wealth of details on the composition and two-dimensional structure of the gas and dust of these disks. In the infrared, the Spitzer Space Telescope performed systematic studies of nearby star-forming regions. The spectral energy distributions (SEDs) revealed the physical structure of disks, e.g., the presence of gaps, source-to-source variations and important statistics on SED types, which allows evolutionary scenarios to be built (cf. Merín et al., 2010). Extensive gas-phase emission line studies with Spitzer provide a first indication of chemical diversity across stellar spectral types (cf. Najita et al., 2009; Pontoppidan et al., 2010; Lahuis et al., 2007). In the near-infared, there have been large ground-based studies with, e.g., the VLT and the Keck telescope resolving the lines to study the kinematics (spatial origin of the lines in hot disk surfaces and winds) and their excitation mechanisms (thermal and fluorescence; Brittain et al., 2010; Pontoppidan et al., 2011; Fedele et al., 2011). In the past two years, the Herschel Space Observatory extended the spectral window to the far-IR and submm, with spectral line scans within the Dust, Ice, and Gas in Time (DIGIT) key program (PI: N. Evans) for many Herbig disks, e.g., HD 100546 (Sturm et al., 2010), water studies of a few selected targets, such as TW Hya (Hogerheijde et al., 2011) from the Water in Star-forming Regions with Herschel (WISH) key program (PI: E.van Dishoeck), and large statistical gas surveys targeting the dominant cooling lines (e.g., Mathews et al., 2010; Meeus et al., 2012; Dent & the GASPS team, 2012; Riviere-Marichalar et al., 2012) in the Gas in Protoplanetary Systems (GASPS) key program (PI: B. Dent). The HIFI and some PACS line detections deal with the cold water, while the 63.3 μm H_2O line possibly probes the inner water reservoir.

Observational studies report trends in emission line strength with the irradiation of the central star. Güdel et al. (2010) find that the [Ne II] emission at 12.81 μm correlates with the X-ray luminosity of the central star; the slope of the correlation for nonjet sources is 0.44 ± 0.18. Pinte et al. (2010) and Meeus et al. (2012) show that the

[O I] 63 μm line flux increases with stellar luminosity and that this is largely driven by the strength of the far-ultraviolet (FUV) luminosity. Riviere-Marichalar et al. (2012) report a tentative trend of the 63.3 μm water line flux with X-ray luminosity.

It is obvious from previous works that the most relevant parameter for the SED is the total stellar luminosity; in most cases, $L_{\rm X}$ and $L_{\rm FUV}$ present only a small fraction of this and hence by themselves do not cause significant SED changes. However, recent near-IR high-contrast imaging with HiCIAO on the Subaru 8.2 m telescope allowed probing of the inner disk structure on scales below 0.1 (Thalmann et al., 2010; Hashimoto et al., 2011). This offers the possibility of a direct probe, e.g., the height of the inner rim as predicted by protoplanetary disk models. Thi et al. (2011) predicted that the height of the inner rim could be a factor two higher when the vertical hydrostatic structure takes into account the gas temperature at the inner rim. Aresu et al. (2011) show that the height of the inner rim increases in disk models with the impinging stellar $L_{\rm X}$.

In the last decade, much theoretical progress has taken place to support the interpretation of the wealth of new observations, specifically the gas observations. The foundation was laid by Chiang & Goldreich (1997), D'Alessio et al. (1998), and Dullemond et al. (2001), whose layered dust disk models have helped to interpret SEDs for irradiated disks (see Dullemond et al. 2007 for a review of disk structure models). Based on this, several groups focussed on the effects of FUV and X-rays on the thermal and chemical structure of the gas in a pre-prescribed protoplanetary disk model, e.g., van Zadelhoff et al. (2003), Kamp & Dullemond (2004), Jonkheid et al. (2004), and Glassgold et al. (2004). In a subsequent step, Nomura & Millar (2005), Gorti & Hollenbach (2008), and Woitke et al. (2009) studied the chemical structure of disks, while self-consistently solving for the vertical hydrostatic equilibrium using the gas temperature. Most recently, Aresu et al. (2011) performed an exploratory study to assess the relative importance of FUV and X-rays by expanding the existing Protoplanetary Disk Model (ProDiMo) code to include X-ray processes. The modeling efforts that solve for the vertical disk structure are computationally expensive because the chemical networks, heating/cooling balance, 2D continuum radiative transfer, and hydrostatic equilibrium have to be solved iteratively. Hence, these studies have largely focussed on a single representative disk model, or at most a handful of models, varying one specific parameter. However, large-model grids are in principle required to understand the potential diagnostic power of certain observables. So far examples for this are large grids (of the order of 200 000-300 000 models) of parametrized dust disk models to study SED diagnostics (Robitaille et al., 2006) and of parametrized gas/dust disks to study the gas emission line diagnostics (Woitke et al., 2011; Kamp et al., 2011).

In this paper, we perform for the first time an extensive analysis of a grid of 240 self-consistent disk models (including the vertical disk structure) to study the effects of X-rays, FUV, and the relative importance of grain size and gas surface density distribution on the thermal, chemical, and physical structure of disks around T Tauri stars. This paper builds on the implementation of X-rays into the ProDiMo code as described in Aresu et al. (2011). While we discuss here foremost the physical and chemical structure of the models and how they change with irradiation, a companion paper (Aresu et al., 2012, paper II), discusses the power of line diagnostic in disentan-

gling these effects. The paper is structured in the following way: Sect. 3.2 describes the updates on the code and the range of parameters used in the grid. The effects on disk temperature and density structure will be discussed in Sect. 3.3. The resulting distribution of various key species and its key reactions are extensively described in Sect. 3.4. Sect. 3.5 shows the radial column density distributions. Those are key in understanding the line profiles, which is the topic of the accompanying paper II. Sect. 3.6 summarizes the conclusions and implications of the paper.

3.2 Updates on ProDiMo and the calculated grid

The original ProDiMo code (Woitke et al., 2009) is based on the code as discussed by Kamp & Dullemond (2004). The original model includes (1) frequency-dependent two-dimensional dust continuum radiative transfer, (2) kinetic gas-phase and FUV photo-chemistry, (3) ice formation, and (4) detailed non-local thermodynamic equilibrium (non-LTE) heating and cooling with (5) a consistent calculation of the hydrostatic disk structure. The models are characterized by a high degree of consistency among the various physical, chemical, and radiative processes, since the mutual feedbacks are solved iteratively. Aresu et al. (2011) included X-ray heating and chemical processes, guided by work from Maloney et al. (1996), Glassgold et al. (2004), and Meijerink & Spaans (2005), while most recently the X-ray chemistry processes are updated following Ádámkovics et al. (2011). This includes an extension of our chemical network with species such as Ne, Ar, and their singly and doubly ionized states, as well as other heavy elements. We added Ne^+, Ne^{2+}, Ar^+, and Ar^{2+} in the heating/cooling balance and also implemented an extended sulfur chemistry (following Leen & Graff, 1988; Meijerink et al., 2008, e.g., SO, SO_2, HS, and their related reactions were added) to achieve a proper calculation of the sulfur-based species abundances. This allowed us to make more realistic predictions of, e.g., the sulfur fine-structure lines. A detailed description on the treatment of X-ray chemistry in the code is given in Appendix A.

Our input spectrum is composed of the stellar spectrum and a FUV excess as described in Woitke et al. (2009), along with an X-ray component as outlined in Aresu et al. (2011). The FUV excess (from 92.5 to 205 nm) spectrum is a power law with $I_\nu(\lambda) \propto \lambda^{1.2}$. The X-ray spectrum (0.1 - 10 keV) has been chosen following Glassgold et al. (2007) and is the same we used in Aresu et al. (2011). It is a bremsstrahlung spectrum with $I_\nu(E) \propto 1/E \times \exp(-E/kT)$ (see Fig. 3.1). We varied those quantities that could potentially affect the penetration of X-ray and FUV radiation and change the energy deposition through the disk. For example, we use two different values for the dust size distribution power law. The first value, generally used in the literature for the ISM, is a power law index of $a_{\rm pow} = 3.5$. It is well known, though, that dust coagulation is the seed process that in timescales of a few million years leads to the formation of planetesimals. To model a disk that could have undergone dust coagulation, we also adopt a shallower power law index of $a_{\rm pow} = 2.5$. For the same reason, we vary the minimum dust size: 0.1, 0.3, and 1 μm. These two parameters ($a_{\rm min}$ and $a_{\rm pow}$) determine the FUV opacity and, as a result, impact the amount of energy reprocessed by the photo-electric heating. Ultimately, the parameters affect the gas thermal balance in the disk. The changing opacity and optical depth also

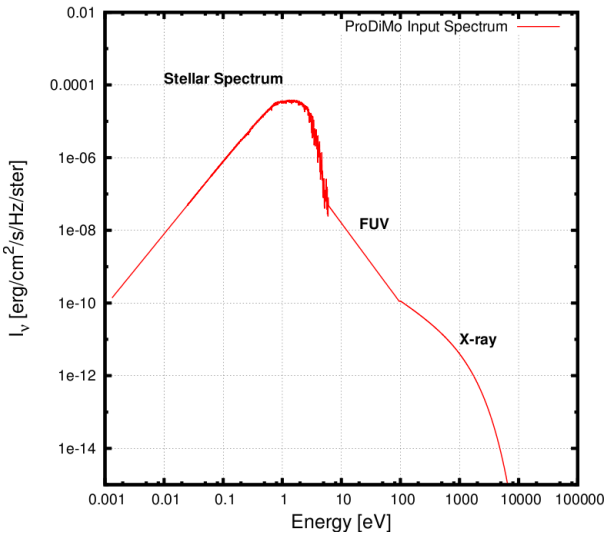

Figure 3.1: Input spectrum for model with $L_{\rm X} = 10^{30}$ erg s^{-1} and $L_{\rm FUV} = 10^{31}$ erg s^{-1}.

impact the dust temperature $T_{\rm dust}$.

Aresu et al. (2011) performed an exploratory study on the influence of X-rays and FUV irradiation on the structure of protoplanetary disks, for X-ray luminosities ranging from $L_x = 10^{29} - 10^{32}$ erg s^{-1}. The range of values for this particular parameter is based on the outcome of the Taurus survey (**?**), which showed that X-ray-active T Tauri stars emit in the range $L_{\rm X} = 10^{29} - 10^{31}$ erg s^{-1}. The model with $L_X = 10^{32}$ erg s^{-1}, on the other hand, is an extreme case with interesting implications in terms of modeling. FUV excess emission from classic T Tauri stars between 6 and 13.6 eV is believed to arise from accretion spots on the surface of the star and stellar activity. The disk is truncated to several stellar radii from the star magnetic field, which channels matter toward the stellar photosphere. Shocks in the outer layers of the star cause the temperature to rise and emit FUV photons, which results in a FUV excess with respect to the stellar luminosity in the same band (Gullbring et al., 2000). Gorti & Hollenbach (2008) infer the FUV excess luminosity (91.2 nm $< h\nu <$ 205 nm) to be between $L_{\rm FUV}/L_* \sim 10^{-2} - 10^{-3}$. In our grid, we decided to scale the FUV flux so that we obtain the same range of luminosities as we use for the X-rays. The adopted values of $L_{\rm FUV}/L_*$ are then $2.6{\times}10^{-2}$, $2.6{\times}10^{-3}$, $2.6{\times}10^{-4}$, and $2.6{\times}10^{-5}$. This way we can directly compare the input energy radiation in the FUV and X-ray band as well as its effects on the disk. We also explore two different values for the surface density power law distribution ϵ, which is defined as $\Sigma(r) = \Sigma(r_0) \times (r/r_0)^{-\epsilon}$: Hayashi (1981) derived the value $\epsilon = 1.5$ in his model for the minimum mass solar nebular (MMSN) and their diagnostic value for our own solar system, while Hartmann (1998) suggested $\epsilon = 1$ for objects older than 1 Myr.

In summary, the current paper discusses the effects of variations in the following parameters: X-ray luminosity (five values), FUV luminosity (four), surface density

Table 3.1: Parameters used in the models.

Quantity	Symbol	Value
Stellar mass	M_*	1 $M_\odot$
Effective temperature	$T_{\rm eff}$	5770 K
Stellar luminosity	L_*	1 $L_\odot$
Disk mass	$M_{\rm disk}$	0.01 $M_\odot$
X-ray luminosity (0.1-50 keV)	$L_{\rm X}$	$0, 10^{29}, 10^{30}$ $10^{31}, 10^{32}$ erg s^{-1}
FUV luminosity	$L_{\rm FUV}$	10^{29}, 10^{30}, 10^{31}, 10^{32} erg s^{-1}
Inner disk radius	$r_{\rm in}$	0.5 AU
Outer disk radius	$r_{\rm out}$	500 AU
Surface density power law index	ϵ	1.0, 1.5
Dust-to-gas mass ratio	ρ_d/ρ	0.01
Min. dust particle size	$a_{\rm min}$	0.1, 0.3, 1.0 μm
Max. dust particle size	$a_{\rm max}$	10 μm
Dust size distribution power index	$a_{\rm pow}$	2.5, 3.5
Dust material mass density	$\rho_{\rm gr}$	2.5 g cm^{-3}
Strength of incident ISM FUV	$\chi^{\rm ISM}$	1
Cosmic ray ionization rate of H_2	$\zeta_{\rm CR}$	5×10^{-17} s^{-1}
Abundance of PAHs relative to ISM	$f_{\rm PAH}$	0.12
Viscosity parameter	α	0

profile (two), and dust size distribution, varying both the minimum grain size a_{min} (three) as well as power law indices (two). This yields a total of 240 models; the summary of the model parameters is given in Table 3.1.

3.3 Disk thermal and density structure

The coupling of gas and dust to the radiation field determines the heating and cooling rates, which in return determine the pressure balance and structure of a disk. FUV and X-rays couple differently to the gas: FUV is absorbed by dust grains and ejects an electron with a small surplus of energy in the form of kinetic energy, which then consequently heats the gas. X-rays, on the other hand, are absorbed by the K-, L-, or M-shell of atoms, where no distinction is made as to whether this atom is part of a molecule, dust grain, or PAH. This assumption might overestimate the X-ray absorption cross section by a factor of approximately ~ 2 at energies $E < 1$ keV, since we do not include self-shielding effects by large grains (see, e.g., Fig. 1 of Fireman, 1974). On the other hand, not much is known about gas and dust phase elemental abundances in disks. The observed abundance of, e.g., neon (dominating the X-ray absorption cross section between ~ 0.9 to 1.2 keV, and, as such, the total absorption of our 1 keV thermal source), already varies over a larger range (see Glassgold et al., 2004, for a discussion on this topic). The electron that is ejected has a large energy

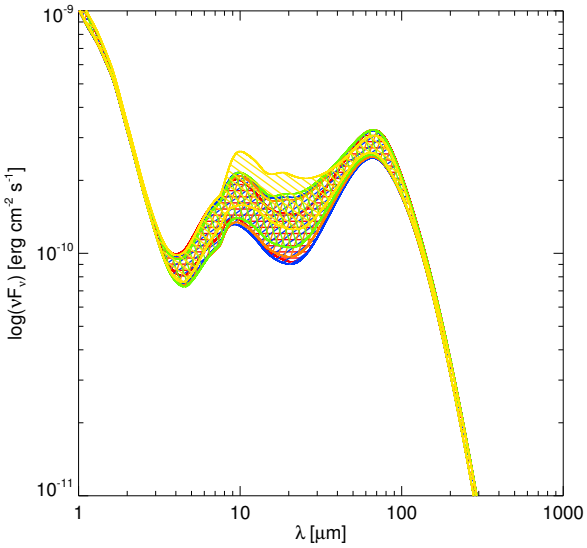

Figure 3.2: Average spectral energy distributions of models with $L_{\rm X} = 0$ (red), 10^{29} (blue), 10^{30} (orange), 10^{31} (green), and 10^{32} erg s^{-1} (yellow).

capable of exciting, ionizing and heating the gas. The efficiency for X-ray heating is much larger, about 10 to 40 percent, depending on the ionization fraction of the gas, while that for FUV heating does not exceed one to three percent. The coupling of X-rays to gas is weaker than for FUV, due to the smaller cross section for the absorption, but the larger efficiency makes sure that it is an important heating source, even when the FUV excess is large. Their relative contribution to the energy budget will result in a different structure and emitted line fluxes. X-rays do not much affect the continuum fluxes, certainly less than $a_{\rm min}$, $a_{\rm pow}$, and ϵ (see Fig. 3.2). It shows that the fluxes change at most by a factor of three between $\lambda = 5 - 100$ μm due to X-rays. The models with $L_{\rm X} = 10^{32}$ erg s^{-1} are affected most, and these high X-ray fluxes are rarely observed for T Tauri stars.

Woitke et al. (2009) have already pointed out that the cooling and heating balance is very important in determining the physical structure of the disk. They present in their Fig. 9 the density structures for (1) a model where the gas temperature is decoupled from the dust and (2) where the gas and dust temperature are coupled. Model 1 shows a very complex structure, where the gas is puffed up at the inner rim and a second bump in the density is seen at a radius $r \sim 10$ AU. Aresu et al. (2011) extended this model by including X-rays and showed for the particular model of Woitke et al. (2009) that the vertical extension inward of 10 AU becomes smoothed out for increasing X-ray fluxes and merges with the inner rim for the largest X-ray fluxes. A minimum in the vertical extension remains visible, though.

In Figs. 3.3 and 3.4, the density and temperature of the disk are shown for FUV luminosities ranging from $L_{\rm FUV} = 10^{29}$, 10^{30}, 10^{31}, and 10^{32} erg/s (left to right)

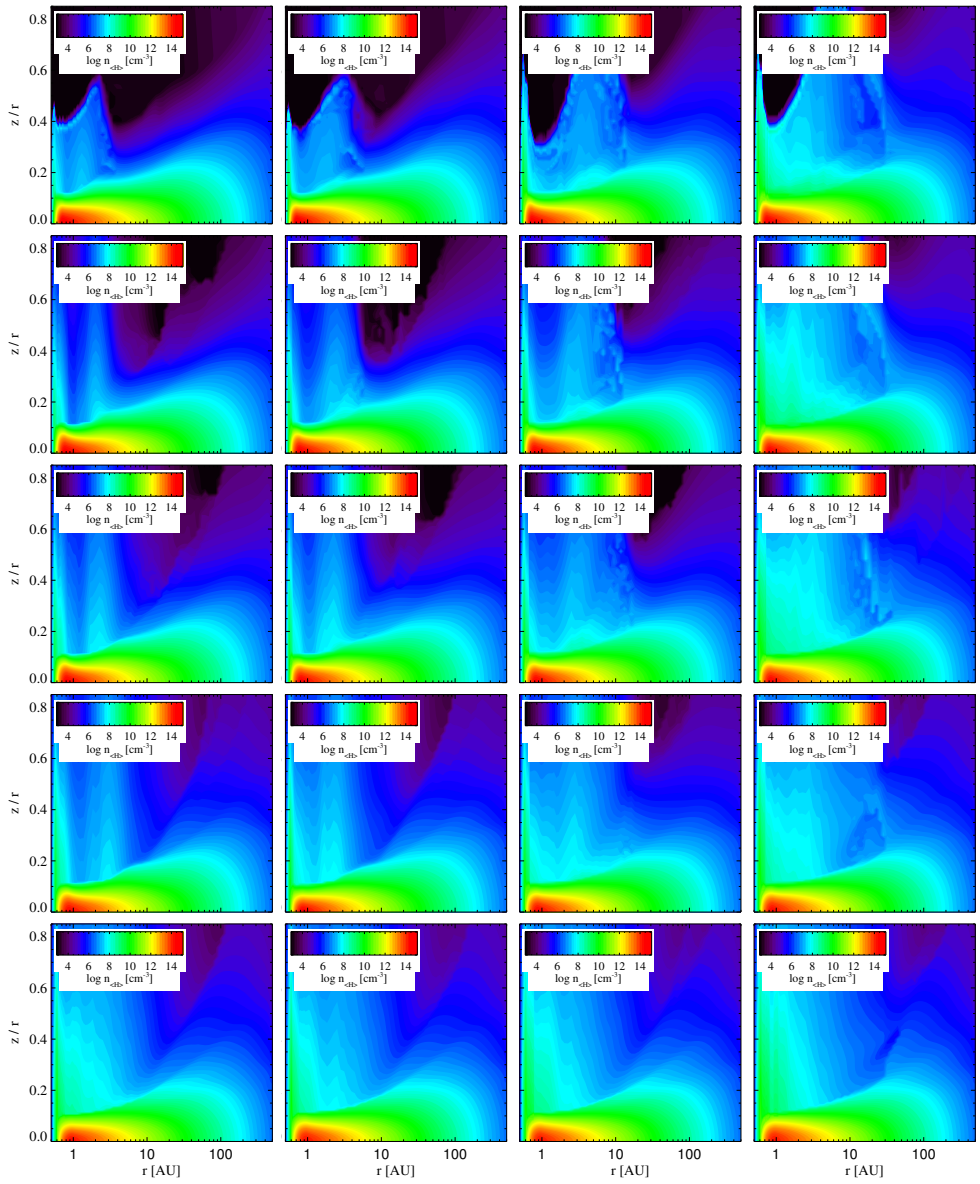

Figure 3.3: Total density: FUV luminosity increasing from $L_{\rm FUV} = 10^{29}$ (left) to 10^{32} erg/s (right). X-ray luminosity increasing from $L_x = 0$ (top) to 10^{32} erg/s (bottom).

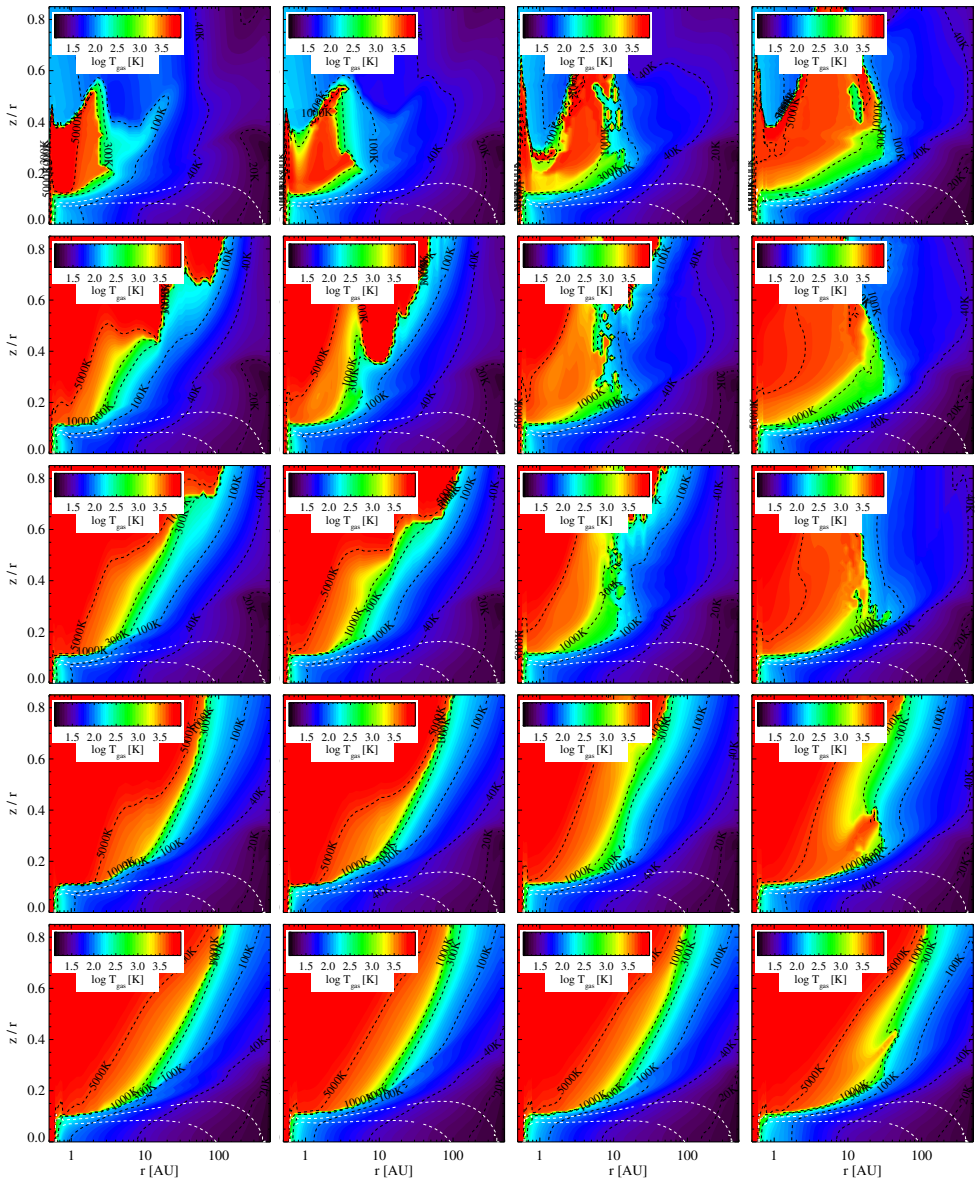

Figure 3.4: Gas temperature distribution: FUV luminosity increasing from $L_{\rm FUV} = 10^{29}$ (left) to 10^{32} erg/s (right). X-ray luminosity increasing from $L_x = 0$ (top) to 10^{32} erg/s (bottom). White contours represent the $A_{\rm v} = 1$ and 10. The black contours represent the gas temperatures.

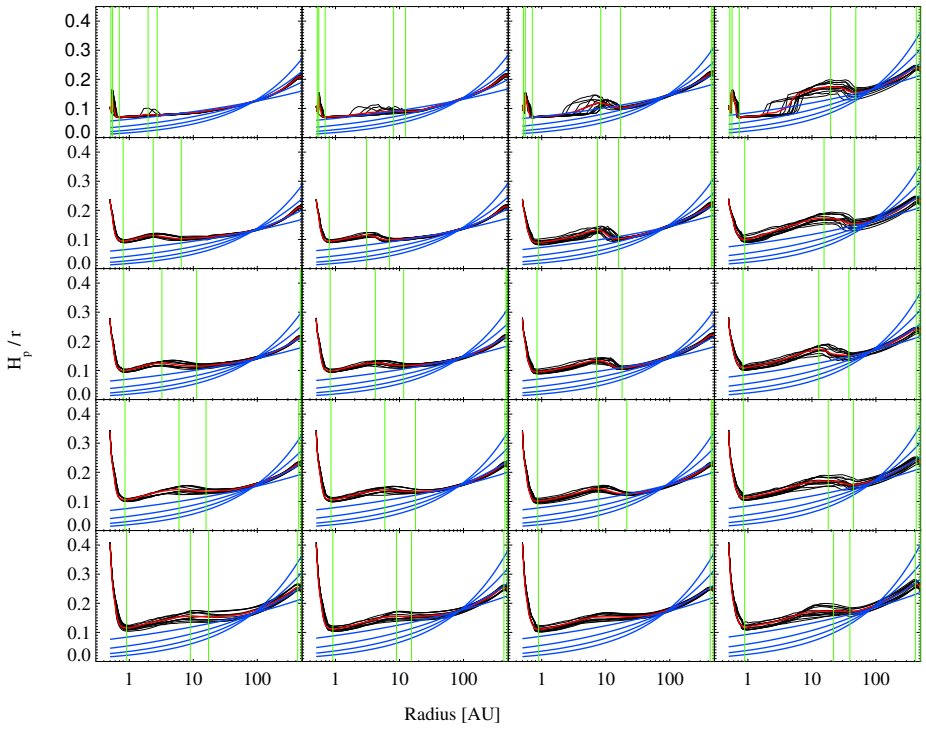

Figure 3.5: Scale height of the disk at $z/r = 0.5$. The black lines show the 12 different models ($a_{\min}$, $a_{\max}$, and ϵ), at a particular L_{FUV} and $L_{\rm X}$. The vertical green lines indicate a maximum or minimum in the scale height. The red line is the average of the 12 models.

and for X-ray luminosities $L_{\rm X} = 0$, 10^{29}, 10^{30}, 10^{31}, and 10^{32} erg/s. There are 12 different possible variations with these X-ray and FUV luminosities (due to the variations in $a_{\rm min}$, $a_{\rm max}$, and ϵ); as a baseline model, we always show the models with $a_{\rm min} = 0.1$ μm, $\epsilon = 1.5$, and $a_{\rm pow} = 3.5$.

3.3.1 Density distribution

Because density and temperature structure are directly related and we assume hydrostatic equilibrium, many of the effects that are seen in the density structure will show up in the temperature structure as well. The FUV-only models show that the inner rim becomes higher and broader for increasing luminosity. The disk right behind the inner wall is shielded, and a second, vertically more extended, density structure thus appears at radii between $r = 2$ and 6 to 30 AU (depending on the FUV luminosity).

The X-rays have a different effect on the density structure. While the peak of the second bump in the density structure appears at larger radii for higher FUV luminosities, the X-rays mostly affect the region within 5 AU. The second bump behind the inner rim expands to smaller and smaller radii for increasing X-ray luminosities (while keeping FUV the same), and the absolute densities become higher (from $n \sim 10^6$ to 10^8 cm^{-3}). Eventually, the puffed-up inner rim and the second bump merge. At the highest FUV luminosity, the merging of the two density structures occurs at the smallest X-ray luminosity.

3.3.2 Temperature structure

When only FUV is included in the models, we find that the temperature structure of the disk shows an inversion in the vertical direction: The temperature reaches a maximum at a certain relative height z/r and shows a fast drop above it. For example, the models with $L_{\rm FUV} = 10^{29}$ erg/s show a region with temperatures $T > 1000$ K out to a radius $r \sim 3$ AU and between relative heights $z/r \sim 0.1$ to 0.4. Noticeable is also that the hot region extends to a slightly higher relative height at the inner rim (up to $z/r = 0.45$) and at a radius $r = 3$ AU (out to $z/r = 0.55$). This is the result of shielding; the disk surface is less heated right behind the inner rim. For larger FUV luminosities, shielding effects are even more prominent and the drop in temperature right behind the inner rim is increasingly pronounced.

Adding X-ray heating changes this picture. These models show a much more extended region with temperatures higher than $T > 1000$ K, even when the X-ray luminosity is much smaller than the FUV luminosity. At radii $r < 5 - 10$ AU, the inversion layer disappears and the temperature just smoothly increases toward larger z/r. At larger radii ($r > 10 - 20$ AU), the inversion layer only disappears when the X-ray luminosity is at least ten percent of the FUV luminosity. In models where the X-ray luminosity is much smaller, temperature distribution is also affected (or even dominated) by the FUV. An example is $L_{\rm FUV} = 10^{32}$ erg/s in combination with $L_{\rm X} = 10^{29}$ erg/s. Although the inversion layer disappears at small radii ($r < 5$ AU), it is still present at larger radii.

3.3.3 Heating and cooling processes

Temperature and density structure are in the end determined by the balance between the heating and cooling processes. Line cooling processes (except Lyman α and [OI] 6300Å line cooling) are treated in an escape probability approximation. The code provides an option to calculate [OI] 6300Å line cooling in an escape probability approximation as well, but this was not used in the present calculation. Before solving the equations for statistical equilibrium, a global continuum radiation transfer calculation is done to estimate the background mean intensities for the radiative excitation and de-excitation rates. Other heating and cooling processes are approximated by an analytical expression. Over 50 different heating and 50 different cooling processes are included in the code. Except for the treatment of X-ray related heating processes, which are described in Aresu et al. (2011), we refer to Woitke et al. (2009, 2011) for a more detailed description. The reason that so many processes are included is that they each play a significant role, depending on the ambient density and radiation field (FUV, X-rays, cosmic rays), which vary over many orders of magnitude. It is beyond the scope of this paper to describe all these processes in detail for the models. However, we do present the dominant heating and cooling processes in Figs. 3.15 and 3.16 for the models for which we are showing the temperature and density structure.

First, we consider the FUV-only models. At the lowest FUV luminosity $L_{FUV} = 10^{29}$ erg s^{-1}, there are three main heating process in the unattenuated part of the disk, namely, background heating by C^+ at the lowest densities, $n_H = 10^5$ cm^{-3} (dark blue), PAH heating within the inner rim and the second extension of the disk (orange), and heating by carbon ionization in the outer disk (blue-green). Increasing the FUV field makes the picture more complicated. Heating by collisional de-excitation of H_2 becomes important in the second bump (light blue), while background heating by FeII is dominant at the inner rim. Locally, other processes, such as photo-electric heating, are important. Going to the more shielded regions of the disk, there is roughly a three-layered structure of dominating heating processes: (1) infrared background heating CO ro-vibrational transitions (black), (2) slightly deeper in the disk heating by thermal accomodation on grains (white), and (3) in the mid-plane cosmic ray heating (red). This three-layered structure becomes more confined toward the mid-plane for higher FUV luminosities.

X-ray Coulomb heating dominates in the upper part of the disk, when the FUV to X-ray luminosity $L_{\rm FUV}/L_{\rm X} \leq 1$. When it is higher than one, X-ray Coulomb heating is restricted to the higher regions of the disk. Adding X-rays increases the temperature significantly in the disk, making [FeII] also dominant in large parts of the second-density extension at the lowest X-ray luminosity, $L_X = 10^{29}$ erg s^{-1}. For large X-ray luminosities, the structure of heating sources becomes less complicated. The entire unshielded part of the disk is dominated by X-ray Coulomb heating, followed by the three-layered structure described above (CO ro-vib, thermal accommodiation on grains, cosmic ray). For the highest two X-ray fluxes, an additional layer with X-ray H_2 dissociation heating as the main heating source is located on top of this three-layered structure.

In the FUV-only case, there are three main coolants in the unattenuated part of the disk: C^+ line cooling (yellow), [FeII] line cooling (blue-green), and [OI] line

cooling. The size of the region, where [FeII] line cooling dominates expands for higher FUV luminosities, while reducing the size of region where [OI] line cooling dominates. When X-rays are added, the region where C^+ line cooling dominates is pushed to the outer part of the disk. Temperatures are much higher in the upper part of the disk, and as a result Lyman α cooling (black) dominates in increasingly larger regions of disk, when X-ray luminosities become larger. At the highest X-ray luminosities, we find a three-layered structure of Lyman α cooling, [FeII] line cooling, and [OI] line cooling. The shielded region of the disk shows a layered structure. CO ro-vibrational (red) and H_2O rotational cooling (green-blue) are on top. Closer to mid-plane, several smaller regions have their own major coolant, such as HCN (purple), and HNC (orange).

3.3.4 Vertical scale height

Another way to show the combined effects of X-rays and FUV on the disk structure is by comparing the scale vertical height. Our definition is the same as the one used by Woitke et al. (2009), and is approximately (i.e., assuming $z \ll r$) given by

$$\left(\frac{H}{r}\right)^2 \simeq \frac{2rc_T}{GM_\star}, \tag{3.1}$$

where H is defined as $\rho(z) \approx \rho(0)\exp(z^2/H^2)$ and c_T is the isothermal sound speed. As mostly the disk atmosphere is affected by the FUV and X-ray irradiation, we plot H/r at the relative height $z/r = 0.5$ in Fig. 3.5. In each panel, we overplot the scale height for all the different parameters in black (twelve models in total), and the red line is the average. Four blue lines are overplotted, indicating flaring index $H/r \propto r^p$ with $p = 0.15 - 0.45$, where the lines are normalized to the vertical scale height at $r = 100$ AU.

A number of things stand out in these plots: (i) The vertical scale height of the inner rim is mostly affected by the X-rays, and almost no response is seen for different FUV luminosities. The scale height is $H/r = 0.15$ without X-rays at the inner rim, and it increases to ~ 0.4 at $L_X = 10^{32}$ erg/s. (ii) The second bump also shows up when plotting H/r and slowly moves outward for increasing X-ray luminosities. (iii) The flaring index p is 0.25 in the outer disk ($r > 100$ AU), similar to the 2/7 exponent found by Chiang & Goldreich (1997). The vertical scale height in the inner disk is elevated, compared to the outer disk. (iv) The $H_0/r \approx 0.1$ and 0.18 at $r_0 = 100$ AU and $z/r = 0.1$ and 0.5, respectively. For a direct comparison to Chiang & Goldreich (1997), we measure H_0/r at $r_0 = 10$ AU, because the approximation of the disk dust temperature being vertically isothermal does not hold in our models at the larger distances. We find a value $H_0/r \approx 0.04$, which is very similar to Chiang & Goldreich (1997), after correcting for the stellar mass and their definition of the scale height. (v) The merging of the inner rim with the second bump is clearly visible, as changes in the vertical scale height in the inner disk ($r = 1 - 10$ AU) become more gradual for larger X-ray luminosities.

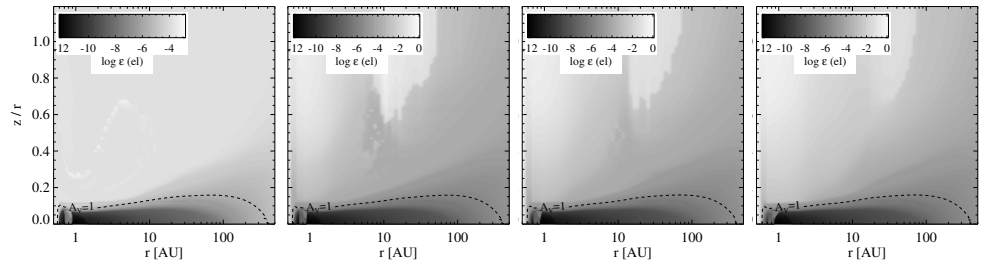

Figure 3.6: Electron abundance: FUV luminosity is fixed at 10^{31} erg/s. X-ray luminosity increases from $L_x = 0$ (left) to 10^{32} erg/s (right). The black dashed line indicates $A_{\rm V} = 1$. The blue lines mark the ionization fractions $x_e = 10^{-2}$ and 10^{-1}.

3.4 The chemical balance in the disk

The combined effects of X-rays and FUV irradiation on the disk are discussed in this section. The density structure is in pressure equilibrium as discussed in the previous section and is altered due to irradiation effects. The chemical rates are density dependent, and as such the pressure balance also influences the abundances of the species.

3.4.1 Electron abundances

The main electron donor in a FUV-only chemistry is atomic carbon, because the incident FUV radiation field is not capable of ionizing atomic hydrogen, leaving cosmic rays as the only ionization source of atomic hydrogen. As a result, the maximum electron abundance will not be higher than $x_{\rm e} \sim 10^{-4} - 10^{-3}$, as can be seen in Figs. 3.6 and 3.17. The maximum electron abundances occur where the disk is unshielded to the radiation source. The inner rim has significant ionization fractions ($x_{\rm e} \sim 10^{-4} - 10^{-3}$) all the way down to the midplane of the disk, while further out the electron abundances are only this high at densities $n < 10^7$ cm^{-3}. The drop of the electron abundances below $x_{\rm e} < 10^{-6} - 10^{-5}$ for higher densities nicely coincides with the $A_V = 1$. Closer to the midplane, when the radiation becomes more shielded and densities are higher, the electron abundance exhibits a fast drop. This is the result of a combination of a decreasing ionization rate, $\zeta \propto n$, and an increasing recombination rate, $k_{\rm rec} \propto n^2$. The abundance drop becomes more gradual at larger radii, which is a result of lower ambient densities and thus lower recombination rates. The region where the transition occurs is moving slightly toward smaller relative heights, when FUV fluxes are higher. The change in the transition location is not much due to the sharp increase of the density toward the midplane ($k_{rec} \propto n^2$): A relatively small increase in the density already compensates for larger FUV fluxes.

This picture changes quite significantly when the radiation fields also contain X-rays. The absorption of an X-ray photon by an arbitrary species creates a fast electron that can produce many ionizations, e.g., a 1 keV electron is able to produce $\sim$ 27 hydrogen ionizations. As a result, the electron abundances are much higher

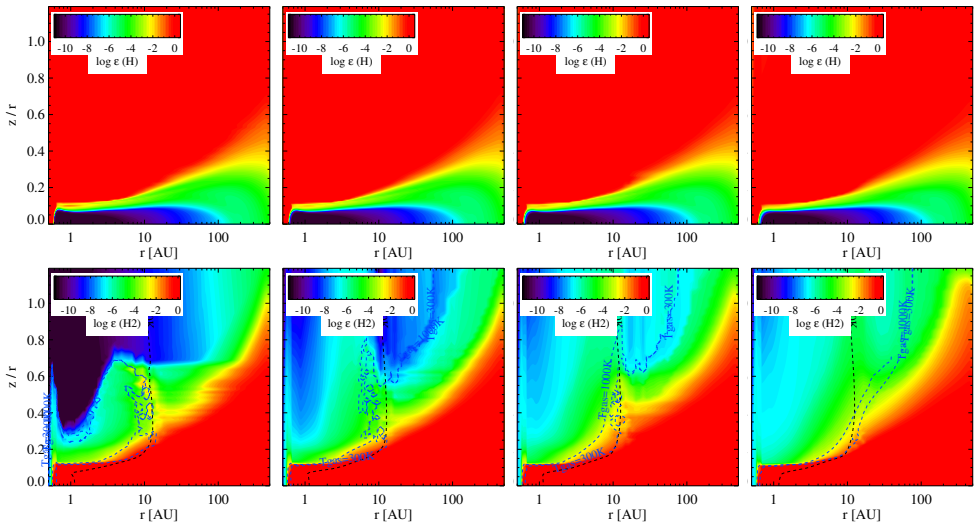

Figure 3.7: Abundance structure of atomic (top) and molecular (bottom) hydrogen. FUV and X-ray fluxes are the same as in Fig. 3.6. The blue contours indicate the gas temperature $T_{\rm gas} = 300$ and 1000 K. The black line indicates $T_{\rm dust} = 100$ K.

when X-rays are included. In the unattenuated part of the disk, ionization fractions are of the order $x_e \sim 10^{-2} - 10^{-1}$ (contours for $x_e = 10^{-2}$ and 10^{-1} are indicated). They can even be higher than $x_{\rm e} > 10^{-1}$ at very small radii ($r < 0.5$ AU) and high relative heights ($z/r \gtrsim 0.5$). Here, low densities ($n_{\rm H} < 10^7$ cm^{-3}) and high temperatures ($T \gg 5000$ K) reduce the recombination rates. Recombination rates decrease with temperature up to $T \sim 10000$ K because they are dominated by radiative recombination, which scales as $k_{\rm rec} \propto n_e n_i (T/10^4)^{-X_{\rm rad}}$, with $X_{\rm rad} \sim 0.6 - 0.9$. We find slightly higher ionization fractions than, e.g., Glassgold et al. (2004). Their calculation at $r = 1$ AU (see their Fig. 4) is truncated at vertical column density $N_{\rm H} \approx 2 \times 10^{18}$ cm^{-2} and density $n_{\rm H} \approx 10^7$ cm^{-3} . Ercolano et al. (2008) (their Figs. 1 and 2) show calculations for lower column densities and densities, and they find ionization fractions slightly higher than $x_e > 1$ at 0.07 AU at vertical column densities $N_{\rm H} < 10^{16}$ cm^{-2}. Both calculations are consistent with those presented here. The electron abundance structure looks a little counterintuitive, especially for the lowest two X-ray fluxes $L_{\rm X} = 10^{29}$ and 10^{30} erg/s. The region with very high ($x_{\rm e} \approx 10^{-2} - 10^{-1}$) becomes smaller for increasing FUV luminosities (Fig. 3.17). This is because the inner rim is puffed up more and even merged with the second bump for the highest FUV fluxes. The densities are elevated to $n_{\rm H} = 10^8$ cm^{-3} in these regions, and the recombination rates are orders of magnitude higher as a result. The outer disk is shielded from radiation. The regions with very high ionization fractions ($x_{\rm e} > 10^{-2}$) are of similar size for all FUV luminosities only for the highest X-ray luminosity (see Fig. 3.17).

When the ionization fraction is increased by orders of magnitude, the gas shows a radically different chemistry, as it will be dominated by ion-molecule reactions. This

will be discussed for some of the key species, and water in particular.

3.4.2 H and H_2 abundances

The abundance structure of atomic hydrogen is shown in the top panel of Fig. 3.7 (and also in Figs. 3.18 and 3.19). The highest abundances ($x_{\rm H} \gtrsim 10^{-2}$) are obtained in the unshielded region of the disk, where FUV and X-rays have high fluxes. At radii $r < 0.6$ AU, the disk is atomic all the way down to the mid-plane of the disk, as it is directly exposed to the central source. At larger radii, the atomic fraction drops below $x_{\rm H} \sim 10^{-2}$ and makes a transition to molecular hydrogen at a relative height of $z/r \sim 0.1$ between $r \sim 0.6 - 5$ AU. The transition occurs at increasingly larger relative heights at larger distances to the central source, and it is at approximately $z/r \sim 0.4-0.5$ (depending on the X-ray flux) at a distance $r \sim 100$ AU. The transition occurs at slightly smaller relative heights at larger X-ray fluxes.

The formation of H_2 on grains is extremely efficient (~ 1) when the dust temperatures are not high, $T_{\rm dust} \sim 10 - 50$ K (Cazaux & Tielens, 2004). At dust temperatures higher than $T_{\rm dust} > 100$ K, the H_2 efficiency drops rapidly and H_2 formation on dust does not occur at $T_{\rm dust} > 1000$ K. H_2 is also formed through the H^- route, $H^- + H \rightarrow H_2 + e^-$, especially when X-rays are present, and the fractional abundance of electrons is relatively high (and thus also H^-). It is possible to maintain an efficient route to form molecular hydrogen in the gas phase at high temperatures, $T_{\rm gas} > 300$ K and $T_{\rm dust} > 100$ K (see contours in Fig. 3.7). Also FUV is much more efficient in destroying H_2, than X-rays. The FUV photo-dissociates H_2 (H_2+ FUV photon $\rightarrow H_2^* \rightarrow H + H$). X-rays predominantly ionize molecular hydrogen indirectly by collisions with fast electrons produced after an X-ray absorption ($H_2 + e^{-*} \rightarrow H_2^+ + e^- + e^{-*}$), while only a small fraction of H_2 is dissociated in this process. After ionization, H_2^+ is able to reform H_2 through $H_2^+ + H \rightarrow H_2 + H^+$, but it will also be able to form H_3^+ through the reaction $H_2^+ + H_2 \rightarrow H_3^+ + H$. This particular species is key in forming molecules through ion-molecule reactions. Because X-rays are destroying H_2 less efficiently and can provide an environment to form H_2 in the gas-phase, a fast ion-neutral chemistry results, which makes it possible to form molecules (and maintain significant abundances) at much higher temperatures than when only FUV is present.

The bottom panel of Fig. 3.7 presents the abundances of H_2. It shows that the H_2 abundance in the warm atmosphere of the disk is largest for the highest X-ray fluxes (as high as $x_{\rm H_2} \sim 10^{-6}$ in the region directly exposed to the central source at $r = 0.6$ AU). This is the result not only of the processes described above, but also of the scale height of the inner rim, which increases with X-ray luminosities, an effect described in the previous section.

3.4.3 H^+, H^-, H_2^+, and H_3^+ abundances

The main drivers of the chemistry in the atmospheres of disks exposed to irradiation are ionic species, starting with H^+, H_2^+, and H_3^+ (see also the discussion of the water chemistry). The H^- abundance structure is shown for completeness, since it can be important in the production of H_2 (see Fig. 3.8 and Figs. 3.20 to 3.23).

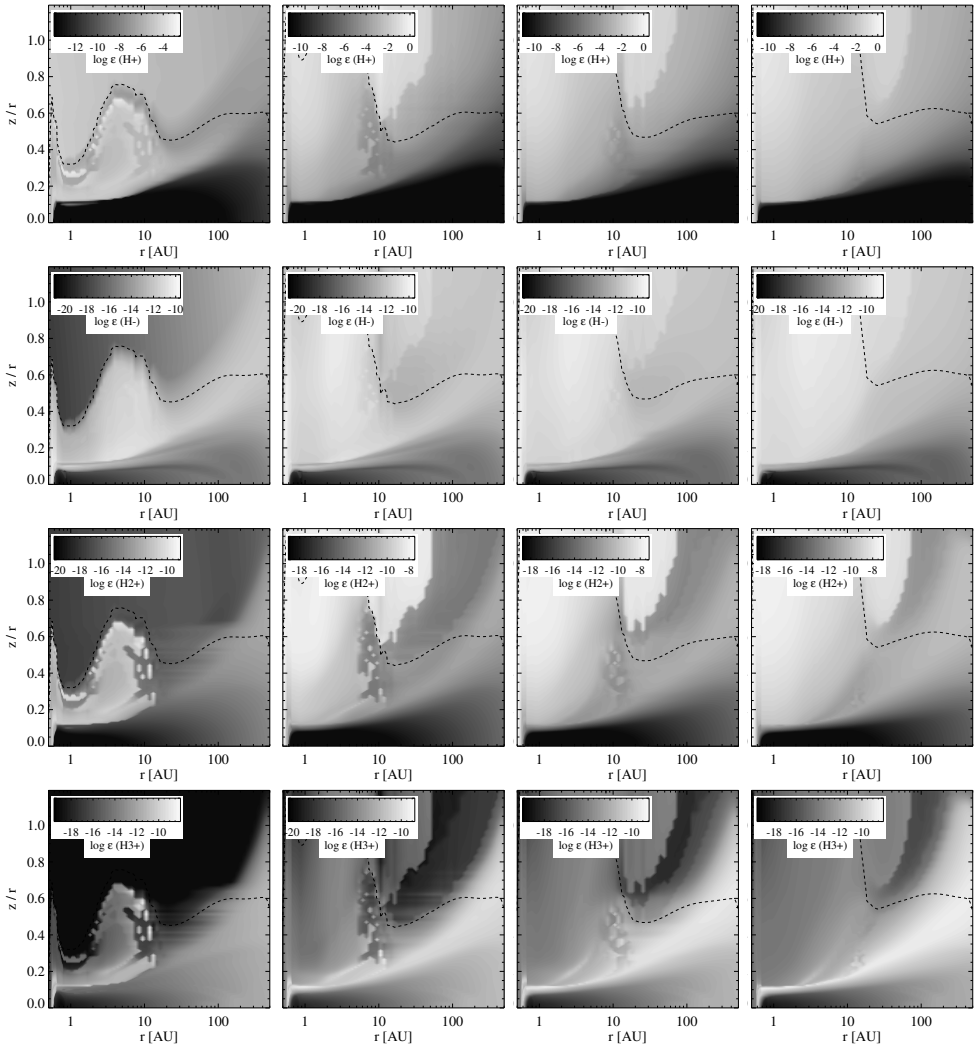

Figure 3.8: Abundance structure of H^+, H^-, H_2^+, and H_3^+. FUV and X-ray fluxes are the same as in Fig. 3.6. Black contour indicates $n_H = 10^5$ cm^{-3}.

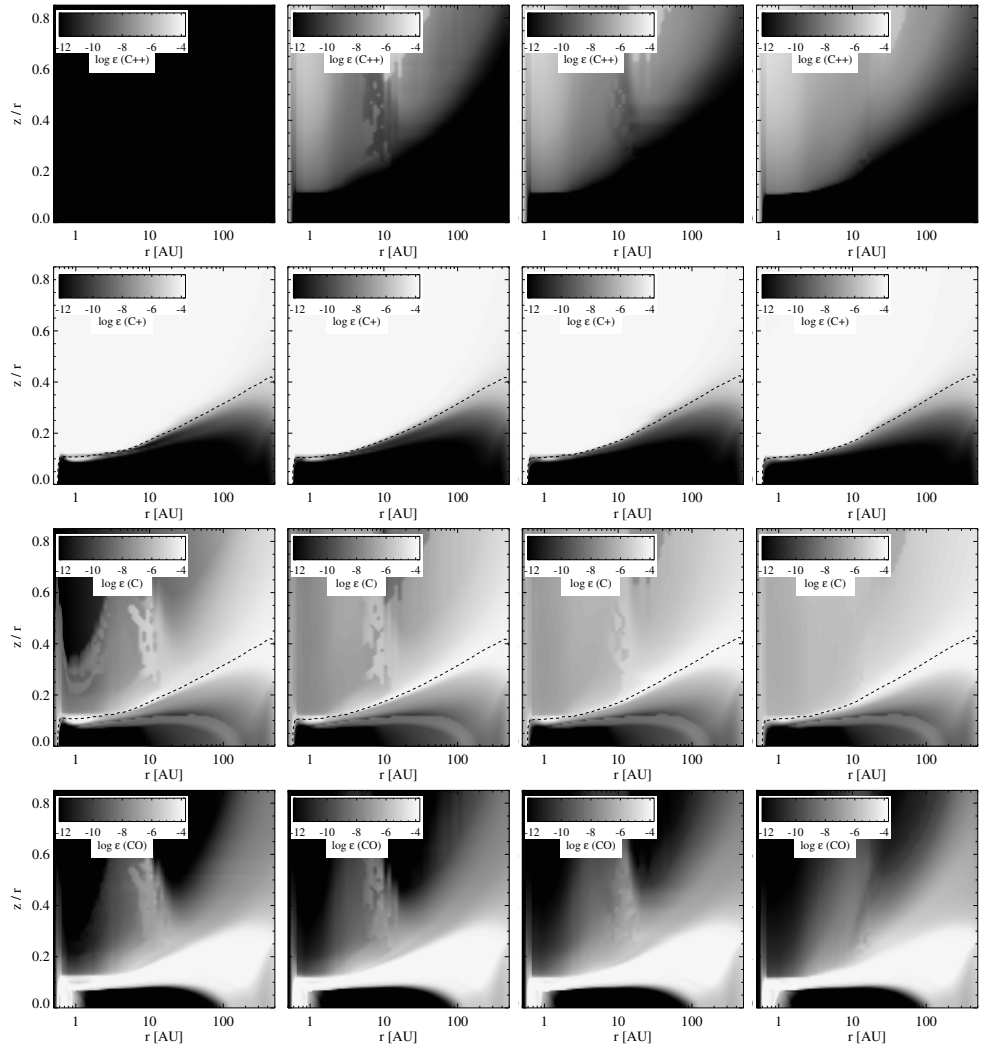

Figure 3.9: C^{2+}, C^{+}, C, CO abundances. The black dashed line indicates $\log(\chi/n_{\rm H}) = -5$. Fluxes are the same as Fig. 3.6.

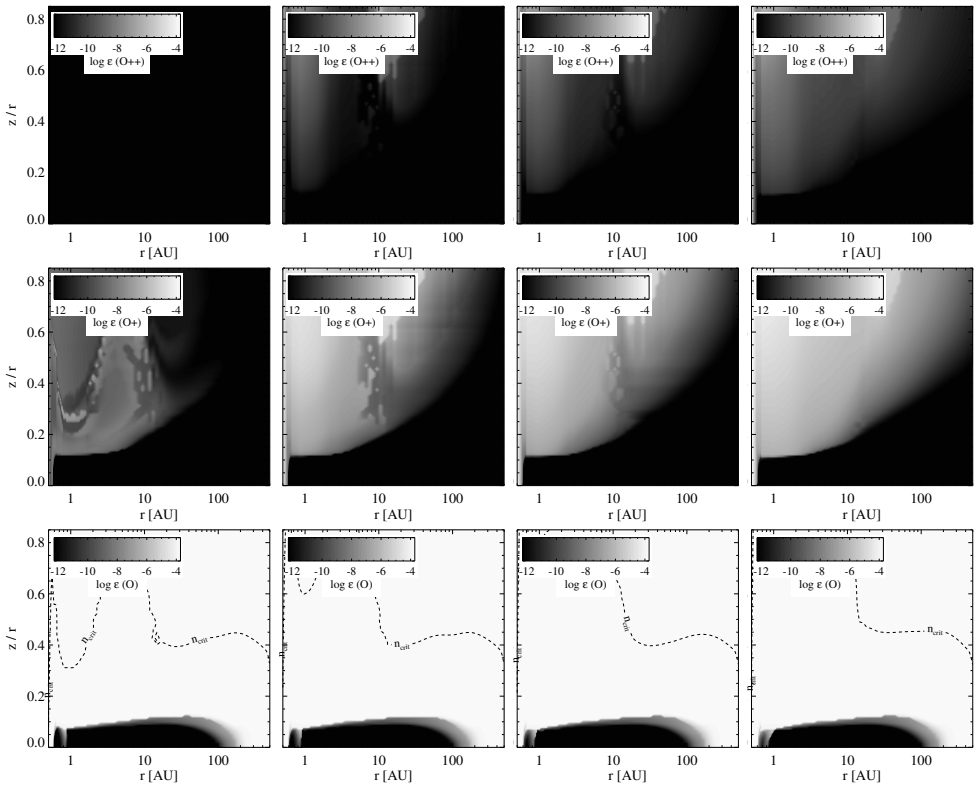

Figure 3.10: O^{2+}, O^{+}, and O abundances. Fluxes are the same as in Fig. 3.6. The black contour in the lower panel indicates the critical density of the [OI] 63 μm line.

The abundance structure of ionized hydrogen shows abundances as high as $x_{\mathrm{H}^+} \sim 10^{-3} - 10^{-2}$, even if there is only FUV irradiation. FUV is not able to photo-ionize atomic hydrogen, and hydrogen ionization is solely done by cosmic rays. This only happens at very low densities ($n < 10^4$ cm^{-3}), though. Once densities of the order of $n \sim 10^5$ cm^{-3} are reached, the ionized hydrogen fractions are closer to $x_{\mathrm{e}} \sim 10^{-5} - 10^{-4}$ or smaller. The ionization balance is regulated by the charge exchange reaction $\mathrm{H} + \mathrm{O}^+ \leftrightarrow \mathrm{H}^+ + \mathrm{O}$. The backward reaction has an energy barrier of $T = 227$ K, so the ratio of O^+ with respect to H^+ decreases with temperature. The charge exchange rates are much faster than the photo-ionization reaction or the recombination rates of the species. The amount of H^+ is thus directly coupled to the production rate of O^+, which is also produced by cosmic ray ionization. Even when X-ray ionization determines the ionization balance of the gas, the charge exchange rates are much faster than the primary and secondary X-ray ionization rates of the species, and the ion abundances are directly coupled. X-rays produce much higher fractions of H^+ (as high as $x_{\mathrm{H}+} > 0.1$ at the lowest densities). The abundance structure strongly resembles that of the electrons, although the H^+ abundance drops faster closer to the mid-plane, and other species such as Na^+ take over as electron donor (see also Ádámkovics et al., 2011).

Once the gas gets more shielded to the radiation, it has higher abundances of molecular species (see, e.g., Fig. 3.19). In those regions, H^+ can also be produced by other reaction paths, such as $\mathrm{CO}^+ + \mathrm{H} \rightarrow \mathrm{CO} + \mathrm{H}^+$ when only FUV is present and secondary X-ray ionization of H_2 when X-rays are present as well. Once cosmic ray ionization is the dominant source of ionization, H^+ is produced by cosmic ray ionization of H_2 or charge exchange with He^+.

The H^- ion is produced by cosmic ray ionization ($\mathrm{H}_2 + \mathrm{CR} \rightarrow \mathrm{H}^+ + \mathrm{H}^-$) or by radiative recombination ($\mathrm{H} + \mathrm{e}^- \rightarrow \mathrm{H}^- + h\nu$). This last reaction is fairly slow at low temperatures due to temperature barriers, but it becomes important in the warm part of the atmosphere of the disk. When only FUV is irradiating the disk, the H^- abundance is high ($x_{\mathrm{H}^-} \sim 10^{-11} - 10^{-10}$) at the inner rim and in the second bump extending out of the disk, and to a lesser extent in the transition zone from atomic to molecular gas. There are two reasons that there is not as much H^- at high altitudes in the disk. The first one is that the electron densities are two to three orders of magnitude lower. The second one is that the ambient temperatures are between 50 and 100 K, which is not very favorable as the reaction rate contains an energy barrier. At the inner rim and in the second bump, both temperatures ($T > 1000$ K) and densities ($n > 10^7$ cm^{-3}, and thus also electron densities) are much higher. When X-ray irradiation plays a role, the abundances structure changes a lot. The temperatures are in excess of $T > 1000$ K to large relative heights (see Fig. 3.4), and electron abundances are much higher (due to higher ionization rates and slower recombination rates). Especially when X-ray luminosities exceed $L_X > 10^{30}$ erg/s, the relative abundances of H^- are one to three orders of magnitude higher (close to $x_{\mathrm{H}^-} \sim 10^{-8}$). In the FUV case, the H^- route to form H_2 is at least three orders of magnitude lower than the formation route on dust grains. It becomes a significant contributor ($\sim 30\%$) to the total H_2 formation rate at the highest X-ray luminosities when these extreme ($x_{\mathrm{H}^-} \sim 10^{-8}$) abundances are reached, and at the same time, H_2 formation on dust is quenched by high dust temperatures.

H_2^+ is formed by cosmic ray ionization ($H_2 + CR \rightarrow H_2^+ + e^-$) in the regions where the gas is molecular and shielded from FUV and X-ray radiation. When the H_2 abundance is high ($x_{H_2} \sim 0.5$), however, the H_2^+ is quickly transformed to H_3^+ ($H_2^+ + H_2 \rightarrow H_3^+ + H$). It is above this layer, that the H_2^+ abundance is increasing. Here, the gas is more exposed to radiation (FUV or X-rays). If X-rays are present, H_2 is ionized through secondary ionizations. In the FUV-only case, where we do not have this last reaction, other routes contribute to the production of H_2^+. One example is $S^+ + H_2 \rightarrow H_2^+ + S$. In the unshielded regions of the disk, where H_2 abundances are low ($x_{H_2} < 10^{-6}$), the only efficient way to form H_2^+ is through radiative association $H^+ + H \rightarrow H_2^+ + h\nu$. However, this is only efficient at relatively high temperatures ($T > 5000$ K) and significant abundance levels of H^+. In Fig. 3.8, the cation H^+ is shown to be more abundant by orders of magnitude when X-rays are present. It is obvious that the production of H_2^+ is much more efficient as well, and hence abundances $x_{H_2^+} \sim 10^{-8} - 10^{-7}$ occur in the high warm atmosphere of the disk. In the FUV-only case, there is only a significant abundance ($x_{H_2^+} > 10^{-12}$) in the inner rim and the second bump.

The dominant way to form H_3^+ is through the ion-molecule reaction $H_2^+ + H_2 \rightarrow H_3^+ + H$. As a result, the H/$H_2$ transition layer and the region below is very suitable to produce large abundances: H_2 is present in reasonable amounts ($x_{H_2} > 10^{-5} - 10^{-3}$, see Fig. 3.7), and radiation is available to produce H_2^+ (see previous paragraph, and Fig. 3.8). Once the H_2^+ drops below an abundance $x_{H_2^+} < 10^{-12}$, the H_3^+ abundance also drops to values below $x_{H_3^+} < 10^{-11}$. Consequently, there is a distinct layer where H_3^+ is formed in the most optimal way. We also saw that the H_2^+ is more efficiently formed when X-rays are abundantly present in the disk. The H_3^+ abundances thus also significantly increase for larger X-ray luminosities and can be as high as $x_{H_3^+} \gtrsim 10^{-8}$. In the FUV-only case, the size of the region where H_3^+ is present in large abundances is smaller, and the maximum abundance is at least an order of magnitude lower compared to the models that include X-rays. It is a key species in driving ion-molecule chemistry, and so the chemistry with and without X-rays will obviously yield significantly different abundance structures.

3.4.4 C^{2+}, C^+, C and CO abundances

The ionization potentials (IP) of the species C and C^+ are $IP = 11.26$ and 24.38 eV, respectively. While FUV photons can ionize neutral carbon, X-rays (or collisions with the resulting fast electrons) and/or cosmic rays are needed to reach a higher degree of ionization. As a result, the abundance patterns of the two species C^+ and C^{2+} respond radically differently to the incident radiation field on the disk. The C^{2+} abundance pattern is, of course, strongly correlated with the X-ray luminosity, and C^{2+} is absent in models without X-rays. The region with significant C^{2+} abundances ($x_{C^{2+}} > 10^{-9} - 10^{-8}$) extends to larger radii and smaller relative heights for higher X-ray luminosities, simply because there is more ionizing radiation available (and not inhibited by dust, since the dominant opacity is caused by the gas). However, the FUV plays an important role in shaping the disk and therefore indirectly affects the abundance distribution as well. The bump in the total H number density (see Fig.

3.3) extends to larger relative heights for larger FUV luminosities, thereby increasing the density at larger relative heights. This causes a larger attenuating column between the central source and the outer part of the disk, thus reducing the amount of ionizing photons. Furthermore, it allows H_2 to form at smaller radii. H_2 is very efficient in reducing C^{2+} by charge exchange reactions, such as $C^{2+} + H_2 \rightarrow C^+ + H$. As a result, the FUV luminosity confines the C^{2+} to smaller radii (see Fig. 3.24). C^+ is present throughout the unattenuated part of the disk. It has an abundance $x_{C^+} \sim 10^{-4}$ down to the mid-plane in the inner rim ($r < 0.6$ AU). Beyond this radius, carbon is only significantly ionized above a relative height $z/r \sim 0.1$ (at $r \sim 0.6$ AU), increasing to $z/r \sim 0.4$ at $r \sim 200$ AU. The width $\Delta z/r$, over which the transition from C^+ to C and CO occurs, is larger toward the outer regions of the disk. Absolute densities of C^+ and e^- in the inner disk are larger, and recombination rates scale with n^2. As a result, the transition from ionized to neutral carbon occurs abruptly, similar to the abundance drop of electrons (at approximately $z/r \sim 0.01$ at $r = 1$ AU). However, in the outer disk ($r = 200$ AU), the transition stretches out from $z/r \sim 0.04$ to 0.01. Although there are variations of a factor a few in the absolute abundance of C^+, the overall appearance of the abundance structure is not significantly affected for different values of the X-ray and FUV luminosity (see Fig. 3.25).

The neutral carbon abundance pattern is very much affected by variations in the X-ray and FUV luminosities. In the case where only FUV is irradiating the disk, one finds a clear transition from C^+ to C to CO (see Fig. 3.9), which is expected in a FUV-dominated PDR (cf. Hollenbach & Tielens, 1999). To guide the eye, we added a contour with value $\log(\chi/n_H) = -5$ (with χ the Draine field). This contour follows the C^+/C/CO transition very well, indicating PDR physics. Neutral carbon is confined in a layer between the C^+ and CO. This picture is more complicated when X-rays are added. Perhaps not entirely intuitive, the overall trend with increasing X-rays is that neutral carbon is more and more abundant in the unattenuated part of the atmosphere (as high as $x_C \sim 10^{-5} - 10^{-4}$). When X-rays are present, neutral carbon is higher by at least one to two orders of magnitude in abundance compared to models that exclude X-rays. The C and C^+ ionization rates are of course higher, but the recombination rates are also higher owing to the increased electron abundances (although the higher temperatures reduce the recombination rates, as already pointed out in Sect. 3.4.1). This is because electrons are now also produced by, e.g., ionization of hydrogen and helium. The fact that C^+ and C coexist in more or less equal amounts, when X-rays are dominating the ionization fraction of gas clouds, was already pointed out in papers by Maloney et al. (1996) (see their Figs. 3a and 4a) and Meijerink & Spaans (2005) (see their Figs. 3 and 4).

The bulk of the CO is situated in the shielded, optically thick part of the disk, and the total CO gas mass does not change when varying the FUV and X-ray radiation field. This molecule could thus serve as a tracer of the total mass of a protoplanetary disk, keeping in mind that the conversion factor depends on the amount of ice formation. A few details should be noted. There is a significant correlation between CO and OH in the unattenuated part of the disk (compare Fig. 3.27 with 3.31). A route to form CO is through the reaction $C + OH \rightarrow CO + H$. While it is possible to obtain an abundance level of $x_{CO} \sim 10^{-7}$ through this channel, it will never go up to $x_{CO} \sim 10^{-4}$ because the OH abundance is $x_{OH} \sim 10^{-7}$. As OH becomes less

abundant for higher FUV luminosities (when X-rays are fixed), the CO also becomes less abundant and slightly more confined to the midplane. In addition, the average abundance of CO drops slowly with increasing X-ray luminosity at the inner rim by destruction through ion-molecule reactions, such as $CO + He^+ \rightarrow C^+ + O + He$. This could have an effect on the ro-vibrational lines that are predominantly produced in these regions.

3.4.5 O^{2+}, O^+, and O abundances

The ionization potentials of O and O^+ are $IP = 13.68$ and 35.12 eV. Even the IP of neutral oxygen is above the threshold of $IP = 13.6$ eV, where neutral hydrogen blocks the radiation efficiently. The implications of this are seen in Fig. 3.10, where the abundances of neutral, singly and doubly ionized oxygen are shown for a FUV luminosity $L_{\rm FUV} = 10^{31}$ erg s^{-1} and all considered X-ray luminosities except $L_{\rm X} = 10^{32}$ erg s^{-1}. The second row of Fig. 3.10 (and also Fig. 3.29 for variations with FUV luminosity) shows the abundance structure of singly ionized oxygen. Unlike the C^+, the abundances of O^+ do not exceed $x_{O^+} \sim 10^{-8} - 10^{-7}$ in the FUV-only case. The abundance of ionized oxygen is mostly set by the charge exchange balance with atomic hydrogen, while the ionization of both hydrogen and oxygen is entirely due to cosmic ray ionization. When X-rays are added, the abundances increase three to four orders of magnitude compared to the FUV-only case, even at low X-ray luminosities ($L_{\rm X} = 10^{29}$ erg s^{-1}). Important to note is that the O^+ is confined to smaller radii for larger FUV luminosities, which is also the case for C^{2+}. This was discussed earlier in Sect. 3.4.4 and explained by the larger recombination rates due to higher densities in the upper atmosphere of the disk and the lower ionization rates due to shielding. The confinement to smaller radii is even stronger for the case of O^{2+}, because this species is not affected by cosmic rays.

The bottom panel of Fig. 3.10 shows the neutral oxygen abundance structure. The critical density is $n_{\rm crit} = 5 \times 10^5$ cm^{-3} for the [OI] 63 μm line, which is indicated by a black dashed contour. This species does not change with X-ray luminosity. Neutral oxygen is the dominant oxygen carrier throughout the disk, except for those regions, where large fractions of the gas are frozen onto dust grains (i.e., the midplane). This species is very insensitive to changes in FUV and the ambient chemistry (see Fig. 3.30). The bulk of atomic oxygen is in LTE for the commonly observed [OI] 63 and 145 μm fine-structure lines and thus sensitive to the average temperature of the region that it is probing. As a result, the [OI] fine-structure lines have the potential to probe the total energy budget of the gas (the combined FUV and X-ray luminosity irradiating the disk). There will be an elaborate analysis of the oxygen fine-structure line emission in paper II.

3.4.6 OH, OH^+, H_2O, H_2O^+, and H_3O^+ abundances

The water chemistry and its related species are significantly affected by X-ray irradiation. The physical circumstances in the disk change with radius r and height z due to radiation shielding and large differences in chemistry, which means that the X-ray and FUV energy deposition per particle, $H_{\rm X}/n$, and χ/n (with $\chi = 1$ the interstellar

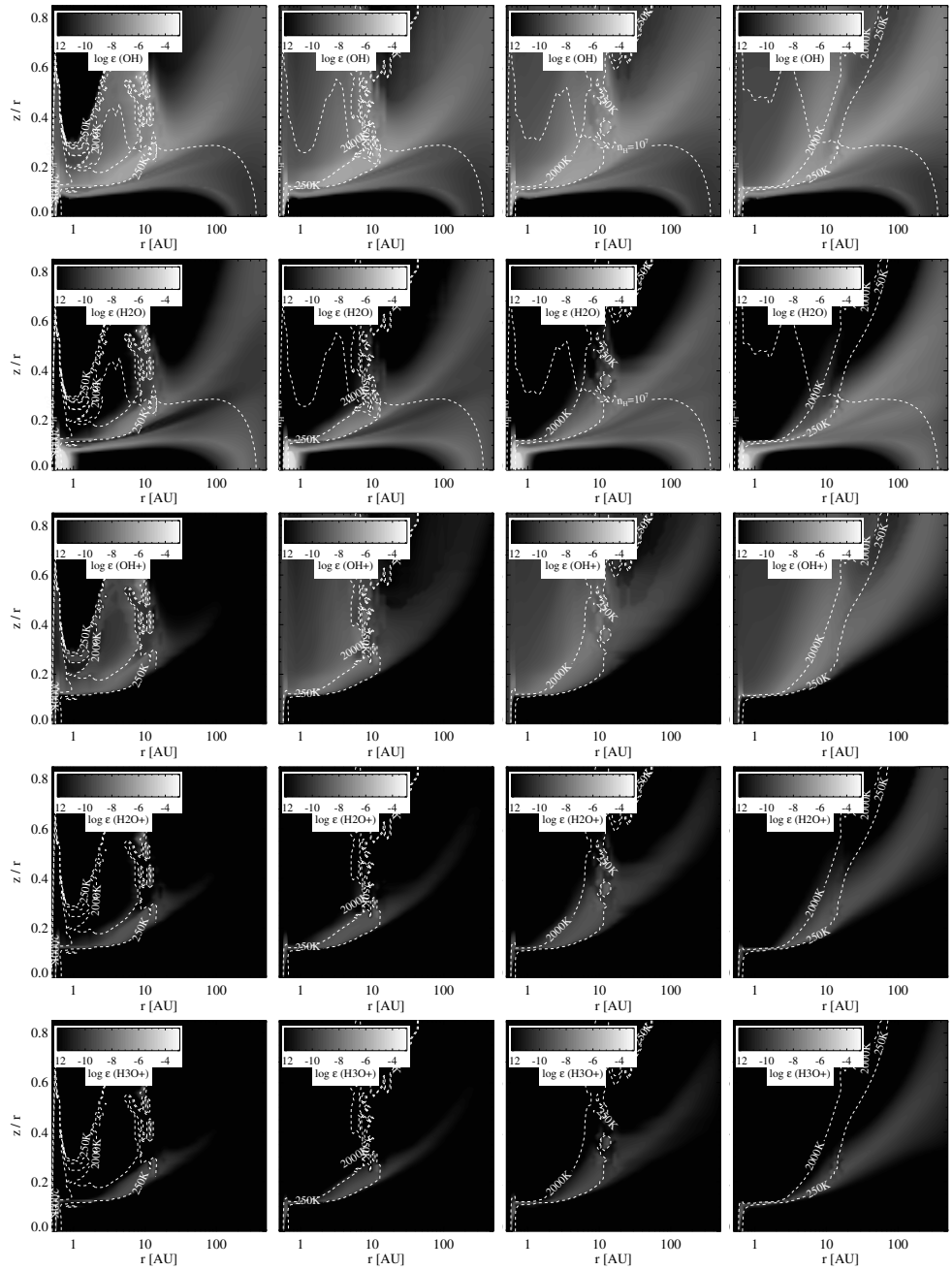

Figure 3.11: OH, H_2O, OH^+, H_2O^+, and H_3O^+ abundances. Fluxes are the same as in Fig. 3.6. The white contours indicate gas temperatures of 250 and 2000 K. The red contour indicates the number density $n_H = 10^6$ cm^{-3}.

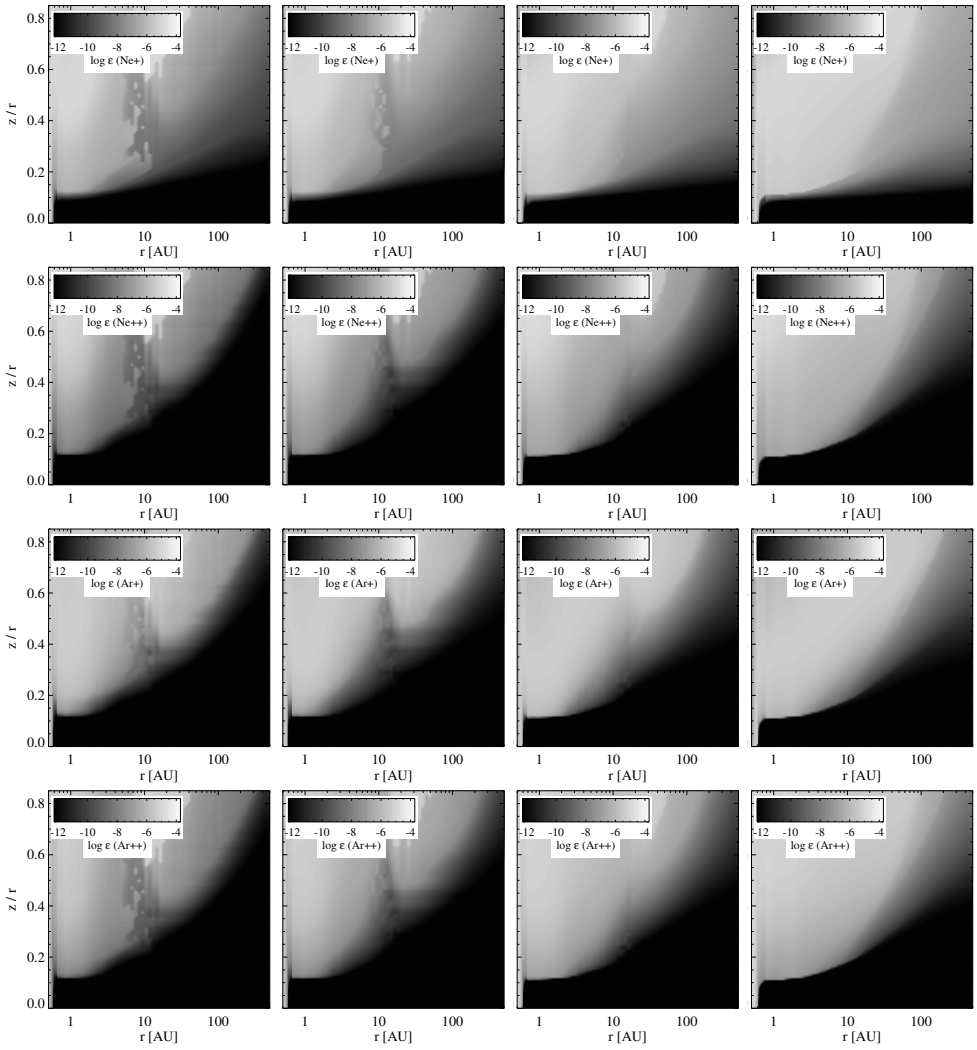

Figure 3.12: Abundance structure of selected heavy elements: Ne^{+} (top), Ne^{2+}, Ar^{+}, and Ar^{2+} (bottom). The FUV luminosity is fixed at $L_{\rm FUV} = 10^{31}$ erg s^{-1}. X-ray luminosities vary between $L_{\rm X} = 10^{29}$ and 10^{32} erg s^{-1}.

radiation field as defined by Draine, 1978; Draine & Bertoldi, 1996, and integrated between 91.2 and 205 nm), and their relative ratio change over orders of magnitude in the disk. As a result, the main chemical pathways forming the molecules OH and H_2O change throughout the disk and the grid.

X-rays heat the gas and therefore the reaction rates with activation barriers increase. They also drive the ionization, which enhances formation routes through ion-molecule reactions. The formation of the neutral species OH and H_2O is either by the neutral-neutral reactions, $H_2 + O \rightarrow OH + H$, and $H_2 + OH \rightarrow H_2O + H$, or by recombination of ionized species, such as $H_3O^+ + e^- \rightarrow H_2O + H$ and $H_2O^+ + e^- \rightarrow OH + H$. Which of these pathways are dominating depends thus strongly on the temperature and ionization fraction. The routes through neutral-neutral reactions have activation barriers, making them efficient only when gas temperatures are sufficiently high, i.e., $T > 200 - 300$ K. One way to increase the neutral-neutral route without the need of higher temperatures is by lowering the activation barrier, which can be done by exciting H_2 to a higher vibrational state after absorption of a FUV photon. At high relative heights ($z/r > 0.5$), this reaction will dominate when only FUV photons are present. The ion-molecule chain is started with cosmic ray or X-ray ionization of H_2 and thus requires significant ionization rates.

It turns out that the neutral-neutral reaction pathways dominate in the inner part of the disk ($r < 5$ AU). The X-rays heat regions deeper in the disk, resulting in the production of a thick warm water layer. Although there is a larger fraction of X-rays ionizing the gas than when only FUV photons are present, the X-ray heating causes the neutral-neutral reactions to dominate. It is remarkable to note that in the outer region ($r \gtrsim 20$ AU) of the disk the ion-neutral reaction network dominates. This is because temperatures are too low for the neutral-neutral reaction pathways to occur. These combined effects become apparent in the distribution of the water throughout the disk, as shown in the second panel from the top in Fig. 3.11 (see also Fig. 3.32 for a more elaborate view on the effects of both FUV and X-rays). In the models without any X-rays (left-hand side), the water shows a strong abundance peak at the inner rim (all the way down to the midplane of the disk) and a warm water layer at a relative height $z/r \approx 0.1$, with an abundance of $x_{H_2O} \sim 10^{-7}$, and a second water reservoir higher up in the disk. This reservoir is located at a relative height $z/r \sim 0.015$ at small radii ($r \sim 1$ AU), and at a relative height of $z/r \sim 0.5$ at a radius of $r \sim 100$ AU, thus following the flaring of the disk. These different water reservoirs were already noted by Woitke et al. (2009) for Herbig AeBe stars. An elaborate discussion on the formation of warm water reservoirs through (the dominant) neutral-neutral reactions and formation on dust grains in the inner regions of an X-ray irradiated disk is also outlined by Glassgold et al. (2009).

In the models where only FUV is included, the second layer is confined to the regions where temperatures are between $T \sim 300 - 1000$ K. The regions at higher temperatures are exposed to FUV fluxes that essentially destroy the water faster than it is formed. When X-rays are included, the second water reservoir extends to increasingly larger radii. Although there is water present in the FUV-only models out to radii $r \sim 200$ AU, the abundances are ultimately one to two orders of magnitude higher when X-rays are added. The additional water is increased since the ion-molecule chemistry is very effective in forming the water. This is illustrated in

the third to fifth panel of Fig. 3.11 (and also Figs. 3.33, 3.34, and 3.35), where the changing abundance structures of the ionic species OH^+, H_2O^+, and H_3O^+ are shown for various combinations of X-ray and FUV luminosities (appendix A only). The ionic species extend to larger radii for larger X-ray fluxes, but larger FUV fluxes decrease the extent. The fact that FUV confines the ionic species to smaller radii is an indirect effect, because FUV tends to puff up the upper layers of the disk and the density becomes higher at larger relative heights (see Fig. 3.3). These larger densities increase the recombination rates and reduce the abundances of these ionic species.

The first layer described above is located in those regions of the disk, where the conventional routes do not work anymore. Temperatures are too low and the ionization fraction is small. This is the region where more exotic reactions take over, such as $NH_2 + NO \rightarrow N_2 + H_2O$. This layer has a smaller vertical extent in relative height for larger FUV fluxes. On the other hand, the second separate layer becomes thicker when X-rays are added. When the $L_X/L_{FUV} \gtrsim 1$ ratio, these two layers merge. The reason for the merging is the enhancement of the transient species OH^+, H_2O^+, and H_3O^+ (see also Fig. 3.33, 3.34 and 3.35). As mentioned earlier, these species react sensitively to the presence of an ionization source and become increasingly abundant with higher X-ray fluxes.

The situation with OH is very similar. OH becomes more abundant in the outer disk, when X-rays are added. OH is located at higher altitudes in the disk (although there is also a large overlap with the regions where the water is located). For this reason, the effect of the X-rays on the abundance in the outer disk is not as pronounced as for water. The H_2 used in the neutral-neutral formation route of OH is on average at higher temperatures, so the relative contribution of the ion-molecule route is smaller.

3.4.7 Ar^+, Ar^{2+}, Ne^+, and Ne^{2+} abundances

These species have ionization potentials that are larger than that for atomic hydrogen, with $IP = 21.56$, 40.96, 15.76, and 27.63 eV for Ne, Ne^+, Ar, and Ar^+, respectively. The only way to produce these species is through direct (photon absorption and Auger effect) or indirect (fast electron collisions) ionization by X-rays. The presence of these ionized species is thus a direct result of the X-ray irradiation of the disk.

The models include a thermal source of temperature, $T_X = 1$ keV. As a result, the cross sections for neon are more favorable for direct ionizations than for argon. The cross section for the absorption is located at approximately ~ 1 keV for neon, while for argon it is ~ 4 keV. On the other hand, the rates for secondary ionizations are a little higher for argon, $\sigma(A)/\sigma(H) = 1.1$, 0.48, 3.7, and 1.8, with A equal to Ne, Ne^+, Ar, Ar^+, respectively. Consequently, the total ionization rates are very comparable. However, there is one big difference in the chemical network of these species. The charge transfer rate of Ne^+ with H_2 is very low ($k < 10^{-14}$ cm^3 s^{-1}), while the other ions have significant rates for charge exchange with molecular hydrogen. The Ne^+ abundance structure thus extends to much smaller relative heights, down to $z/r \sim 0.01$, than Ar^+, which is abundant above $z/r \sim 0.01 - 0.06$ at radii $r \gtrsim 10 - 200$ AU. The abundance structure of Ar^+ is very similar to those for Ne^{2+} and Ar^{2+}.

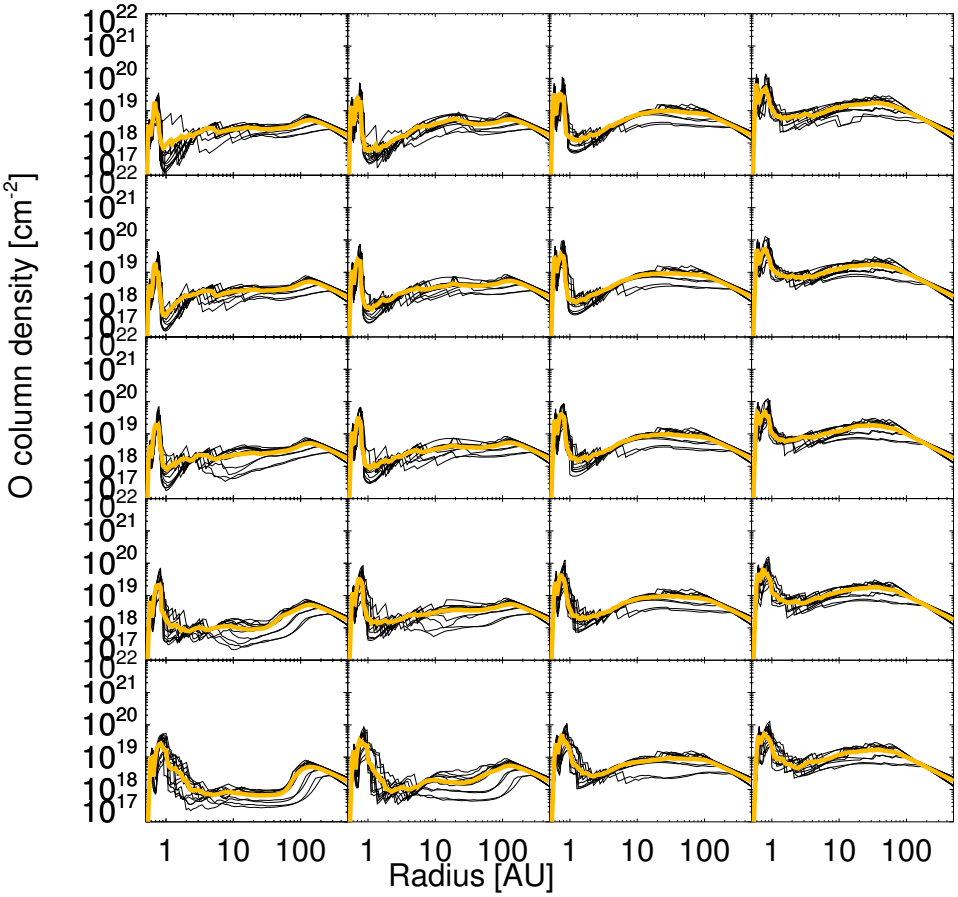

Figure 3.13: Radial column density distribution of O. FUV and X-ray fluxes are the same as Fig. 3.3.

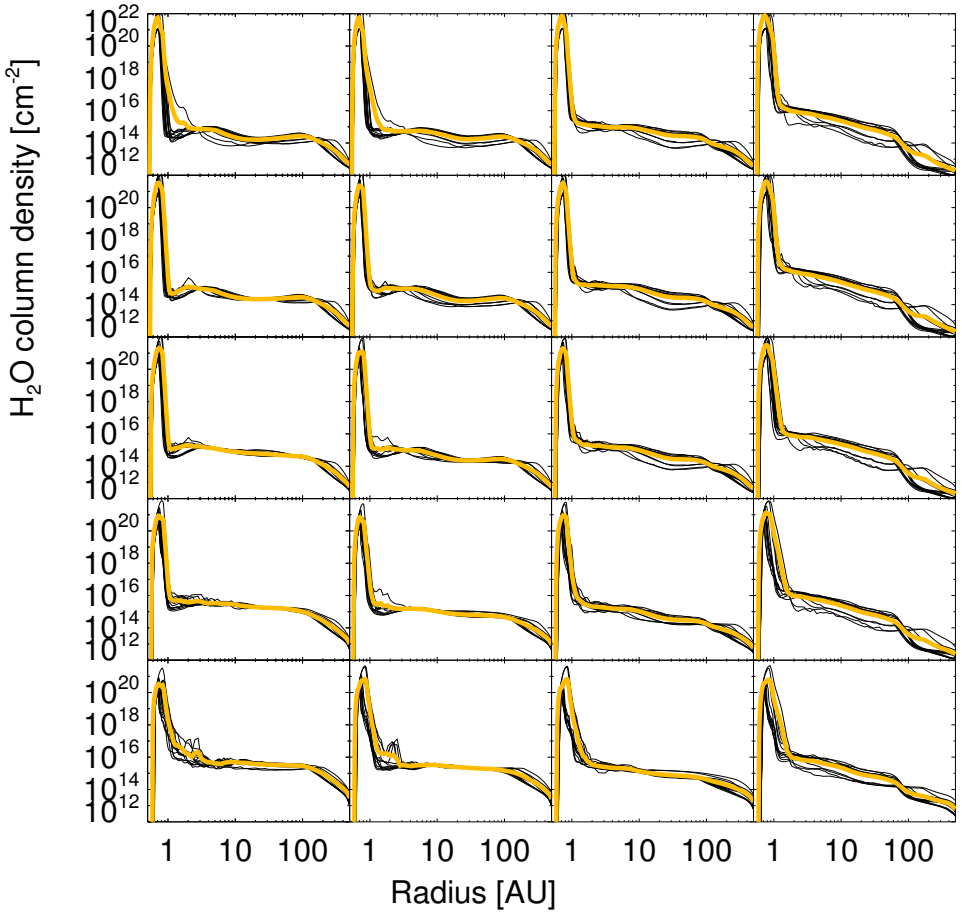

Figure 3.14: Radial column density distribution of H_2O. FUV and X-ray fluxes are the same as Fig. 3.3.

3.5 Radial column density profiles

Although the abundance distributions of species well illustrate the change in the chemistry due to different combinations of X-ray and FUV luminosities, it is necessary to look at the integrated properties of the disk that are observed by our telescopes. The focus in this is on the species C^+, O, H_2O, and Ne^+, as their line intensities and line profiles are extensively discussed the paper II. The figures show the average column density in yellow, while the black lines represent the 12 models at fixed FUV and X-ray luminosities. Changing parameters other than those for FUV and X-rays does not affect the results significantly.

C^+ column density profile (Fig. 3.40): The column density of C^+ is strongly related to the inicident FUV flux at the inner rim, where it increases from $N_{C^+} \sim 10^{17}$ to 10^{19} cm^{-2}, when the FUV luminosity increases from $L_{FUV} = 10^{29}$ to 10^{32} erg s^{-1}. Right after the peak at the inner rim, there is a sharp drop in the column density, which is caused by the inner rim casting a shadow and therefore reducing ionizing radiation. A second peak in the column density profile is seen between $r \sim 5-10$ AU. The peaks moves to larger radii for higher FUV luminosities. The X-rays affect the column density profile in a different way. They reduce the minimum column density right after the inner rim and smooth the radial distribution. The combination of the highest FUV and X-ray fluxes gives the flattest distribution.

O column density profile (Fig. 3.13): The column density profiles of neutral oxygen do not change as much as those for C^+. The maximum column density, $N_O \sim 3 - 10 \times 10^{19}$ cm^{-2}, is located right behind the inner rim and only varies with a factor of at most ten, which is again caused by the FUV irradiation. The width of the oxygen column density peak broadens a bit for higher FUV and X-ray fluxes. This makes the mininum in the column density less prominent in the radial column density profile. Because the column density is not very affected by radiation, it is a clean probe of the properties of a disk temperature ([OI] fine-structure lines), since there are no strong dependencies on uncertainties in the chemical network.

H_2O column density profile (Fig. 3.14): The highest water column densities, $N_{H_2O} \sim 10^{20} - 10^{22}$ cm^{-2}, are found at the inner rim, $r \sim 0.5$ AU. As discussed, the water abundances are enhanced by higher temperatures and higher ionization fractions throughout the disk. The FUV counteracts this to some extent, and the most favorable situation is a high X-ray to FUV luminosity ratio. FUV irradiation puffs up the inner rim, and shields the outer disk, thus allowing less ionizing radiation to penetrate into the outer regions of the disk. As a result, it confines the water to smaller regions of the disk. The bottom panel ($L_X = 10^{32}$ erg s^{-1}) of Fig. 3.14 shows that the column density distribution is flat for the lowest FUV flux, dropping steadily as a function of radius for the highest FUV flux. The only region in the disk where the column density becomes smaller is at the inner rim due to reactions with ions such as $H_2O + He^+ \rightarrow H^+ + He + OH$. The water column density is almost two orders of magnitude smaller for the models with the highest X-ray luminosities compared to those with only FUV.

Ne^+ column density profile (Fig. 3.41): Ne^+ is only produced by X-rays and therefore only the models that include X-rays show significant column densities. The

profiles show a peak in the column density at the inner rim and a second bump at a few AU. The second bump smoothes out for larger X-ray fluxes, while the maximum column density increases from $N_{\mathrm{Ne}^+} \sim 10^{15}$ to 10^{17} cm^{-2}. The FUV tends to confine the Ne^+ to smaller radii for the lower X-ray luminosities, which becomes apparent in the line profile (see paper II).

3.6 Conclusions

In this paper, we discussed the combined effects of FUV and X-rays on both the density structure and the thermal and chemical balance of disks around T Tauri stars for an expected range of parameters (dust size distribution, density profile, etc.), yielding a total of 240 models. Here we highlight the main results and a few implications:

3.6.1 The disk thermal and chemical structure

Temperature structure: The extent of the disk where the temperature is higher than $T > 1000$ K is much larger when X-rays are included. X-rays have a much higher heating efficiency than FUV, $30 - 50\%$ compared to $< 3\%$, respectively.

Density structure: Increasing FUV luminosities does not change the scale height of the inner rim; it only alters the width and height of the second bump in the disk that is created at intermediate radii ($r \sim 3 - 10$ AU), behind the region shielded by the puffed-up inner rim. Gas temperatures at the inner rim are much higher when X-rays are included and, as a result, the inner rim is puffed up to higher and higher altitudes for increasing X-ray luminosities. As a direct extension of this theoretical work, the existence of the second bump could potentially be tested by continuum imaging face-on protoplanetary disks in the near-infrared with, e.g., VLT or Keck.

Scale height: Considering only FUV, we see that the scale height shows a maximum in the unattenuated parts ($z/r > 0.5$) of the disk. When X-rays are added we find that this maximum is smoothed over a larger region (out to $r \sim 10$ AU). The scale height in these regions is larger than one would expect from the flaring index in the outer regions of the disk. When moving to smaller relative height, e.g, $z/r = 0.1$, the break in the flaring index disappears. Another observational possibility would be to do continuum interferometry in the near-IR (VLTI) to directly measure the physical height of the inner rim.

3.6.2 Chemical balance

Ionization fraction: The ionization fraction reaches values as high as $x_{\mathrm{e}^-} \sim 10^{-2}$ in exceptional cases in our FUV-only models, whereas X-rays easily maintain these ionization fractions throughout large portions of the disk. Even when the gas becomes partially shielded, it can still maintain a significant ionization fraction, leading to an ion-molecule chemistry that can form molecules at low temperatures, which is not possible with neutral-neutral reactions as they usually have temperature barriers.

Formation of H_2 through the H^- route: Formation of H_2 dust is usually much more efficient in environments that have solar metallicities. Because of the high ionization fraction due to X-ray irradiation, the formation route $H^- + H \rightarrow H_2 + e^-$ is able to provide a significant addition of order 50% percent to the H_2 on dust formation route. Overall, the H_2 to H abundance ratio is increased by at least two orders of magnitude when X-rays are present.

Formation of water and OH: The OH and H_2O abundances are more concentrated toward the inner regions of the disk, when only FUV is irradiating the disk. This is because the temperature is only there sufficient to drive the neutral-neutral formation route. The outer disk shows significant enhancements (up to two orders of magnitude) when X-rays are added. The higher ionization fractions make it possible to form the species through ion-molecule reactions and sustain abundance levels of $x_{H_2O} \sim 10^{-6}-10^{-7}$. Such abundance levels cannot be reached in outer disk models without X-rays. Only the warm inner disks allow even higher levels of water abundance through warm neutral-neutral chemistry.

Resulting abundance structures and radial column density profiles: Whereas neutral oxygen and CO are very stable to both FUV and X-rays, this is not the case for, e.g., C^+, Ne^+, and H_2O. Ne^+ is strongly enhanced by X-rays and confined to the inner regions by larger FUV luminosities. This latter aspect will certainly affect the line widths. A high L_X/L_{FUV} ratio is favorable for water formation, especially in the outer disk.

3.6.3 Outlook

In paper II, we will perform a radiation transfer analysis of the aforementioned species and correlate line fluxes and line widths directly to the FUV and X-ray luminosities. This will allow a discussion of the diagnostic value of these species and provide a theoretical framework for the interpretation of observational data. We will also discuss our results in the context of data obtained within several observational efforts (Spitzer, Herschel, and ground-based observing programs).

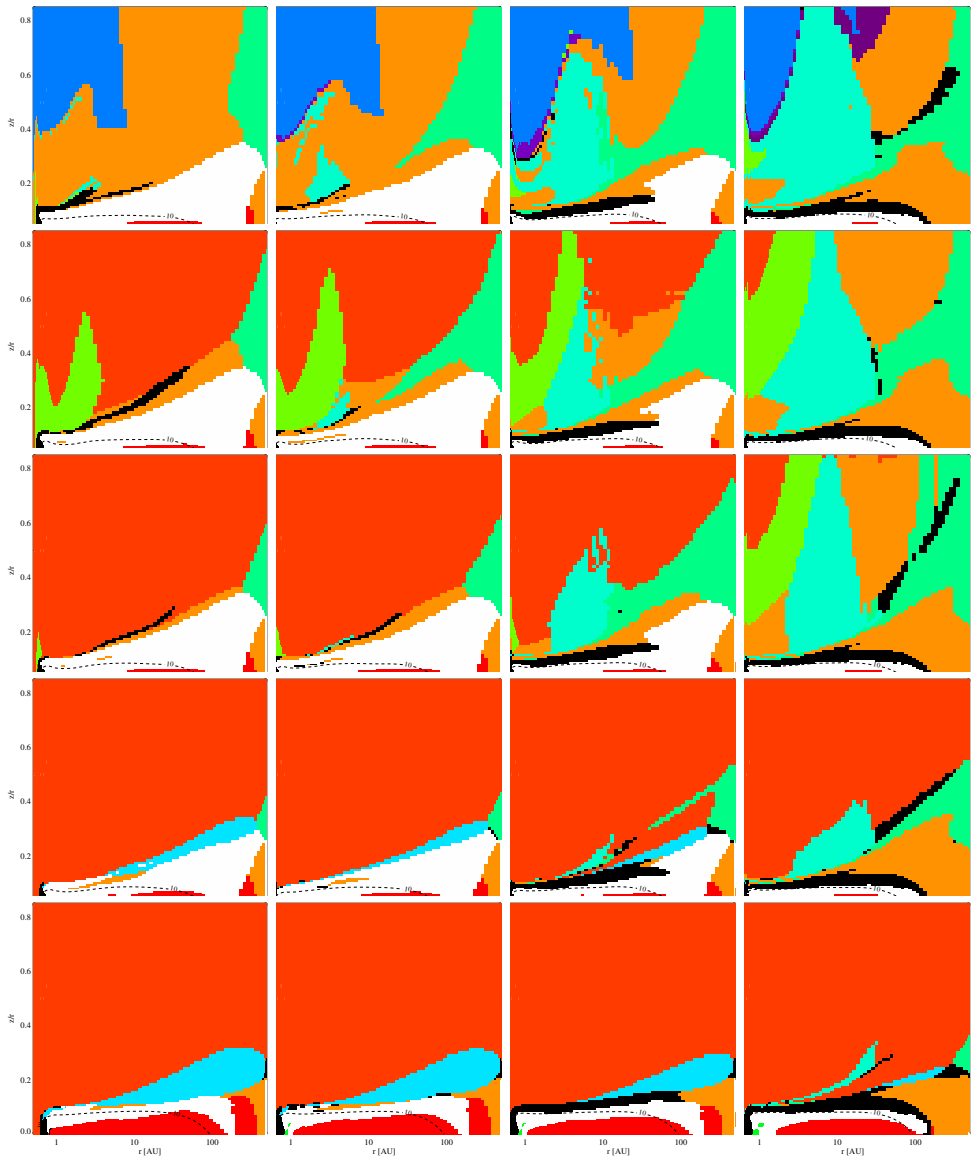

Figure 3.15: Main heating sources throughout the disk: FUV luminosity increasing from $L_{FUV} = 10^{29}$ (left) to 10^{32} erg/s. X-ray luminosity increasing from $L_x = 0$ to 10^{32} erg/s. background heating by [CII] (blue), PAH heating (orange), photo-electric heating (dark purple), X-ray Coulomb heating (light red), heating by collisional de-exciation of H_2 (blue-green), CI ionization heating (green-blue), infrared background by CO ro-vibrational lines (black), heating by thermal accomodation grains (white), cosmic ray heating (red), X-ray H_2 dissociation heating (light blue), free-free absorption (green), background heating by FeII (light green), background heating by SiII (green-yellow), infrared background heating by H_2O rotational transitions (yellow), heating by H_2 formation on dust (dark blue), and background heating by [OI] (purple).

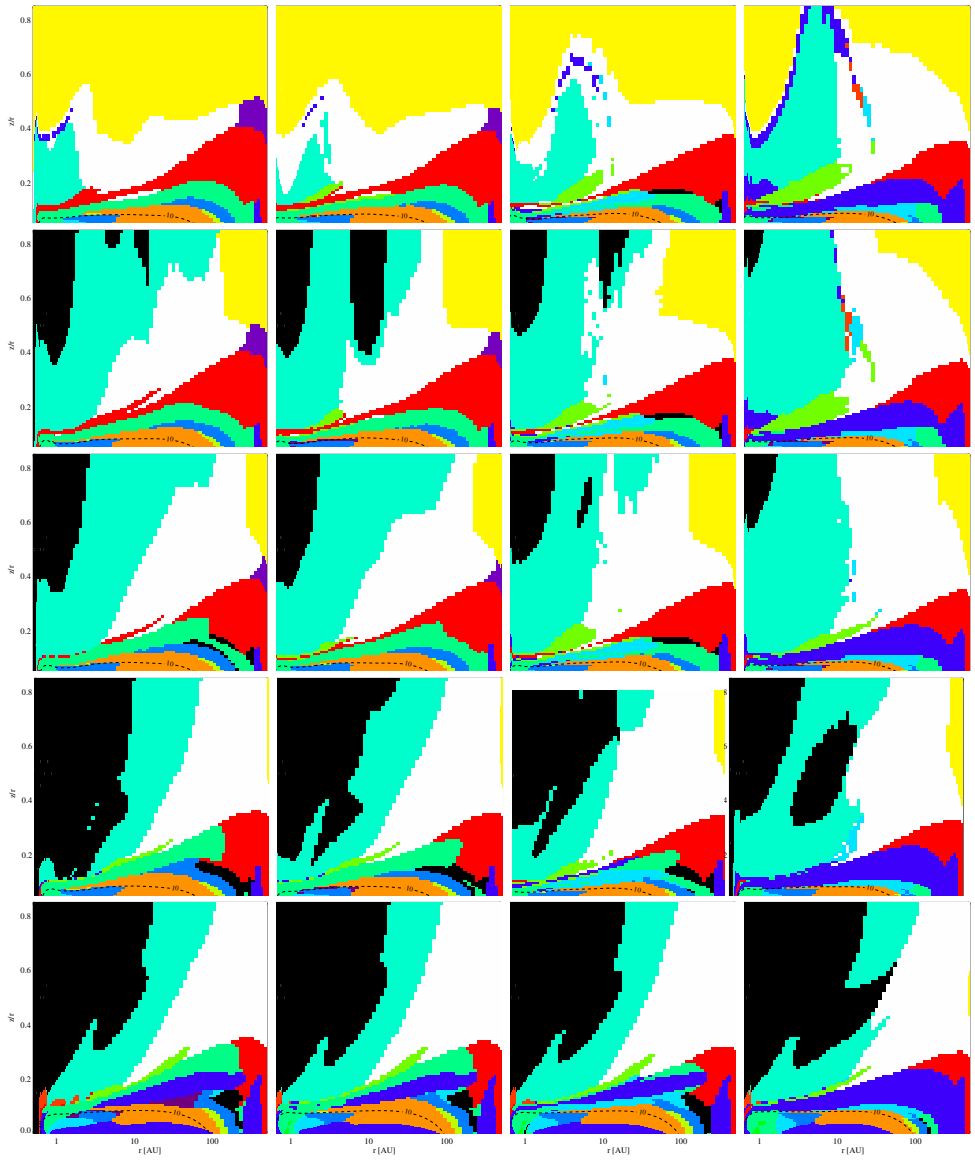

Figure 3.16: Main cooling sources throughout the disk: FUV luminosity increasing from $L_{FUV} = 10^{29}$ (left) to 10^{32} erg/s. X-ray luminosity increasing from $L_x = 0$ to 10^{32} erg/s. Lyman α cooling (black), [FeII] line cooling (blue-green), [OI] line cooling (white), [CII] line cooling (yellow), CO rotational and ro-vibrational cooling (red), H_2O rotational cooling (green-blue), OH rotational cooling (light green), HCN line cooling (dark purple), [CI] line cooling (light purple), HNC line cooling (blue), cooling by thermal accomodation on grains (dark blue), CS line cooling (yellow-green), H_2 line cooling (light blue), chemical cooling (red-orange), and free-free emission (green).

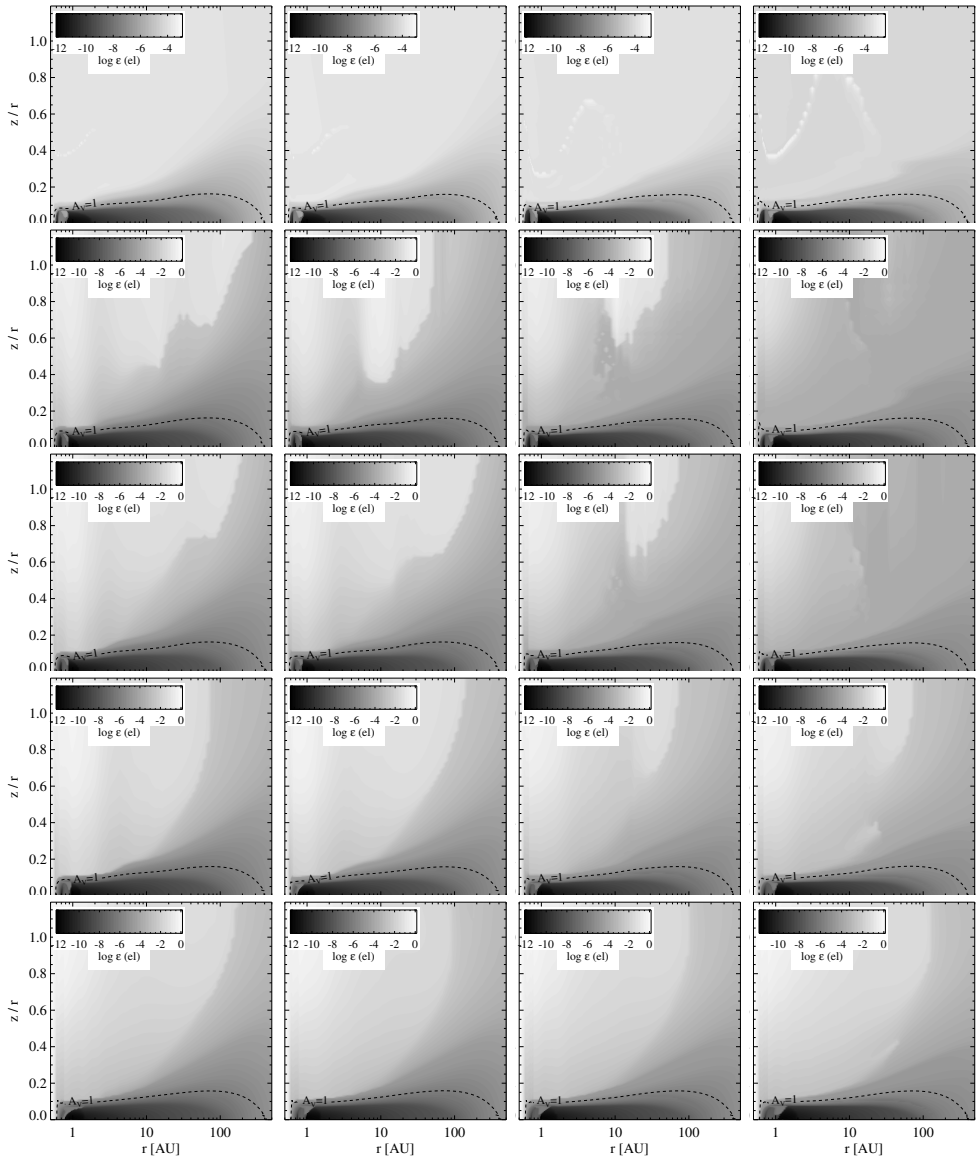

Figure 3.17: Electron abundance: FUV luminosity increasing from $L_{FUV} = 10^{29}$ (left) to 10^{32} erg/s (right). X-ray luminosity increasing from $L_x = 0$ (top) to 10^{32} erg/s (bottom).

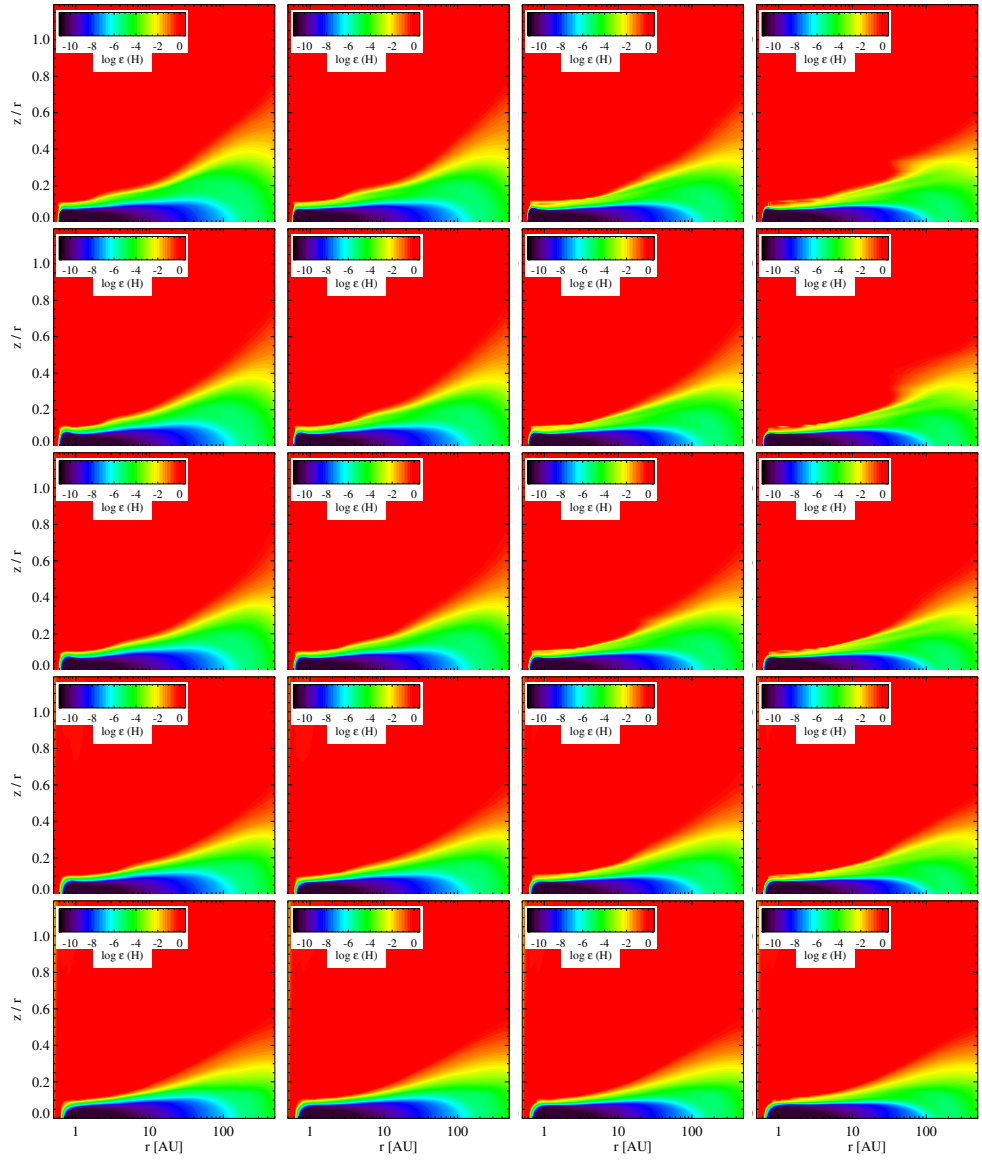

Figure 3.18: H abundances. FUV and X-ray fluxes are the same as Fig. 3.17.

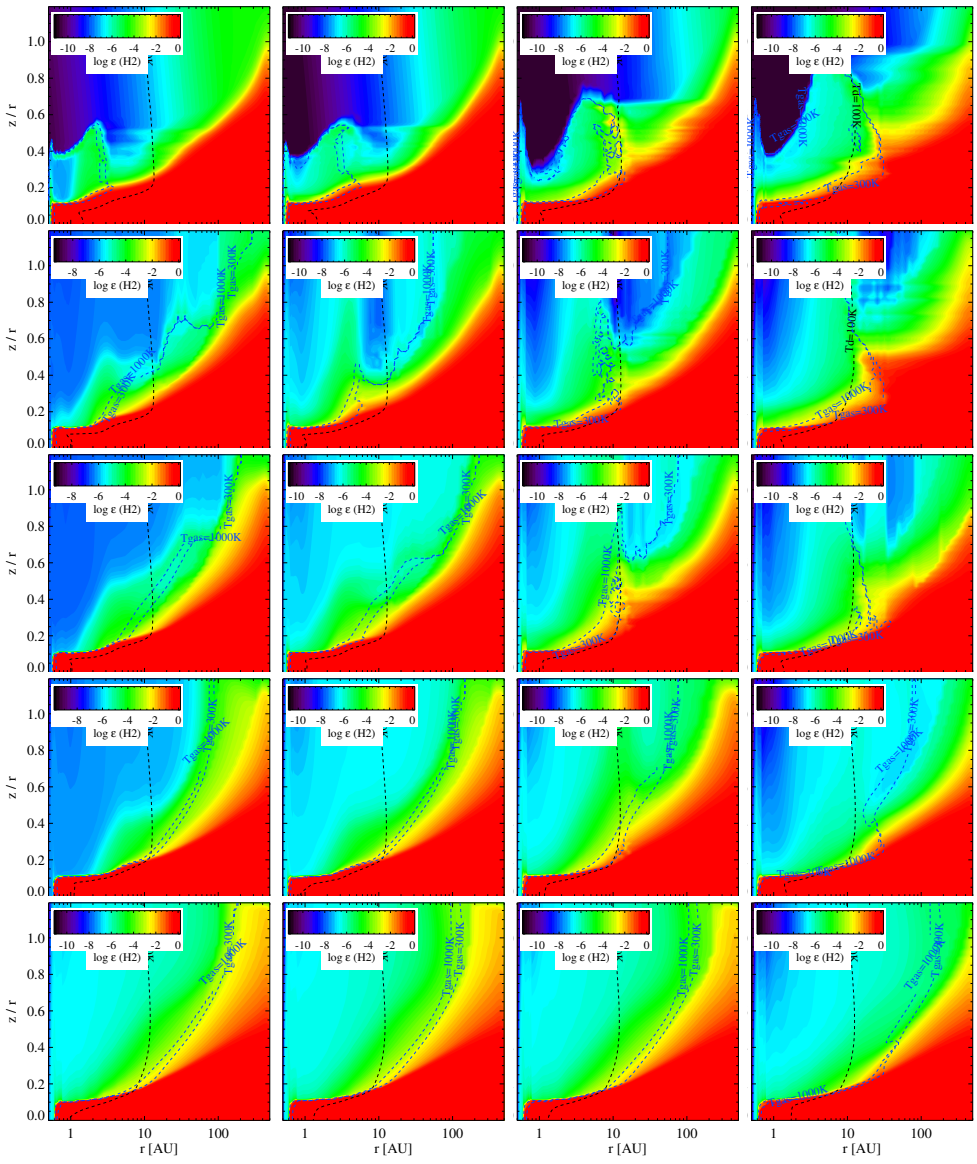

Figure 3.19: H_2 abundances. FUV and X-ray fluxes are the same as Fig. 3.17.

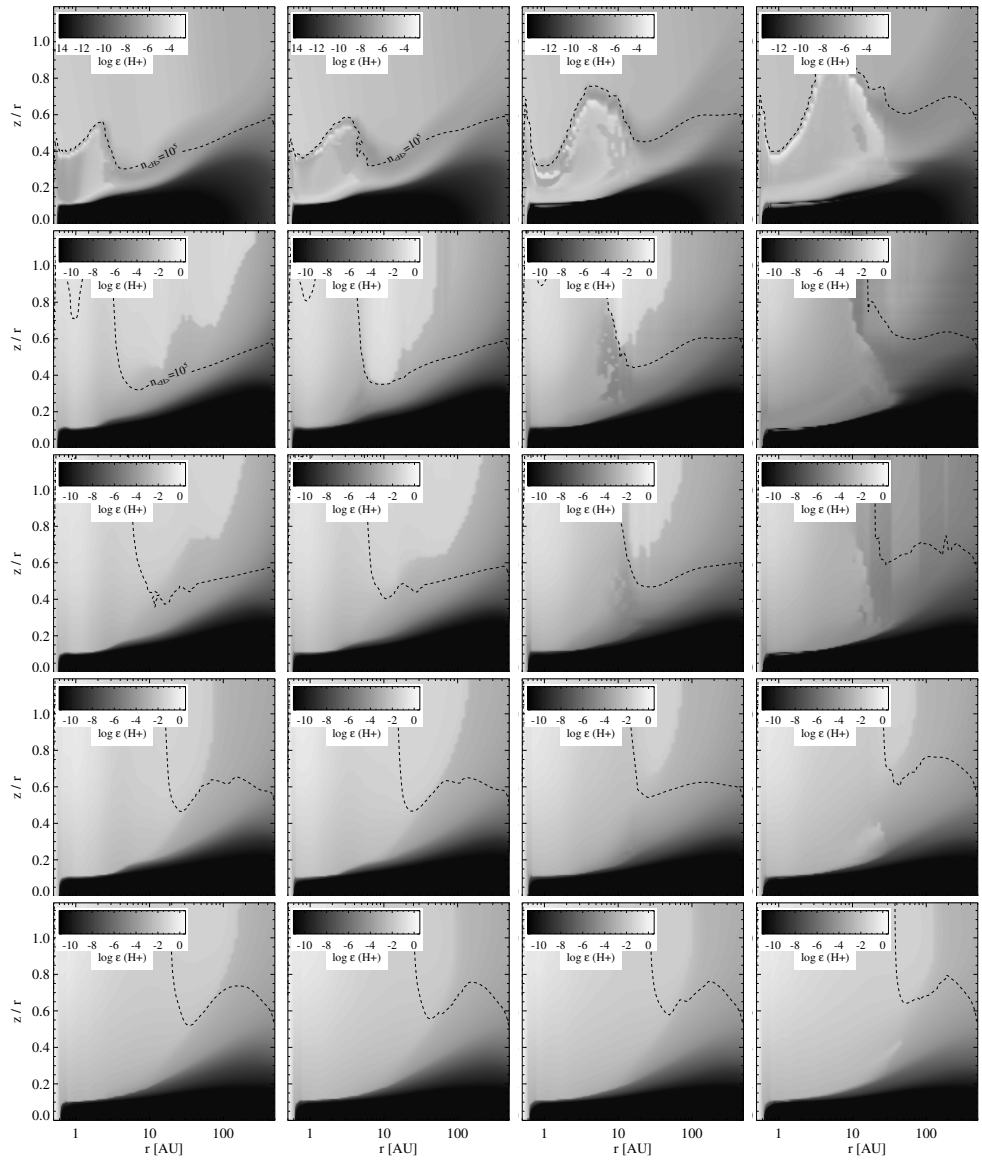

Figure 3.20: H^+ abundances. FUV and X-ray fluxes are the same as Fig. 3.17.

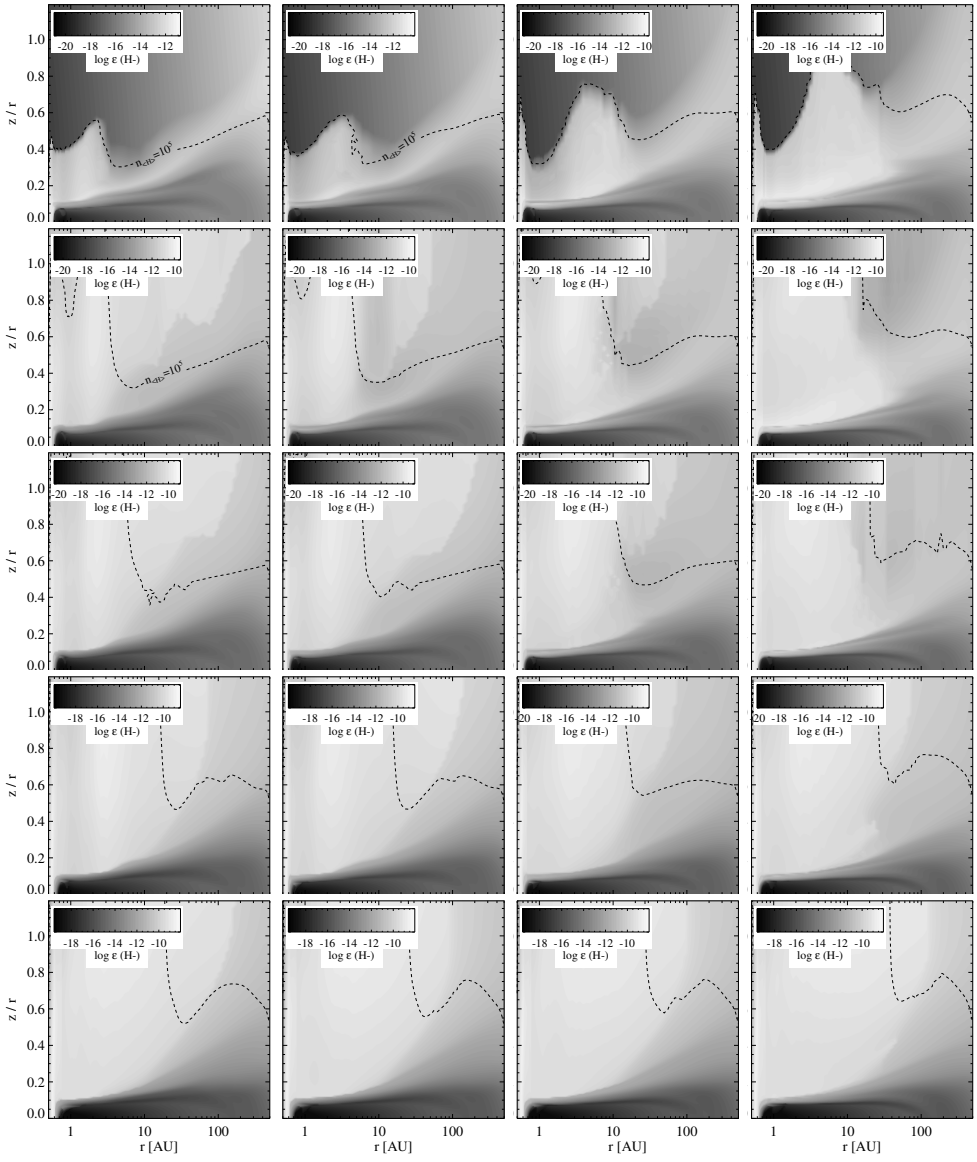

Figure 3.21: H^- abundances. FUV and X-ray fluxes are the same as Fig. 3.17.

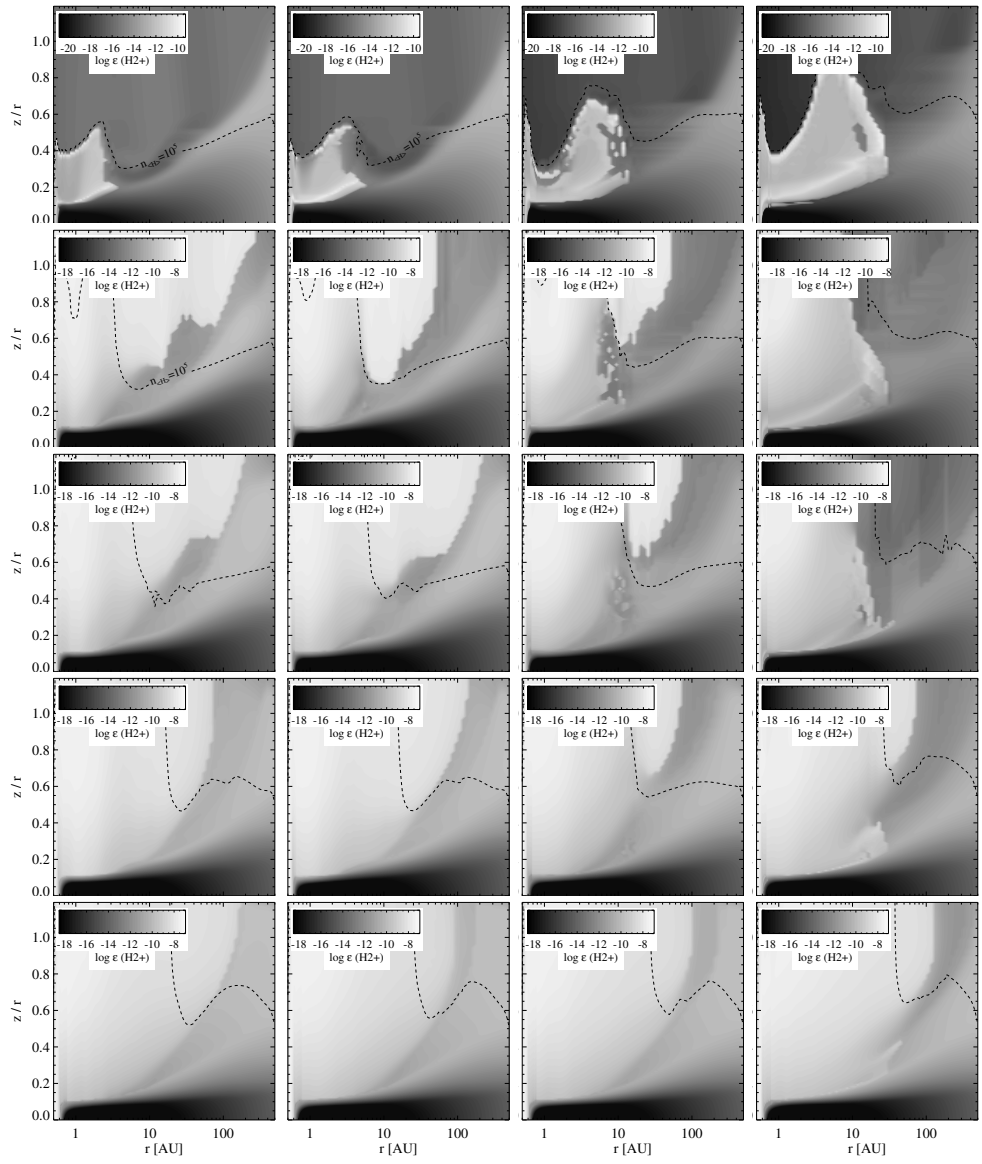

Figure 3.22: H_2^+ abundances. FUV and X-ray fluxes are the same as Fig. 3.17.

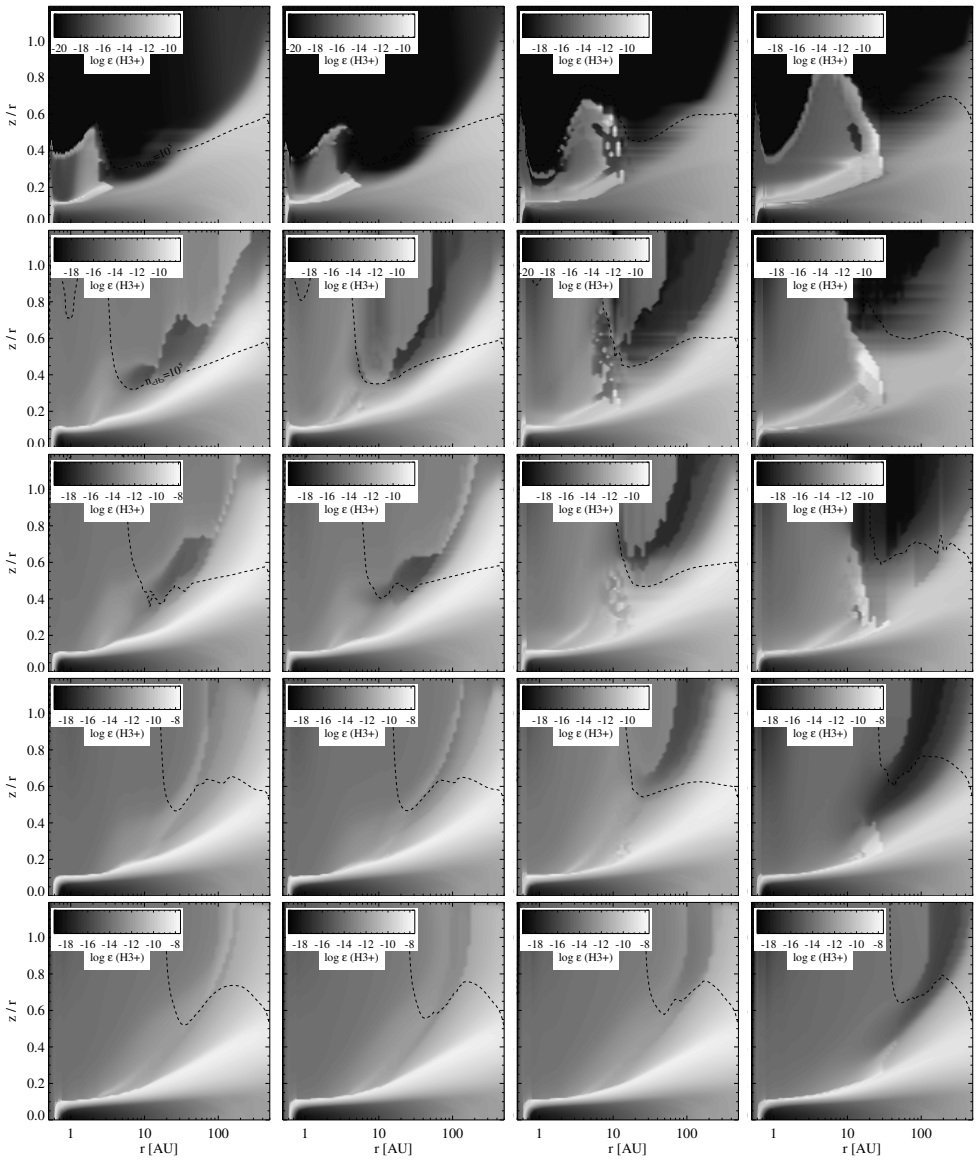

Figure 3.23: H_3^+ abundances. FUV and X-ray fluxes are the same as Fig. 3.17.

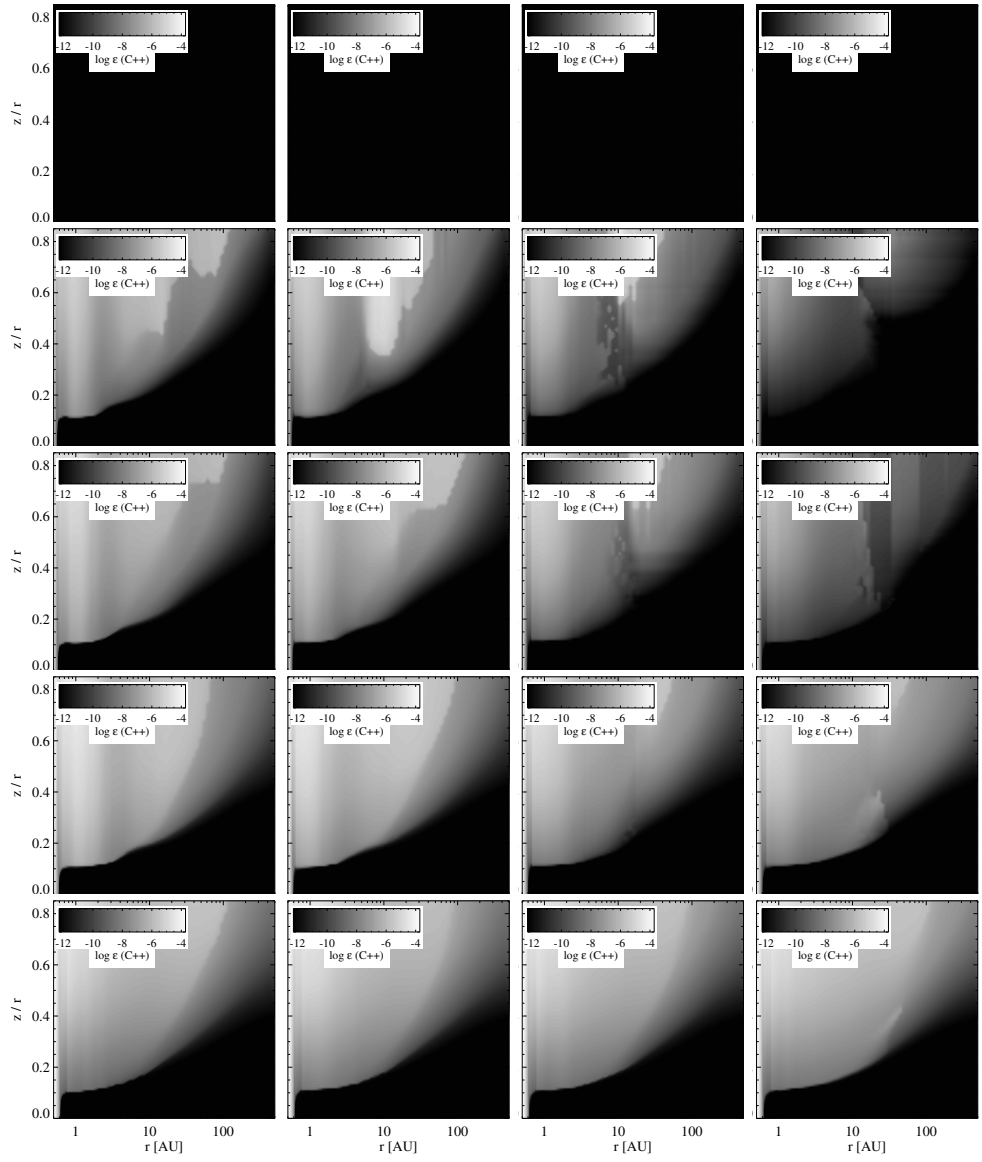

Figure 3.24: C^{2+} abundances. FUV and X-ray fluxes are the same as Fig. 3.17.

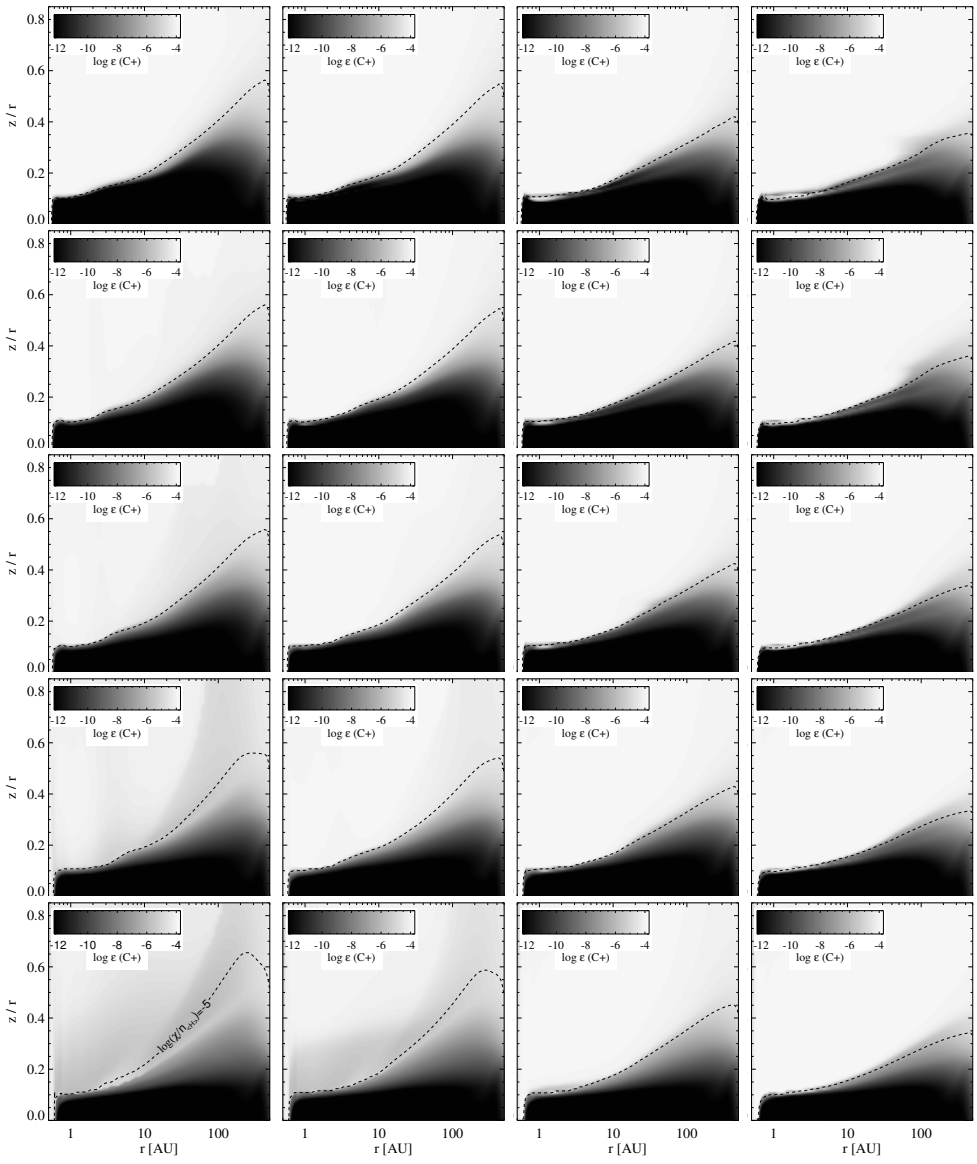

Figure 3.25: C^+ abundances. FUV and X-ray fluxes are the same as Fig. 3.17.

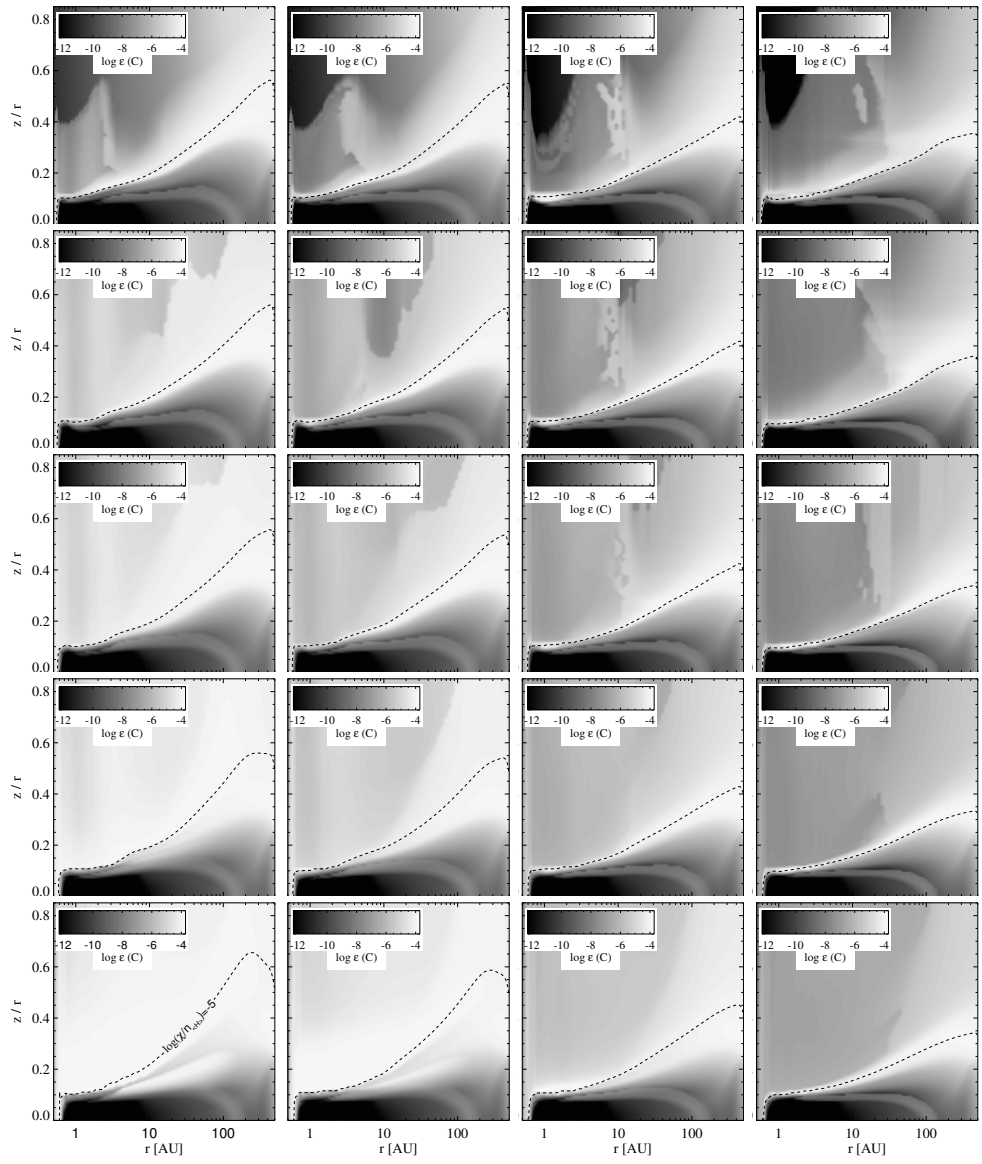

Figure 3.26: C abundances. FUV and X-ray fluxes are the same as Fig. 3.17.

Figure 3.27: CO abundances. FUV and X-ray fluxes are the same as Fig. 3.17.

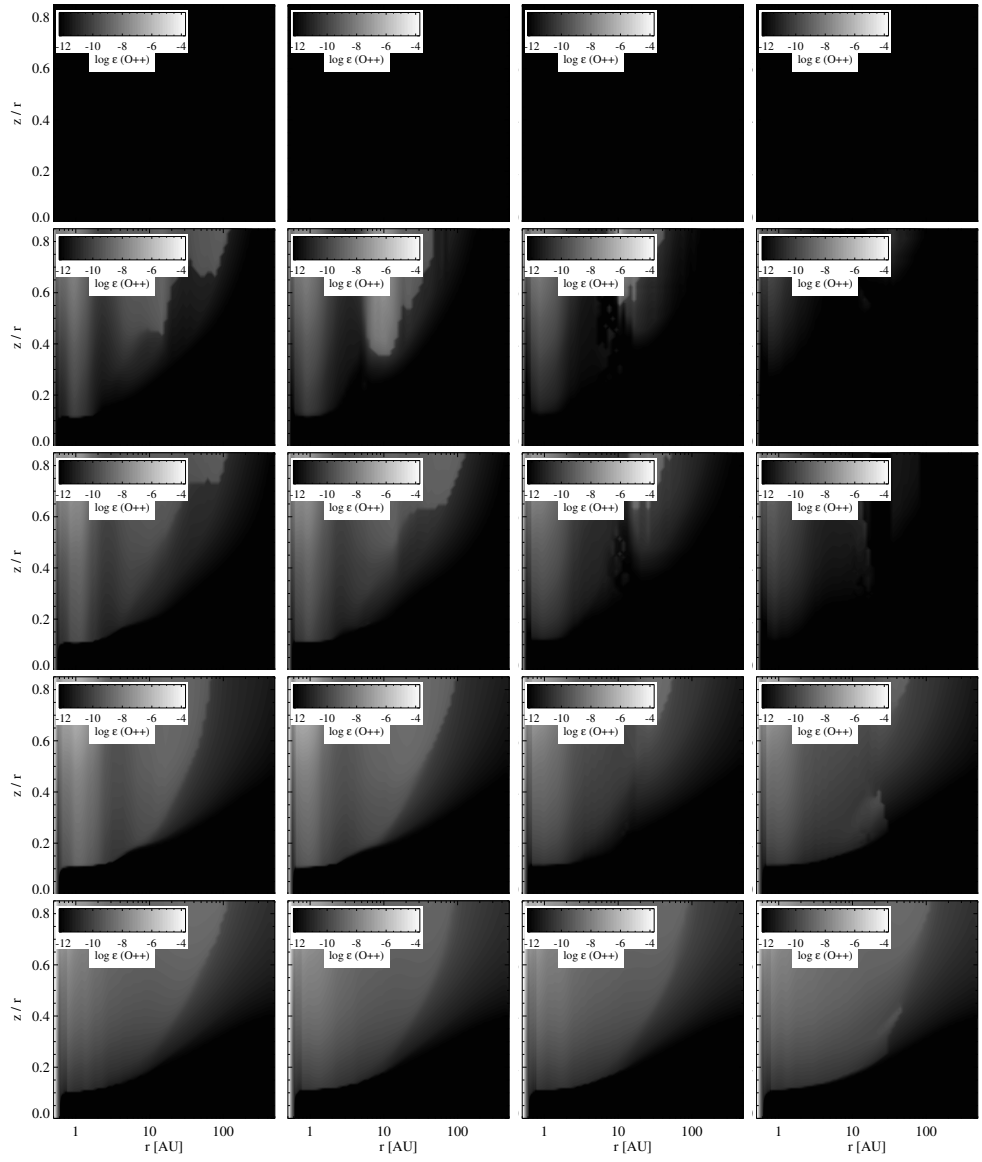

Figure 3.28: O^{2+} abundances. FUV and X-ray fluxes are the same as Fig. 3.17.

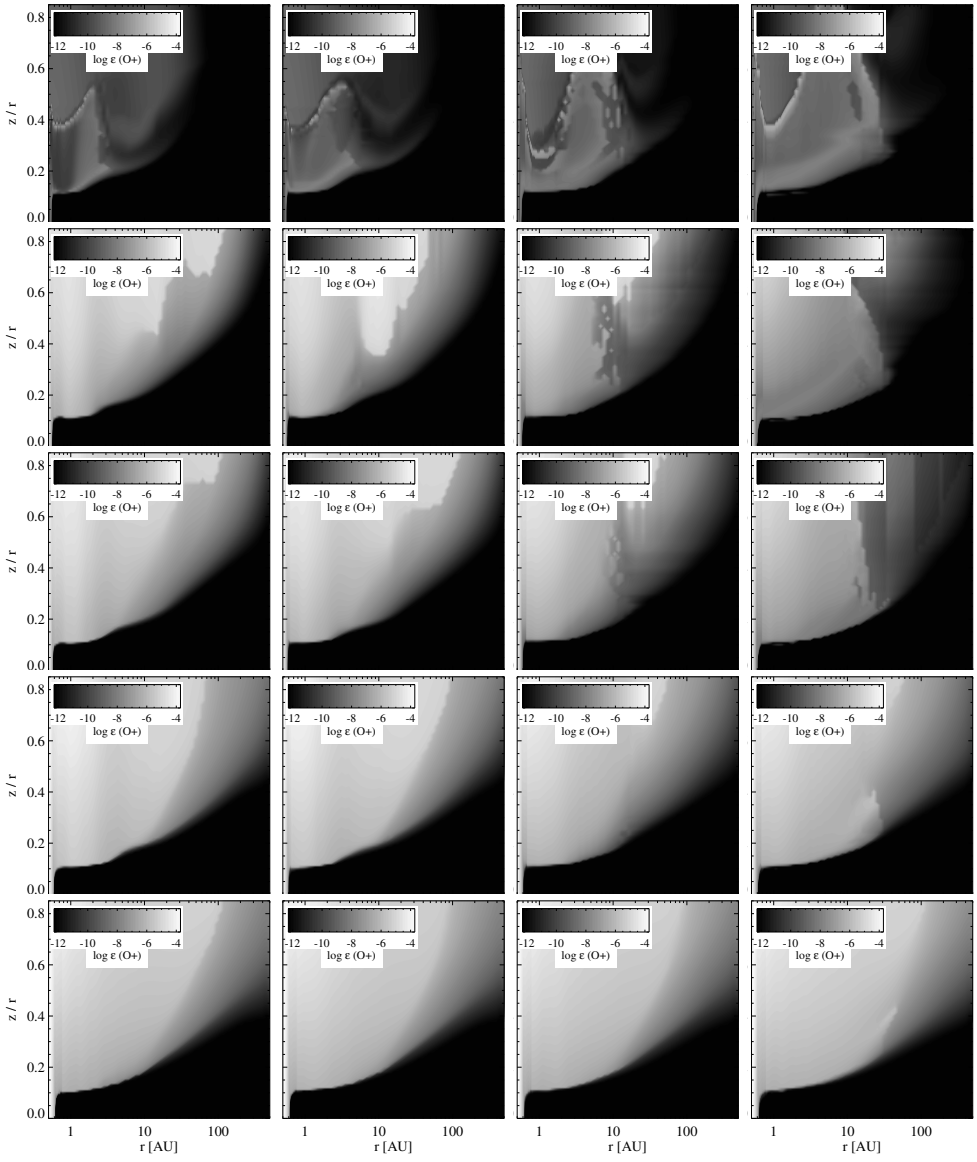

Figure 3.29: O^+ abundances. FUV and X-ray fluxes are the same as Fig. 3.17.

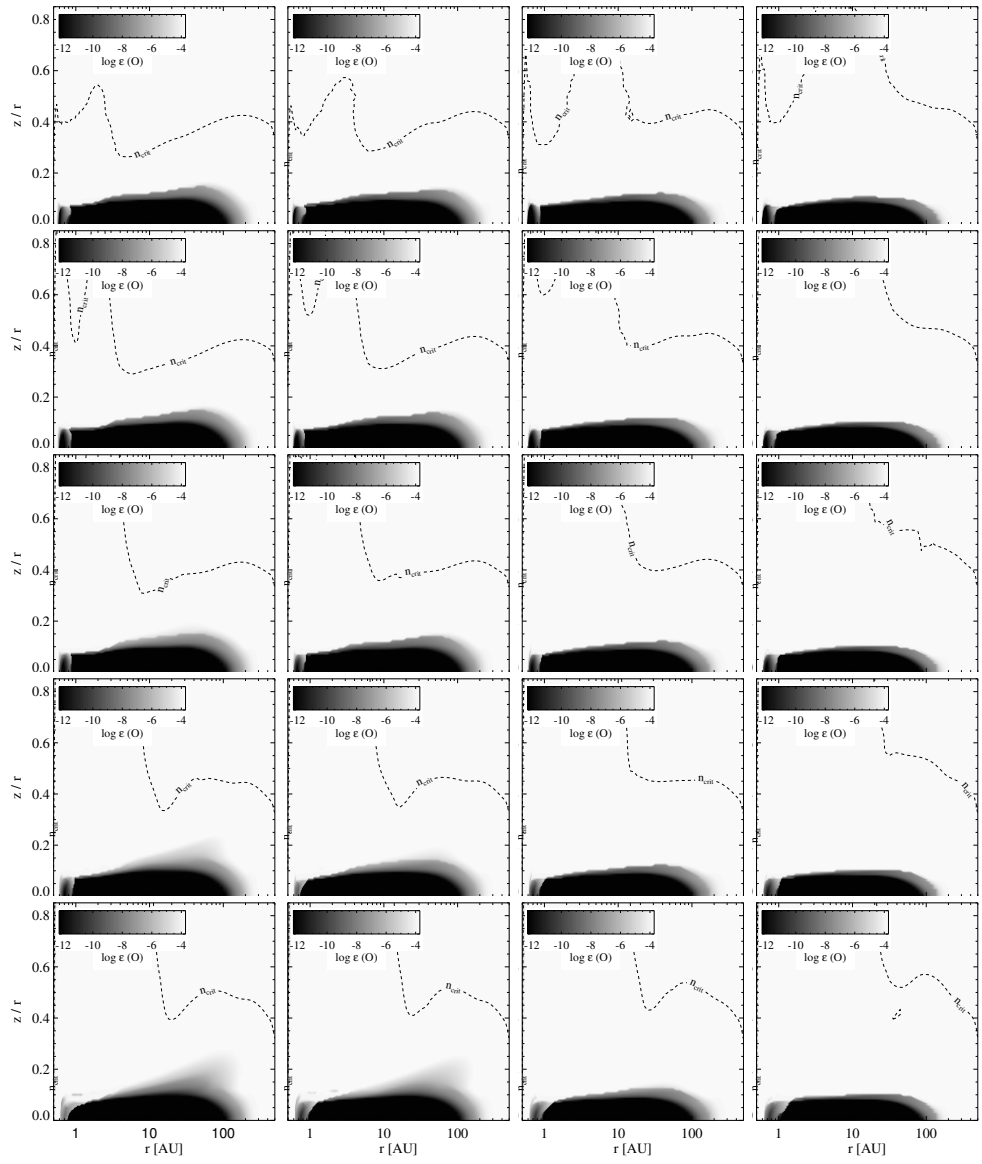

Figure 3.30: O abundances. FUV and X-ray fluxes are the same as Fig. 3.17.

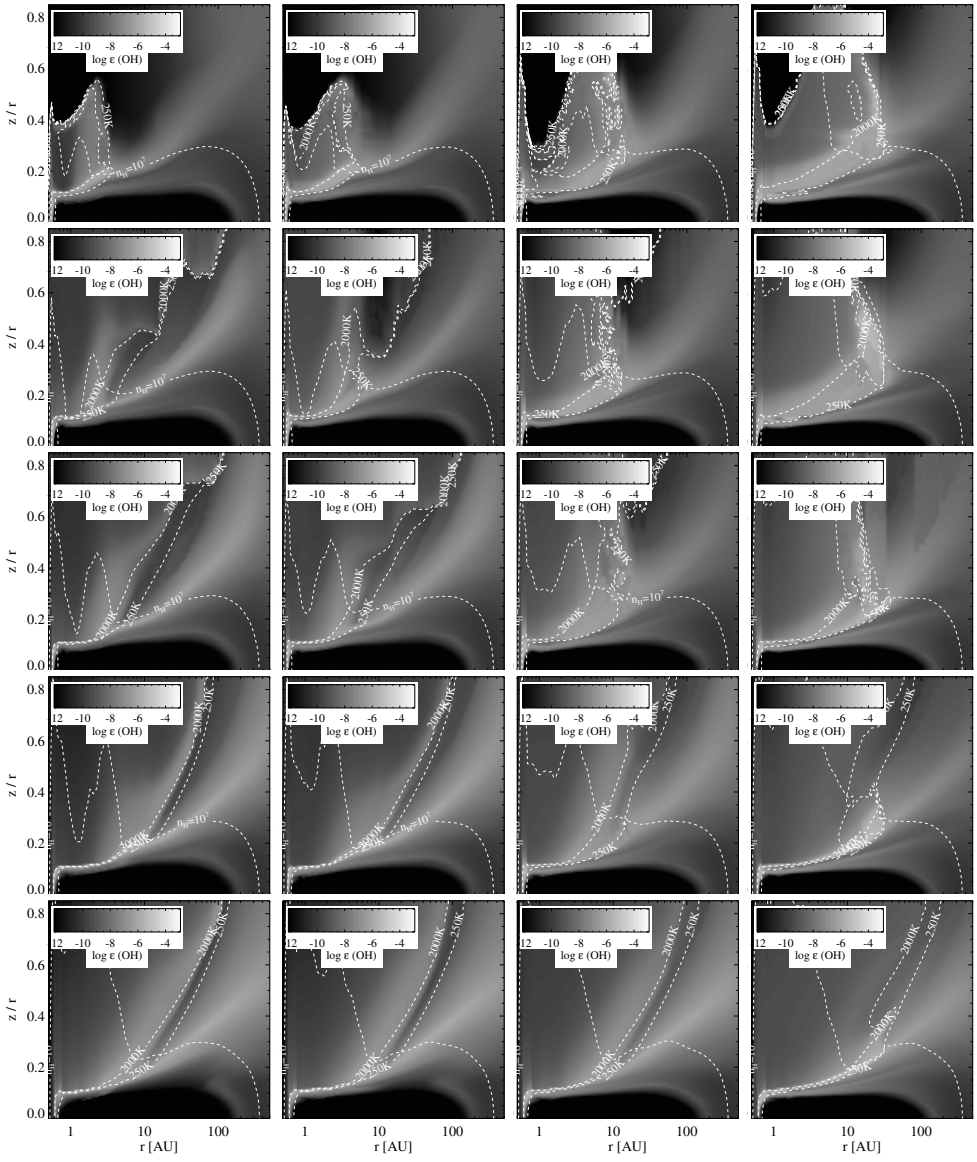

Figure 3.31: OH abundances. FUV and X-ray fluxes are the same as Fig. 3.17.

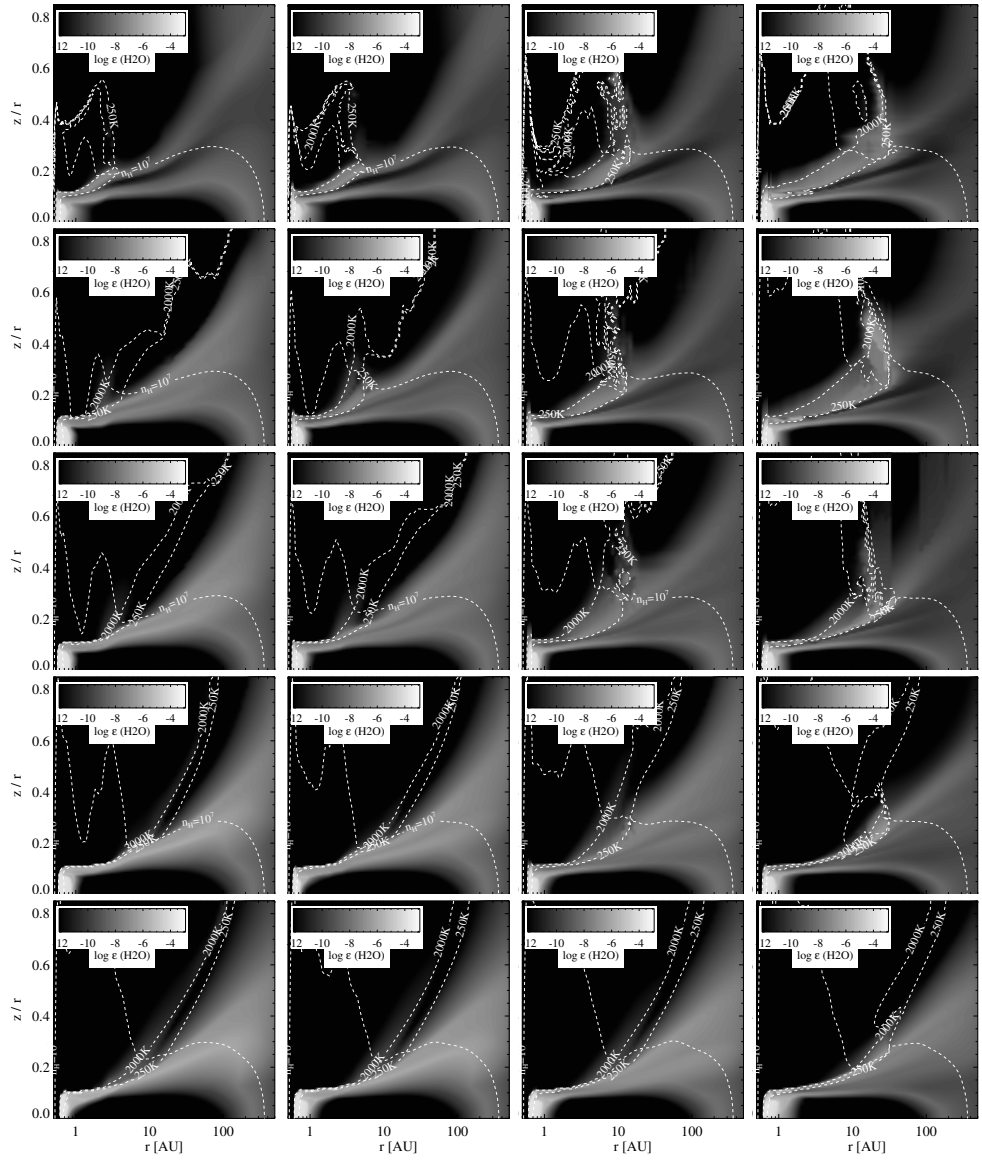

Figure 3.32: H_2O abundances. FUV and X-ray fluxes are the same as Fig. 3.17.

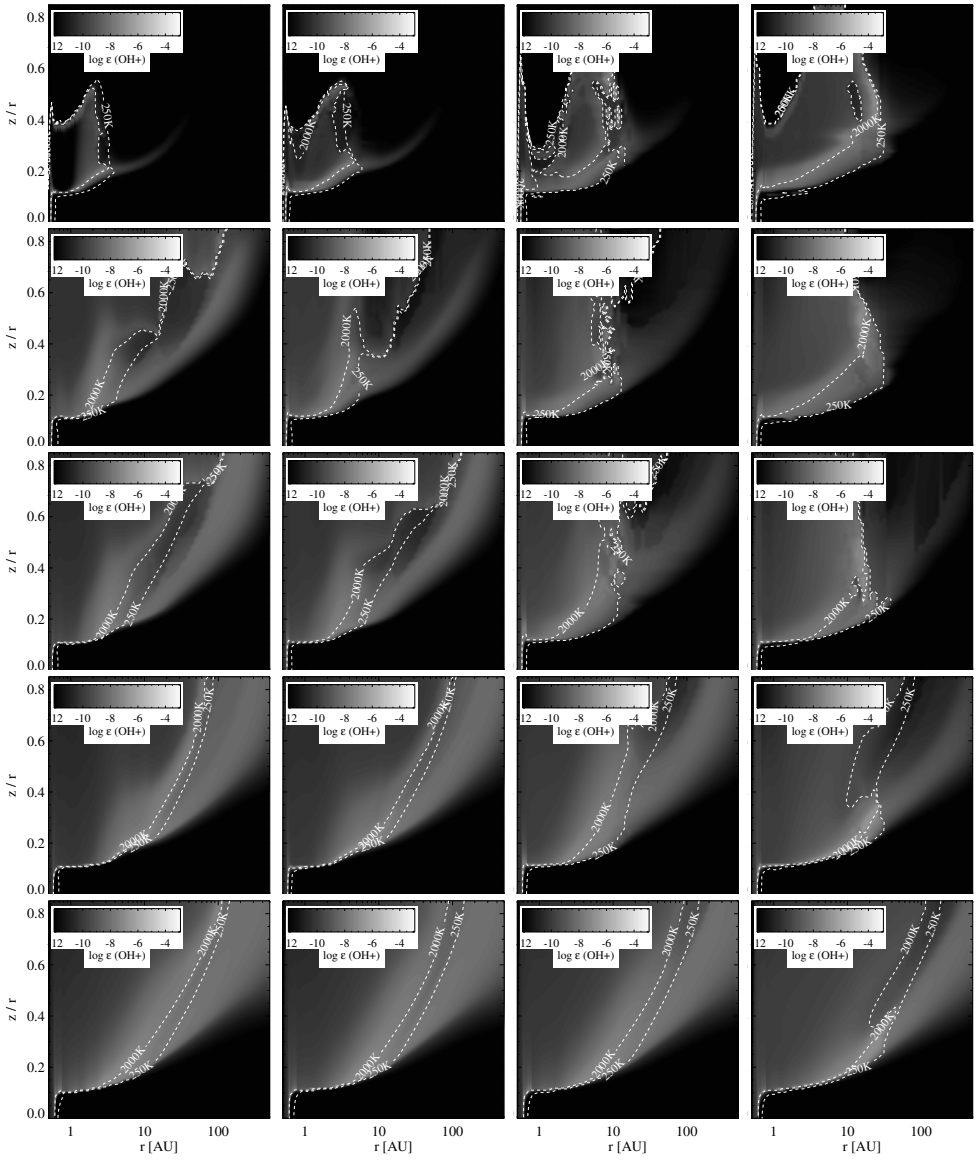

Figure 3.33: OH^+ abundances. FUV and X-ray fluxes are the same as Fig. 3.17.

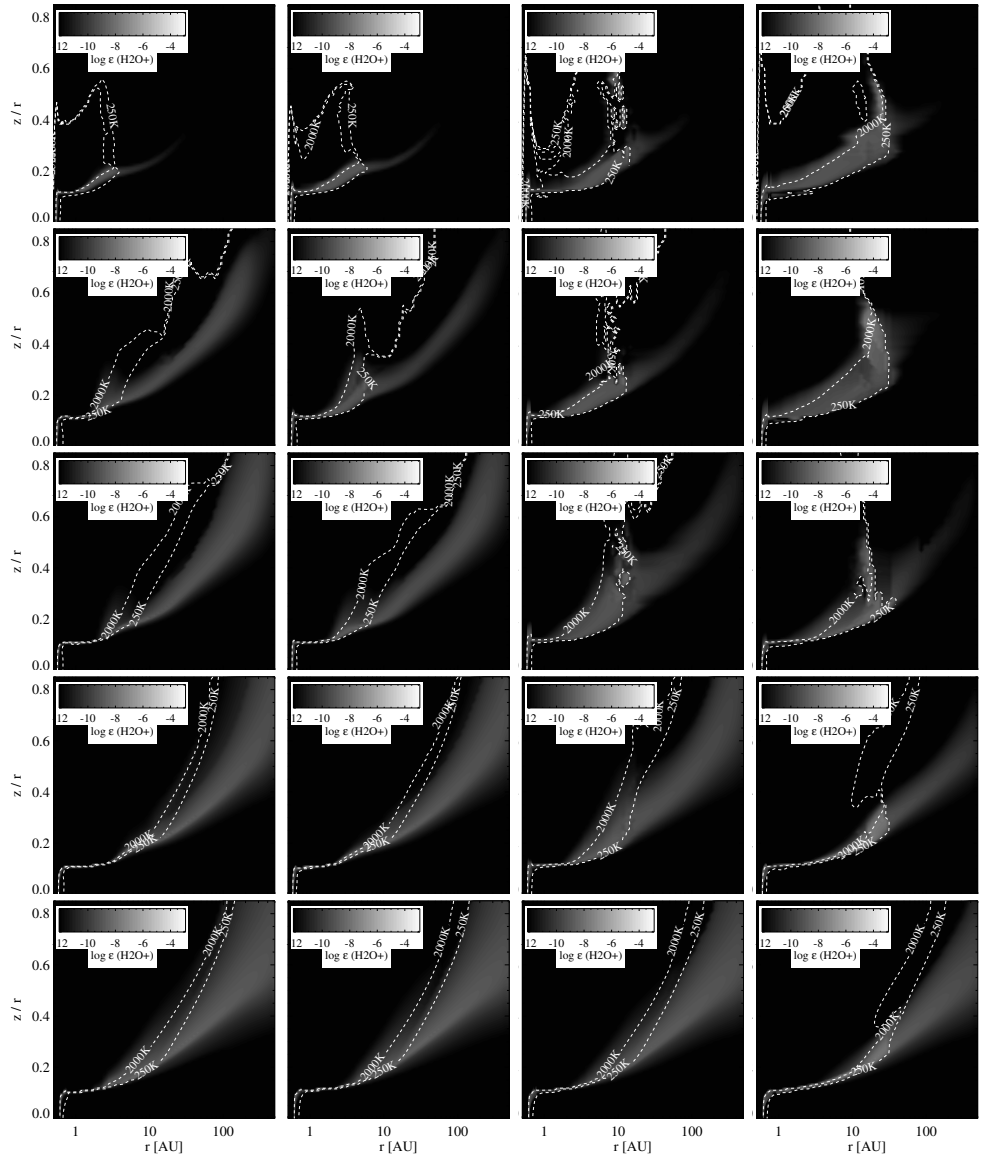

Figure 3.34: H_2O^+ abundances. FUV and X-ray fluxes are the same as Fig. 3.17.

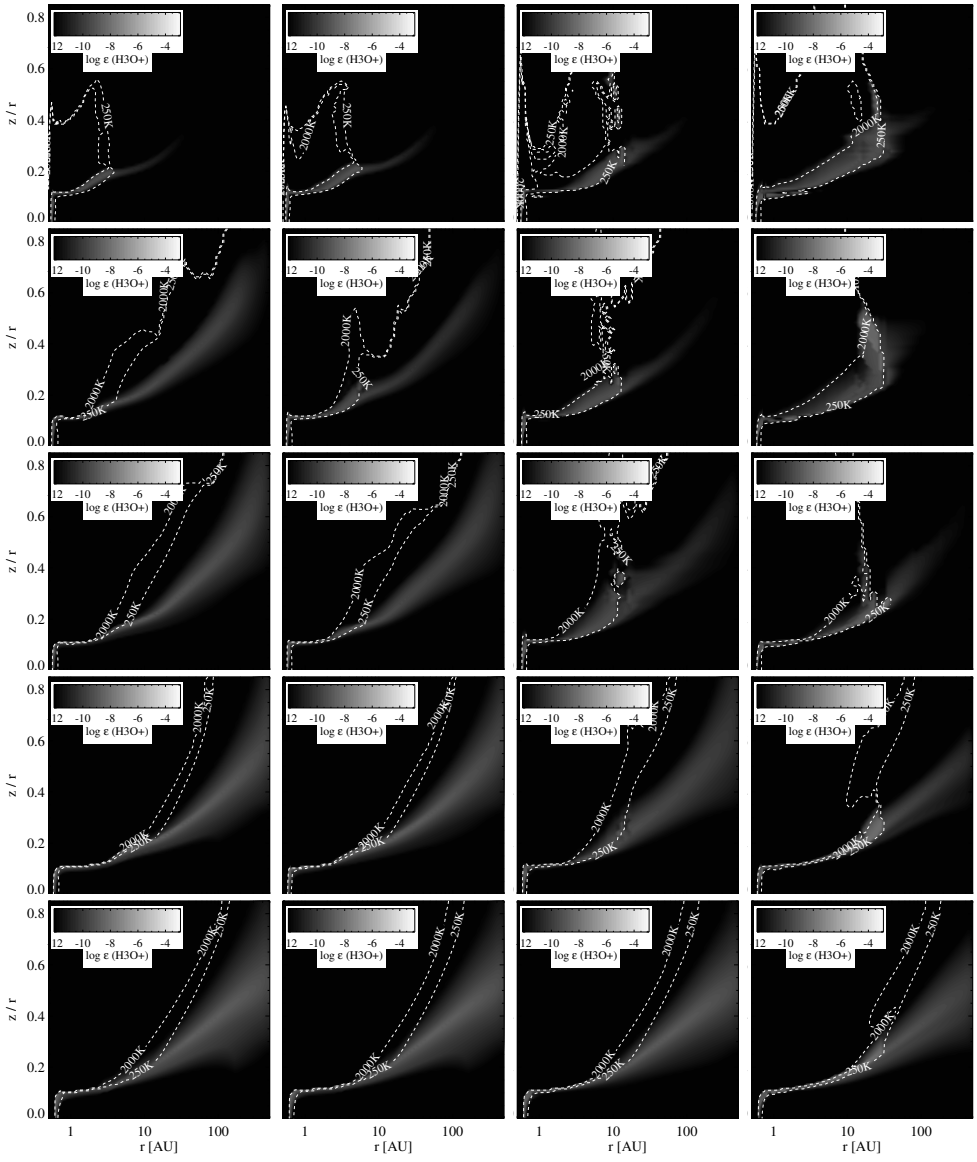

Figure 3.35: H_3O^+ abundances. FUV and X-ray fluxes are the same as Fig. 3.17.

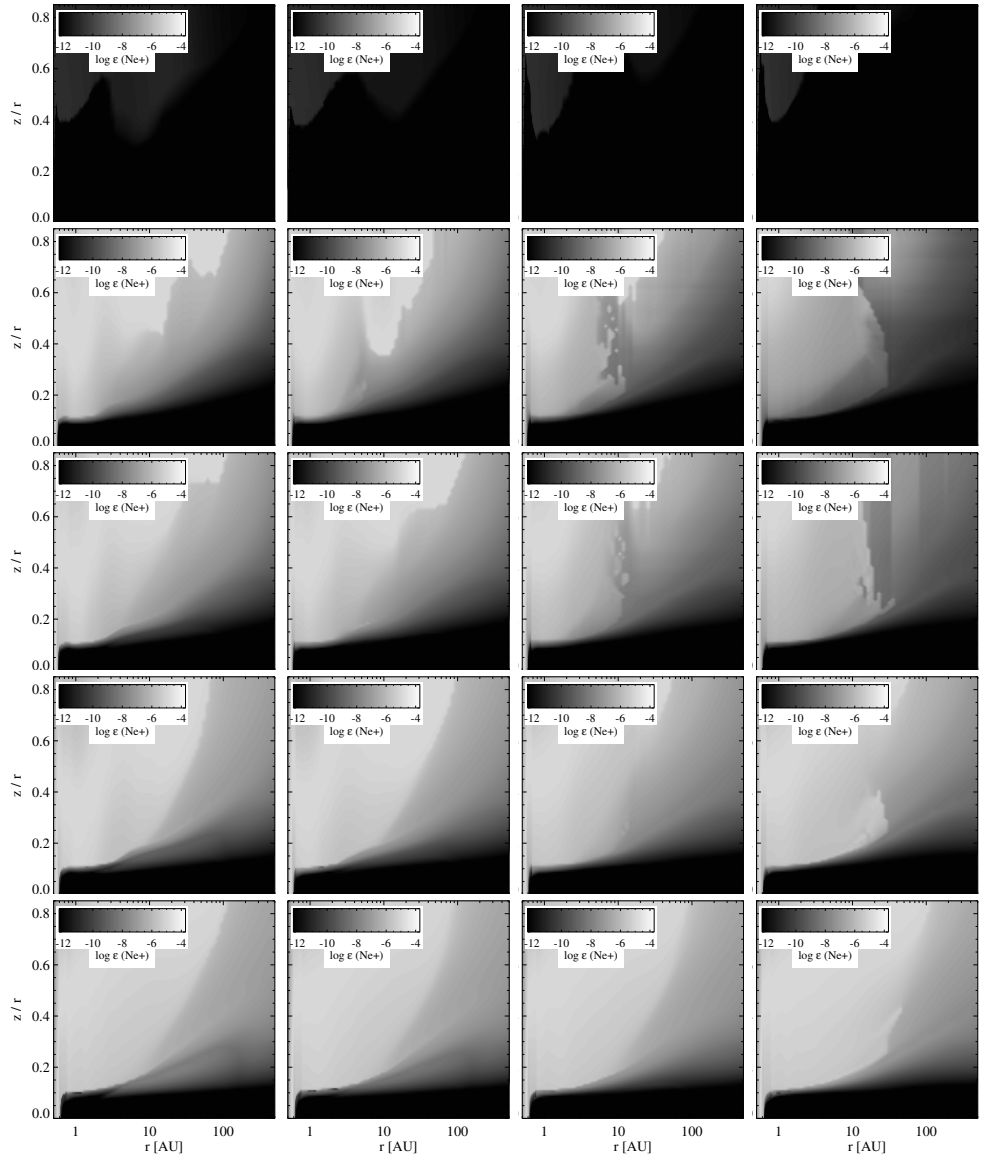

Figure 3.36: Ne^+ abundances. FUV and X-ray fluxes are the same as Fig. 3.17.

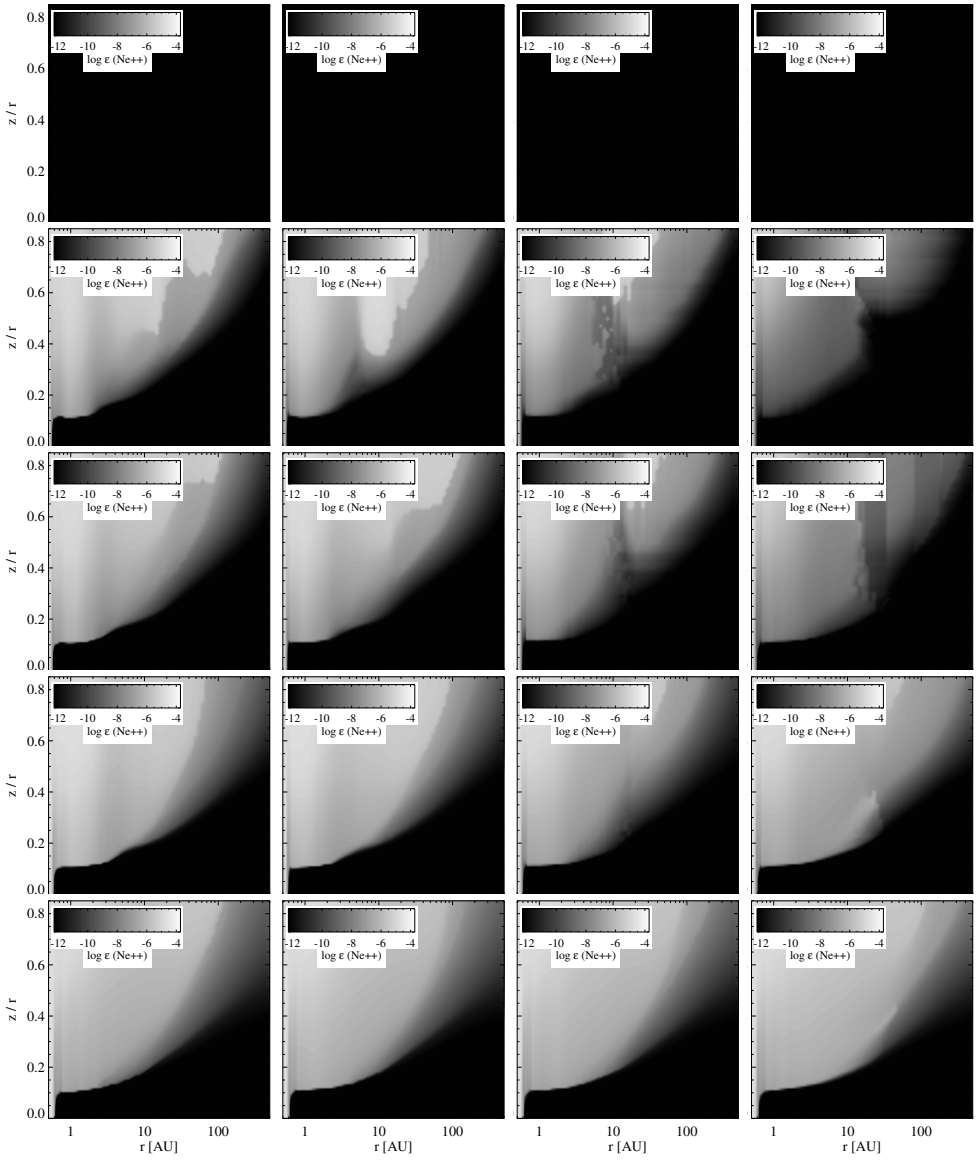

Figure 3.37: Ne^{2+} abundances. FUV and X-ray fluxes are the same as Fig. 3.17.

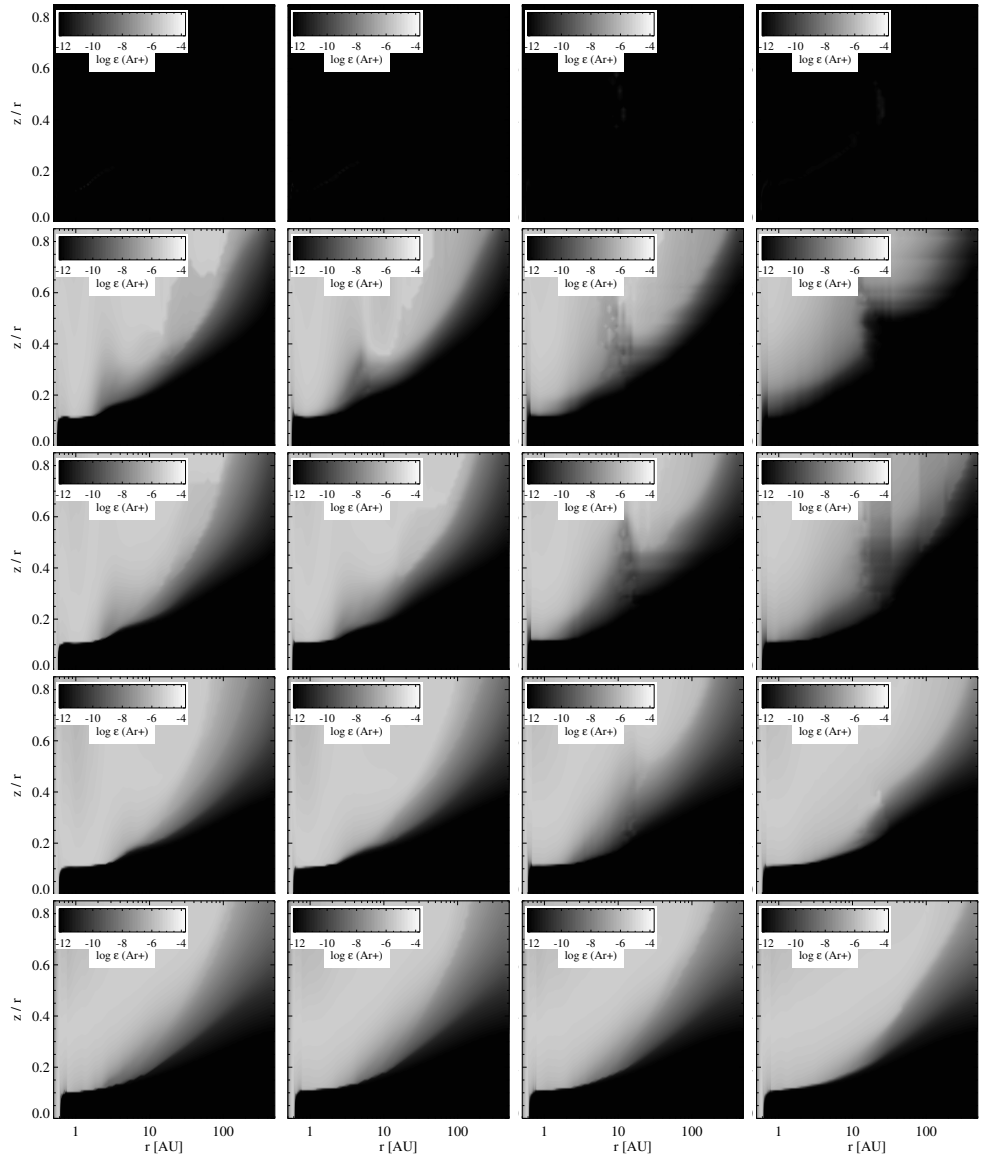

Figure 3.38: Ar^+ abundances. FUV and X-ray fluxes are the same as Fig. 3.17.

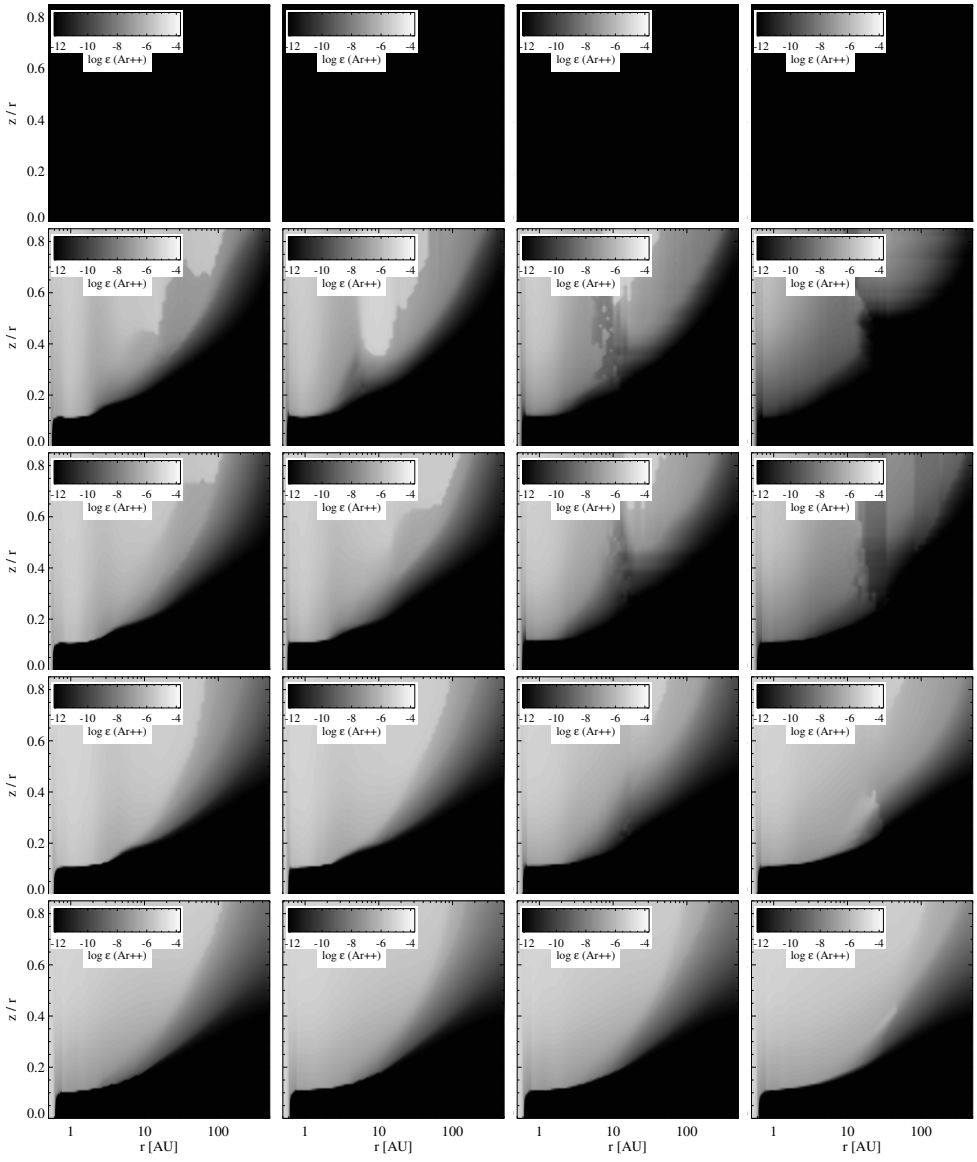

Figure 3.39: Ar^{2+} abundances. FUV and X-ray fluxes are the same as Fig. 3.17.

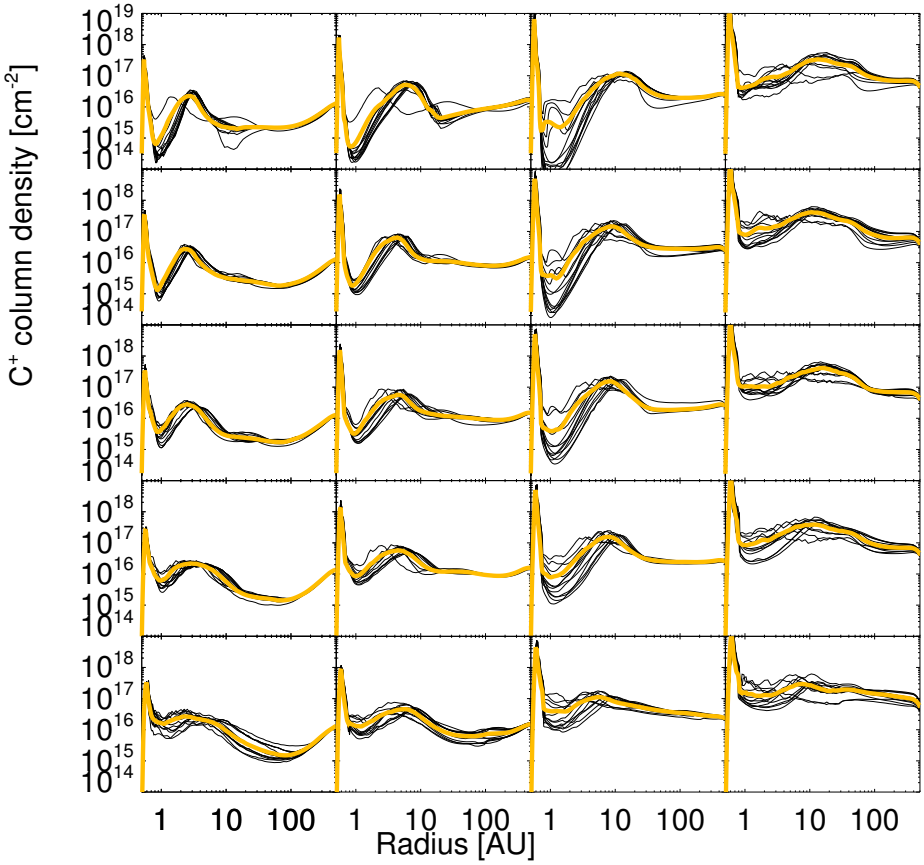

Figure 3.40: Radial column density distribution of C^+. FUV and X-ray fluxes are the same as Fig. 3.17.

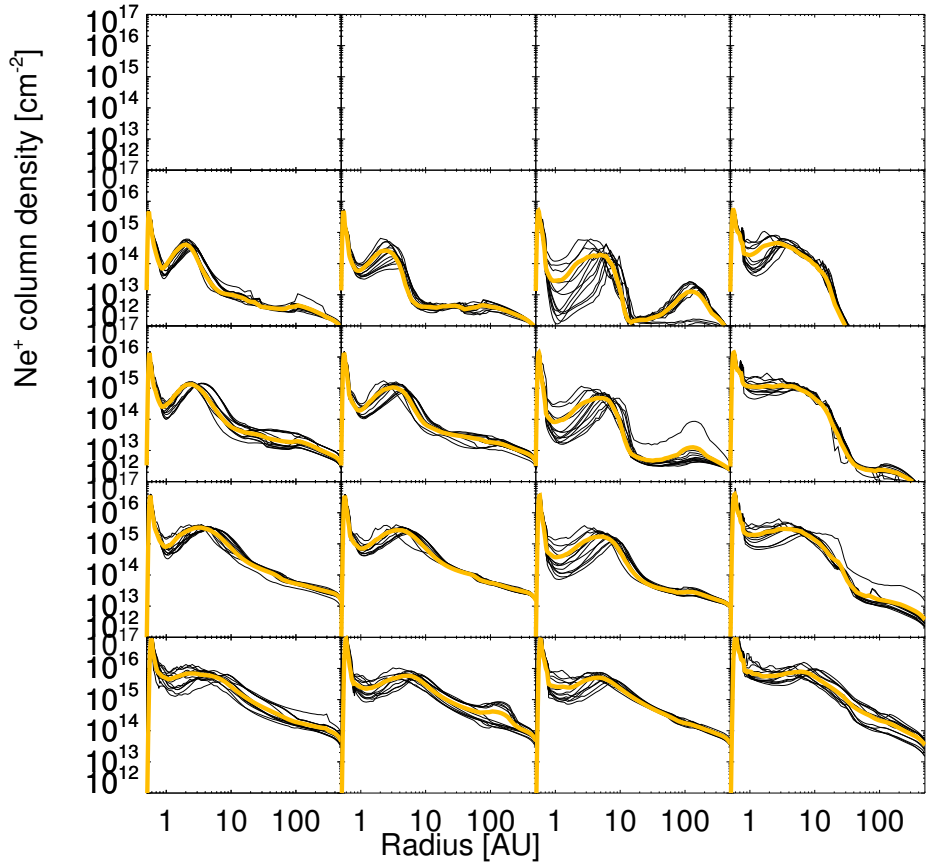

Figure 3.41: Radial column density distribution of Ne^{2+}. FUV and X-ray fluxes are the same as Fig. 3.17.

Chapter 4

FUV and X-ray irradiated protoplanetary disks: a grid of models II - Gas diagnostic line emission

G. Aresu, R. Meijerink, I. Kamp, M. Spaans, W.-F. Thi, P. Woitke
Astronomy & Astrophysics, 2012, 547, A69

Abstract

Most of the mass in protoplanetary disks is in the form of gas. The study of the gas and its diagnostics is of fundamental importance in order to achieve a detailed description of the thermal and chemical structure of the disk. The radiation from the central star (from optical to X-ray wavelengths) and viscous accretion are the main source of energy and dominates the disk physics and chemistry in its early stages. This is the environment in which the first phases of planet formation will proceed. We investigate how stellar and disk parameters impact the fine-structure cooling lines [Ne II], [Ar II], [O I], [C II] and H_2O rotational lines in the disk. These lines are potentially powerful diagnostics of the disk structure and their modelling permits a thorough interpretation of the observations carried out with instrumental facilities such as Spitzer and Herschel. Following Aresu et al. (2011), we computed a grid of 240 disk models, in which the X-ray luminosity, UV-excess luminosity, minimum dust grain size, dust size distribution power law and surface density distribution power law, are systematically varied. We solve self-consistently for the disk vertical hydrostatic structure in every model and apply detailed line radiative transfer to calculate line fluxes and profiles for a series of well known mid- and far-infrared cooling lines. The [O I] 63 μm line flux increases with increasing $L_{\rm FUV}$ when $L_{\rm X} < 10^{30}$ erg s^{-1}, and with increasing X-ray luminosity when $L_{\rm X} > 10^{30}$ erg s^{-1}. [C II] 157 μm is mainly driven

by $L_{\rm FUV}$ via C^+ production, X-rays affect the line flux to a lesser extent. [Ne II] 12.8 μm correlates with X-rays; the line profile emitted from the disk atmosphere shows a double-peaked component, caused by emission in the static disk atmosphere, next to a high velocity double-peaked component, caused by emission in the very inner rim. Water transitions, depending on the disk region they arise from, show different slopes in the correlation with the [O I] 63 μm line.

4.1 Introduction

Protoplanetary disks are the intermediate step between the cloud collapse and the planetary system stage. The understanding of the chemical and physical properties of disks provides the initial conditions for planet formation. The study of the gaseous component has gained increasing interest in the last few years as it dominates the mass budget in the disk in its early stages and because the increased sensitivity of new instrumentation allowed us to observe it, e.g. Spitzer, Herschel, VLT, ALMA.

Observations with the Spitzer Space Observatory were used to estimate that the lifetime of the inner "dusty" disk is of the order of 10 Myr (Strom et al., 1989; Haisch et al., 2001; Hernández et al., 2008). Finding the corresponding timescale for the gaseous component of the disk is rather complex, because there is not a single gas tracer that can be used; instead recent modelling efforts suggest that a suite of several gas tracers may be necessary to cover the wide range of chemical and excitation conditions in disks (Gorti et al., 2011; Kamp et al., 2011). Fedele et al. (2010) looked at accretion signatures to indirectly study the lifetime of the gas component. They found no accretion rate higher than 10^{-11} $M_\odot$ yr^{-1} for objects older than 10 Myr; assuming an exponential decay they infer a timescale of 2.3 Myr. Mechanisms such as photo-evaporation can remove the gaseous disk on short timescales ($\sim 10^5$ yr^{-1}) (Hollenbach et al., 1993; Haisch et al., 2001; Alexander, 2008). The accretion rates found by Fedele et al. (2010) would then indicate that the gas and dust lifetime are very similar.

The gas densities and temperatures in disks are suitable for the excitation of IR fine-structure transitions of species such as O, C^+, Ne^+ and Ar^+. Different molecular species (e.g. CO, H_2O) probe different disk regions, thereby allowing to build a coherent picture of the whole disk, from a complete suite of observation (see Bergin (2009) for a comprehensive review). These are among the diagnostic tools that are used to infer disk and stellar properties from observations with IR satellites like Spitzer and Herschel. The latter covers some major disk cooling lines such as [O I] 63 μm and [C II] 157 μm.

The origin of [O I] 63 μm emission from protoplanetary disks is not unique: it can originate from excitation in the disk and from the interaction of jet/outflows with the circumstellar environment (Ceccarelli et al., 1997; Nisini et al., 1999). Without spatially resolved observations, the contribution of these two mechanisms is difficult to disentangle (Podio et al., 2012).

[O I] 63 μm is recognized to be a temperature tracer for the surface layers of protoplanetary disks between 10 and 100 AU (Woitke et al., 2009). An exploratory study with the DENT grid (Woitke et al. (2010), 300000 disk models based on the junction

of the thermo-chemical code ProDiMo and the radiative transfer code MCFOST) was carried out by Pinte et al. (2010) for a sample of T Tauri and Herbig stars. They show that FUV radiation, potentially arising from accretion onto the star, plays a dominant role in T Tauri stars. Meijerink et al. (2008) investigated the effect of X-rays, finding a correlation between the line flux and the X-ray luminosity. Gorti & Hollenbach (2008) calculated the [O I] line for models with different FUV and X-ray luminosity, finding a major impact on the line flux by $L_{\rm FUV}$. Aresu et al. (2011) considered X-rays and FUV radiation, finding that for their fiducial solar-type star model X-rays become important above $L_{\rm X} \sim 10^{30}$ erg s^{-1}.

Glassgold et al. (2007), followed by work from Gorti & Hollenbach (2008) and Ercolano & Owen (2010), predicted emission of ionized neon at 12.8 μm in the atmosphere of an X-ray irradiated protoplanetary disk as a probe of physical conditions of the hot atmosphere ($\sim$ 4000 K) in the inner disk ($<$ 20 AU). The line was detected for the first time the same year with the infra-red spectrometer (IRS) on board of Spitzer (Pascucci et al., 2007; Espaillat et al., 2007; Lahuis et al., 2007). The origin of the [Ne II] 12.8 μm line is still under debate. Güdel et al. (2010) analysed a collection of more than 50 [Ne II] detections, and suggested different mechanisms responsible: emission from (a) the disk, (b) the photo-evaporative flow from the disk surface and (c) the jet itself (Shu et al., 1994; Shang et al., 2010). Sacco et al. (2012) and Baldovin-Saavedra et al. (2012) analysed high spectral resolution [Ne II] lines. They infer from the position of the peak with respect to the stellar velocity and from the line profiles that the lines are mostly excited both in photoevaporative flows and in jets. Spectrally resolved observations (Najita et al., 2009) also found a few sources where the [Ne II] is most likely emitted in a disk atmosphere.

The study of the gaseous disk remains an important challenge, where modelling can provide further insights. Thorough computing of the disk thermal and chemical structure, when coupled to observations of gas tracers of different disk regions, can be used as a powerful baseline to predict the fate of protoplanetary disks. Many protoplanetary disk models include X-rays, as there is general consensus that this radiation plays an important role in the chemistry, and in the thermal balance of the disk.

In this context several groups developed numerical codes dedicated to the modelling of protoplanetary disk (Gorti & Hollenbach, 2004; Glassgold et al., 2007; Nomura et al., 2007; Ercolano et al., 2008; Woitke et al., 2009; Gorti et al., 2009; Hollenbach & Gorti, 2009; Woods & Willacy, 2009). Woitke et al. (2010) and Kamp et al. (2011) investigated the effect of a wide parameter space on disk properties and studied the line emission of species such as CO, O and C^+. Meijerink et al. (2008) studied the effect of X-rays on Ne^+ and Ne^{2+}, different ionization stages of S, C, C^+ as well as O for a low mass star disk model. Gorti et al. (2009) investigated the role of FUV ($6 < h\nu < 13.6$ eV), EUV (13.6 eV $< h\nu < 100$ eV) and X-rays ($h\nu > 100$ eV) on the emission of [ArII] at 7 μm, [NeII] at 12.8 μm, [SI] at 25 μm, [FeII] at 26 μm, [OI] 63 μm and also pure rotational lines of H_2 and CO. They also investigated the properties of EUV/X-ray driven photo-evaporative flows in the upper layers of protoplanetary disks and their potential impact on diagnostic lines.

Fogel et al. (2011) studied the effects of grain settling and Lyα line scattering on the chemistry finding that both effects are important for molecules like CO, CN, HCN

and H_2O, and in general for the carbon and oxygen molecular chemistry. Heinzeller et al. (2011) showed that viscous heating and turbulent mixing also impact the molecular layer, thereby modifying the thermo-chemical conditions.

The scope of this paper is to follow up earlier work of Aresu et al. (2011) and to study the relative importance of X-rays and FUV in setting the thermal and chemical conditions in the disk. This work will investigate how selected atomic and molecular diagnostics respond to the different energy input. Meijerink et al. (2012), hereafter Paper I, show the respective roles of X-rays and FUV stellar radiation on the disk physical and chemical structure. The grid consists of 240 models, where we varied $L_{\rm X}$, $L_{\rm FUV}$, dust properties ($a_{\rm min}$, $a_{\rm pow}$) and the power law for the surface density distribution (ϵ). We provide, here in the second paper, an extensive study of the line diagnostics such as [O I], [C II], [Ne II], [Ar II] and water and investigate the thermo-chemical conditions behind the excitation of these lines.

This paper is structured as follows: in Sect. 2 we briefly recall the setup of our model grid. In Sect. 3 we list and explain the results obtained, in Sect. 4 we compare our findings to those of previous works. In Sect. 5 we summarize and provide an outlook for future work, in Sect. 6 we draw the conclusions.

4.2 The grid of disk models

We use the thermo-chemical code ProDiMo to compute thermo-chemical disk models in hydrostatic equilibrium. The parameters adopted are listed in Table 4.1. We consider a Sun-like T Tauri star surrounded by a 10^{-2} $M_\odot$ disk. To study the impact of the stellar radiation on the disk physics and chemistry we vary X-ray ($L_{\rm X}$) and FUV ($L_{\rm FUV}$) luminosities, dust properties (minimum dust size and dust size distribution power law) and the surface density distribution power law. The dust to gas mass ratio is kept fixed (ρ=$\rho_{\rm d}/\rho_{\rm g}$=0.01).

Every disk model is composed of 100 radial and vertical points where we solve for the thermal and chemical balance. The resulting vertical temperature profile is then used to compute the vertical disk structure until hydrostatic equilibrium is reached (see Woitke et al. 2009). A self consistent treatment of the disk flaring is needed to compute reliable optical depths through the disk.

The source of the FUV and X-ray radiation is assumed to be centred at the stellar position (a representative spectrum is shown in paper I). No X-ray scattering was considered. We ran the grid on the Millipede cluster of the University of Groningen, see paper I for more information.

4.2.1 Line radiative transfer

The line radiative transfer is calculated as explained in Woitke et al. (2011), section A.7. We chose an inclination of 45 degrees and a maximum range of ±30 km/s for the width of the lines. The line profile is calculated taking into account thermal and turbulent broadening, the latter is set to $v_{\rm turb}$ =0.15 km/s. The flux is calculated for a disk at 140 pc with an inclination (i) of 45°. For a subset of 20 models with varying $L_{\rm X}$ and $L_{\rm FUV}$, and $a_{\rm min}$= 0.1, $a_{\rm pow}$= 3.5 and ϵ= 1.5, the line fluxes have been

Table 4.1: Parameters used in the models.

Quantity	Symbol	Value
Stellar mass	M_*	1 $M_\odot$
Effective temperature	$T_{\rm eff}$	5770 K
Stellar luminosity	L_*	1 $L_\odot$
Disk mass	$M_{\rm disk}$	0.01 $M_\odot$
X-ray luminosity (0.1-50 keV)	$L_{\rm X}$	$0, 10^{29}, 10^{30}$ $10^{31}, 10^{32}$ erg s^{-1}
FUV luminosity	$L_{\rm FUV}$	10^{29}, 10^{30}, 10^{31}, 10^{32} erg s^{-1}
Inner disk radius	$r_{\rm in}$	0.5 AU
Outer disk radius	$r_{\rm out}$	500 AU
Surface density power law index	ϵ	1.0, 1.5
Dust-to-gas mass ratio	ρ_d/ρ	0.01
Min. dust particle size	$a_{\rm min}$	0.1, 0.3, 1.0 μm
Max. dust particle size	$a_{\rm max}$	10 μm
Dust size distribution power index	$a_{\rm pow}$	2.5, 3.5
Dust material mass density	$\rho_{\rm gr}$	2.5 g cm^{-3}
Strength of incident ISM FUV	$\chi^{\rm ISM}$	1
Cosmic ray ionization rate of H_2	$\zeta_{\rm CR}$	5×10^{-17} s^{-1}
Abundance of PAHs relative to ISM	$f_{\rm PAH}$	0.12
viscosity parameter	α	0

calculated also for $i = 0°$, $60°$, $75°$, $90°$. The transitions described in this paper are listed in Table 4.2.

4.2.2 Data

The chemical network counts ∼1500 reactions, part of it is composed of UMIST reactions (Woodall et al., 2007), while the reactions involving X-ray primary and secondary ionization of all the elements are taken from Meijerink & Spaans (2005) and Ádámkovics et al. (2011). The treatment of molecular dissociation due to X-ray absorption is explained in Table 1 in Aresu et al. (2011). Charge exchange reactions between single or double ionized ions with neutral species are taken from Ádámkovics et al. (2011).

In Table 4.2 we show the references for the collisional rates used for oxygen, ionized carbon, ionized sulfur and water. The electron excitation cross section for Ar^+ and Ar^{2+} were computed in the Iron Project (Hummer et al., 1993). Collisional rates for Ne^+ and Ne^{2+} are taken from the CHIANTI database Dere et al. (1997, 2009).

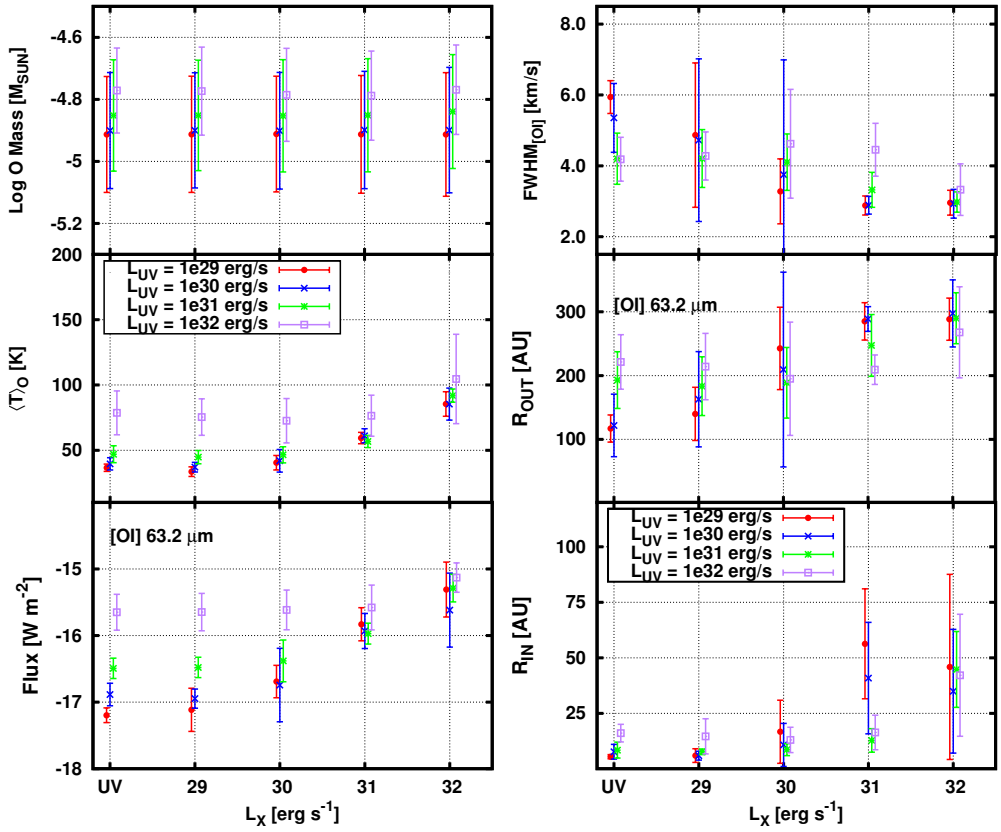

Figure 4.1: From lower to upper panel on the left: flux of the [O I] 63 μm line, oxygen mass averaged temperature and total oxygen mass in the disk versus X-ray luminosity. See Sect. 3 for the description of the error bars. Since the line is optically thick, its flux is sensitive to the thermal conditions in the disk. From lower to upper panel on the right: [OI] 63 μm emitting region inner and outer radius and FWHM of the line. As the emitting region gets pushed to larger radii, the FWHM of the line decreases accordingly.

Table 4.2: List of transitions considered in the line radiative transfer. From left to right we list the species name, the transition label, the excitation temperature, the Einstein coefficient for spontaneous emission, the collisional partners included in our model and approximately the region of the disk that the transition traces.

Species	Transition	λ [μm]	T_{ex}[K]	A (s^{-1})	Coll. part.	Region	Ref.
O	$^3P_1$-$^3P_2$	63	230	8.91 $\times10^{-5}$	H_2, H, H^+, e^-	20-200 AU 20-200 AU	1,2, 3,4
O	$^3P_0$-$^3P_1$	145	326	1.75 $\times10^{-5}$	H_2, H e^-	20-200 AU 20-200 AU	1,2, 3,4
C^+	$^2P_{1/2}$-$^2P_{3/2}$	157	91	2.30 $\times10^{-6}$	H_2, H, e^-	Outer Disk 20-200 AU	1,2
Ne^+	$^2P_{1/2}$-$^2P_{3/2}$	12.8	1122	8.59 $\times10^{-3}$	H, e^-	Inner Disk	5,6
Ne^{2+}	$^3P_1$-$^3P_2$	15.5	925	5.97 $\times10^{-3}$	H	Inner Disk	5,6
Ar^+	$^2P_{1/2}$-$^2P_{3/2}$	6.9	2060	5.30 $\times10^{-2}$	H	Inner Disk	7
o-H_2O	$2_{12} \rightarrow 1_{01}$	179	114	5.59 $\times10^{-2}$	H_2, H	Outer disk	1,8
o-H_2O	$8_{18} \rightarrow 7_{07}$	63.3	1071	1.751	H_2, H	Hot belt	1,8
o-H_2O	$8_{45} \rightarrow 7_{16}$	23.9	1615	1.05	H_2, H	Inner wall	1,8

References for the collisional rates: (1) Schöier et al. (2005), (2) Ralchenko (2009), (3) Krems et al. (2006), (4) (Störzer & Hollenbach, 2000), (5,6) Dere et al. (1997, 2009), (7) Hummer et al. (1993), (8) The rates for collisions with atomic hydrogen are a scaled version of the H_2 data.

4.3 Results

In this section we describe the resulting line fluxes for [O I] 63 μm, [C II] 157 μm, [Ne II] 12.8 μm and [Ar II] 7 μm. For a better understanding of the thermal and chemical conditions under which these species emit, we also give a description of the mass averaged gas temperature (defined below) and the total species mass. In addition, ProDiMo computes both the location of the line emitting region (defined below) and the FWHM of the line. These quantities will be used to investigate how the different stellar and disk parameters affect the emission of the coolants.

The dominant factors controlling these lines are $L_{\rm FUV}$ and $L_{\rm X}$. Hence the quantities we will describe in the following are averaged among models with fixed $L_{\rm FUV}$ and $L_{\rm X}$. The effect of varying $a_{\rm min}$, $a_{\rm pow}$ and ϵ is then shown in form of an error bar. Defining a "series" as a suite of models with fixed $L_{\rm X}$ and $L_{\rm FUV}$ but different $a_{\rm min}$, $a_{\rm pow}$and ϵ, we count 12 models in each series. This way, we consider for a given physical quantity Q in the series k, the simple arithmetic mean $\overline{Q}_k$. To avoid overshoot in the error bars due to a handful of models (n < 10) that did not reach optimal global convergence, we make use of the weighted mean for plotting purposes. The squared distance of $q_{k,i}$ from the arithmetic mean is then calculated and the inverse is used

as weight ($\omega_{k,i} = 1/\sigma^2_{k,i}$) to compute the weighted average of the quantity Q for the k-th series:

$$Q_W = \frac{\sum_{i=1}^{12} q_{k,i} \cdot \omega_{k,i}}{\sum_{i=1}^{12} \omega_{k,i}} \tag{4.1}$$

We computed the variance σ^2_k for each series and the error bars in the plots represent then the 2σ deviation from the Q_W. This approach is used for all the quantities discussed in this paper (flux, mass averaged temperature, mass of species sp, $R_{\rm in}$ etc.)

We also use the mass averaged temperature for a species sp, defined as:

$$\langle T \rangle_{\rm sp} = \frac{\int T_{\rm gas}(r,z)\, n_{\rm sp}(r,z) m_{\rm sp} dV}{\int n_{\rm sp}(r,z) m_{\rm sp} dV} \tag{4.2}$$

We calculate the mass averaged temperature only in the emitting region of the considered species: applying a 1D escape probability line radiative transfer, we calculate the radial ($R_{\rm in}$ and $R_{\rm out}$) and vertical coordinates that enclose the region where up to half of the total flux of the line is emitted. This volume is then used to perform the integration in Eq. 4.3. This allows to relate the temperature directly to the flux of the emitted line.

4.3.1 Oxygen

The lower left panel of Fig. 4.1 shows how the line flux changes as a function of the X-ray luminosity; color coded is the UV luminosity. Plotted is the weighted flux for models with a given X-ray and FUV luminosity and the error bars represent the 2σ scatter due to the variation of the flux with respect of the other parameters in the grid.

In the absence of X-rays, [O I] emission is driven by $L_{\rm FUV}$: the 63 μm line flux increases by a factor $\sim$10 from the lowest FUV model with $L_{\rm FUV} = 10^{29}$ erg s^{-1} to $L_{\rm FUV} = 10^{31}$ erg s^{-1} and another factor $\sim$ 10 when $L_{\rm FUV}$ is increased to 10^{32} erg s^{-1}. For constant $L_{\rm FUV}$, X-rays always start to impact the [O I] 63 μm emission beyond a threshold of $L_{\rm X} \sim 10^{30}$ erg s^{-1}. The only exception is the highest $L_{\rm FUV}$, where [O I] 63 μm stays constant up to $L_{\rm X} \sim 10^{31}$. For the highest X-ray luminosity, [O I] reaches a plateau, which represents the maximum value of $\sim 10^{-15}$ W/m^2 in our series of models.

The middle left panel of Fig. 4.1 shows the mass averaged temperature of atomic oxygen vs $L_{\rm X}$ in the region of the disk where 50% of the total flux is emitted. The behaviour is similar to the one discussed for the line flux: the temperature increases with increasing input energy (see also Fig. 2 in paper I). In the UV only models $\langle T \rangle_{\rm O}$ slightly increases from T = 35 K in the low $L_{\rm FUV}$ models, until it reaches about 80 K for $L_{\rm FUV} = 10^{32}$ erg s^{-1}. The models with the highest FUV luminosity show also the bigger scatter in temperature ($\Delta T \pm$ 20 K). When we let $L_{\rm X}$ increase, the temperature for the low $L_{\rm FUV}$ models starts to increase when $L_{\rm X} \sim 10^{30}$ erg s^{-1}. In higher $L_{\rm X}$ models, the temperature in the [O I] emitting region is set by X-ray energy deposition, regardless of the $L_{\rm FUV}$ contribution.

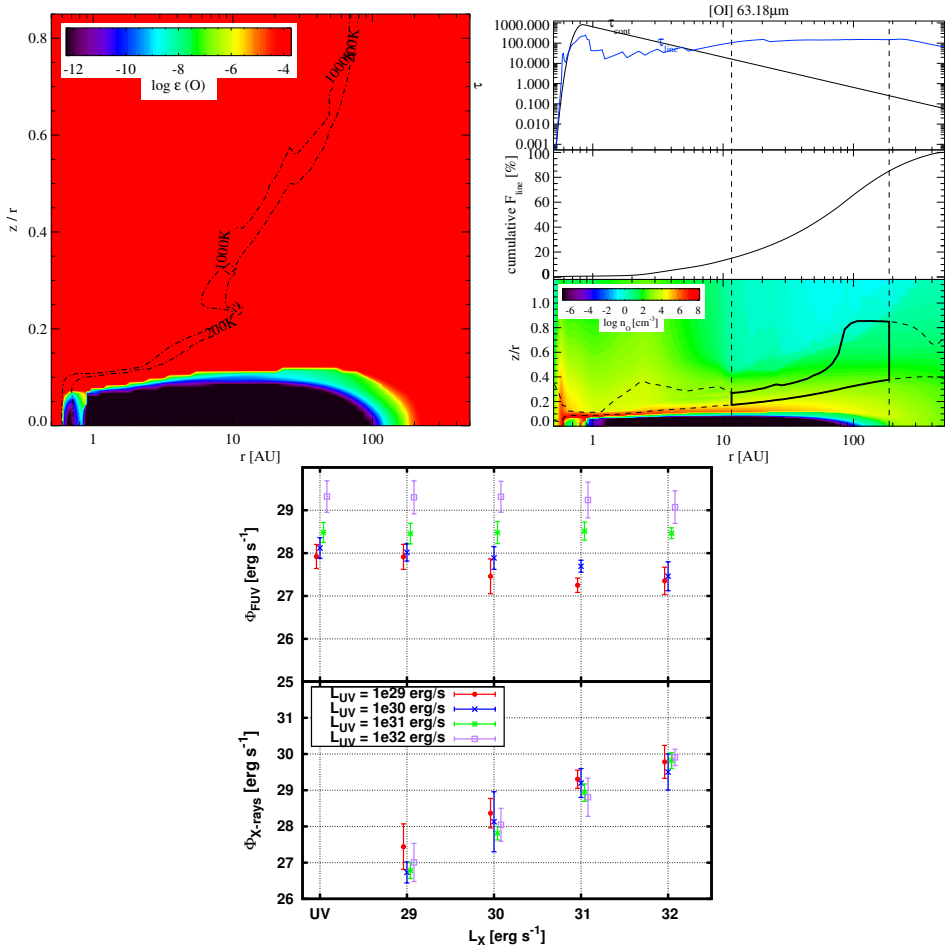

Figure 4.2: Left panel: O abundance (relative to hydrogen nuclei). The black contours are iso-temperature curves at 200 and 1000 K. Central panel: optical depth of the line (blue) and of the continuum (black) in the top mini-panel, below is the cumulative flux of the line, which shows which percent of the final flux is built and where, the lower mini-panel shows the oxygen density, the contour indicates where the contribution to the line flux goes vertically from 15% to 85% at every radius. Right panel: FUV (top) and X-ray (bottom) heating rates. These rates are obtained integrating the volumetric heating rate Γ over the volume of the [OI] emitting region for every model. Averages and error bars have the same meaning as described in section 4.3. The first two panels are taken from a representative model with $L_{\rm X}$= 10^{30} erg s^{-1}, $L_{\rm FUV}$= 10^{31} erg s^{-1}, $a_{\rm min}$= 0.1 μm, $a_{\rm pow}$= 3.5 and ϵ= 1.5.

In the upper left panel of Fig. 4.1, we show the variation of the total oxygen mass in the disk. The OI mass only varies within a factor 2.5 across all the models. The scatter caused by different dust properties ($a_{\rm min}$, $a_{\rm pow}$) and mass distribution in the disk (ϵ) for a series of 12 models is at most ~ 2.3, hence is higher than the variation of the averaged oxygen mass with $L_{\rm FUV}$in different series of models (maximum variation of a factor 1.4). On the other hand the X-ray luminosity does not affect the total oxygen mass in the disk. This is also explained in section 4.5 of paper I.

The [O I] emission is optically thick in all models. Its flux is then sensitive to temperature variations. The mutual FUV/X-ray contribution in creating the thermal conditions that drive [O I] emission becomes clear from Fig. 4.2 (right panel). We calculated the volume integral for the volumetric heating rate of X-rays and FUV, obtaining the respective heating rates in the oxygen emitting region:

$$\Phi_{\rm i} = \int \Gamma_{\rm i}(r,z) dV \qquad [{\rm erg\,s^{-1}}] \tag{4.3}$$

Here $\Gamma_{\rm i}$ is the volumetric heating rate in the i-th model for X-rays or FUV radiation in units of erg s^{-1} cm^{-3}. We used our previous definition of the oxygen emitting region as integration volume. The FUV emitting rate is the sum of all relevant FUV related processes: photoelectric heating, PAH heating, carbon ionization heating and H_2 dissociation heating (see Woitke et al. 2009). In the lower panel, we show how the X-ray heating rate scales roughly proportional to $L_{\rm X}$: $\Phi_{\rm X-rays} \sim 0.01\ L_{\rm X}$. In the upper panel, we show the FUV heating rate, we find approximately that $\Phi_{\rm FUV} \sim 0.01-0.001$ $L_{\rm FUV}$. Note how for low $L_{\rm FUV}$ models increasing X-rays causes progressive decreasing in the FUV heating rate. This is due to a general decrease of the local FUV radiation field at high $L_{\rm X}$, which causes FUV heating to decrease, especially PAH heating, which is the main FUV related heating process in the oxygen emitting region (see appendix in Woitke et al. (2011) for the treatment of PAH heating in ProDiMo). X-ray energy deposition becomes comparable with FUV when $L_X \sim 10^{30}$ erg s^{-1}. It is the competition between PAH and Coulomb heating that sets the temperature in the oxygen emitting region, thereby impacting directly on the flux of the line.

The location of the [O I] emitting region varies through the models, especially for the highest values of $L_{\rm X}$. Inner and outer radius of the emitting region generally both increase with increasing X-ray luminosity (lower and middle right panel of Fig. 4.1). Inner and outer radius also increase with $L_{\rm FUV}$. Thereby suggesting a dependence on the total energy input (in the X-rays and FUV band).

In the top right panel of Fig. 4.1, we show the full width half maximum (FWHM) of [O I] throughout the model parameter space. The FWHM decreases for increasing $L_{\rm X}$, which is in accordance with the changes in the line forming region.

4.3.2 Carbon

The ionized carbon fine-structure line flux at 157 μm clearly depends on $L_{\rm FUV}$ for the UV only models. UV radiation ($\lambda < 1100$ Å) sets C^+ abundances in the outer disk (see paper I). The increasing X-rays can contribute to the line intensity for the lowest two FUV luminosities for $L_{\rm X} < 10^{30}$ erg s^{-1}. After this value a "plateau" is reached: even though X-rays increase the temperature in the ionized carbon emitting region,

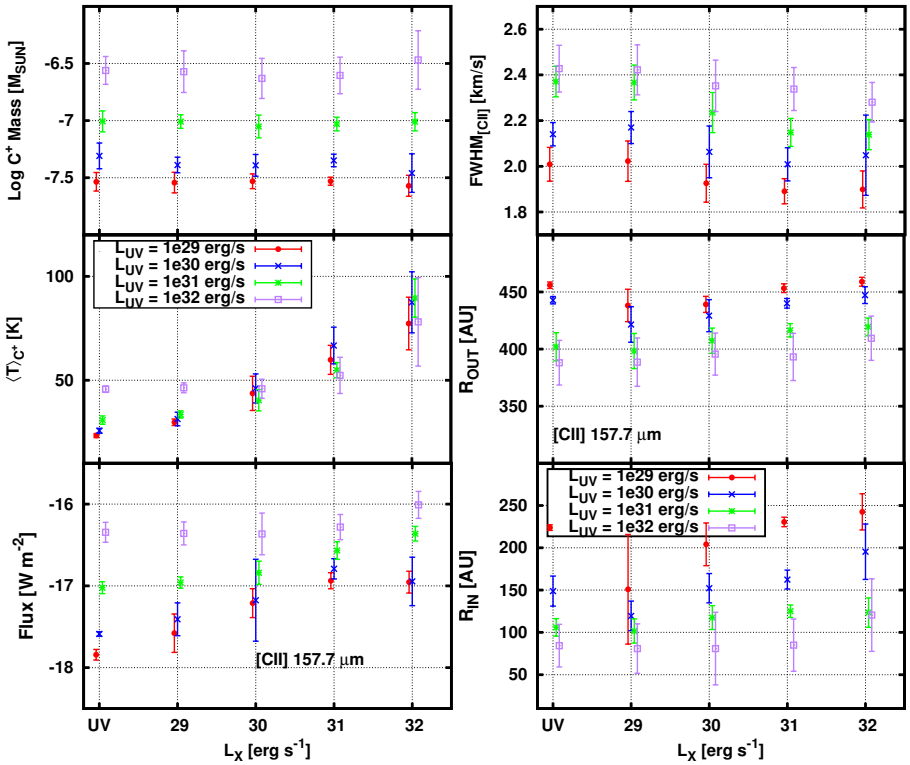

Figure 4.3: Lower and central panel: inner and outer radius of the emitting region. Top panel: full width half maximum of the line. See Sect. 3 for the description of color coding and error bars. LEFT figure: [O I] at 63 μm. The oxygen emitting region is generally pushed further as $L_{\rm X}$ increases, this is also reflected by the FWHM, which on average slightly decreases with $L_{\rm X}$. RIGHT panel: [C II] at 157.7 μm. Ionized carbon traces the outer disk, its emitting region extends inward as $L_{\rm FUV}$ increases. X-rays do not impact considerably $R_{\rm IN}$, $R_{\rm OUT}$ or the FHWM of the line.

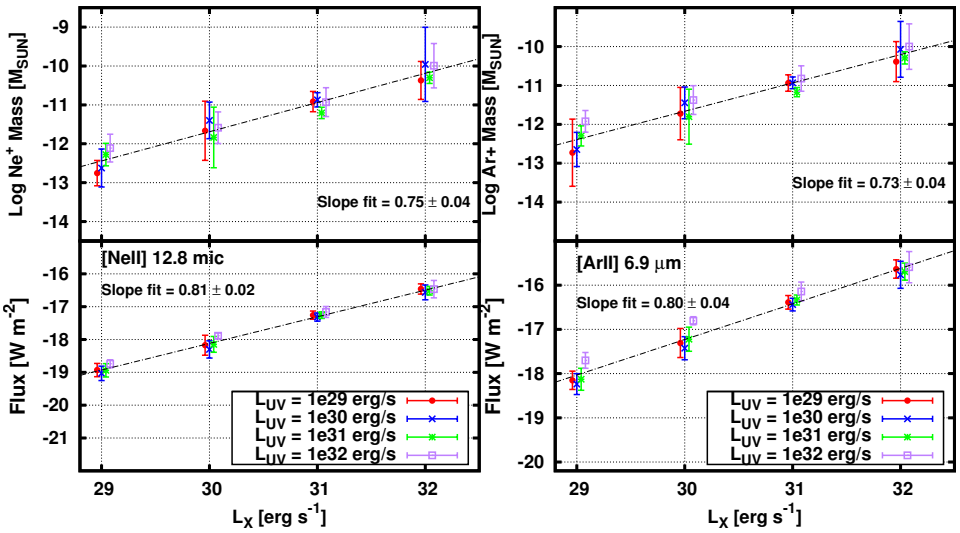

Figure 4.4: From lower to upper panel: flux of the line, mass averaged temperature and total species mass in the disk versus X-ray luminosity. See section 3 for the description of the error bars. LEFT figure: ionized neon fine-structure line emission at 12.8 μm. The line is produced in a high temperature X-ray heated environment, where the density is low ($n_H \sim 10^{6-7}$ cm^{-3}). The line is optically thin and hence very sensitive to the total ionized neon mass, which correlates with L_X. Hence, in our models, [Ne II] correlates with L_X. RIGHT figure: ionized argon fine-structure line emission at 6.9 μm. [Ar II] behave very similarly to [Ne II], and it can be used as a tracer for the same region.

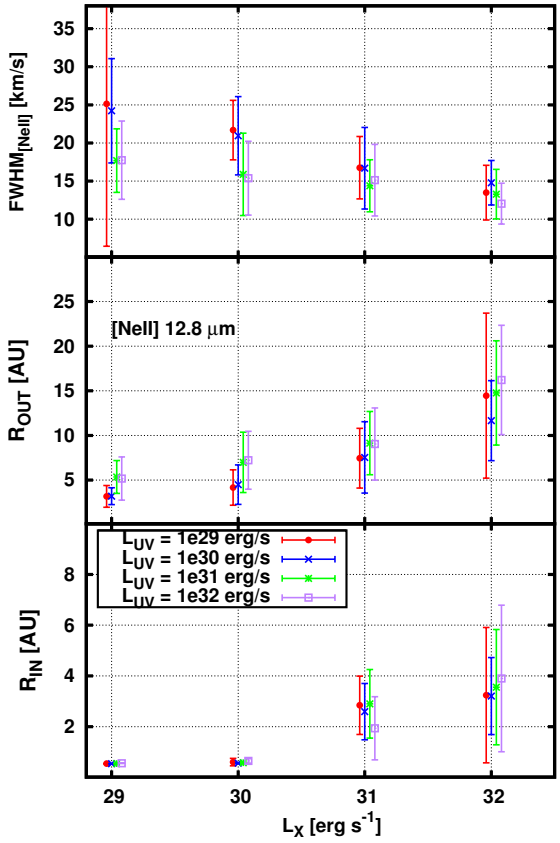

Figure 4.5: Lower and central panel: inner and outer radius of the Ne^{+} emitting region. Top panel: full width half maximum of the line. See section 3 for the description of color coding and error bars.

the column density in the same region of the disk is decreasing (see the first two panels in the last three rows of Fig. A.24 in paper I), hence the latter effect compensates for the temperature increase. For the high FUV models the column densities do not vary for models with different $L_{\rm X}$. Hence the line flux is mainly increasing with $L_{\rm FUV}$, with a minor contribution of $L_{\rm X}$, through thermal effects, as in the [O I] 63 μm case.

For $L_{\rm X}< 10^{30}$ erg s^{-1}, the C^+ temperature is UV driven and increases for the highest $L_{\rm FUV}(10^{30}$ erg s^{-1}) by a factor 2 compared to the low $L_{\rm FUV}$ (10^{29} erg s^{-1}). At higher $L_{\rm X}$, the C^+ temperature is entirely controlled by X-rays driving it up to $\sim$ 100 K in the most extreme case.

In the top left panel of Fig. 4.3, we plot the total mass of C^+ as a function of X-ray luminosity. The role of $L_{\rm FUV}$ in the formation of ionized carbon is clearly shown: the total mass spans roughly one order of magnitude from 3.2×10^{-8} $M_\odot$ for the lowest $L_{\rm FUV}$ to 3.2×10^{-7} $M_\odot$ for the highest one. X-rays and the other free parameters affect the total C^+ mass to a lesser extent: for a given $L_{\rm FUV}$, m_{C^+} changes at most by a factor 2.

The [C II] emission is generally very close to being optically thick. In this regime the line is sensitive both to the column density of the species and to the gas temperature (see paper I, A. 24). Indeed in our models, the ionized carbon flux is mainly dependent on its total mass in the disk. However, if the temperature of the emitting region changes, the flux varies accordingly. These two effects are caused from a combination of FUV radiation, which controls the production of C^+ (top left panel of Fig. 4.3), and from X-ray radiation, which, similarly to oxygen, contributes to the thermal balance in the ionized carbon emitting region.

The location of the emitting region is mainly dependent on the FUV flux (Fig. 4.3). In the high luminosity models, C^+ emits closer to the central star, starting from $r \sim 80$ AU. For constant $L_{\rm FUV}$, the inner radius of the emitting region $R_{\rm in}$, increases only weakly with $L_{\rm X}$. However, it shows a strong inverse dependence on $L_{\rm FUV}$: it increases by a factor 3 from high to low $L_{\rm FUV}$ models. The outer radius of the emitting region shows the same trend. The different radial location of the ionized carbon emitting region causes the FWHM of the line to change as shown in the upper right panel of Fig. 4.3. The variation is less than a factor 2 from high to low $L_{\rm FUV}$ models. As expected, the FWHM is not noticeably affected by $L_{\rm X}$.

4.3.3 Neon

Ionized neon is expected to be sensitive to the X-ray radiation, because neutral neon has a primary ionization for the K-shell of $\sim$ 900 eV. In the lower left panel of Fig. 4.4, we show the flux of [Ne II] versus $L_{\rm X}$. UV only models are not shown as they do not produce significant [Ne II] emission. The dependency of [Ne II] on parameters other than $L_{\rm X}$ is weak, as reflected in the small error bars for every series of models. The linear fit gives a slope of 0.81 for the correlation of the line flux with $L_{\rm X}$.

In the upper panel of Fig. 4.4, we show the total Ne^+ mass in the disk. The higher $L_{\rm X}$, the more ionized neon is produced. Other parameters also affect the total Ne^+ mass budget, but the overall trend is driven by X-rays. The linear fit gives a slope of 0.75.

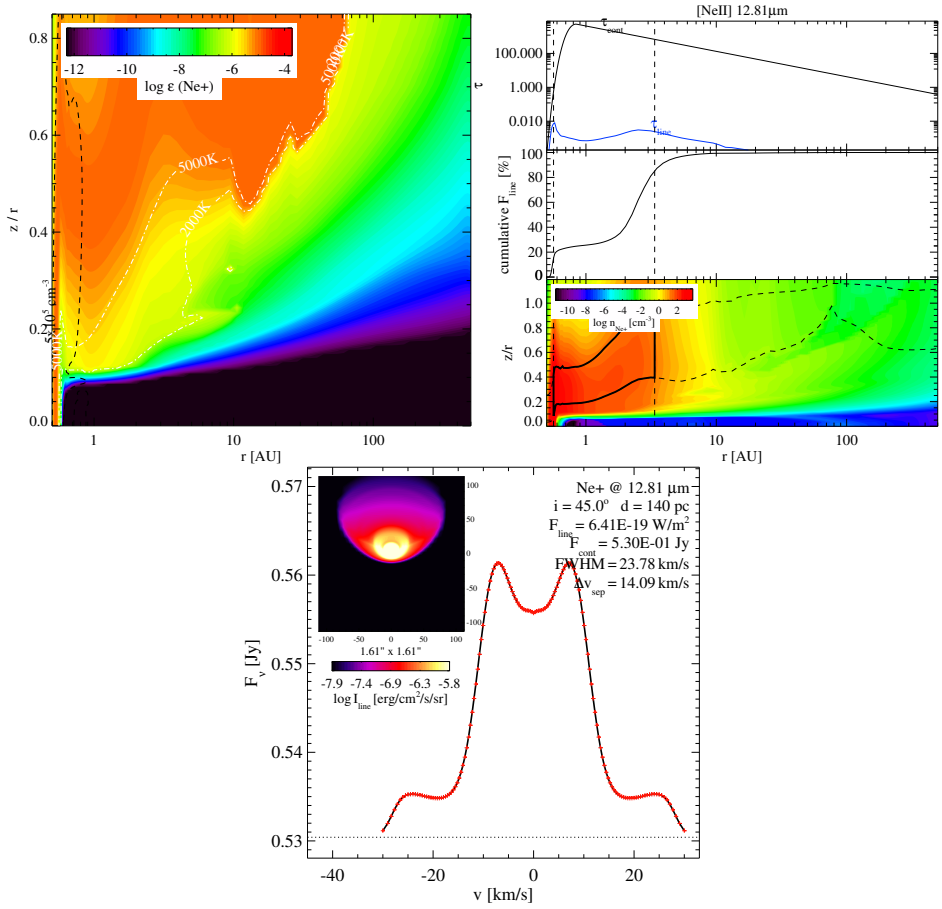

Figure 4.6: Left panel: Ne^+ abundance (relative to hydrogen nuclei). The black contour encloses the region in the disk where the electron density exceeds the critical density for the collisional excitation of the 12.8 μm line. Central panel: optical depth of the line (blue) and of the continuum (black) in the top mini-panel, below is the cumulative flux of the line, which shows which percentage of the final flux is built and where, the lower mini-panel shows again the ionized neon density, the contour indicates where the contribution to the line flux goes vertically from 15% to 85% at every radius. Right panel: line profile and image for a distance of 140 pc and an inclination of 45°.

The lower and upper left panel of Fig. 4.1 shows clearly that ionized neon fine-structure line emission is controlled by X-ray ionization of neon. The mass averaged temperature, not shown, in the [Ne II] emitting region ranges between 2000 K and 5000 K. The electron fractions in the upper layers within 20-30 AU are generally high ($x_{\rm el} \leq 0.1$) but the total electron density where most of the line forms is below $n_{\rm cr}$ (few times 10^5 cm^{-3}) causing the line emission to be mostly not in LTE and optically thin. Its intensity is then regulated by the column density of the species at a given radius, which is clearly set by the X-ray luminosity (see paper I, A. 27).

The lower and central left panel of Fig. 4.5 show how [Ne II] emission is confined within 20 AU. The emitting region is pushed further out as $L_{\rm X}$ increases. As a result, the FWHM of the line decreases accordingly (upper left panel, fig. 4.5) from 25 to 12 km/s.

Collisions with H

Collisions with H are potentially important in the excitation of the fine-structure lines of Ne^+. In our grid, we only considered collisional excitation of ionized neon with electrons ($\zeta_{coll,H} = \zeta_1 = 0$). A collisional excitation rate for atomic hydrogen is given in Bahcall & Wolf (1968): $\zeta_{coll,H} \sim 2 \times 10^{-9}$ cm^3 s^{-1} (ζ_2). This value does not take into account the spin interaction between H and the target electron and hence overestimates the rate by almost a factor 10. Following Meijerink et al. (2008), we therefore adopt $\zeta_{coll,H} \sim 2 \times 10^{-10}$ s^{-1} (ζ_3). Using ζ_2 and ζ_3 we run a subset of three models with increasing $L_{\rm X}$ from 10^{29} to 10^{31} erg s^{-1}, all other parameters remain unchanged from what refer to as the "standard model" (paper I). Table 4.3 shows

Table 4.3: Line fluxes for the 12.8 μm transition of Ne^+ considering only collisions with electrons and two different rates for excitation collisions with H.

$L_{\rm X}$[erg s^{-1}]	10^{29}	10^{30}	10^{31}
ζ [cm^3 s^{-1}]	Flux [W m^{-2}]	Flux [W m^{-2}]	Flux [W m^{-2}]
2×10^{-9}	4.5e-19	2.6e-18	1.6e-17
2×10^{-10}	2.3e-19	1.3e-18	7.4e-18
0	1.6e-19	1.0e-18	5.7e-18

how the collisions with H tend to increase the line flux with respect to the standard models, by a factor ~ 3 for $\zeta_{coll,H} = \zeta_2$ and by a factor 1.3-1.4 for $\zeta_{coll,H} = \zeta_3$.

Collisions with hydrogen affect the total [Ne II] flux by at most a factor of a few, and the trend is systematic through all models. Given the uncertainties in the collisional rates, we did not further consider excitation by H collisions in the grid of disk models presented here.

4.3.4 Argon

In Fig. 4.4 (right figure, lower panel), we show the fluxes for ionized argon fine-structure emission at 6.9 μm. In the same figure, central and upper panel show the mass averaged temperature and the total Ar^+ mass in the disk. Except for the

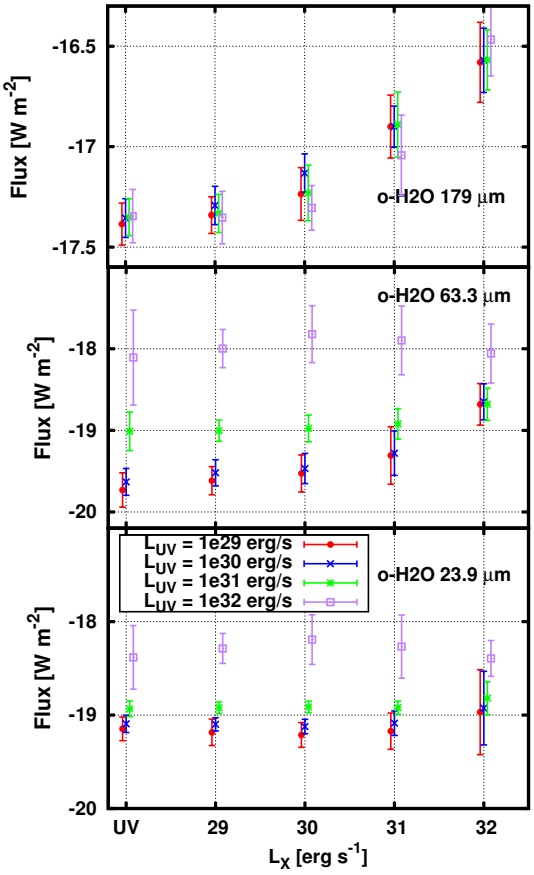

Figure 4.7: From lower to upper panel: water line fluxes for the 23.9 μm, 63.3 μm and 179 μmtransition versus the X-ray luminosity. Colour coding is the same as shown in Fig. 4.1. The X-ray impact is more evident as we move toward the outer disk.

absolute value of the line flux ($F_{\mathrm{Ar^+}} \sim 10\times\ F_{\mathrm{Ne^+}}$), all the results described above for $\mathrm{Ne^+}$ apply. The thermal properties in the [Ar II] emitting region are the same as described above for $\mathrm{Ne^+}$. The total mass of $\mathrm{Ar^+}$ follows the same behaviour, in terms of magnitude and dependence from L_{X}, as found for $\mathrm{Ne^+}$.

4.3.5 Water

We included in the line radiative transfer also a few rotational water transitions (Table 4.2). Given the high number of transitions and their broad range of excitation temperatures, the water molecule emits over a wide range of radii, tracing disk regions that can differ vastly in terms of chemical and temperature properties. Understanding the water excitation conditions offers the chance to extract information on the radial disk structure. Following Woitke et al. (2009), we choose to divide the disk into three

representative zones: the cold water in the outer disk, the warm to hot water in a zone above the midplane ranging from $R_{\rm in}$ to well beyond the snow line and the warm to hot main gas phase water reservoir behind the inner rim (Fig. 4.10). In Table 4.2, we list the transitions which are well suited to trace these regions: 179 μm (cold region), 63.3 μm (hot surface water) and 23.9 μm (inner wall water). In Fig. 4.7, we show how the different transitions respond to variations in $L_{\rm X}$ and $L_{\rm FUV}$ in our grid. We can identify three different behaviours. The line emitted in the inner wall (23 μm line, lower panel) is not altered by the X-ray radiation, unless $L_{\rm X}$= 10^{32} erg s^{-1}, but only responds to $L_{\rm FUV}$. The line formed in the hot water layer shows an oxygen-like behaviour: X-rays increase the line fluxes beyond a given threshold, 10^{31} erg s^{-1} (vs 10^{30} erg s^{-1} for oxygen). The outer disk line flux (179 μm) also increases with increasing $L_{\rm X}$, and it shows no dependency on $L_{\rm FUV}$. To understand these trends, we show in Fig. 4.10 the emitting regions for this lines in a subsample of models: starting from the top left panel, $L_{\rm FUV}$ increases horizontally from 10^{29} to 10^{32} erg s^{-1} while $L_{\rm X}$ increases vertically from 0 to 10^{32} erg s^{-1}. The grey scales shows the water density distribution. We overplot the emitting regions for the o-H_2O transitions at 179, 63 and 23 μm. The boxes enclose the disk region where the contribution to the total line flux for a given transition is about 50%. All the lines discussed here are highly optically thick, hence they are sensitive to temperature variations. We also show the [O I] 63 μm transition emitting region previously described for comparison. Red contours are iso-temperature curves at $T_{\rm gas}$ = 2000, 200 and 50 K, black contours indicate the τ(1 keV) = 1 and AV = 1 lines.

o-H_2O 23.9 μm

This line is emitted in the inner disk in a high density region ($n_{\rm H} \sim 10^{10}$ cm^{-3}), where the disk faces directly the stellar radiation and the water abundance relative to the hydrogen atomic nuclei is 10^{-4}. The emitting region is optically thick to the X-ray radiation but coincides with the AV=1 line. Increasing $L_{\rm FUV}$ indeed seems to affect the total emitted flux, while $L_{\rm X}$ radiation does not play a role (Fig. 4.7, lower panel). The temperature in the line emitting region is set by FUV heating.

o-H_2O 63.3 μm

The line traces the high temperature regions above the midplane in the inner disk. In this hot water layer, we can recognize a heating pattern similar to that discussed for oxygen in Sect. 3.1 (Fig. 4.7, central panel). Only after a given luminosity threshold, 10^{31} erg s^{-1}, X-rays are able to contribute to the heating in this region; below $L_{\rm X}$= 10^{31} erg s^{-1}, FUV heating dominates. The line is formed in the region that lays between τ(1 keV) = 1 and the AV = 1. For X-rays to contribute to the thermal balance in the hot water belt, $L_{\rm X}$ has to be higher than 10^{31} erg s^{-1} and $L_{\rm X} > L_{\rm FUV}$.

o-H_2O 179 μm

This transition is excited in the outer disk ($r \sim$ 30-200 AU). The line flux is more sensitive to the X-ray radiation because water forms in the outer disk through ion-

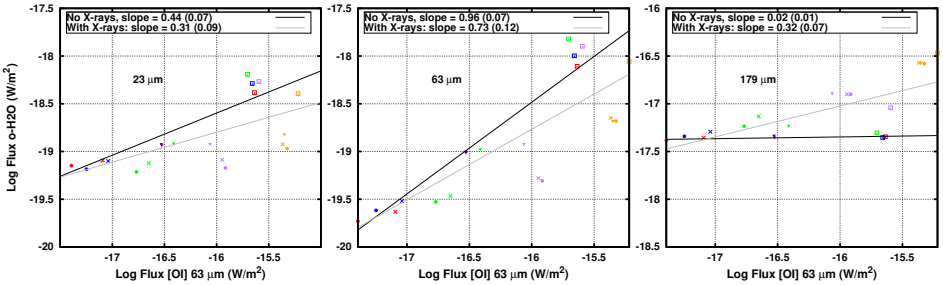

Figure 4.8: Correlation of water lines with the [O I] 63 μm lines. From left to right: 23 μm, 63 μm and 179 μm. Color coded is $L_{\rm X}$, different symbols indicates different FUV luminosities. The linear fit for the UV only model and the UV+X-rays model are drawn with a black and grey line respectively.

molecule chemistry (see paper I) and X-rays dominate the thermal balance there. The excitation conditions for this transition are then shifted to higher layers with respect to the FUV only models; these are layers where the X-ray optical depth approaches one at 1 keV (and AV < 1) and the temperature is set by Coulomb heating. Fig. 4.10 shows how the emitting region "moves" upwards as $L_{\rm X}$ increases. Note that apart from the extreme $L_{\rm X}$ model, the 179 μm flux only increases by a factor ~ 3.

Correlation with [O I] 63 μm.

In Fig. 4.8, we show the water lines fluxes versus the [O I] 63 μm line flux. At low X-ray luminosities, the 23 μm line weakly correlates with [O I] 63 μm. The correlation is due to the increase of $L_{\rm FUV}$, which heats both emitting regions, causing both line fluxes to increase. The slope of the correlation would be lower than one because, for a given change in $L_{\rm FUV}$, the [O I] flux increases more than the water 23 μm flux, since the latter is shielded by the inner rim. At higher X-ray luminosity, the line flux for [O I] increases, while the o-H_2O line does not change anymore. Increasing the FUV luminosity no longer affects the oxygen flux, while the 23 μm water line still increases with $L_{\rm FUV}$. The X-ray models then fall below the previous correlation, causing more scatter in the plot (Fig. 4.8, left panel). Although we do not provide a "best fit", we still show a line for the whole set of models, to illustrate how the slope would change when X-ray models are included.

The same effect can be seen in the correlation between water emission at 63 μm and [O I] 63 μm. Except in this case, the correlation at low X-ray luminosity is almost linear (0.96), because an increasing FUV luminosity causes a uniform increase in both line fluxes. For $L_{\rm X}\sim 10^{30}$ erg s^{-1}, the global correlation is again shallower (0.74).

No correlation is present between o-H_2O 179 μm emission and [O I] at low $L_{\rm X}$. The former line is indeed not affected by $L_{\rm FUV}$. Though, when $L_{\rm X}$ is higher than $\sim 10^{30}$ erg s^{-1}, both line fluxes increase. The slope of the correlation is small and ends up comparable with that of the 23 μm line (0.3), even though the cause is fundamentally different.

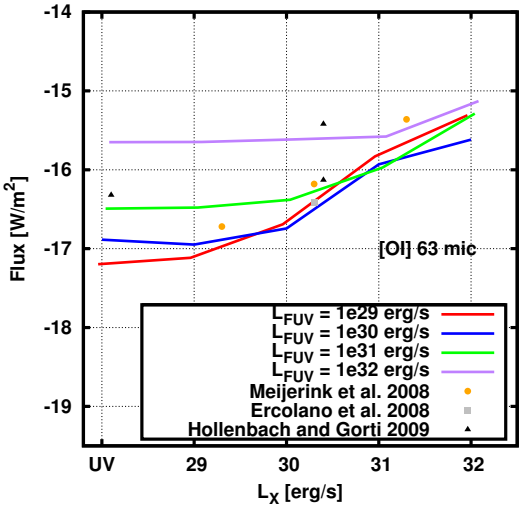

Figure 4.9: Our [O I] 63 μm results compared with other models.

4.4 Discussion

In this section, we discuss our results, comparing them with previous works and analysing their diagnostic potential in the interpretation of disk observations.

4.4.1 [O I] at 63 μm

The [O I] flux is both dependent on $L_{\rm X}$ and $L_{\rm FUV}$. Except in the presence of strong FUV excess ($L_{\rm FUV}$= 10^{32} erg s^{-1}) our results suggest that $L_{\rm X}$ has to be larger than 10^{30} erg s^{-1} for the [O I] flux to increase notably. At the threshold, Coulomb heating contributes as much as FUV heating to the thermal balance in the line emitting region.

The total oxygen mass is independent of the X-ray luminosity, while it increases by a factor ∼2-3 with increasing $L_{\rm FUV}$ due to enhanced photodissociation of H_2O and OH in the outer disk. Since the line is optically thick, such changes in mass ∼ 2-3 do not affect the total line flux.

The oxygen emitting region is generally pushed further out with increasing $L_{\rm X}$, as the disk is overall warmer (PaperI). This is also reflected in the FWHM of the [O I] line, being narrower for high $L_{\rm X}$. However, high spectral resolution, such as SOFIA/GREAT is needed (R ∼ 75000) to observe this effect.

In Fig. 4.9, we show the results from our model grid for [O I] 63 μm together with the fluxes found by other authors. Our results are in good agreement with Meijerink et al. (2008): their flux at $L_{\rm X}$= 2×10^{30} erg s^{-1} matches our values for low $L_{\rm FUV}$ models. Their prediction for $L_{\rm X}$ = 2×10^{29} erg s^{-1} is lower than ours, but as noted in Aresu et al. (2011) this is due to the absence of FUV in their X-ray irradiated model. They predict a slightly higher flux for their highest X-ray luminosity ($L_{\rm X}$ = 2×10^{31} erg s^{-1}).

The Ercolano et al. (2008) value (log $F_O \sim$ -16.41 W/m^2 for $L_X = 2\times10^{30}$ erg s^{-1} and no FUV) is in very good agreement with our predictions for low L_{FUV}.

Our values are somewhat higher compared with the ones of Gorti & Hollenbach (2008). In their models, they consider $L_{FUV} = 5\times10^{31}$ergs^{-1} and $L_X \sim 2\times10^{30}$ergs^{-1} (fiducial model A). They also calculate a model without X-rays (model C) and a model D with 10 times higher L_{FUV}. They consider different absolute values for L_{FUV}, but we reproduce the same [O I] flux variation for models where L_{FUV} is scaled by a factor 10. Increasing the FUV luminosity by an order of magnitude (from model A to model D) causes the flux to increase by a factor $\sim$ 5, which is the same factor we find for such an FUV luminosity variation. The discrepancy in the absolute fluxes might arise from further differences in the model, e.g. their grain size distribution goes from 50 Å to 20 μm.

The dust parameters we explored in the grid cause a spread in the [O I] flux of less than a factor 3. The same holds for the range of surface density power law exponent explored here (i.e. 1, 1.5). Their impact on the [O I] 63 μm line flux is marginal for our grid, but should definitely be taken into account if the goal is to perform multi-wavelength fitting of an individual source. In that case L_X and L_{FUV} are no free parameters, and the secondary disk parameters play the dominant role.

4.4.2 [C II] at 157 μm

The FUV luminosity controls the line emission, mainly via carbon ionization. Thermal effects impact the line similarly to what happens for [O I], but to a lesser extent. The inner and outer radius of the C^+ emitting region respond to the FUV radiation.

Our fluxes are higher than the values calculated by Meijerink et al. (2008) and Ercolano et al. (2008), because these authors do not consider FUV radiation in their models. X-rays alone are not able to sustain enough C^+ production for the flux to be on the observable limit of Herschel. However, in many of our models presented here, we overpredict the C^+ line: only few sources in Taurus were observed with fluxes above 10^{-17} W m^{-2} (Howard et al., 2012, in prep.). One reason for this discrepancy might be the shape of the FUV spectrum. As noted already by Bergin et al. (2003) and Fogel et al. (2011), the spectral shape in this range is far from being the simple power law that we adopted for this study. Many emission lines from highly ionized species, especially a very strong Lyα line (10.1 eV, 1215 A), contribute to the total L_{FUV}. The lines in a typical T Tauri FUV spectrum can carry up to 75% of the total flux for energies lower than the carbon ionization potential (11.2 eV, $\sim$ 1090 Å). The C^+ mass for a given L_{FUV}, depends on how much flux in the FUV range is carried by these lines longward of 1090 Å.

In our case of power law continuum, we likely overestimate, for a given L_{FUV}, the continuum flux between 11.2 and 13.6 eV, and this might lead to an overproduction of C^+. X-rays do not contribute significantly to the C^+ production, because upon X-ray ionization, C^+ likely loses more than one electron through the Auger effect. X-rays also destroy C^+ via direct ionization, which has roughly the same rate as neutral carbon X-ray ionization. Subsequent recombination channels form C^+, but also neutral carbon. X-rays do not sustain the same level of carbon ionization as FUV photons (see also the column densities in PaperI).

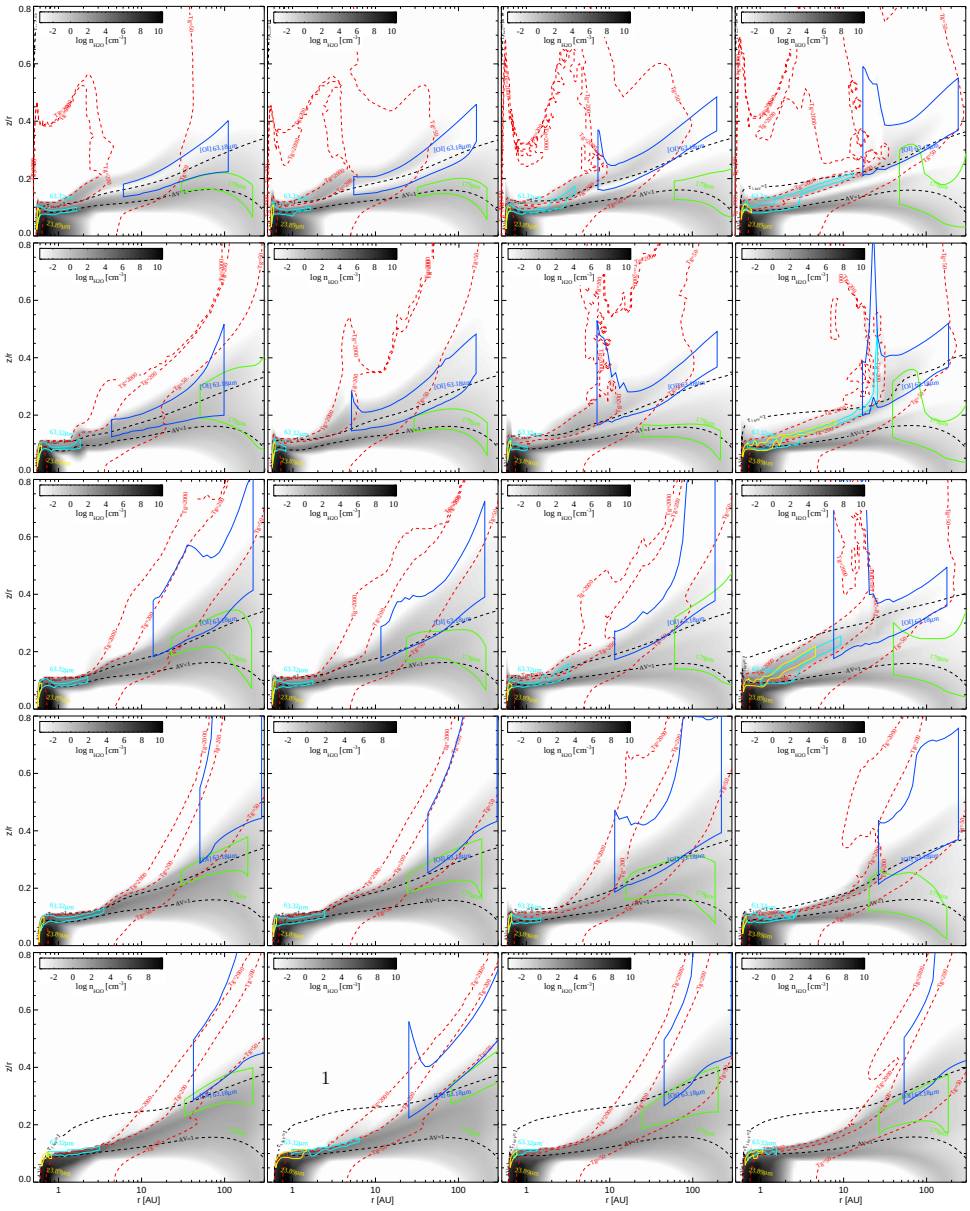

Figure 4.10: Water emitting regions for a subsample of models with $a_{\rm min}$= 0.1 μm, $a_{\rm pow}$= 3.5 and $\epsilon = 1.5$. Yellow, cyan and green mark respectively the emitting region of the o-H_2O rotational transitions at 23.8, 63.3 and 179 μm. Blue is the emitting region of [O I] 63 μm. In grey scale we plot the water density. From left to right are models with increasing $L_{\rm FUV}$ from 10^{29} to 10^{32} erg s^{-1}, from upper to lower panel $L_{\rm X}$ increases from 0 to 10^{32} erg s^{-1}.

4.4.3 [Ne II] at 12.8 μm

[Ne II] at 12.8 μm probes the innermost high temperature conditions in the top layers of our protoplanetary disk models. The X-ray photons are necessary to produce ionized neon and heat the gas there. The temperatures needed to excite the transition via electron collisions ($T_{\rm ex} \sim 1000$ K) can only be achieved in the innermost ~ 50 AU in a X-ray (or EUV) irradiated disk.

Our models predict a correlation between [Ne II] and X-rays; all other parameters explored in this paper contribute marginally to the formation of the line. The slopes in the fits for $M_{\rm Ne^+}$ and $F_{\rm [NeII]}$ vs $L_{\rm X}$ are very similar confirming that the line is optically thin. The higher the X-ray flux, the more extended is the emitting region. This causes the FWHM of the line to anticorrelate with X-rays, changing from ~ 25 to ~ 15 km s^{-1} when $L_{\rm X}$ goes from 10^{29} to 10^{31} erg s^{-1}. The line is mainly observed in sources that drive outflows or jets (Sacco et al., 2012; Baldovin-Saavedra et al., 2012), theoretical calculations have shown that the line can be indeed excited in such outflows, providing line fluxes and profiles in accordance with the observation (Ercolano & Owen, 2010).

A line probably emitted purely from a disk was observed by Najita et al. (2009) toward GM Aur ($L_{\rm X}$= 1.2×10^{30} erg s^{-1}, Güdel et al. (2010)). The authors note the line is centred at the stellar velocity and has a FWHM of 14 km/s. Our model predictions are consistent with this value (Fig. 4.5), and confirm that such FWHM values can be readily reached. The same line shows a redshifted contribution at ~ 50 km/s. Interestingly this could be either a contribution from a jet component (though no known jets/outflow are associated with GM Aur, Güdel et al. (2010) and references therein) or from the inner rim of the disk (the authors suggest 0.1 to 0.5 AU). The blushifted counter part was not observed because of atmosphere issues and its presence or absence can thus not be assessed. In Fig. 4.6, we show our prediction for a generic model, where the disk inner radius is 0.5 AU. Though we are not able to reproduce the high velocity shift of the second component, we clearly predict the presence of two components in the line profile. The high velocity component originates close to the inner rim (25 km/s correspond to $\sim$ 1-2 AU in our model), while the second lower velocity component originates between 2 and 5 AU.

In this case, the emission is in LTE since the electron density in the inner rim exceeds the critical density for this line. If the high velocity component is confirmed to be symmetric, it could present an interesting diagnostic tool for studying the geometry (height, position, shape) of the inner rim.

In our models the correlation between [Ne II] and $L_{\rm X}$ is clear, although we rely on one set of fiducial disk parameters and the X-ray spectrum is scaled to match the required $L_{\rm X}$, leaving its shape unvaried. Observations include sources that have different disk properties, which can affect [Ne II] as well. This was investigated by Schisano et al. (2010). They could reproduce the 1 dex scattering in $L_{\rm [NeII]}$ observed by Güdel et al. (2010) by varying the hardness of their X-ray spectrum and the flaring angle of the disk model.

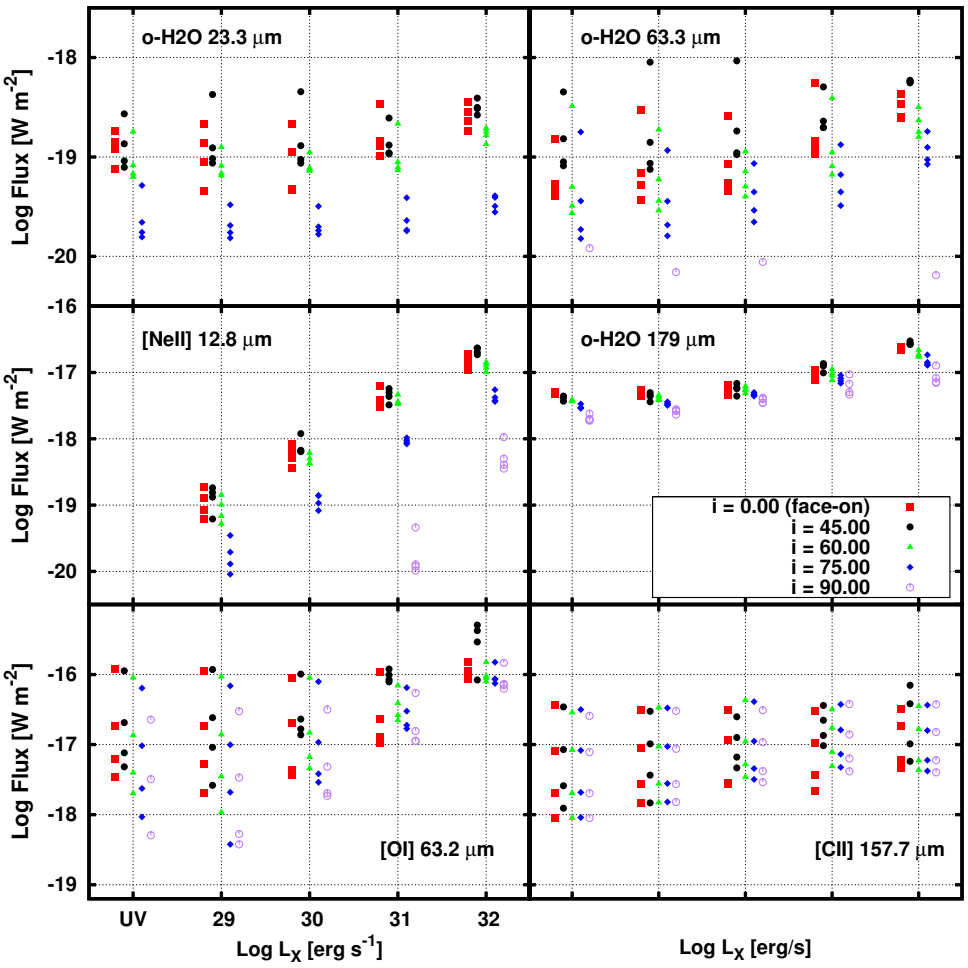

Figure 4.11: Line fluxes for all the tracers discussed in this paper, for different inclinations of the disk: $i = 0$ (face-on), 45, 60, 75, 90.

4.4.4 [Ar II] at 6.9 μm

Our [Ar II] 6.9 μm results are very similar to the [Ne II] results described above. The [Ar II] line traces exactly the same region, since the chemistry and excitation of these two species are almost identical. We need to stress here, that the collisional rates used to calculate the [Ar II] line fluxes are a factor ~ 10 higher than the collisional rates for Ne^+. Given the same basic chemistry for these two species, this is the main reason for the discrepancy in the calculated fluxes. Nevertheless, we are interested in the qualitative behaviour of this tracer, which appears to be an interesting complement to [Ne II].

Also Hollenbach & Gorti (2009) give prediction for this tracer concluding that the total fluxes of [Ne II] and [Ar II] are comparable. A study of Spitzer IRS archival spectra was able to detect this line in protoplanetary disks (Szulágyi et al., 2012, subm.). More observation are needed to confirm the diagnostic of this tracer. Our estimates for the ionized argon flux are higher than those predicted by other groups (Gorti & Hollenbach, 2008). This might be due to the different recipe used for the collisional rates.

4.4.5 Influence of inclination

So far we restricted the discussion to $i = 45°$, however to estimate the flux variation of the tracers discussed in this paper, we selected a sub-set of 20 models, in which we vary the X-ray and FUV luminosities. The other parameters are fixed: $a_{\rm min}$= 0.1, $a_{\rm pow}$= 1.5 and ϵ= 1.5. For these 20 models, we run the line radiative transfer for four more different inclinations (0° face-on, 60°, 75° and 90°). In Fig. 4.11 we plot the line fluxes versus $L_{\rm X}$, color coded are the different inclinations at which the disk is seen by the observer.

The [O I] flux (Fig. 4.11, bottom left panel) is marginally affected (0.1-0.2 dex) for $L_{\rm X} \leq 10^{30}$ erg s^{-1} and inclinations lower than 75°. The flux naturally drops (factor 5-10) for an edge-on disk. When $L_{\rm X} > 10^{30}$ the scatter introduced by models with i different than 45 is $\sim$ 1 dex. Even considering these extreme inclinations, there are no models with [O I] fluxes below 10^{-17} W/m^2; hence our threshold for [O I]is very robust.

The ionized carbon flux and water flux at 179 μm are only marginally affected by different disk inclinations, as it is expected for outer disk tracers. The [Ne II] flux (as well as [Ar II], not shown) do not depend on the inclination when $i < 75°$, while the flux drops by $\sim$ 1 dex for $i = 75°$ and by more than 2 dex for an edge-on disk. Sources with inclination higher than 60° are then likely to contribute to the scatter in the [Ne II] line observed by Güdel et al. (2010) and modelled by Schisano et al. (2010).

The water line emission at 23 μm and 63 μm is sensitive to the disk inclination, because the lines are emitted in the inner disk. The scatter is of the order of 0.3 dex or the face-on and $i = 60°$ models, and $\sim$ 1 dex for $i = 90°$. The inclination is then an important parameter to take into account when the correlation between these two water lines and [O I] is evaluated from a random sample of sources.

4.4.6 Future

The results of this grid provide the tool to understand observations of a larger sample of disks. In the context of the GASPS open time key project with Herschel (Gas in Protoplanetary disks, P.I. Bill Dent), observations of [C II] and [O I] are available for more than 100 sources in Taurus (Dent et al., in preparation). The [O I] fluxes obtained in the GASPS sample are in qualitative and quantitative good agreement with the predictions made in this work (Howard et al., in preparation). A detailed comparison with the predictions made in this work is the topic of a future paper.

The Spitzer satellite observed the [Ne II] line in many sources (Güdel et al., 2010). Due to the low spectral resolution, it is difficult to assess the location of the emitting region. Recent observations with high spectral resolution instruments provide a chance to disentangle the line origin. Currently there are too few sources to carry out a statistical study of the disk emission versus jet emission. Clearly more high spectral resolution ground based observations are needed.

A range of water lines with different excitation energy probe different disk regions, ranging from hot water in the inner rim to the outermost cold water that originates from photodesorption and ion-molecule chemistry. The correlation of water lines with the [OI] fine structure line at 63 μm could give information on the disk structure and the excitation conditions in the disk atmosphere. Riviere-Marichalar et al. (2012), for example, shows how the correlation between the water and the oxygen line at 63 μm has a slope lower than 1 as predicted here. Dedicated modelling for this and other water observations (Pontoppidan et al., 2010) will also be addressed in a future paper.

4.5 Conclusions

As shown in paper I, changes in the disk structure due to different luminosity ratios $L_{\rm X}/L_{\rm FUV}$ affect the optical thickness and height of the inner rim as well as the position of what we define as the "second bump". Hence, models differing only in the X-ray luminosity have different optical depth structure. This modifies the shadowing effects on the outer region of the disk, and impacts directly the thermo-chemical conditions there, hence changing the physical conditions that drive the line emission of different tracers.

Here, we presented an extensive description of fine-structure emission lines of oxygen, ionized carbon, ionized neon, argon and water.

- The [O I] 63 μm line emission is optically thick, and probes thermal conditions of the gas above the molecular layers. The line flux increases with temperature. For $L_{\rm X} < 10^{30}$ erg s^{-1}, FUV dominates the thermal balance, above that, $L_{\rm X} \geq 10^{30}$ erg s^{-1}, X-rays dominate.

- [C II] 157 μm is mainly driven by $L_{\rm FUV}$ via carbon ionization. X-rays affect the line flux to a lesser extent through Coulomb heating in the [C II] emitting region. The detailed emission line spectrum and continuum flux levels of the FUV spectrum are important in order to explain observed [C II] line fluxes.

- The [NeII] emission from our static modeled disk atmosphere correlates with X-rays. The line probes thermal conditions in the upper layers of the disk in the region between 1 and 10 AU. Our line profile predictions can be tested with high spectral resolution ground based observation. Especially the presence of a high velocity double-peaked component in the line profile, next to a low velocity double-peaked component, could give informations about the position of the gas inner rim independent of dust observations. This line profile is meant to be compared to sources for which disk emission has been established, as it cannot reproduce line profiles arising from gas in radial motion, such as in photoevaporative flows or jets.

- [Ar II] traces the same disk regions as [Ne II]. Recent work (Szulàgy et al., 2012, subm.) confirm the detection of this line in protoplanetary disks in few objects.

- Water emits over a wide range of radii, from the inner to the outer disk. Water line fluxes behave differently depending on the disk region they arise from. The diverse correlations with [O I] 63 μm can confirm the validity of the overall chemical and thermal structure of disk atmospheres as modelled with thermo-chemical codes such as ProDiMo.

Chapter 5

[O I] disk emission in the Taurus star forming region: heating mechanisms at work.

G. Aresu, I. Kamp, C. Howard, G. Sandell and GASPS

Based on Aresu et al., in preparation

Abstract

The structure of protoplanetary disks is thought to be linked to the temperature and chemistry of its dust and gas. Whether the disk is flat or flaring, depends on the amount of radiation that it absorbs at a given radius, and on the efficiency with which this is converted into thermal energy. The understanding of these heating and cooling processes is crucial to provide a reliable disk structure for the interpretation of dust continuum emission and gas line fluxes. Especially in the upper layers of the disk, where gas and dust are thermally decoupled, the infra-red line emission is strictly related to the gas heating/cooling processes.

We analyse here [O I] 63 μm observations of circumstellar disks in the Taurus star forming region taken with the PACS instrument on board the Herschel Space Observatory, as part of the Herschel Open Time Key Program GASPS (PI: B. Dent). We apply the results of the grid of models presented in Meijerink et al. (2012) and Aresu et al. (2012) to infer the thermal properties of the disk in the oxygen line emission region, and to investigate on the relative importance of X-ray and FUV radiation for the heating balance there.

We find that [O I] emission is mainly affected by $L_{\rm FUV}$, because in the observed Taurus sample, the FUV luminosity is systematically higher than the X-ray luminosity. The line does not correlate with $L_{\rm X}$, instead correlates with $L_{\rm FUV}$ and $L_{\rm SUM}$=$L_{\rm X}$+$L_{\rm FUV}$. The theoretical grid can explain and reproduce the correlation when a sub-sample of models with $L_{\rm FUV}$> $L_{\rm X}$ is considered.

Heating caused by the FUV radiation (e.g. PAH heating) appears to be the main

heating agent in the disk regions where the oxygen far-IR fine structure lines are emitted. More $L_{\rm FUV}$ measurements are needed to better constrain the correlations and draw robust conclusions on the thermal processes that dominate the atmosphere of protoplanetary disks surrounding T Tauri stars.

5.1 Introduction

Planet formation is strongly linked to the physical properties of the hosting disk. Important constraints on the timescale for the gas accretion of giant planets are posed by photoevaporation models, the results of such models are essential in order to estimate the mass loss rates, and hence the survival time of gas in disks (Alexander et al. 2006; Gorti et al. 2009). The stellar radiation, especially in the high energy regime (E > 6 eV), is responsible for the thermo-chemical conditions in the disk atmosphere, as it provides most of the energy that causes the gas temperature to exceed the dust temperature there (Kamp & Dullemond, 2004). However, the thermal processes that heat and shape protoplanetary disks are poorly constrained from observations as they cannot be directly measured. These are the processes that are also believed to control the emission of neutral oxygen at 63 micron in disk atmospheres (Gorti & Hollenbach, 2008; Meijerink et al., 2008; Aresu et al., 2012).

T Tauri stars emit radiation at high energies, due both to cromospheric activity and accretion of disk material onto the stellar surface. The FUV luminosity between 7 and 10 eV, has been measured by Yang et al. (2012) for a sample of accreting sources in Taurus: they found values between 10^{30} and few times 10^{32} erg/s. The emission is in excess when compared to the stellar emission in the same energy band for non-accreting young stars of the same spectral type. This suggests that accretion is responsible for this emission, in which case it is caused by shocks created by the magnetic field that channels disk material toward the stellar surface (Calvet & Gullbring, 1998; Valenti et al., 2000). EUV ($13.6 < E(\mathrm{eV}) < 100$) radiation is believed to impact mainly the upper disk surface at small radii, as the high cross section for absorption only allows penetration of small columns of $N_{\rm H} \sim 10^{19}$ cm^{-2}. The XEST survey (Güdel et al., 2007) has shown that young stars are also active X-ray emitters, mainly due to cromospheric activity, and can reach luminosities between 10^{29} and 10^{31} erg/s. The high energy depositions ($>0.01L_*$) and heating efficiencies ($\sim 30\%$) of X-rays, cause the tenuous disk atmospheres to heat up to temperatures of the order of a few thousand Kelvin.

Recent observations, carried out with the Herschel Space Observatory toward the Taurus forming region, offer the chance to test model predictions on the excitation mechanism of the [O I] 63.2 μm line. This line is predicted to arise from the disk atmosphere in the radial region between a few 10 AU and 200 AU (Woitke et al., 2009; Aresu et al., 2012). The emission region is directly exposed to the stellar radiation and models suggests that FUV and X-ray radiation are the main heating agents there. PAH and dust photoelectric heating as well as Coulomb heating, cause the gas temperature to be of the order of $\sim$ 200-300 K (Gorti & Hollenbach, 2008; Meijerink et al., 2008, 2012).

In this work, we explore possible correlations of the [O I] emission with X-ray lumi-

nosity and FUV luminosity, and compare the Aresu et al. (2012) model predictions for the [O I] 63 μm emission with data collected within the GASPS (GAS in Protoplanetary DiskS) Open Time Key Program, taken with the PACS instrument on board the Herschel Space Observatory (P.I. Dent, see Dent et al. 2012 in preparation).

In Sect.5.2 we present the collected observational data set and in Sect.5.3 we explain the main findings of the models studied in Aresu et al. (2012). In Sect.5.4 we show the results of the comparison between model predictions and observations, these will be discussed in Sect.5.5. Conclusions and remarks about future work are summarised in Sect.5.6.

5.2 Observations

In Table 5.1 we list the sources studied in this paper, together with the observed [O I] fluxes, and the collected X-ray and FUV luminosities with references. The Taurus forming region contains a rich population of pre-main sequence stars, with an age between 1-3 Myr. The sources in this sample have spectral types G, K or M, and the majority of these are Class II objects. Below we describe the origin of each observed quantity listed in Table 5.2.

Oxygen line fluxes

The data reduction is described in Howard et al., in preparation. The [O I] 63 μm line was detected in 76% (48 out of 63) of the observed objects in Taurus (Table 5.2). 50% of the sources, for which the [O I] 63 μm emission was detected, show optical extended emission associated to outflow/jet activity; these are labelled with a Y in Table 5.1. Podio et al. (2012) showed that for two of these sources (T Tau, DG Tau A) the oxygen emission at 63 μm is extended. They compared shock and disk model predictions for the fluxes of the [O I] 63 μm line, suggesting that these are likely dominated by jet/outflow emission. We decided to not consider T Tau for the calculations in this work as T Tau is a multiple stellar system driving two jets, and requires deeper dedicated modeling. DG Tau A shows misplacement between the continuum and the line emission at 63 μm, suggesting that most of the line flux is produced in the outflow. However, Howard et al. (2012, in preparation) notes that there is a tight correlation, when considering the whole sample, between the [O I] flux and the continuum at 63 μm. The sources that fall above this correlation are also the one that power optical jets or molecular outflows. In this way, the disk contribution for DG Tau A is estimated to be $\sim$ 15% of the total emission, which is a non-negligible value, given the total brightness of the [O I] line. Therefore, we included DG Tau in the correlation analysis performed in this work.

X-ray luminosities

Of the 63 sources with detected [O I] emission, we could retrieve X-ray luminosities for 39 of them (Table 5.2). The observations were carried out with the XMM-Newton spacecraft toward the Taurus forming region, performed in the context of the XEST

Name	Class	[O I]63 μm [1e-17 W/m^2]	$L_{\rm FUV}$ [1e30 erg/s]	$L_{\rm X}$ [1e30 erg/s]	Outflow [YES/NO]
AATau	II	2.24	28.82	$1.24^{+1.36}_{-1.11}$	Y
BPTau	II	0.95	58.64	$1.36^{+1.40}_{-1.35}$	N
CITau	II	3.26	*13.32*	$0.19^{+0.89}_{-0.16}$	N
CWTau	II	7.21	111.13	$2.84^{+4.00}_{-0.28}$	Y
CXTau	II	0.69	0.68	-	N
CYTau	II	1.15	13.32	$0.13^{+0.29}_{-0.13}$	N
DETau	II	1.04	30.41	-	N
DFTau	II	6.11	*9.95*	-	Y
DGTau	FS	134.00	318.04	$0.55^{+0.78}_{-0.39}$	Y
DHTau	II	<1.35	-	$8.46^{+8.64}_{-8.23}$	Y
DKTau	II	1.64	*18.58*	$0.92^{+0.96}_{-0.87}$	N
DLTau	II	2.15	13.97	-	N
DMTau	II	0.69	58.28	$2.00^{+2.83}_{-1.41}$	N
DNTau	II	0.58	6.52	$1.15^{+1.17}_{-1.14}$	N
DOTau	II	7.11	470.60	$0.24^{+0.34}_{-0.17}$	Y
DPTau	II	14.80	96.29	$0.10^{+0.18}_{-0.04}$	Y
DQTau	II	2.06	*0.82*	-	N
DSTau	II	0.90	*49.96*	-	N
FFTau	II	<1.01	-	$0.80^{+1.12}_{-0.69}$	N
FMTau	II	0.99	4.89	$0.53^{+0.56}_{-0.51}$	N
FOTau	II	1.20	-	$0.06^{+0.52}_{-0.05}$	N
FQTau	II	<0.92	-	$0.12^{+0.83}_{-0.05}$	N
FSTau-A	FS	35.80	-	$3.22^{+3.36}_{-3.09}$	Y
FXTau	II	<1.38	-	$0.50^{+2.36}_{-0.39}$	N
GGTau	II	5.09	*10.51*	-	N
GHTau	II	<0.85	-	$0.11^{+0.12}_{-0.10}$	N
GI-KTau	X	3.06	10.86	$0.83^{+1.06}_{-0.73}$	N
GMAur	II	2.38	28.24	$1.60^{+2.26}_{-1.13}$	N
GOTau	II	<5.38	-	$0.25^{+0.36}_{-0.22}$	N
HBC358	II	<1.4	-	$0.38^{+0.44}_{-0.37}$	N
HKTau	FS	3.39	-	$0.08^{+0.12}_{-0.06}$	N
HLTau	I	51.30	-	$3.84^{+4.73}_{-3.22}$	Y
HNTau	II	4.07	*21.29*	$0.32^{+0.45}_{-0.23}$	Y
HOTau	II	<1.03	-	$0.05^{+0.05}_{-0.04}$	N
Haro6-1	FS	6.96	-	$0.80^{+0.91}_{-0.14}$	Y
IPTau	II	0.59	4.05	-	N
IQTau	II	1.51	-	$0.42^{+1.17}_{-0.33}$	N
IRAS043	X	4.89	-	$0.40^{+0.50}_{-0.37}$	Y
LkCa15	II	1.02	4.45	-	N
RWAur	II	15.40	-	$1.60^{+2.26}_{-1.13}$	Y
RYTau	II	10.50	1042.56	$5.52^{+6.38}_{-4.82}$	Y

Name	Class	[O I]63 μm [1e-17 W/m^2]	$L_{\rm FUV}$ [1e30 erg/s]	$L_{\rm X}$ [1e30 erg/s]	Outflow [YES/NO]
SUAur	II	8.62	127.42	$9.46^{+9.70}_{-8.42}$	Y
UYAur	II	31.40	*27.73*	$0.40^{+0.57}_{-0.28}$	Y
UZTau	II	4.47	-	$0.89^{+1.35}_{-0.51}$	Y
V710Tau	II	1.04	-	$1.38^{+1.49}_{-1.32}$	Y
V773Tau	II	6.55	-	$9.49^{+9.54}_{-9.39}$	Y
V819Tau	II	<0.898	-	$2.44^{+2.61}_{-2.33}$	N
XZTau	X	36.10	-	$0.96^{+1.12}_{-0.86}$	Y

Table 5.1: Sources analysed in this work and their properties: Class, [O I] flux, $L_{\rm X}$ and $L_{\rm FUV}$, and presence of an optical jet/outflow. The class of the objects are taken from Andrews & Williams (2005), X-ray luminosities between 0.3 and 10 kev are taken from Güdel et al. (2007, 2010), FUV luminosities are retrieved from Ingleby et al. (2009), except the one reported in italic, which are taken from Gullbring et al. (1998). These values are then scaled by a factor 3.6 to estimate the luminosity in the 6-13.6 eV range. Outflow sources are objects for which extended emission in the optical, associated to jet, has been observed.

Sample	[O I] detections	Outflow	No outflow	$L_{\rm X}$	$L_{\rm FUV}$	$L_{\rm X}$ and $L_{\rm FUV}$
63	48	24	24	39	27	18

Table 5.2: Taurus sources from GASPS. Outflow sources are objects for which extended emission in optical, associated to jet, has been observed. $L_{\rm X}$ is measured between 0.3 and 10 keV, $L_{\rm FUV}$ is measured between 7 and 10 eV.

survey (P.I. M. Guedel). The X-ray luminosities range between 10^{29} and 10^{31} erg/s, these values and the associated errors are taken from Güdel et al. (2007) for all the sources, except DG Tau, DM Tau, DO Tau, GM Aur, HN Tau, RW Aur, and UY Tau. For these objects $L_{\rm X}$ was taken from Güdel et al. (2010). In the latter case, as suggested by the authors, an error of $\sqrt{2}$ is associated with the X-ray luminosity value to account for intrinsic variability, which is the dominant source of error.

FUV luminosities

We could retrieve FUV luminosities for 21 sources from Yang et al. (2012) (Table 5.1), the associated errors for this values are of the order of ∼30%. The observations were performed with the ACS camera and STIS spectrograph on board the Hubble Space Telescope. The FUV luminosity is obtained integrating over the dominant line emission of, e.g., C IV1459 Å, Si IV 1394 Å, in the 7 to 10 eV range, after continuum subtraction.

The FUV luminosity correlates with the Hα luminosity, C IV 1459 Å line luminosity, and with the accretion luminosity, $L_{\rm acc}$. To extend the number of $L_{\rm FUV}$ measurements, we attempted to derive FUV luminosities for those objects in our sample that are not listed in Yang et al. (2012), using the correlations they provide for these three different parameters and $L_{\rm FUV}$:

$$\begin{aligned} \log(\mathrm{L_{FUV}}) &= 1.06 + 1.023\log(\mathrm{L_{Civ}}) \\ &= -1.67 + 0.84\log(\mathrm{L_{acc}}) \\ &= -1.63 + 0.76\log(\mathrm{L_{H\alpha}}) \quad \text{[for CTTS]} \\ &= -2.31 + 0.62\log(\mathrm{L_{H\alpha}}) \quad \text{[for WTTS]}. \end{aligned} \tag{5.1}$$

We collected C IV fluxes from Gómez de Castro & Marcos-Arenal (2012) and accretion luminosities from Gullbring et al. (1998) and Ingleby et al. (2009). Gullbring et al. (1998) measures the accretion luminosity as follows: the excess flux in the energy range 2.4-3.9 eV is estimated computing the relative veiling in the 2.8-3 eV and 2.6-3.9 eV bands, where clear veiled absorption lines are available. The spectra are then corrected for the extinction. The accretion luminosity has to be calculated also outside the 2.4-3.9 eV band. The emission there is estimated considering a slab of constant temperature and density to model the accretion spots on the stellar surface. The statistical equilibrium equation are solved for H, and an escape probability method is applied to estimate the emitted flux. They find that the total excess flux, which is converted to accretion luminosity once the distance is known, is ∼3.5 times higher than the flux excess in the 2.4-3.9 eV band. Gullbring et al. (1998) also note that the accretion luminosity is proportional to the luminosity in the dereddened U-band, and provide fit parameters for this relation. This is used by Ingleby et al. (2009) to compute accretion luminosity for several other objects. In Table 5.1 we indicate in italic $L_{\rm FUV}$ estimated from $L_{\rm acc}$ values taken from Gullbring et al. (1998), all the others are taken from Ingleby et al. (2009).

These two measurements provide a direct estimate for $L_{\rm FUV}$. To get Hα luminosities, we used Hα equivalent widths (EW) and R band magnitudes (corrected for extinction), to estimate the Hα fluxes. We then calculated Hα luminosities

Name	$L_{\rm FUV}$ (Hα)	ratio	$L_{\rm FUV}$ (C IV)	ratio	$L_{\rm FUV}$ ($L_{\rm acc}$)	ratio	$L_{\rm FUV}$
AATau	0.7	41.9	-	-	15.1	1.9	28.8
BPTau	0.9	62.1	7.1	8.3	24.4	2.4	58.6
CITau	1.1	12.7	-	1124.2	44.4	0.3	13.3
CXTau	-	-	-	19.2	-	-	0.7
CYTau	0.5	29.4	0.4	33.0	5.7	2.4	13.3
DETau	-	-	2.0	15.6	18.0	1.7	30.4
DFTau	0.9	10.7	5.3	1.9	35.5	0.3	10.0
DLTau	2.0	7.0	1.2	11.8	32.2	0.4	14.0
DMTau	-	-	1.5	39.7	10.1	5.8	58.3
DNTau	0.3	24.5	0.8	8.2	5.7	1.2	6.5
DOTau	1.1	415.6	-	-	29.6	15.9	470.6
DPTau	0.2	470.1	-	-	1.8	54.3	96.3
DSTau	0.6	78.8	6.3	7.9	22.5	2.2	50.0
FMTau	0.4	13.8	0.3	17.0	30.5	0.2	4.9
GI-KTau	0.4	27.4	0.1	184.5	11.6	0.9	10.9
GMAur	-	-	2.5	11.1	19.9	1.4	28.2
HNTau	0.8	28.3	-	-	5.1	4.2	21.3
IPTau	0.1	36.3	0.5	8.1	3.2	1.3	4.1
RYTau	1.0	993.1	2.2	480.4	123.5	8.4	1042.6
SUAur	0.2	552.0	4.2	30.3	12.2	10.5	127.4
TTau	3.9	184.2	10.9	66.6	76.4	9.5	724.0

Table 5.3: Luminosities in the FUV range obtained using three different proxies: Hα flux, C IV flux, and $L_{\rm acc}$. For each of these methods, in the first column the luminosities are expressed in units of 10^{30} erg/s, in the second column the ratio between the latter and $L_{\rm FUV}$ listed in Yang et al. (2012) is calculated. Hα are taken from the GASPS collection of data, C IV line fluxes are taken from Gómez de Castro & Marcos-Arenal (2012), accretion luminosities are retrieved from Gullbring et al. (1998) and Ingleby et al. (2009), see also Table 5.1.

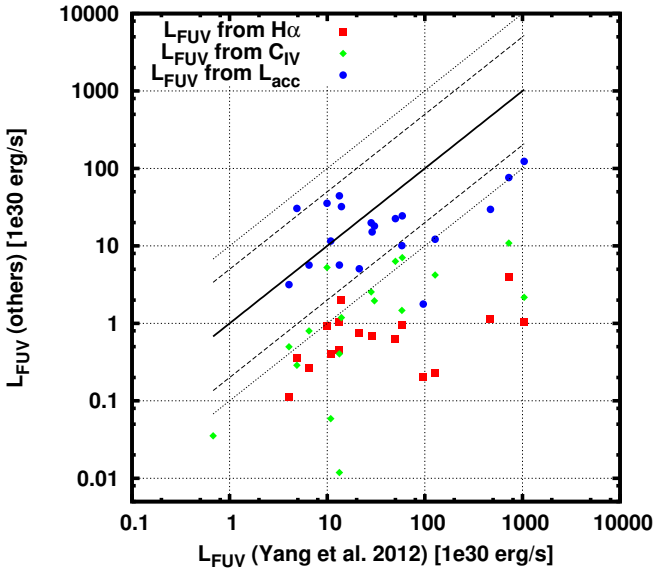

Figure 5.1: Comparison of the $L_{\rm FUV}$ luminosities obtained from Hα luminosity (red boxes), C IV 1459 Å (green diamonds) luminosity, and $L_{\rm acc}$ with the FUV luminosity listed in Yang et al. (2012). The solid line indicates a one-to-one ratio; dashed and dotted line encloses the region where the new $L_{\rm FUV}$ are a factor 5 and 10 higher/lower than $L_{\rm FUV}$ obtained by Yang et al. (2012), respectively.

by scaling for the distance to the Taurus star forming region (d $\sim$ 140 pc) and derive $L_{\rm FUV}$ using eq. 5.1. The results obtained with these three different methods are listed in Table 5.3. Comparing the agreement of our derived FUV luminosities with the sources in common with Yang et al. (2012), we can estimate which of the above methods is the most reliable to compute new $L_{\rm FUV}$ values.

The results suggest that $L_{\rm acc}$ is the most trustworthy parameter, as both Hα and C IV show strong discrepancy with the observed $L_{\rm FUV}$ for a handful of sources (Fig. 5.1). This is likely due to non-contemporary observation of the Hα and C IV lines considered here and the one used in the Yang et al., 2012 sample. The FUV emission in young stars is related to accretion, which is expected to be variable in time ($\sim$0.5 dex in days/months, Nguyen et al., 2009). Correlations between different parameters that trace accretion should be tested and used only when these are observed in the same time period. This effect is probably more dramatic when a single line is used to estimate the whole flux in the FUV band.

In our case we also suffer from time discrepancy between the Hα EW and the R band observations, introducing more uncertainties on the calculation of the Hα flux. The accretion luminosity, on the other hand, is calculated either considering a collection of photometry and spectral points, or from the correlation with the U broad band emission. This likely guarantees a better estimate of the overall continuum flux in the FUV band, causing variability to average out. We were able to collect $L_{\rm FUV}$ for seven sources for which [O I] has been detected, extending the sample from 21 to 28 (Table 5.3). The error associated to the derived $L_{\rm FUV}$ is dominated by the mean scatter in the correlation with $L_{\rm acc}$ (0.38 dex).

It is important to note that our models define the FUV luminosity in the range between 6 and 13.6 eV (92-250 nm), while Yang et al. (2012) provides integrated fluxes from 7 to $\sim$10 eV (125-170 nm). In our models we fit the spectrum shown in Woitke et al. (2009) (which uses the chromospheric flux of HD 129333 as a young sun template, Dorren & Guinan 1994) in the FUV range and find that the flux is proportional to $\lambda^{0.2}$.

If we apply this dependency to extrapolate the FUV luminosity from the 7-10 eV band to the 6-13.6 band, we estimate that:

$$L_{\rm FUV}^{(6-13.6{\rm eV})} = 3.62 L_{\rm FUV}^{(7-10{\rm eV})}. \tag{5.2}$$

From now on we will refer to $L_{\rm FUV}$, as the FUV luminosity between 6 and 13.6 eV. A very important contribution in the FUV band is given by the Lyα line emission which can carry up to 70-90% of the total FUV flux between 7 and 10 eV (Schindhelm et al., 2012). However, the calculation of the Lyα fluxes, and their exact contribution to $L_{\rm FUV}$, would require a source-to-source study, which is beyond the scope of this work.

5.3 Models

In this work we use the results obtained in Aresu et al. (2012), where the [O I] 63 μm line flux is calculated for a grid of 240 models. The varying parameters in the grid

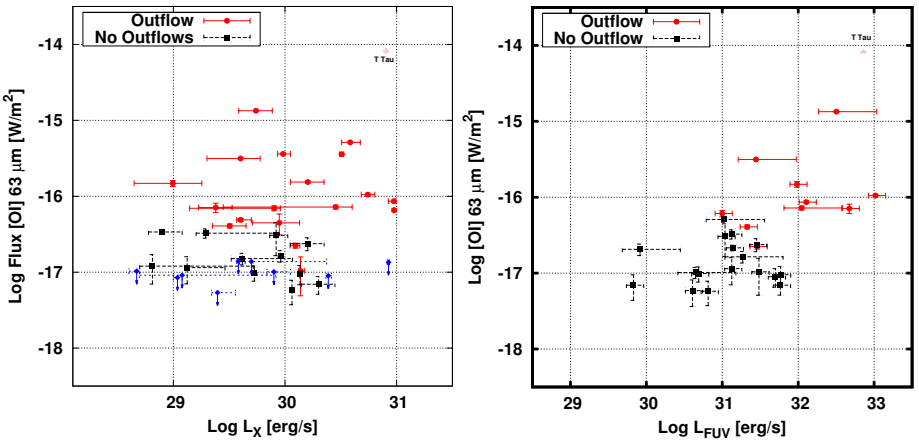

Figure 5.2: Red dots identify sources for which extended optical emission associated with outflow activity has been observed, black boxes are sources for which no extended emission was present, blue arrows are upper limits. Left-hand panel: flux of the [O I] 63 μm emission versus the X-ray luminosity. Right-hand panel: flux of the [O I] 63 μm emission versus the FUV luminosity.

are $L_{\rm X}$ (0, 10^{29}, 10^{30},10^{31}, and 10^{32} erg/s), $L_{\rm FUV}$ (10^{29}, 10^{30},10^{31}, and 10^{32} erg/s), minimum dust grain size $a_{\rm min}$ (0.1, 0.3, and 1 μm), dust size distribution power law $a_{\rm pow}$ (2.5,3.5), and surface density distribution power law ϵ (1.0,1.5). As described in Aresu et al. (2012), the main impact on [O I] is caused by $L_{\rm X}$ and $L_{\rm FUV}$, we then calculate the mean [O I] flux over each series of models with a given value of $L_{\rm X}$ and $L_{\rm FUV}$. One series is composed of 12 models, which differ for values of $a_{\rm min}$, $a_{\rm pow}$ and ϵ. The error bars accompanying the mean flux take into account a deviation of 2σ in that sub-series of 12 models.

In our grid of models we consider a single star, of spectral type G (see Meijerink et al. 2012, Table 1). The spread in spectral types in Taurus is restricted to objects of spectral type G, K and M, showing a range of temperature and bolometric luminosity with respect to our Sun-like model. This might influence the SED properties of such systems, but it does not play a role in the gas physics and chemistry in the upper layers, as this is regulated by high energy radiation.

5.4 Results

We describe the results of the observations of oxygen emission in Taurus, and investigate the correlation between the oxygen fine-structure line at 63 μm and $L_{\rm X}$, $L_{\rm FUV}$ and their sum. We then compare the data results to the model predictions described in Aresu et al. (2012), to study the thermal properties of the region where [O I] is emitted.

Table 5.4: In the first two columns we list Spearman and Kendall coefficients for the correlation between [O I] and L_X, L_{FUV} and L_{SUM}(in brackets, the coefficient for a random population). In the last three columns the slope of the correlation has been calculated for the observational data, the models with L_X between 10^{29} and 10^{31} erg/s (SUBSET 1), and the models for which $L_{FUV} > L_X$(SUBSET 2).

Observable	Spearman	Kendall	Data Slope	SUBSET 1	SUBSET 2
L_X	0.063 (0.51)	0.067 (0.60)	-	-	-
L_{FUV}	0.001 (0.40)	0.001 (0.41)	0.5 (0.1)	0.3 (0.1)	0.53 (0.04)
L_{SUM}	0.001	0.001	0.6 (0.2)	0.62 (0.05)	0.56 (0.04)

5.4.1 Observed data

In the left-hand panel of Fig.(5.2), we plot the [O I] fluxes versus the X-ray luminosity. Red dots represent sources for which outflow activity (jets or molecular outflows) in the optical has been detected, black boxes identify systems for which such activity was not observed, blue diamonds are upper limits. The X-ray luminosity range spans ~ 2 dex, as well as the range in [O I] fluxes. Due to the presence of upper limits, to investigate quantitatively the presence of a correlation we perform survival analysis using the ASURV package (Feigelson & Nelson, 1985; Isobe et al., 1986). In Table 5.4, we summarize the results obtained listing the probability that the correlation is not present using a Spearman and Kendall statistical test. This has been done for the data sample and for a random population of values in the same ranges (in brackets).

In the right-hand panel of Fig.(5.2), we plot the [O I] fluxes versus L_{FUV}. Sources that show extended emission have higher FUV luminosities compared with non outflow sources. There appears to be much less scatter compared to the left-hand panel of Fig. (5.2). The statistical analysis suggests that it is highly unlikely for the correlation to be randomly caused. We also tested the correlation between [O I] and $L_{SUM} = L_X + L_{FUV}$, finding similar results.

5.4.2 Modeling

In the left-hand panel of Fig.(5.3) we show the results taken from the grid of models described in Meijerink et al. (2012) and Aresu et al. (2012), each coloured stripe is a series of [O I] fluxes for models with a given FUV luminosity. The thickness of the stripe accounts for all the models with different dust parameters and disk surface density distribution (see Aresu et al. 2012 for the details). The models agree quantitatively with the data, reproducing the same [O I] flux range from low to high FUV luminosity along the 2 dex interval in L_X. The models do not predict a correlation between [O I] and L_X, rather they predict a threshold behaviour, as for $L_X > 10^{30}$ erg/s and $L_X > L_{FUV}$, [O I] emission should be dominated by X-rays.

The models also suggest that at a given X-ray luminosity, the [O I] line flux scales with L_{FUV}. To test this on a qualitative basis, in the right-hand panel of Fig.(5.3), we plot the [O I] observed line fluxes versus the X-ray luminosity, colour coding for the observed FUV luminosity. The predicted [O I] fluxes from the models seem to overestimate (factor $\sim$5) the observations at a given L_{FUV}. This can be also seen in

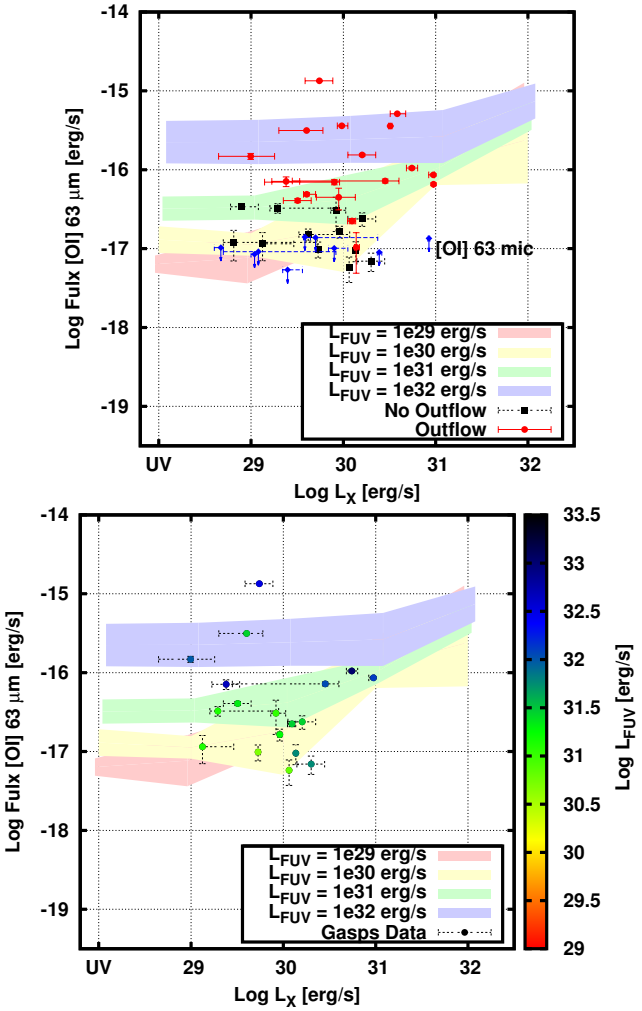

Figure 5.3: Models and observations. FUV luminosity ranges from 10^{29} (red stripe) to 10^{32} erg/s (blue stripe). When stripes overlap, the stripe representing a higher luminosity is shown.

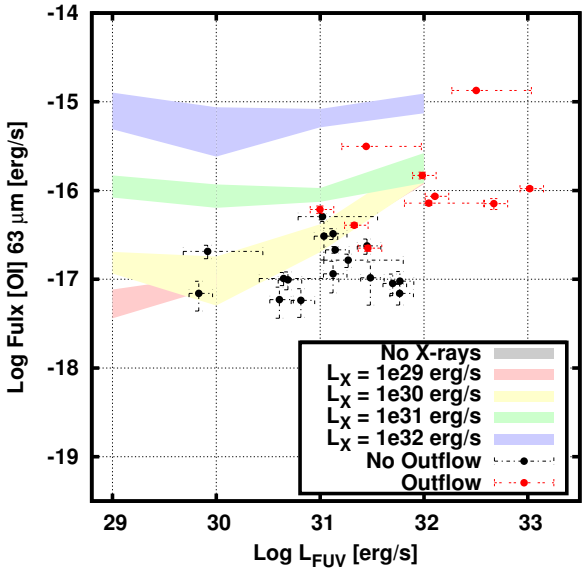

Figure 5.4: Flux of the [O I] 63 μm line versus $L_{\rm FUV}$. Observations symbols are explained in the previous figure. The coloured stripes represents predicted values for different $L_{\rm X}$.

Fig.(5.4), where the predicted [O I] is on average higher than the data. In this plot the stripes are colour coded for different $L_{\rm X}$. In this respect it is very important the FUV luminosity scaling from the 7-10 eV band to the 6-13.6 band. We use a non-accreting stellar template to estimate the variation of the flux in the full FUV range, this might not be applicable to accreting objects. Moreover, we do not consider the Lyα flux in our models, this causes an overestimate of the continuum flux in the FUV band, that could cause extra FUV heating, hence strengthening the [O I] fluxes.

In Table 5.4 we report the results of the survival statistical analysis, which suggests the presence of a correlation between [O I] and $L_{\rm FUV}$ and [O I] and $L_{\rm SUM}$. Fig. 4.2 (right-hand panel) shows that the energy deposition rates associated with $L_{\rm X}$ and $L_{\rm FUV}$ are comparable. Hence, we explored a correlation with the simple sum of these luminosities. In both cases we fit the data and the models using a linear function. The left-hand panel of Fig.(5.5) shows the fit to the data points and to the models. The red line is the linear fit for the observed [O I] line fluxes, the slope is 0.5. We considered two sub-samples of models for comparison with the data. Given that all the sources observed have $L_{\rm X}$ between 10^{29} and 10^{31} erg/s, we did not include the models with $L_{\rm X}$= 0 or 10^{32} erg/s (black line, SUBSET 1), obtaining a slope of 0.3. Moreover, considering that for all the sources in our sample $L_{\rm FUV} > L_{\rm X}$, we have excluded all the models that violates this constraint (gray line, SUBSET 2), we obtain a slope of 0.5.

In the right-hand panel we follow the same approach for $L_{\rm SUM}$, obtaining a slope of 0.6 for the observed line fluxes, and a slope of 0.62 and 0.56 for SUBSET 1 and SUBSET 2 respectively.

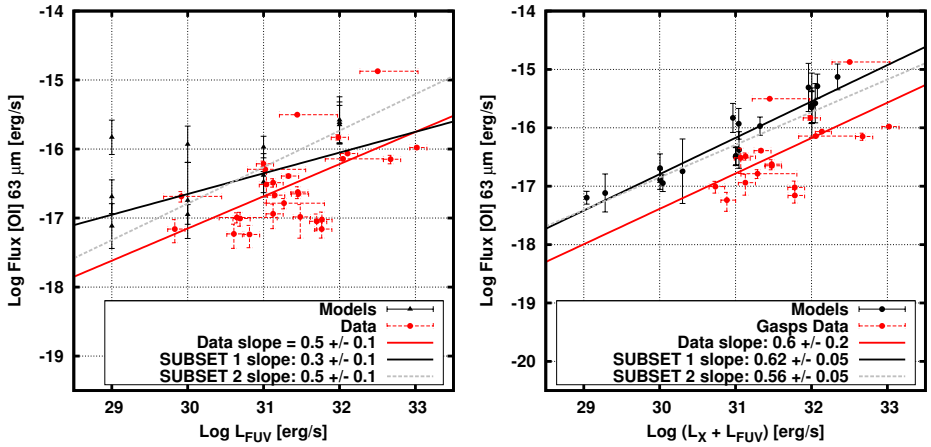

Figure 5.5: Fits for the correlation of the [O I] line with $L_{\rm FUV}$ (left-hand) panel, and $L_{\rm SUM}$ (right-hand panel). The red, black and grey lines are the fits for the observed data, the models with $L_{\rm X}$ between 10^{29} and 10^{31} erg/s (SUBSET 1), and the models also with $L_{\rm FUV} > L_{\rm X}$ (SUBSET 2), respectively.

5.5 Discussion

We discuss here the results presented in the previous section, analysing the capability of the models in interpreting the data and suggest improvements to be made.

Possible correlations

Both the models and the data suggest that there is no correlation between [O I] 63 μm and $L_{\rm X}$. This is due to the fact that FUV-related heating processes affect the line at a given X-ray luminosity, causing a vertical scatter ($\sim$ 2 dex) comparable with the range of X-ray luminosities observed in T Tauri stars.

On the other hand the models predict a similar vertical scatter when [O I] is plotted against $L_{\rm FUV}$. This is caused by X-ray heating due to different $L_{\rm X}$ at a given $L_{\rm FUV}$ for models with $L_{\rm X} > L_{\rm FUV}$. This scatter is not seen in the data, and the correlation between [O I] and $L_{\rm FUV}$ as a result is strong. In our sample of data, there is indeed not one single source for which $L_{\rm X} > L_{\rm FUV}$ (Table 5.1). All the sources investigated here have $L_{\rm FUV} > L_{\rm X}$, and 90% of them have $L_{\rm FUV} > 10 \times L_{\rm X}$.

Heating mechanism

$L_{\rm FUV}$ appears to be the dominating heating agent in the [O I] emitting region in this Taurus disk sample, and $L_{\rm X}$contributes to a lesser extent. In Aresu et al. (2012) we suggest a threshold mechanism for [O I] with respect to $L_{\rm X}$, this tentatively shows in the data, but not for the reason the models predict. Simply, all the sources for which $L_{\rm X} > 10^{30}$ erg/s have $L_{\rm FUV} \sim 10^{32}$ erg/s. Hence, FUV heating dominates, causing the line emission to be bright. Consequently, the line also correlates with the sum of the

X-ray and FUV luminosity. However, we note that the sample becomes smaller, since not all the sources, for which we could retrieve the FUV luminosity, have a measured $L_{\rm X}$.

5.6 Outlook and Conclusions

Accreting sources in Taurus show high FUV luminosities ($> 10^{30}$ erg/s), on the other hand the XEST survey clearly detected $L_{\rm X}$ between 10^{29} and 10^{31} erg/s in the Taurus star forming region. This indicates that FUV radiation dominates the heating balance in the atomic layer of disk atmospheres. The arguments are as follows:

- Observations show no correlation between X-ray luminosity and the [O I] 63 μm line emission.
- The [O I] 63μm line correlates with FUV luminosity, and with the total excess luminosity ($L_{\rm X}$+$L_{\rm FUV}$).
- Thermo-chemical disk models calculated with ProDiMo, qualitatively agree with the observations, although the predicted fluxes are overestimated for those sources for which no optical extended emission was observed. However, the models can reproduce the slope of the correlations found in the observation when only models with $L_{\rm FUV} > L_{\rm X}$ are considered.

To increase the sample size, more measurements of $L_{\rm FUV}$ would be necessary. Moreover, to test the threshold mechanisms proposed in our previous work, observations of [O I] of sources with $L_{\rm X} > L_{\rm FUV}$ are essential.

High spatial and spectral resolution observations of [O I] emission are required to disentangle the location of the emission region of the line. In many sources that drive outflows, the contribution of the disk to the total flux of the line is unclear.

These results support the picture where accretion generated FUV radiation is the main cause of disk photoevaporation (Gorti et al., 2009), as it dominates the energy budget in the oxygen line emission region. The line is expected to be produced in the intermediate disk region (r ∼10-200 AU) that survive the longest (t $\sim 3.5 \times 10^6$). Its observation, for a sample of objects with different ages, could test photoevaporation model predictions for gas survival time in the disk.

Chapter 6

Highlights and outlook

In this thesis I studied the impact that high energy radiation (X-rays and FUV) from the central star has on the chemistry and thermal structure of the surrounding protoplanetary disk. I highlight here the main results from chapters 2, 3, 4, and 5, and suggest possible lines of future research, either concerning the development of the code ProDiMo or in terms of new observations to test the modeling results.

- Increasing X-ray luminosities cause the inner disk temperatures to reach up to ∼5000 K, as a result, the inner rim is puffed up to higher altitudes with respect to UV only models. The FUV radiation leaves the scale height of the inner rim unchanged; it only alters the width and height of the second bump in the disk that is created at intermediate radii ($r \sim 3 - 10$ AU), behind the region shielded by the puffed-up inner rim. The existence of the second bump could potentially be tested by continuum imaging of face-on protoplanetary disks in the near-infrared with, e.g., VLT or Keck.

- X-ray energy deposition is dominant in the tenuous disk atmospheres ($z/r \gtrsim 0.4$), while FUV heating takes over deeper in the disk ($z/r \sim 0.2$). In the future, we will also investigate the importance in the thermal balance of X-ray scattering, which is currently being implemented in ProDiMo.

- Due to their ionization potential and excitation temperatures, Ne^+ and Ar^+ fine-structure line emission at 12.8 μm and 6.9 μm respectively, are high temperature tracers in the region where X-rays (and likely EUV) cause the gas temperature to exceed 2000 K. In this context, it is crucial to isolate the disk contribution to the line flux, as these lines are also excited in slow photo-evaporative outflows and in jets. High resolution spectroscopy (e.g., TEXES on Gemini, VISIR on VLT) shows that the fraction of objects for which static disk atmosphere emission is dominant is very low, but more observations are needed to enlarge the sample.

- [O I] 63 μm line emission is an excellent tracer of the gas temperature of the disk atmosphere in the radial region between 10 and 100 AU. The heating in the oxygen line emission region is predicted to be driven by FUV and X-ray radiation, depending on their luminosities. We find that $L_{\rm FUV}$ heating dominates,

unless $L_X \gtrsim 10^{30}$ erg s^{-1} and $L_X \gtrsim L_{FUV}$, because Coulomb heating takes over in this regime. Observations toward the Taurus star forming region show that FUV luminosities are higher than X-rays, hence FUV dominates the thermal balance in the region where the oxygen line forms. In the GASPS sample of [O I] observations in Taurus, more FUV and X-ray luminosity measurements are needed to fully test the model predictions, i.e. a sub sample of few objects with $L_X \gtrsim 10^{30}$ erg s^{-1} and $L_X \gtrsim L_{FUV}$ would be the ideal test for the threshold mechanism proposed in this work.

- Observations of water lines can be used complementary to the oxygen line described above: the nature of the slope in the correlation of different water lines with the [O I] 63 μm line, potentially gives information on the dominant heating mechanisms from the inner disk ($r \sim$1-10 AU, water emission at 23 and 63 μm) to the outer disk ($r >$200 AU, water emission at 179 μm), but also on the radial gas temperature gradient, and on the X-ray energy deposition radial dependency. Predicted water line emission is deeply linked with underlying modeling assumptions (e.g. surface chemistry for water formation, ice formation, metal abundances), which need better understanding. Future infrared missions (e.g. Spica-SAFARI) will guarantee higher sensitivity and are likely to increase the detection rate of water lines, hence providing a larger sample of data to compare with, and possibly improve, the models.

- Molecules such as OH^+, H_2O^+ and H_3O^+ are tracers of X-ray chemistry in the ion-molecule layer between the atomic to molecular transition. The H_3O^+ emission is predicted to be weak ($\sim 10^{-20}$ W/m^2), well below the detection threshold of current and near future IR instruments, e.g. Herschel or Spica-SAFARI. On the other hand, OH^+ and H_2O^+ line flux predictions are currently impeded by lack of collisional data. The line emission of these molecules would probe ion-molecule X-ray chemistry in protoplanetary disks.

From the modeling point of view, many other interesting lines of developing are opened for the future. In addition to the results obtained running the grid of X-ray models described in this thesis, there are some not yet analysed, e.g. the line fluxes of the CO rotational transitions, which are potentially observable with ALMA. Moreover, the following questions will be addressed: what is the impact that variability (of both X-ray and FUV radiation) has on the chemistry and thermal properties of the upper layers? How does X-ray scattering change the energy deposition in the deeper layers of the disk? Does this impact the electron fraction in the active layers, where the magneto-rotational instability is supposed to drive accretion? Theoretical work from other groups has been carried out considering different positions of the X-ray source to account for, e.g. soft emission from jets. Would a different position of the X-ray source change the results discussed in this work? The increasing computer power and the fact that we are living in the middle of the space telescope era, suggests that a full understanding of the X-ray importance in the evolution of the properties of protoplanetary disks is not only possible, but very likely achievable in the years to come.

Appendix A

X-ray chemistry

Our chemical network is composed of $N_{\rm sp}$=110 species (see Table A.1), linked by ∼1500 reactions.

Table A.1: Species included in the chemical network.

110 species
H, H^+, H^-, H_2, H_2^+, H_2^*, H_3^+, He, He^+, O, O^+, O^{2+}, O_2, O_2^+,
OH, OH^+, H_2O, H_2O^+, H_3O^+, CO, CO^+,CO_2, CO_2^+, HCO, HCO^+,
H_2CO,
N, N^+, N^{2+}, NO, NO^+, C, C^+, C^{2+}, CH, CH^+, CH_2, CH_2^+, CH_3, CH_3^+,
CH_4, CH_4^+, CH_5^+, Si, Si^+, Si^{2+}, SiO, SiO^+, SiH, SiH^+, SiH_2^+, $SiOH^+$,
S, S^+, S^{2+}, SO, SO^+, SO_2, SO_2^+, OCS, CS, CS^+, HS, HS^+, HCS^+,
H_2S^+, H_3S^+,
Mg, Mg^+, Mg^{2+}, Fe, Fe^+, Fe^{2+}, Ne, Ne^+, Ne^{2+}, Ar, Ar^+, Ar^{2+}, Na,
Na^+, Na^{2+},
NH, NH^+, NH_2, NH_2^+, N_2H^+, NH_3, NH_3^+, NH_4^+, N_2, HN_2^+, CN, CN^+,
HCN, HCN^+, HNC, C_2H_2, $C_2H_3^+$, $HCNH^+$, CO#, H_2O#, CO_2#,
CH_4#, NH_3#,
PAH, PAH^-, PAH^+, PAH^{2+}, PAH^{3+}

References for the rate coefficients: Millar et al. (1986); Lennon et al. (1988); Landini & Fossi (1991); Anicich (1993); Badnell (2006)

For a given species i, the net formation rate reads (following Woitke et al. 2009):

$$\begin{aligned}\frac{dn_i}{dt} &= \sum_{jkl} R_{jk\to il}(T_{\rm g}) n_j n_k + \sum_{jl}\left(R^{\rm ph}_{j\to il} + R^{\rm cr}_{j\to il} + R^{\rm Xpr}_{j\to il} + R^{\rm Xsec}_{j\to il}\right) n_j \\ &- n_i\left(\sum_{jkl} R_{il\to jk}(T_g) + \sum_{jk}\left(R^{\rm ph}_{i\to jk} + R^{\rm cr}_{i\to jk} + R^{\rm Xpr}_{i\to jk} + R^{\rm Xsec}_{i\to jk}\right)\right) \quad \text{(A.1)}\end{aligned}$$

The terms involved are

- $R_{jk\rightarrow il}$, the temperature-dependent rate for a two-body reaction where species i and l are formed out of species j and k
- $R^{\rm ph}_{i\rightarrow jk}$, a photo-reaction rate that depends on the local strength of the FUV radiation field
- $R^{\rm cr}_{i\rightarrow jk}$, a reaction that depends on the cosmic ray ionization rate
- $R^{\rm Xpr}_{j\rightarrow il}$ and $R^{\rm Xsec}_{j\rightarrow i}$, the X-ray primary and secondary ionization reaction rates.

Assuming statistical equilibrium $\left(\frac{dn}{dt}=0\right)$, we obtain $N_{\rm sp}$ non-linear equations for the $N_{\rm sp}$ unknown particle densities n_k,

$$F_i(n_k)=0. \tag{A.2}$$

For the species densities n_k, this system of nonlinear equations is solved through a Newton-Raphson iterative method, which expands F_i into a Taylor series in the neighborhood of n_k,

$$F_i(n_k+\delta n_k)=F_i(n_k)+\sum_j \frac{\partial F_i}{\partial n_k}\delta n_k + O(\delta n_k^2). \tag{A.3}$$

The code then needs to calculate the Jacobi matrix:

$$J_{ik}=\frac{\partial F_i}{\partial n_k}. \tag{A.4}$$

Neglecting terms of the order of δn_k^2, the math SLATEC routines are used to find a set of n_k that satisfies $F_i(n_k+\delta n_k)=0$:

$$J_{ik}\cdot\delta n_k=-F_i. \tag{A.5}$$

When the rate of a given reaction does not depend on the particle density n_k, the derivative of F_i is straightforward, e.g, a photo-reaction that destroys species i:

$$J_{ik}=\frac{\partial F_i}{\partial n_k}=-R^{\rm ph}_{i\rightarrow j}\cdot\delta_{ik}. \tag{A.6}$$

X-ray reaction rates, however, depend on the electron density $n_{\rm e}$, atomic hydrogen density $n_{\rm H}$, and/or molecular hydrogen density $n_{\rm H_2}$. These densities determine how much of the absorbed X-ray photons will go into the different channels for heating, ionization, and excitation. If the rate R shows a dependency on the particle densities, for example, the electron density ($n_{\rm el}$), atomic hydrogen density ($n_{\rm H}$), and/or molecular hydrogen density ($n_{\rm H_2}$), the Jacobian can be expressed as:

$$J_{ik}=\frac{dF_i}{dn_k}=\frac{\partial F_i}{\partial n_k}+\frac{\partial F_i}{\partial n_{\rm el}}\frac{\partial n_{\rm el}}{\partial n_k}+\frac{\partial F_i}{\partial n_{\rm H}}\frac{\partial n_{\rm H}}{\partial n_k}+\frac{\partial F_i}{\partial n_{\rm H_2}}\frac{\partial n_{\rm H_2}}{\partial n_k}. \tag{A.7}$$

ProDiMo calculates this term analytically to ensure an accurate chemical solution. Here we describe how the Jacobian terms for the X-ray reactions rates are calculated. We define the following quantities, which will be used below:

$$n_{\langle \mathrm{H} \rangle} = \sum_j n_j Q(j, \mathrm{H}) \tag{A.8}$$

$$n_{\mathrm{el}} = \sum_j n_j q_j, \tag{A.9}$$

where $n_{\langle \mathrm{H} \rangle}$ is the total hydrogen nuclei density, Q(j,H) is the stoichiometric coefficient for the hydrogen nuclei (which is 0 for all those species that do not contain hydrogen, while for species containing hydrogen we have: Q(H,H)=1, Q(H_2,H)=2, Q(H_3^+,H)=3, etc.). The electron density is denoted as n_{el} and q_j is the charge of the particle j.

A.1 Primary ionization

For the generic atomic species A, A^+ and molecular species AB, these are reactions of the kind:

$$\begin{aligned} \mathrm{A} + X_{\mathrm{ph}} &\rightarrow \mathrm{A}^{2+} + 2\mathrm{e}^- && \text{(A.10)} \\ \mathrm{A}^+ + X_{\mathrm{ph}} &\rightarrow \mathrm{A}^{2+} + \mathrm{e}^- && \text{(A.11)} \\ \mathrm{AB} + X_{\mathrm{ph}} &\rightarrow \mathrm{A}^{2+} + \mathrm{B} + 2\mathrm{e}^- && \text{(A.12)} \\ &\rightarrow \mathrm{A}^+ + \mathrm{B}^+ + 2\mathrm{e}^- \\ &\rightarrow \mathrm{A} + \mathrm{B}^{2+} + 2\mathrm{e}^-, \end{aligned}$$

where X_{ph} is an X-ray photon. When the i-th species is molecular (A.12), the reaction rate $R^{\mathrm{Xpr}}_{i \rightarrow jl}$ for the reaction that destroys the species i has two indices j, and l, for the resulting species. Otherwise the reaction rate should simply read $R^{\mathrm{Xpr}}_{i \rightarrow j}$ as only one species is produced out of reactions A.10 and A.11. For simplicity, from now on, we use the molecular reaction rate as an example for X-ray primary ionization. The rate is calculated as

$$R^{\mathrm{Xpr}}_{i \leftarrow jl} = \int_{E_i}^{\infty} \sigma_i(E) F(E, r) dE \qquad [\mathrm{s}^{-1}]. \tag{A.13}$$

It depends on the X-ray radiation field $F(E, r)$ at the point r where it is computed and on the cross section σ_i of the species i. It does not depend on the local particle density. From equations A.3 and A.6, we see that the contribution to the equilibrium equation for the species i can be written as

$$F_i = F_{\mathrm{oth}} - \sum_{jl} R^{\mathrm{Xpr}}_{i \leftarrow jl} \cdot n_i + \sum_{jl} R^{\mathrm{Xpr}}_{j \rightarrow il} \cdot n_j. \tag{A.14}$$

The contribution to the Jacobi element of this reaction is then

$$J_{ik} = \frac{\partial F_{\mathrm{oth}}}{\partial n_k} - \sum_{jl} R^{\mathrm{Xpr}}_{i \leftarrow jl} \cdot \delta_{ik} + \sum_{jl} R^{\mathrm{Xpr}}_{j \rightarrow il} \cdot \delta_{jk}. \tag{A.15}$$

A.2 Secondary ionization

We consider X-ray secondary ionization for all the atomic species A and only for a single molecule H_2:

$$\begin{aligned} A + e^- &\rightarrow A^+ + 2e^- && \text{(A.16)} \\ H_2 + e^- &\rightarrow {H_2}^+ + 2e^- && \text{(A.17)} \\ &\rightarrow H + H^+ + 2e^-. && \text{(A.18)} \end{aligned}$$

The reaction rate for the X-ray secondary ionization of species i is

$$R_{i\rightarrow j}^{\text{Xsec}} = r_i \frac{H_X n_{\langle \text{H} \rangle}}{W n_H} \qquad [\text{s}^{-1}], \tag{A.19}$$

where r_i is a parameter that takes into account the geometrical cross section of species i compared to the hydrogen cross section, $n_{\langle \text{H} \rangle}$ is the total hydrogen nuclei density, H_X is the X-ray energy deposition (Maloney et al., 1996), and W [eV] is the mean energy consumed per ion pair (Dalgarno et al., 1999).

W for hydrogen and all the other atomic elements except He is

$$W_\text{H} = W_{0,\text{H}} \left(1 + c_1 \left(\frac{n_\text{el}}{n_{\langle \text{H} \rangle}}\right)^\alpha\right) \left(1 + c_2 \frac{n_{\text{H}_2}}{n_H}\right) \qquad [\text{eV}], \tag{A.20}$$

where $W_{0,\text{H}}$ is the collisional ionization rate for H in a pure neutral atomic gas (13.6 eV), n_el is the electron density, n_{H_2} is the molecular hydrogen density, and α, c_1 and c_2 are fitting parameters.

W_H is then the energy needed to collisionally ionize hydrogen in a gas mixture with n_el, n_H and n_{H_2}. The values for other atomic elements are scaled up, considering the geometrical factor $r_i = \sigma_i^{coll}/\sigma_H^{coll}$ (Ádámkovics et al., 2011). W has been calculated for He and H_2 as well; these cases will be treated separately further on.

Hydrogen

The X-ray energy deposition is a quantity defined per unit of hydrogen nuclei as follows:

$$H_X = \int \sigma_\text{tot}(E) F(E, r) dE \qquad [\text{erg } \langle \text{H} \rangle^{-1}], \tag{A.21}$$

where σ_tot is given by

$$\sigma_\text{tot}(E) = \sum_{i=1}^{N_\text{sp}} \sigma_i(E) n_i / n_{\langle \text{H} \rangle} \qquad [\text{cm}^2], \tag{A.22}$$

and $F(E, r)$ is the radiation field in unit of erg s^{-1} cm^{-2} eV^{-1}. For a given atomic species i, at the equilibrium, the contribution of the secondary ionization to the volumetric rate is

$$\begin{aligned} F_i &= F_{\rm oth} + F_i^{\rm Xsec} \\ &= F_{\rm oth} - R^{\rm Xsec}_{i\leftarrow j}\cdot n_i + R^{\rm Xsec}_{j\rightarrow i}\cdot n_j \\ &= F_{\rm oth} - r_i \frac{H_X n_{\langle \rm H\rangle}}{W_H n_H} n_i + r_j \frac{H_X n_{\langle \rm H\rangle}}{W_H n_H} n_j. \end{aligned} \tag{A.23}$$

Following Eq. A.7, the derivative of $F_i^{\rm Xsec}$ with respect to n_k is

$$\begin{aligned} \frac{dF_i^{\rm Xsec}}{dn_k} &= -r_i \times \\ &\left[\frac{n_i}{W_{\rm H} n_{\rm H}}\frac{\partial\left(H_X n_{\langle \rm H\rangle}\right)}{\partial n_k} - \frac{H_x n_{\langle \rm H\rangle} n_i}{W_{\rm H}^2 n_{\rm H}}\frac{\partial W_{\rm H}}{\partial n_k} - \frac{H_x n_{\langle \rm H\rangle} n_i}{W_{\rm H} n_{\rm H}^2}\delta_{{\rm H},k} + \frac{H_x n_{\langle \rm H\rangle}}{W_{\rm H} n_{\rm H}}\delta_{ik}\right]. \end{aligned} \tag{A.24}$$

Here we develop separately the partial derivative for all involved terms:

$$\begin{aligned} \frac{\partial\left(H_X n_{\langle \rm H\rangle}\right)}{\partial n_k} &= \frac{\partial}{\partial n_k}\int \Sigma_j n_j \sigma_j(E) F(E,r) dE \\ &= \int \sigma_k(E) F(E,r) dE \\ &= D_K \end{aligned} \tag{A.25}$$

$$\begin{aligned} \frac{\partial W_{\rm H}}{\partial n_k} &= \frac{\partial}{\partial n_k}\left[W_{0,\rm H}\left(1 + c_1\left(\frac{n_{\rm el}}{n_{\langle \rm H\rangle}}\right)^{\alpha}\right)\left(1 + c_2\frac{n_{\rm H_2}}{n_{\rm H}}\right)\right] \\ &= W_{0,\rm H}\, c_1 \frac{\alpha q_k n_{\rm el}^{\alpha-1}}{n_{\langle \rm H\rangle}^{\alpha}}\left(1 + c_2\frac{n_{\rm H_2}}{n_{\rm H}}\right) \\ &- W_{0,\rm H}\, c_1 \frac{\alpha n_{\rm el}^{\alpha} Q_{k,\rm H}}{n_{\langle \rm H\rangle}^{\alpha+1}}\left(1 + c_2\frac{n_{\rm H_2}}{n_{\rm H}}\right) \\ &+ W_{0,\rm H}\left(1 + c_1\frac{n_{\rm el}^{\alpha}}{n_{\langle \rm H\rangle}^{\alpha}}\right)\frac{c_2}{n_{\rm H}}\delta_{{\rm H_2},k} \\ &- W_{0,\rm H}\left(1 + c_1\frac{n_{\rm el}^{\alpha}}{n_{\langle \rm H\rangle}^{\alpha}}\right) c_2\frac{n_{\rm H_2}}{n_{\rm H}^2}\delta_{{\rm H},k}. \end{aligned}$$

Substituting these results in Eq. A.24 we obtain seven terms:

$$\begin{aligned}
\frac{dF_i^{\mathrm{Xsec}}}{dn_k} &= -r_i \frac{n_i}{W_H n_H} D_K \\
&- r_i \frac{H_X n_{\langle \mathrm{H} \rangle}}{W_{\mathrm{H}} n_{\mathrm{H}}} \delta_{ik} \\
&- r_i \frac{H_X}{W_{\mathrm{H}}^2 n_{\mathrm{H}}} n_i W_{0,\mathrm{H}} c_1 \alpha \left(\frac{n_{\mathrm{el}}}{n_{\langle \mathrm{H} \rangle}} \right)^{\alpha} \left(1 + c_2 \frac{n_{\mathrm{H}_2}}{n_{\mathrm{H}}} \right) Q(k, \mathrm{H}) \\
&- r_i \frac{H_X n_{\langle \mathrm{H} \rangle} n_i}{W_{\mathrm{H}}^2 n_{\mathrm{H}}^2} W_{0,\mathrm{H}} \left(1 + c_1 \left(\frac{n_{\mathrm{el}}}{n_{\langle \mathrm{H} \rangle}} \right)^{\alpha} \right) c_2 \frac{n_{\mathrm{H}_2}}{n_{\mathrm{H}}} \delta_{\mathrm{H},k} \\
&+ r_i \frac{H_X}{W_{\mathrm{H}}^2 n_{\mathrm{H}}} n_i W_{0,\mathrm{H}} c_1 \alpha \left(\frac{n_{\mathrm{el}}}{n_{\langle \mathrm{H} \rangle}} \right)^{\alpha - 1} \left(1 + c_2 \frac{n_{\mathrm{H}_2}}{n_{\mathrm{H}}} \right) q_k \\
&+ r_i \frac{H_X n_{\langle \mathrm{H} \rangle} n_i}{W_{\mathrm{H}}^2 n_{\mathrm{H}}^2} W_{0,\mathrm{H}} \left(1 + c_1 \left(\frac{n_{\mathrm{el}}}{n_{\langle \mathrm{H} \rangle}} \right)^{\alpha} \right) c_2 \delta_{\mathrm{H}_{2,k}} \\
&+ r_i \frac{H_X n_{\langle \mathrm{H} \rangle} n_i}{W_{\mathrm{H}} n_{\mathrm{H}^2}} \delta_{\mathrm{H},k}.
\end{aligned} \tag{A.26}$$

The seven terms can be interpreted as follows:

1. The first term represents the variation of the energy deposition H_{X} when n_k is increased. According to this term only, increasing n_k brings more fast electrons in the gas phase via primary ionization of the species k. Hence more electrons are available for the secondary ionization of the species i.

2. The second term directly impacts $R_{i \leftarrow j}^{\mathrm{Xsec}}$ if i=k more particles are available for secondary ionization.

3. The third calculates the variations in W if the species considered contains hydrogen.

4. The fourth term comes from the dependency of W_{H} on n_{H} (the higher n_{H} the closer is W_{H} to $W_{0,\mathrm{H}}$).

5. Analogous to the previous one, the fifth term shows that if the molecular hydrogen density increases (atoms are less likely to be ionized by fast electrons because) W_{H} will be higher.

6. If the density of a positively charged particle increases, the electron density must increase at the same time as well. This favors Coulomb losses in energy of the incoming fast electrons over secondary ionization of species i. If k =H^-, this sixth term becomes negative because fewer electrons will be in the gas phase, favouring secondary ionization over Coulomb heating.

7. The seventh term comes directly from the secondary ionization rate. The higher the atomic hydrogen density, the lower is $R_{i \leftarrow j}^{\mathrm{Xsec}}$.

Molecular Hydrogen and Helium

The mean energy per ion pair for H_2 is

$$W_{H_2} = W_{0,H_2} \left(1 + c_1 \left(\epsilon^*_{el}\right)^{\alpha}\right) \left(1 + c_2 \frac{n_H}{n_{H_2}}\right), \tag{A.27}$$

while for helium, it is

$$W_{He} = W_{0,He} \left(1 + c_1 \left(\epsilon_{el}\right)^{\alpha}\right) \tag{A.28}$$

where ϵ^*_{el} is

$$\epsilon^*_{el} = \frac{1.83\epsilon_{el}}{1 + 0.83\epsilon_{el}}, \tag{A.29}$$

with ϵ_{el} is the electron fraction ($n_{el}/n_{\langle H \rangle}$). Inserting these terms into A.23 and generating the derivative with respect to n_k gives the Jacobi elements for molecular hydrogen and helium respectively. Since they look very similar to Eq. A.26, we will not write them out.

Bibliography

Ádámkovics, M., Glassgold, A. E., & Meijerink, R. 2011, ApJ, 736, 143

Aikawa, Y. 2007, ApJ, 656, L93

Alexander, R. 2008, New A Rew., 52, 60

Alexander, R. D., Clarke, C. J., & Pringle, J. E. 2006, MNRAS, 369, 216

Andre, P., Ward-Thompson, D., & Barsony, M. 1993, ApJ, 406, 122

Andrews, S. M. & Williams, J. P. 2005, ApJ, 631, 1134

Andrews, S. M. & Williams, J. P. 2007, ApJ, 671, 1800

Andrews, S. M., Wilner, D. J., Hughes, A. M., Qi, C., & Dullemond, C. P. 2010, ApJ, 723, 1241

Anicich, V. G. 1993, Journal of Physical and Chemical Reference Data, 22, 1469

Apai, D., Pascucci, I., Bouwman, J., et al. 2005, Science, 310, 834

Aresu, G., Kamp, I., Meijerink, R., et al. 2011, A&A, 526, A163+

Aresu, G., Meijerink, R., Kamp, I., et al. 2012, ArXiv e-prints

Armitage, P. J. 2010, Astrophysics of Planet Formation

Bachiller, R. 1996, in IAU Symposium, Vol. 178, Molecules in Astrophysics: Probes & Processes, ed. E. F. van Dishoeck, 103

Badnell, N. R. 2006, ApJS, 167, 334

Bahcall, J. N. & Wolf, R. A. 1968, ApJ, 152, 701

Balbus, S. A. & Hawley, J. F. 1998, Reviews of Modern Physics, 70, 1

Baldovin-Saavedra, C., Audard, M., Carmona, A., et al. 2012, ArXiv e-prints

Beckwith, S. V. W. & Sargent, A. I. 1991, ApJ, 381, 250

Beckwith, S. V. W., Sargent, A. I., Chini, R. S., & Guesten, R. 1990, AJ, 99, 924

Benz, A. O., Bruderer, S., van Dishoeck, E. F., et al. 2010, A&A, 521, L35+

Bergin, E., Calvet, N., D'Alessio, P., & Herczeg, G. J. 2003, ApJl, 591, L159

Bergin, E. A. 2009, ArXiv e-prints

Black, J. H. 1987, in Astrophysics and Space Science Library, Vol. 134, Interstellar Processes, ed. D. J. Hollenbach & H. A. Thronson, Jr., 731–744

Blum, J. & Wurm, G. 2008, ARA&A, 46, 21

Brittain, S. D., Rettig, T. W., Simon, T., Gibb, E. L., & Liskowsky, J. 2010, ApJ, 708, 109

Bruderer, S., Benz, A. O., van Dishoeck, E. F., et al. 2010, A&A, 521, L44+

Bruderer, S., van Dishoeck, E. F., Doty, S. D., & Herczeg, G. J. 2012, A&A, 541, A91

Calvet, N. & Gullbring, E. 1998, ApJ, 509, 802

Carmona, A., van der Plas, G., van den Ancker, M. E., et al. 2011, A&A, 533, A39

Cazaux, S. & Tielens, A. G. G. M. 2004, ApJ, 604, 222

Ceccarelli, C., Haas, M. R., Hollenbach, D. J., & Rudolph, A. L. 1997, ApJ, 476, 771

Chiang, E. I. & Goldreich, P. 1997, ApJ, 490, 368

D'Alessio, P., Canto, J., Calvet, N., & Lizano, S. 1998, ApJ, 500, 411

Dalgarno, A., Yan, M., & Liu, W. 1999, ApJs, 125, 237

Dartois, E., Dutrey, A., & Guilloteau, S. 2003, A&A, 399, 773

Davis, A. M., Alexander, C. M. O., Nagahara, H., & Richter, F. M. 2005, in Astronomical Society of the Pacific Conference Series, Vol. 341, Chondrites and the Protoplanetary Disk, ed. A. N. Krot, E. R. D. Scott, & B. Reipurth, 432

Dent, W. & the GASPS team. 2012, in prep.

Dere, K. P., Landi, E., Mason, H. E., Monsignori Fossi, B. C., & Young, P. R. 1997, A&AS, 125, 149

Dere, K. P., Landi, E., Young, P. R., et al. 2009, , 498, 915

Dominik, C., Blum, J., Cuzzi, J. N., & Wurm, G. 2007, Protostars and Planets V, 783

Dorren, J. D. & Guinan, E. F. 1994, ApJ, 428, 805

Draine, B. T. 1978, ApJs, 36, 595

Draine, B. T. & Bertoldi, F. 1996, ApJ, 468, 269

Dullemond, C. P. & Dominik, C. 2004, A&A, 417, 159

Dullemond, C. P., Dominik, C., & Natta, A. 2001, ApJ, 560, 957

Dullemond, C. P., Hollenbach, D., Kamp, I., & D'Alessio, P. 2007, Protostars and Planets V, 555

Dullemond, C. P., van Zadelhoff, G. J., & Natta, A. 2002, A&A, 389, 464

Dutrey, A., Guilloteau, S., & Guelin, M. 1997, A&A, 317, L55

Ercolano, B., Drake, J. J., Raymond, J. C., & Clarke, C. C. 2008, ApJ, 688, 398

Ercolano, B. & Owen, J. E. 2010, , 406, 1553

Espaillat, C., Calvet, N., D'Alessio, P., et al. 2007, ApJl, 664, L111

Evans, II, N. J., Dunham, M. M., Jørgensen, J. K., et al. 2009, ApJs, 181, 321

Fedele, D., Pascucci, I., Brittain, S., et al. 2011, ApJ, 732, 106

Fedele, D., van den Ancker, M. E., Henning, T., Jayawardhana, R., & Oliveira, J. M. 2010, A&A, 510, A72

Feigelson, E., Townsley, L., Güdel, M., & Stassun, K. 2007, Protostars and Planets V, 313

Feigelson, E. D. & Nelson, P. I. 1985, , 293, 192

Fireman, E. L. 1974, ApJ, 187, 57

Flaccomio, E., Micela, G., & Sciortino, S. 2003, A&A, 397, 611

Flaccomio, E., Micela, G., Sciortino, S., et al. 2005, ApJs, 160, 450

Fogel, J. K. J., Bethell, T. J., Bergin, E. A., Calvet, N., & Semenov, D. 2011, ApJ, 726, 29

Glassgold, A. E., Meijerink, R., & Najita, J. R. 2009, ApJ, 701, 142

Glassgold, A. E., Najita, J., & Igea, J. 1997, ApJ, 480, 344

Glassgold, A. E., Najita, J., & Igea, J. 2004, ApJ, 615, 972

Glassgold, A. E., Najita, J. R., & Igea, J. 2007, ApJ, 656, 515

Gómez de Castro, A. I. & Marcos-Arenal, P. 2012, , 749, 190

Gorti, U., Dullemond, C. P., & Hollenbach, D. 2009, ApJ, 705, 1237

Gorti, U. & Hollenbach, D. 2004, ApJ, 613, 424

Gorti, U. & Hollenbach, D. 2008, ApJ, 683, 287

Gorti, U., Hollenbach, D., Najita, J., & Pascucci, I. 2011, ApJ, 735, 90

Gregory, S. G., Wood, K., & Jardine, M. 2007, MNRAS, 379, L35

Güdel, M., Briggs, K. R., Arzner, K., et al. 2007, A&A, 468, 353

Güdel, M., Lahuis, F., Briggs, K. R., et al. 2010, A&A, 519, A113+

Güdel, M., Skinner, S. L., Mel'Nikov, S. Y., et al. 2007, A&A, 468, 529

Güdel, M., Telleschi, A., Audard, M., et al. 2007, A&A, 468, 515

Gullbring, E., Calvet, N., Muzerolle, J., & Hartmann, L. 2000, ApJ, 544, 927

Gullbring, E., Hartmann, L., Briceno, C., & Calvet, N. 1998, , 492, 323

Haisch, Jr., K. E., Lada, E. A., & Lada, C. J. 2001, ApJl, 553, L153

Hartmann, L. 1998, Accretion Processes in Star Formation, ed. Hartmann, L.

Hartmann, L., Calvet, N., Gullbring, E., & D'Alessio, P. 1998, ApJ, 495, 385

Hartmann, L. & Kenyon, S. J. 1985, ApJ, 299, 462

Hashimoto, J., Tamura, M., Muto, T., et al. 2011, ApJl, 729, L17

Hayashi, C. 1981, Progress of Theoretical Physics Supplement, 70, 35

Heinzeller, D., Nomura, H., Walsh, C., & Millar, T. J. 2011, ApJ, 731, 115

Henning, T., Semenov, D., Guilloteau, S., et al. 2010, ApJ, 714, 1511

Herbig, G. H. 1977, ApJ, 217, 693

Herczeg, G. J., Linsky, J. L., Valenti, J. A., Johns-Krull, C. M., & Wood, B. E. 2002, ApJ, 572, 310

Herczeg, G. J., Linsky, J. L., Walter, F. M., Gahm, G. F., & Johns-Krull, C. M. 2006, ApJs, 165, 256

Hernández, J., Hartmann, L., Calvet, N., et al. 2008, ApJ, 686, 1195

Hogerheijde, M. R., Bergin, E. A., Brinch, C., et al. 2011, Science, 334, 338

Hollenbach, D. & Gorti, U. 2009, ApJ, 703, 1203

Hollenbach, D., Johnstone, D., Lizano, S., & Shu, F. 1994, ApJ, 428, 654

Hollenbach, D., Johnstone, D., & Shu, F. 1993, in Astronomical Society of the Pacific Conference Series, Vol. 35, Massive Stars: Their Lives in the Interstellar Medium, ed. J. P. Cassinelli & E. B. Churchwell, 26

Hollenbach, D. J. & Tielens, A. G. G. M. 1999, Reviews of Modern Physics, 71, 173

Hughes, A. M., Wilner, D. J., Qi, C., & Hogerheijde, M. R. 2008, ApJ, 678, 1119

Hummer, D. G., Berrington, K. A., Eissner, W., et al. 1993, , 279, 298

Igea, J. & Glassgold, A. E. 1999, ApJ, 518, 848

Imanishi, K., Koyama, K., & Tsuboi, Y. 2001, ApJ, 557, 747

Imanishi, K., Nakajima, H., Tsujimoto, M., Koyama, K., & Tsuboi, Y. 2003, PASJ, 55, 653

Ingleby, L., Calvet, N., Bergin, E., et al. 2009, , 703, L137

Ingleby, L., Calvet, N., Herczeg, G., & Briceño, C. 2012, ApJl, 752, L20

Isobe, T., Feigelson, E. D., & Nelson, P. I. 1986, , 306, 490

Johns-Krull, C. M., Valenti, J. A., & Linsky, J. L. 2000, ApJ, 539, 815

Jonkheid, B., Faas, F. G. A., van Zadelhoff, G.-J., & van Dishoeck, E. F. 2004, A&A, 428, 511

Kamp, I. & Dullemond, C. P. 2004, ApJ, 615, 991

Kamp, I., Tilling, I., Woitke, P., Thi, W., & Hogerheijde, M. 2010, A&A, 510, A18+

Kamp, I., Woitke, P., Pinte, C., et al. 2011, A&A, 532, A85

Kenyon, S. J. & Hartmann, L. 1987, ApJ, 323, 714

Konigl, A. & Pudritz, R. E. 2000, Protostars and Planets IV, 759

Koyama, K., Maeda, Y., Ozaki, M., et al. 1994, PASJ, 46, L125

Krems, R. V., Jamieson, M. J., & Dalgarno, A. 2006, ApJ, 647, 1531

Lada, C. J. 1987, in IAU Symposium, Vol. 115, Star Forming Regions, ed. M. Peimbert & J. Jugaku, 1–17

Lahuis, F., van Dishoeck, E. F., Blake, G. A., et al. 2007, ApJ, 665, 492

Landini, M. & Fossi, B. C. M. 1991, A&As, 91, 183

Latter, H. N. & Balbus, S. 2012, MNRAS, 424, 1977

Leen, T. M. & Graff, M. M. 1988, ApJ, 325, 411

Lennon, M. A., Bell, K. L., Gilbody, H. B., et al. 1988, Journal of Physical and Chemical Reference Data, 17, 1285

Maloney, P. R., Hollenbach, D. J., & Tielens, A. G. G. M. 1996, ApJ, 466, 561

Mathews, G. S., Dent, W. R. F., Williams, J. P., et al. 2010, A&A, 518, L127

Mathis, J. S., Rumpl, W., & Nordsieck, K. H. 1977, ApJ, 217, 425

McKee, C. F. & Ostriker, J. P. 1977, ApJ, 218, 148

Meeus, G., Montesinos, B., Mendigutia, I., et al. 2012, ArXiv e-prints

Meijerink, R., Aresu, G., Kamp, I., et al. 2012, ArXiv e-prints

Meijerink, R., Glassgold, A. E., & Najita, J. R. 2008, ApJ, 676, 518

Meijerink, R. & Spaans, M. 2005, A&A, 436, 397

Merín, B., Brown, J. M., Oliveira, I., et al. 2010, ApJ, 718, 1200

Millar, T. J., Adams, N. G., Smith, D., Lindinger, W., & Villinger, H. 1986, MNRAS, 221, 673

Min, M., Dullemond, C. P., Dominik, C., de Koter, A., & Hovenier, J. W. 2009, A&A, 497, 155

Mulders, G. D., Waters, L. B. F. M., Dominik, C., et al. 2011, A&A, 531, A93

Najita, J., Carr, J. S., & Mathieu, R. D. 2003, ApJ, 589, 931

Najita, J. R., Doppmann, G. W., Bitner, M. A., et al. 2009, ApJ, 697, 957

Nguyen, D. C., Scholz, A., van Kerkwijk, M. H., Jayawardhana, R., & Brandeker, A. 2009, , 694, L153

Nisini, B., Benedettini, M., Giannini, T., et al. 1999, A&A, 343, 266

Nomura, H., Aikawa, Y., Tsujimoto, M., Nakagawa, Y., & Millar, T. J. 2007, ApJ, 661, 334

Nomura, H. & Millar, T. J. 2005, A&A, 438, 923

Ormel, C. W., Dullemond, C. P., & Spaans, M. 2010, Icarus, 210, 507

Owen, J. E., Ercolano, B., Clarke, C. J., & Alexander, R. D. 2010, MNRAS, 401, 1415

Pascucci, I., Gorti, U., Hollenbach, D., et al. 2006, ApJ, 651, 1177

Pascucci, I., Hollenbach, D., Najita, J., et al. 2007, ApJ, 663, 383

Pinte, C., Ménard, F., Duchêne, G., & Bastien, P. 2006, A&A, 459, 797

Pinte, C., Woitke, P., Menard, F., et al. 2010, ArXiv e-prints

Podio, L., Kamp, I., Flower, D., et al. 2012, A&A, 545, A44

Pontoppidan, K. M., Blake, G. A., & Smette, A. 2011, ApJ, 733, 84

Pontoppidan, K. M., Salyk, C., Blake, G. A., & Käufl, H. U. 2010, ApJl, 722, L173

Pravdo, S. H., Feigelson, E. D., Garmire, G., et al. 2001, Nature, 413, 708

Ralchenko, Y. 2009, Physica Scripta Volume T, 134, 014025

Riviere-Marichalar, P., Ménard, F., Thi, W. F., et al. 2012, A&A, 538, L3

Robitaille, T. P., Whitney, B. A., Indebetouw, R., Wood, K., & Denzmore, P. 2006, ApJs, 167, 256

Sacco, G. G., Flaccomio, E., Pascucci, I., et al. 2012, ArXiv e-prints

Schindhelm, E., France, K., Herczeg, G. J., et al. 2012, , 756, L23

Schisano, E., Ercolano, B., & Güdel, M. 2010, MNRAS, 401, 1636

Schöier, F. L., van der Tak, F. F. S., van Dishoeck, E. F., & Black, J. H. 2005, A&A, 432, 369

Semenov, D., Pavlyuchenkov, Y., Henning, T., Wolf, S., & Launhardt, R. 2008, ApJl, 673, L195

Shakura, N. I. & Sunyaev, R. A. 1973, A&A, 24, 337

Shang, H., Glassgold, A. E., Lin, W.-C., & Liu, C.-F. J. 2010, ApJ, 714, 1733

Shu, F., Najita, J., Ostriker, E., et al. 1994, ApJ, 429, 781

Shu, F. H. & Adams, F. C. 1987, in IAU Symposium, Vol. 122, Circumstellar Matter, ed. I. Appenzeller & C. Jordan, 7–22

Shu, F. H., Najita, J. R., Shang, H., & Li, Z. 2000, Protostars and Planets IV, 789

Shull, J. M. & van Steenberg, M. E. 1985, ApJ, 298, 268

Stelzer, B. & Neuhäuser, R. 2001, A&A, 377, 538

Störzer, H. & Hollenbach, D. 2000, ApJ, 539, 751

Strom, K. M., Strom, S. E., Edwards, S., Cabrit, S., & Skrutskie, M. F. 1989, AJ, 97, 1451

Sturm, B., Bouwman, J., Henning, T., et al. 2010, A&A, 518, L129+

Thalmann, C., Grady, C. A., Goto, M., et al. 2010, ApJl, 718, L87

Thi, W.-F., Woitke, P., & Kamp, I. 2011, MNRAS, 412, 711

Tielens, A. G. G. M. 2005, The Physics and Chemistry of the Interstellar Medium

Uzawa, A., Tsuboi, Y., Morii, M., et al. 2011, PASJ, 63, 713

Valenti, J. A., Johns-Krull, C. M., & Linsky, J. L. 2000, ApJs, 129, 399

van der Werf, P. P., Isaak, K. G., Meijerink, R., et al. 2010, A&A, 518, L42+

van Zadelhoff, G.-J., Aikawa, Y., Hogerheijde, M. R., & van Dishoeck, E. F. 2003, A&A, 397, 789

Verner, D. A. & Yakovlev, D. G. 1995, A&AS, 109, 125

Vicente, S. M. & Alves, J. 2005, A&A, 441, 195

Walter, F. M., Brown, A., Mathieu, R. D., Myers, P. C., & Vrba, F. J. 1987, in Bulletin of the American Astronomical Society, Vol. 19, Bulletin of the American Astronomical Society, 1096

Weidenschilling, S. J. 1977, MNRAS, 180, 57

Weidenschilling, S. J. & Ruzmaikina, T. V. 1993, in Lunar and Planetary Inst. Technical Report, Vol. 24, Lunar and Planetary Institute Science Conference Abstracts, 1499–1500

Williams, J. P. & Cieza, L. A. 2011, ARA&A, 49, 67

Woitke, P., Kamp, I., & Thi, W. 2009, A&A, 501, 383

Woitke, P., Pinte, C., Tilling, I., et al. 2010, MNRAS, 405, L26

Woitke, P., Riaz, B., Duchêne, G., et al. 2011, A&A, 534, A44

Wolk, S. J., Harnden, Jr., F. R., Flaccomio, E., et al. 2005, ApJs, 160, 423

Woodall, J., Agúndez, M., Markwick-Kemper, A. J., & Millar, T. J. 2007, A&A, 466, 1197

Woods, P. M. & Willacy, K. 2009, ApJ, 693, 1360

Yang, H., Herczeg, G. J., Linsky, J. L., et al. 2012, ApJ, 744, 121

Zsom, A., Ormel, C. W., Güttler, C., Blum, J., & Dullemond, C. P. 2010, A&A, 513, A57

Samenvatting in het Nederlands

De mensheid heeft zichzelf altijd existentile vragen gesteld gedurende zijn eigen sociale en technische evolutie. Juist deze vragen hebben naar alle waarschijnlijkheid gezorgd voor een constante vooruitgang van de natuurwetenschappen. Sterrenkunde is een van deze natuurwetenschappen. Een van de meest fascinerende uitdagingen is inderdaad hoe het leven is ontstaan. Dit onderwerp kan bestudeerd worden zowel vanuit een kosmologisch oogpunt - door de eerste momenten van het universum te bestuderen - als wel vanuit antropisch oogpunt - gefocust op het menselijke leven en het bestaan hiervan op de planeet aarde.

Vanuit het tweede oogpunt bezien is de link tussen het begin van het leven en de omgeving die daarvoor nodig is meteen duidelijk: om het ontstaan van de mensheid te kunnen bevatten is het noodzakelijk om te begrijpen hoe sterren en planeten zijn gevormd.

In de laatste tien jaar heeft een indrukwekkende hoeveelheid theoretische en observationele studies ons in staat gesteld om volgens een evolutionair schema de sterformatie te beschrijven. Met de tijd worden de betrouwbaarheid en de voorspellende kracht van dit schema steeds groter. De Kepler missie demonstreert in het bijzonder dat in het universum de vorming van planeten zeer frequent is. De toekomstige uitdaging voor sterrenkunde en astrobiologie is om te onderzoeken of dit ook geldt voor het ontstaan van leven. De reis die leidt van het interstellaire medium naar de vorming van een planeet kan weergegeven worden als een serie stappen die begint met de zwaartekracht implosie van een absorptienevel (Fig. 1). Deze regios met hoge dichtheid worden in het algemeen gedomineerd door zwaartekracht: de implosie begint als de zwaartekracht niet meer in balans is met de interne turbulentie of de rotatie van de absorbtienevel. Een absorbtienevel waarvan de massa vergelijkbaar is met die van de zon en die zo groot is als een fractie van een parsec ($\sim 3{\times}10^{17}$ cm) krimpt tot een volume dat kleiner is dan duizend astronomische eenheden ($\sim 10^{16}$ cm). Behoud van impulsmoment schrijft voor dat materie niet rechtstreeks naar de vormende centrale kern vloeit, maar dat het op een accretieschijf rondom de kern neerslaat. In de eerste fases van deze overgang is het systeem gemaakt van een centraal object (de toekomstige ster) met daaromheen een accretieschijf en een halo van

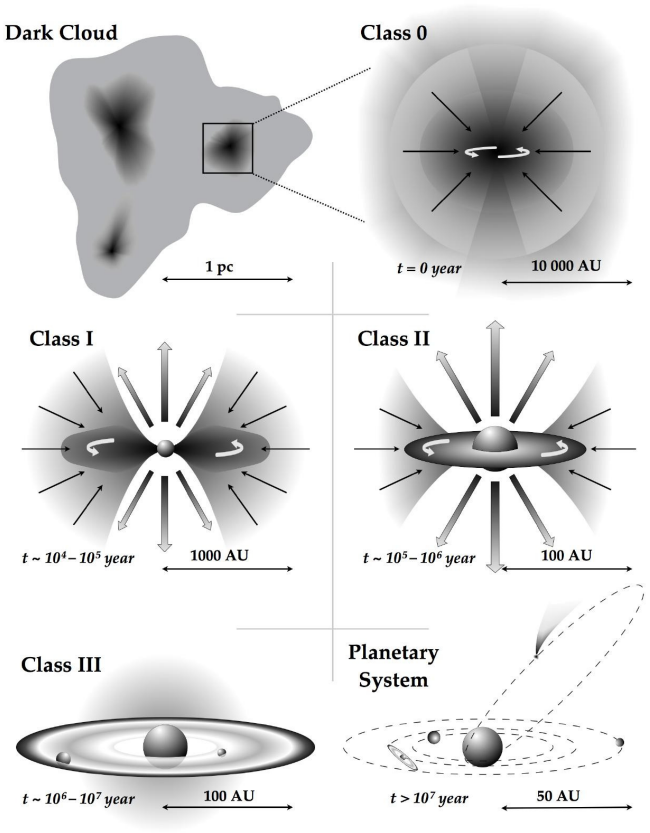

Figure 1: Schets van de evolutie, van de instorting van een moleculaire wolk naar de formatie van een schijf en vervolgens naar een planetair stelsel rond een centrale ster.

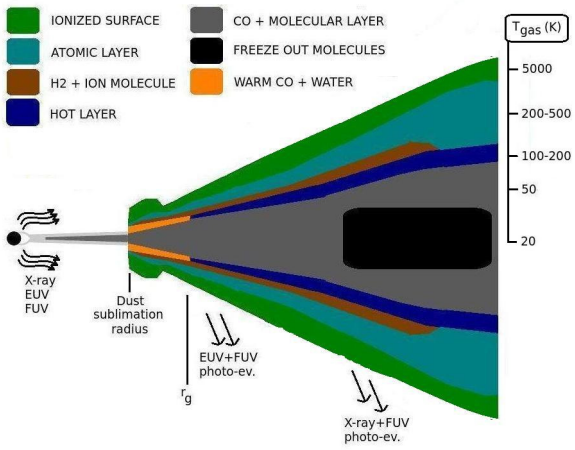

Figure 2: Stratificatie van de schijf in de gasvormige component. Het centrale object emiteert energetische straling, die zowel de chemische processen benvloedt als de thermische processen van.

materie die neerslaat op deze schijf. Dankzij deze schijf kan de materie gemakkelijker naar de kern vloeien. Deze kern groeit als gevolg van periodieke episodes van accretie. Als alle materie in de halo verplaatst is naar het systeem van ster en schijf spreken we van een protoplanetaire schijf waar gas en stof van de originele absorptienevel in een Kepler baan rondom de centrale nucleus beweegt. Nucleaire reacties staan op het punt te beginnen in de centrale nucleus en deze zullen de eigenschappen van de hoofdreeksster bepalen.

De dichtheid van de materie in de protoplanetaire schijf is hoger dan die van de materie in het interstellaire medium. Dit verschil maakt het mogelijk om stofdeeltjes met een gewicht van 0.1 m te vormen. Deze stofdeeltjes groeien groter en groter en bereiken in een tijdsspanne van 1 miljoen jaar een omvang van $\sim$ 1 km. Dit zijn de primordiale fases van planeetvorming en waarschijnlijk werd zon 4.6 miljard jaar geleden ook de nucleus van de aarde op deze manier gevormd.

Zowel de groei van de stofdeeltjes van $\sim$ 1 μm tot tientallen kilometers als de daarop volgende formatie van een atmosfeer rond een protoplaneet wordt sterk benvloed door de omgeving. De beschikbaarheid van gas wordt beperkt doordat de ster ook gas aantrekt en door een proces dat photoevaporation heet dat veroorzaakt wordt door de absorptie van energetische straling (E $>$ 6 eV) in de hoogste lagen van de schijf. Na enkele miljoenen jaren hebben we een systeem van planeten die rond een jonge ster draaien: in de bewoonbare zone zou een van deze planeten geschikt kunnen zijn voor de vorming van leven en het onderhouden hiervan.

De structuur van de protoplanetaire schijf wordt getoond in Fig. 2. Verschillende kleuren representeren verschillende onderdelen van de schijf, elk met hun eigen typische dichtheid en temperatuur van het gas.

In dit proefschrift bestudeer ik de impact van de straling van de centrale ster op

de chemische en fysische eigenschappen van deze schijf. Dit werk werd uitgevoerd met gebruikmaking van de code ProDiMo (protoplanetary disk model) die ik heb aangepast om zo ook chemische reacties en verwarmingsprocessen die veroorzaakt worden door rntgenstraling mee te nemen. In het tweede hoofdstuk voer ik een exploratieve studie uit van de impact van rntgenstraling op de schijf. Gemotiveerd door de verkregen resultaten focus ik mij in de daaropvolgende hoofdstukken (3 en 4) op de rol van de ver-ultraviolette straling (far-ultraviolet radiation) ($6 < \mathrm{E(eV)} < 13.6$) en rntgenstraling ($0.1 < \mathrm{E(keV)} < 10$) die de drijfveren van de thermale eigenschappen van de schijf zijn, die op hun beurt de emissie van bepaalde atomische en moleculaire lijnen bepalen. Voor dit werk heb ik een verfijnder modelraamwerk gebruikt om zo het belang van de andere parameters als eigenschappen van de stofdeeltjes en de variatie van de oppervlaktedichtheid van de schijf met de straal te bestuderen. Schijven kunnen geobserveerd worden dankzij de continuum straling afgegeven door stofdeeltjes. Deze straling geeft ons informatie over de ruimtelijke distributie van de deeltjes, hun grootte, samenstelling en massa. Aanvullend kunnen we een aantal van de atomische transities in verschillende regios van het elektromagnetische spectrum observeren. Deze atomische en moleculaire transities worden veroorzaakt door verscheidene opwekkingsmechanismen die afhangen van de positie van de emitterende soorten op de schijf. Dit levert ons een set van waarneembare hoeveelheden die erg bruikbaar zijn om de observaties te vergelijken met de modellen en om de modellen te kalibreren. In het laatste hoofdstuk analyseer ik de data in het infrarood genomen met de Herschel Space Observatory, waar we de helderste atomische transitie van de schijven kunnen observeren: de zuurstof emissielijn op 63 micron. De hoofdresultaten van dit proefschrift kunnen als volgt worden samengevat:

- De rntgenstraling warmt de bovenste lagen van de schijf op tot een temperatuur van ongeveer 5000 K. Gas in deze regios is voor het merendeel geoniseerd en de hoge temperatuur zorgt ervoor dat de schijf verticaal uitbreid om zo een drukevenwicht te bereiken.

- Sommige chemische soorten (bijvoorbeeld N^+, OH^+) zijn extreem gevoelig voor rntgenstraling en worden gevormd door een chemische kettingreactie die begint bij de aanwezigheid van diffuus geoniseerd waterstofgas. Hun emissielijnen observeren is echter gecompliceerd omdat de voorspelde flux van de lijnen laag is bij een afstand van 140 parsec, waar we een beroemde sterformatie regio vinden in de constellatie van de Stier. De voorspelde fluxen zijn, in feite, 2-3 orders van grootte lager dan wat men met de huidige instrumenten kan observeren.

- De omvang van de regio van de schijf waar de temperatuur hoger is dan 1.000 K is groter als we de rntgenstraling in de modellen meenemen. Dit omdat rntgenstralen efficinter zijn in het opwarmen van de schijf dan de verre ultraviolette straling.

- Rntgenstraling verhoogt de productie van H en de moleculaire waterstof door de reactie $\mathrm{H + H \rightarrow H_2 + e^-}$. Zij dragen tot 50% bij aan de formatie van H_2 op de stofdeeltjes.

- Observaties van de 63 micron neutrale zuurstof transitie in de stervormende regio in de Stier constellatie suggereert dat ver ultraviolette straling de belangrijkste warmtebron is van de schijf. Dit resultaat zou het belang van ver ultraviolette straling voor de photoevaporation processen van de schijf bevestigen, wat aangeeft dat de schijf na $\sim$ 3 miljoen jaar veel gas heeft verloren.

In de toekomst zullen resultaten afkomstig van modellen die niet onderzocht zijn in deze studie (bijvoorbeeld voorspellingen voor emissielijnen afkomstig van water en geoniseerd neon) samen gebruikt worden met observaties met als doel het vergaren van verdere informatie over de structuur en evolutie van de schijf.

Resùmini in sardu

S'umanidadi at sèmpiri arresonau a pitzus de is preguntas esistentzialis chi cun issa ant acumpangiau su cresci sociali e tecnològicu. Est probabili meda ca custus arcanus apant donau cussa impèllida morali pro s'istùdiu in totus is matèrias ca tenint cummenti acabu sa connoscéntzia de sa natura etotu. S'astronomia est unu de custas. Su disafiu prus bellu est su comprendòniu de is fattus chi ant portau a sa nàscida de sa vida. De totu custu si podit arrexonai aintru de sa cosmologia, castiendi a is primus momentus a pustis de sa nascita de s'universu, o pentzendi sceti a sa vida umana e a totu cussu chi ddi pertocat, in una cuncetzioni prus strinta, a pitzus de unu praneta cummenti sa Terra nostra.

Cunsiderendi custa ùrtima possibilidadi ndi sighit sa relatzioni intra sa vida umana e su sfundu pretzisu chi issa bolit po si manifestai: cumprendi s'orìgini de s'umanidadi depit trantziri po su stùdiu de sa formatzioni de is isteddus, e de is pranetas a ingìriu.

In custus ùrtimus binti annus ci funt stètius unu iaxi de stùdius e datus osservativus nous, chi ant permìtiu de donai una strutura bàlida a sa formatzioni de is isteddus, sighendi unu schema evolutivu chi dogna dii donat sèmpiri prus cunfiàntzia e tenit prus abilidadi de intzertai. Sa missioni Kepler dimustrat ca sa formatzioni de is pranetas est una cosa normali, fintzas fitiana in s'universu. Su disàfiu pro s'astronomia (e astrobiologia) de su tempus benidori, est su de cumprendi chi sa pròpia cosa si podit narai pro sa formatzioni de sa vida etotu.

Su biaxi chi portat de su mèdiu interstellari (ISM) a sa formatzioni de unu praneta podit èssiri spràtziu in una pariga de passus, cumentzendi cun su collassu gravitatzionali de una nui scuria (Fig. 1). In custus logus densus meda est sa gravidadi ca dòminat: candu no est prus apportada de is motus treuladoris de aintru, o de s'arrodiamentu de sa nui, su collassu cumentzat. Struturas de massa cumparàbili a sa de su soli, e chi funt mannas fratzionis de parsec ($\sim 3 \times 10^{17}$ cm) si cuncentrant in unu logu ca podit essi piticu fintzas unas centinas de unidadis astronòmicas ($\sim 10^{16}$ cm). Sa cunservatzioni de su momentu de arrodiamentu bolit chi sa matèria no dda acabit deretu in su coru centrali, ma chi custa dda acabit atesu, assempiendi unu discu de acrescimentu. In is primu fasis de custa transitzioni, in su sistema ddui est unu corpus centrali, unu discu a pagu a pagu ammanniendisì a ingìriu e unu arrodeu de matèria chi acrèsciri a pitzus de su discu. Est su discu ca fait fàcili sa tragada de matèria a pitzus de su corpu centrali, ammanniendindi su pesu. Candu su discu at acabau de acresci sa matèria de s'aloni dessintotu, amus a tenni unu discu protopranetàriu,

aundi su gas e is granus de sa nui de su cumentzu si movint de motu keplerianu a ingìriu de su corpus centrali. Aintru de custu, is reatzionis nuclearis funt acanta de si allui, intzimendi su corpus de mudai in un'isteddu.

Is densidadis in su discu protopranetàriu e in su mèdiu interstellari funt divertzas, prus mannas in su primu, aundi est prus fàcili sa coesioni e su ammanniamentu de is granus (custus funt partixeddas mannas $\sim$0.1 μm). Aici cummentzat sa crèscida de is granus, chi ant a formai corpus sèmpiri prus mannus e grais, fintzas chilometrus, a pustis de una pariga de millionis de annus. Aici si formant is pranetas, e aici si est formau su centru de su praneta Terra, agiumai 4.6 miliardus de annus a oi.

Sa crèscida de is partixeddas de dimensionis de su micron fintzas una pariga de chilometrus, e su fatu ca una borta mannus custus protopranetas achirint una atmosfera de gas, funt acapiaus meda cun s'ambienti a ingìriu. Cantu gas ddui est disponìbili est limitau de su tempus chi bolit sa matèria po lompi a pitzus de s'isteddu, o su tempus chi pigat sa fotoevaporatzioni in is pillus prus artus de su discu po imperdi sa matèria. Apustis de calincunu millioni de annus su sistema depit essi cumpostu de una pariga de pranetas a ingìriu de un'isteddu giòvunu: podit essi ca in unu de custus pranetas ddui funt totus is conditzionis pro sa nàscida e sa froridura de sa vida.

Sa strutura de su discu protopranetàriu si podit castiai in Fig. 2. Totus is coloris afigurant is diversas cunditzionis de densidadi e temperadura de su gas.

In custa tesi deu stùdiu su chi fait sa radiatzioni de energia manna chi benit de s'isteddu a is reatzionis chìmicas e in is conditzionis fisicas de su discu protopranetàriu. Su traballu est istètiu fatu mainendi su programma de computadora ProDiMo (protoplanetary disk model), aundi apu aciuntu is reatzionis chìmicas e is protzessus de callentamentu intzimaus de sa radiatzioni X. In su segundu capìtulu apu studìau su atùmbidu de sa radiatzioni X a pitzus de su discu. In is capìtulus chi sighint (su de tres e su de cuatru) profundau s'arrolu chi rajus ultratanaus atesus (FUV, $6 < E\,(\mathrm{eV}) < 13.6$) e rajus X ($0.1 < E\,(\mathrm{keV}) < 10$) tenint pro determinai is cunditzionis de temperadura basilaris chi dominant sa emitidura de una pariga de arrigas atòmicas e molecularis. In custu traballu apu impreau una cardiga de modellus prus manna pro studiai puru s'arrolu de is atras cantidadis, cummenti: propriedadis de is granus e sa dipendèntzia de sa densidadi superficiali de su discu a pitzus de sa distàntzia de s'isteddu.

Is discus funt castiaus po mèdiu de s'emitidura in su continuum de is granus, chi donat informatzionis a pitzus de s'estensioni spatziali, distributzioni de mannària, cumpositzioni e massa, ma puru po mèdiu de is arrigas atòmicas in un pariga de intervallus aintru de sa variedadi elettromagnètica. Is transitzionis atòmicas e molecularis funt intzimadas de prus mecanismus de intzulamentu chi cambiant cun sa positzioni in su discu de spetzias chi dda emitint, afiantziendi diaci totus is osservatzionis ùtilis meda pro cunfrontai is modellus o po sa calibradura etotu. In su ùrtimu capìtulu analizu is datus osservaus de su Herschel Space Telescope in su infra-arrùbiu, aundi est castiada sa transitzioni atòmica prus luxenti in is discus: s'arriga in emitidura de s'ossìgenu a 63 micron.

Is arresurtaus printzipalis de custa tesi, podint essi resuminaus cummenti sighit:

- Is rajus X intzimant sa calentura de is stèrridas prus artus des su discu, portendidda acanta de 5000 K. In cussus logus su gas est ionizau meda e is artas

temperaduras intzimant sa alladiadura verticali de su discu, poita ca su armùdiu de pressioni bolit agatau.

- Calincunas spetzias chìmicas (es. N^+, OH^+) funt sensìbilis meda a sa radiatzioni X, e benint formadas sighendi reatzionis chìmicas chi partint de su H^+ in su gas. S'osservatzioni de is arrigas in emitidura est problematica, poita is flussus funt piticus, chi cunsideraus una distàntzia de 140 parsec, i.e. aundi s'agatat unu logu connotu de formatzioni de isteddus piticus in sa costellatzioni de su Malloru. Custus funti centus o milli bortas prus piticus de is flussus mìnimus chi si podint osservài cun is strumentus de oi.

- Su tretu de su logu de su discu aundi sa temperadura est prus manna de 1000 K est prus manna candu sa radiatzioni X benit incluida in is modellus. Is rajus X tenint unu atòliu de calori/temperadura prus mannu de is ultratanaus.

- Is rajus X abbundint sa produtzioni de H^-, e cun sa reatzioni $H^- + H \rightarrow H_2 + e^-$, sa produtzioni de idrogenu moleculari, fintzas a intzumai su 50% de sa formatzioni de H_2 a pitzus de is granus.

- Is osservatzionis de sa transitzioni a 63 μm de s'ossigenu nèutru faci a su logu de formatzioni de is isteddus in sa costellatzioni de su Malloru, insinuant ca is rajus ultratanaus dominant sa temperadura in s'atmosfera de su discu. Custu cunfirmat s'importàntzia de is FUV in is protzessus de foto-evaporatzioni de su discu, chi benit sbudiau meda de su gas apustis $\sim$3 millionis de annus.

In is annus chi benint, atras cosas chi no emus studiau innoi cun is modellus (es. is arrigas de s'acua e de su neon ionizau), ant a essi carculadas impari a is osservatzionis pro tenni atras informatzionis a pitzus de sa strùtura de su discu e de cummenti cambiat in su tempus.

Riassunto in italiano

Il genere umano si è sempre interrogato sulle domande esistenziali che lo hanno accompagnato nel corso della sua evoluzione sociale e tecnologica. Proprio questi quesiti hanno probabilmente fornito una costante spinta verso la ricerca in tutti quei campi che hanno come fondamentale obiettivo la comprensione della natura, nel suo complesso. L'astronomia è uno di questi. La sfida forse più affascinante è infatti la comprensione delle fasi che hanno portato alla nascita della vita. L'argomento si può affrontare sia in termini cosmologici, studiando i primi istanti di vita dell'universo, che in termini antropici, restringendo il campo alla vita umana e alla sua manifestazione in scala locale, su un pianeta come la nostra Terra.

Nel secondo caso risulta immediatamente evidente il collegamento tra il fiorire della vita e l'ambiente necessario perchè questa si manifesti: la comprensione dell'origine dell'uomo deve passare per lo studio della formazione delle stelle, e dei pianeti intorno ad esse.

Negli ultimi decenni una impressionante quantità di studi teorici e dati osservativi ha permesso di strutturare la formazione stellare secondo uno schema evolutivo che acquista sempre più affidabilità e capacità predittive col passare del tempo. In particolare la missione Kepler dimostra che la formazione dei pianeti è un evento comune e anzi frequente nell'universo. La sfida per l'astronomia (e astrobiologia) del futuro prossimo, è capire se la stessa conclusione possa essere formulata per la formazione della vita.

Il viaggio che porta dal mezzo interstellare alla formazione di un pianeta può essere schematizzato attraverso diversi passaggi che cominciano con il collasso gravitazionale di una nube oscura (Fig. 1). Queste regioni sovra-dense sono generalmente dominate dalla gravità: quando quest'ultima non è più supportata dai moti turbolenti interni o dalla rotazione della nube stessa, il collasso comincia. Strutture aventi massa comparabile a quella solare che si estendono per qualche frazione di parsec ($\sim 3 \times 10^{17}$ cm) vanno a concentrarsi in regioni di spazio più piccole di un migliaio di unità astronomiche ($\sim 10^{16}$ cm). La conservazione del momento angolare impone che la materia non confluisca direttamente sul nucleo centrale che va progressivamente formandosi, ma che questa atterri ad una certa distanza, andando a formare un cosidetto disco di accrescimento. Nelle prime fasi di questa transizione il sistema è quindi composto da un oggetto centrale, un disco in formazione attorno ad esso ed un alone di materia che accresce sul disco. Quest'ultimo favorisce il trasporto di materia sull'oggetto centrale

aumentandone la massa per mezzo di eventi periodici di accrescimento. Quando la materia dell'alone viene completamente accresciuta dal sistema stella-disco, ci troviamo di fronte ad un disco protoplanetario, dove gas e polveri della nube primordiale orbitano in moto kepleriano attorno all'oggetto centrale, vicino ormai alla accensione al suo interno delle reazioni nucleari che ne determineranno lo stato di stella in sequenza principale.

Le diverse condizioni di densità nel disco protoplanetario rispetto al mezzo interstellare, favoriscono la coesione e la crescita dei grani di polvere (particelle solide delle dimensioni di $\sim$0.1 μm). Questi vanno a formare progressivamente corpi più grandi e massicci, sino a raggiungere le dimensioni dei chilometri, dopo tempi paragonabili al milione di anni. Si tratta dei primordi della formazione dei pianeti, e molto probabilmente degli stessi processi che hanno generato il nucleo del pianeta Terra circa 4.6 miliardi di anni fa.

La crescita degli agglomerati solidi dalle dimensioni del micron alle decine di chilometri, e la successiva acquisizione di una atmosfera da parte del protopianeta, sono strettamente correlate all'ambiente circostante. La disponibilità di gas è infatti limitata dall'accrescimento dello stesso sulla stella e dalla sua foto-evaporazione causata dall'assorbimento di radiazione energetica ($E > 6$ eV) negli strati più elevati del disco. Dopo qualche milione di anni il sistema si manifesta in quello che potrebbe essere un insieme di pianeti attorno ad una stella giovane: uno di questi pianeti, nella zona abitabile, potrebbe essere adatto alla formazione e sostentamento della vita.

La struttura del disco protoplanetario è mostrata in Fig. 2. Diversi colori rappresentano i diversi regimi di densità e temperatura del gas.

In questa tesi studio l'impatto della radiazione stellare sulle carattersitiche chimiche e fisiche del disco primordiale. Il lavoro viene svolto utilizzando il codice computazionale ProDiMo (protoplanetary disk model), nel quale ho incluso le reazioni chimiche e i processi di riscaldamento causati dalla presenza di radiazione X. Nel secondo capitolo affronto uno studio esplorativo sull'impatto della radiazione X sul disco. Motivato dai risultati ottenuti, nei capitoli successivi (terzo e quarto) mi concentro sul ruolo che raggi ultravioletti lontani (FUV, $6 < E\,(\mathrm{eV}) < 13.6$) e raggi X ($0.1 < E\,(\mathrm{keV}) < 10$) assumono nel determinare le condizioni termiche di base che guidano l'emissione di alcune righe atomiche e molecolari. In questo caso ho utilizzato una griglia di modelli più ampia al fine di studiare anche l'importanza di altri parametri quali le proprietà dei grani di polvere e la dipendenza radiale della densità superficiale del disco.

I dischi vengono osservati sia tramite l'emissione nel continuo dei grani di polvere, la quale dà informazioni sulla loro estensione spaziale, distribuzione di grandezza, composizione e massa, ma anche per mezzo di numerose transizioni atomiche in diverse bande dello spettro elettromagnetico. Queste transizioni atomiche e molecolari sono causate da diversi meccanismi di eccitazione a seconda della posizione nel disco della specie che le emette, garantendo quindi un set di diagnostici osservativi molto utili per il confronto coi modelli o per la loro calibrazione. Nell'ultimo capitolo analizzo i dati osservati dallo Herschel Space Observatory nel infra-rosso, dove viene osservata la transizione atomica più luminosa nei dischi: la riga in emissione dell'ossigeno a 63 micron.

I risultati principali di questa tesi, possono essere riassunti come segue:

- La radiazione X causa il riscaldamento degli strati superiori del disco, portando la temperatura a raggiungere i 5000 K circa. In quelle stesse zone il gas è prevalentemente ionizzato e le alte temperature causano una progressiva espansione verticale del disco al fine di raggiungere l'equilibrio di pressione tra i suoi strati.

- Alcune specie chimiche (es. N^+, OH^+) sono fortemente sensibili alla radiazione X, e vengono formate attraverso un network di reazioni chimiche che parte dalla presenza diffusa di idrogeno ionizzato in fase gas. L'osservazione delle loro righe in emissione risulta tuttavia problematica visti i bassi flussi predetti ipotizzando una distanza di 140 parsec, i.e. dove si trova una famosa regione di formazione stellare nella costellazione del Toro. Quest'ultimi sono attualmente 2-3 ordini di grandezza inferiori ai flussi minimi osservabili con le strumentazioni odierne.

- L'estensione della zona del disco dove la temperatura supera i 1000 K è maggiore quando la radiazione X viene inclusa nei modelli. I raggi X hanno infatti una maggiore efficienza di riscaldamento rispetto agli ultravioletti lontani.

- I raggi X aumentano la produzione di H^-, e tramite la reazione $H^- + H \rightarrow H_2 + e^-$, la produzione di idrogeno molecolare, sino a contribuire per il 50% alla formazione di H_2 sui grani di polvere.

- Le osservazioni della transizione a 63 μm del ossigeno neutro verso la regione di formazione stellare nella costellazione del Toro, suggeriscono che i raggi ultravioletti lontani siano la fonte di riscaldamento principale dell'atmosfera del disco. Questo risultato confermerebbe l'importanza degli FUV nei processi di foto-evaporazione del disco, indicando che quest'ultimo viene fortemente depauperato del suo gas dopo $\sim$3 milioni di anni.

In futuro, i risultati dei modelli non approfonditi in questo lavoro (es. predizioni sulle righe dell'acqua e del neon ionizzato), verranno utilizzati assieme alle osservazioni per ottenere ulteriori informazioni sulla struttura del disco e sul suo stato evolutivo.

Acknowledgments

Quando il sole alzò la testa tra le spalle della notte
c'erano solo cani e fumo e tende capovolte
tirai una freccia in cielo
per farlo respirare
tirai una freccia al vento
per farlo sanguinare
la terza freccia cercala sul fondo del Sand Creek
Fabrizio De Andrè

The human brain is a wonderful thing.
It starts working the moment you are born,
and never stops until you stand up to speak in public.
George Jessel

..and finally these pages. This time spent in the Netherlands was precious to me. It was a huge experience as a person, and from a professional point of view. Many people were part of it, and I'm happy to use this space to acknowledge them. As usual, not by chance, the first words are dedicated to supervisors and collaborators.

Inga, I still remember the moment I walked into the room to give my talk for the PhD position with you. You were really serious and asked me to turn the lights on, with a quite firm voice tone. Only, you did it in Dutch. Of course I didn't get a single word, and I just couldn't do anything, standing there trying to understand whether I should have learnt Dutch for the interview, or hoping you were maybe confused by the constant Dutch/English switch. Luckily it was the second one, and you gave me a big smile, even apologizing for the mix-up. That put me at ease, and that feeling persisted throughout the whole PhD. You've been a fantastic supervisor, I can't recall a single "bad" discussion in the last four years. Whenever we disagreed on something you were always ready to listen and give precious feedback, and that forced me to grow my own ideas. When someone questions your opinions instead of imposing his own, you need to come up with valid ones. And this is probably a big thing to learn in science (and not only). Something you taught me, and I am still learning. You are an impressive scientist, and I will always admire the passion you put in your work and the (for me) unbelievable efficiency in the way you organize it. But I guess the last one just makes you a normal German :D. I was shocked when I realized I was your first PhD student. Thanks for all your patience, help and understanding of personal issues. Without you these book would have hardly taken shape. I'm glad I could join many barbecues with you and Ulli, very rich barbecues :), it was a lot of fun!

Marco, thanks for your fundamental contribution all over these years, and for being there when things were getting complicated. It happened especially during the iterations with the referee/editor for the first paper, I was quite confused about the whole thing, but with your help I could handle the situation better and from that work depended much of this book. Thanks for your important presence at the ISM dinners, and for the outstanding easiness you talk and explain science, which is great source of motivation.

Rowin, I really like the two intermediate chapter, which are the core of this thesis. We have been discussing so much about it, and for such a long time, having the two papers published now is a great gratification. Thanks for the huge help and for dedicating so much time to this, and for providing reactions, rates, formulas and so on. Needless to say, without it, it would have been very hard to even start this work. I wish the conference in Toledo was coming up now, so we could celebrate with lot more sangria.

Inga, Marco, and Floris, thanks for giving me the opportunity to be the tutor for the Star and Planet formation and ISM courses. It was a nice and useful experience for me. I would like to thank Peter Woitke and Wing-Fai Thi for the precious comments, new ideas, fix-ups and impressive speed in developing ProDiMo. I've learnt a lot just looking at your routines. Thanks for hosting me in Grenoble for the ProDiMo X-rays "official" implementation. I'm deeply indebted with the whole GASPS team, for the [O I] data, which shaped Chapter 5 and for many things I discussed and learnt during the meetings. Thanks to Peter and Manuel Guedel for inviting me to Vienna, where I had a very fruitful and pleasant time. I had many useful trips for conferences or working visits in these years, thanks to NWO and Lkbf funding.

I also thank the *beoordelingscommissie* for the thorough reading of the thesis and for providing comments and suggestions with perfect timing.

Thanks to all (former and current) members of the ISM group for the meetings, and always fun and enjoyable dinners around Groningen. There are many things to take care beside work itself at the Kapteyn Institute, and there is people always ready to help, which is something one shouldn't give for granted. I would like to thank Hennie, Jackie, Gineke and Lucia for the precious help with documents, paper works, deadlines and so many other things. Thanks to Wim, Eite and Martin for providing continuous support for the computers (an especially printers), even in the second floor. Thanks to Alicia, Seungyoup, Julianne, Sofia, Niels and Anastasia for always keeping the office a comfortable place to work.

Before starting my PhD I was already in Groningen, where I took a 8 months stage period. Mariano, thanks for giving me the possibility to come to the Netherlands in the first place, I've learned a lot in those months. Everything was new, and your help, supervision, and suggestions were really precious to me. The High Energy meetings where always useful and enjoyable, thanks to Beike, Diego, Andre and Guobao.

Usually the first weeks abroad are not easy, it takes a bit to acclimate and to get to know people, but I feel like this has been a lot easier for me. Facu & Anto, thanks for all the dinners and the good time we had together, I wish you guys (and River) a great life together. Matias and JP, thanks for being defenders allowing me to play forward and never come back to help :), and for all the great times we shared. Boris, if it wasn't for you I would have never seen the Assen circuit, shame on me. Peter, sorry for trying to kiss you during your defense, after knowing the Dutch culture I realised how dangerous that move was :). Aycin, I could now use this space to tease you one more time, but I'll behave, and just thank you for all the good Turkish food you cooked and for the countless times you gave me a wrong pass, oops, I did it again..Andre, sharing a house wasn't easy, but I'm glad we left that behind, after all it was a lot of fun, apart from the scopa 15 matches :).

Chiara and Andy, thanks for making our house a pleasant place to stay day by day. I hope the next house mate will be a bit less ghostly than I was, although I'm sure you will

miss my ectoplasm traces all over the place :).

Before the Italian invasion I even started having Dutch classes, trying to be a proper citizen of the world. But there were just too many new people, all of a sudden, and I couldn't avoid it. My English almost died, I had pasta dreams all over again, and recovered insulting Berlusconi on a daily basis. For this I blame all of you. Lelli, sguattero di un certo livello, thanks for all the time we shared and for being patient with all mine *no, not today, i'm tired, i have to work, it's late etc.*, I'll wait to finally have the "svolta" we both deserve. Stephs, what a fantastic random person. Thanks for being so easy-going about everything, I hope one day I will be worthy of the clown dress in which you would like to see me packed. Linda, I never knew it was possible to drop so many things in such a short time. Not the mention the curious way you adopt to break other people windows. It was all impressive, and fun to talk about because your self irony is just enviable. Garufi, stimatissimo dott. Garufi, ma anche bella rega Garufi. Grande personaggio, you have something other people can only dream about: the avahdfhsj. Thanks for that, and for counting how many stroopwafels you ate. Giuliana, I'm glad I met you, one of the few times I walked out a bar after 5 am it was with you, such an onor! Paolo, da *terùn* a *bauscia*, you are a great cook, thanks for the dinners and for all the fun we had going out, it was great to see you getting together with Jenny to produce the next Italian top scorer at the World Cup..no pressure..(need an agent for Marco?).

German, I knew you were going to be a great dad when you provided food for me in Munich, when I got sick :), I wish you and your beautiful family the best. Pratyush, I don't know when and where, but I bet we will be able to have our "at the pool table" night, I promise ;). Many other people were part of these 4-5 years, thanks to Parisa, Jan, Esra, Stephanie, Rag. Antonellini, Robyn, Silvia, Kyle, Oscar and Teresa, Carlos, Rosina, Mark, for everything we shared, from lunches to concerts to park barbecues to observing trips (thanks Burcu!!). I do hope I am not forgetting too many..

Paolè, thanks for being my Sardinian reference abroad, it made the transition way easier at the beginning, and in the end too. I'll miss our endless discussions about everything, and your books or movies suggestions which always turned out to be great. I'm looking forward to pay back a good number of pasta with bottarga, I am going to be among the ones that will bother you and Miri for a visit every time you come back to Sardinia, be ready! Mirjam, thanks so much for helping with the Dutch translation of the summary and for all the good times we had in Groningen, hearing you swearing in Sardinian was priceless! Sophie(cina), thanks for teaching me which sound the lion makes and for having such a marvelous laugh.

È stato difficile coniugare due vite parallele, cosa sicuramente sostenibile solo per un breve periodo di tempo. Grazie a tutti i miei amici, è anche colpa/merito vostro se non sono mai veramente partito. Andre e Sergio, conservo ancora gelosamente la vostra foto, preziosa nei momenti di sconforto e fonte di stimolo..in tutti i sensi. Sono felice di ricominciare a vedervi come prima. La gita in ogliastra tre mesi dopo la mia partenza ha distrutto ogni mia convinzione di voler stare all'estero per sempre. Mascia ti reputo responsabile per quella ed altre gite, con la collaborazione di Michela, Roberta, Antonio e tanti altri, ci vogliamo forse dimenticare la statua a forma di Cavani in Gallura? Grazie anche agli ex-colleghi di studi per i pranzi/cene degli esuli, mangiare *a totu tubu* roba sarda DOC ha aiutato parecchio. Vale, non ho ancora capito il senso del caffè alla vaniglia ma mi autoinviterò ancora per gustarlo (?) e parlare delle nuove sfighe che il mondo si inventa. Cla, con l'augurio di poterci rivedere senza per forza doverci raccontare cos'è successo negli ultimi 2 anni che non ci siamo sentiti. E magari potrò prestarti io un libro, for a change! Ale, grazie mille per l'aiuto nella traduzione *de su resùmini in sardu*, era una "piccola cosa" alla quale tenevo molto. Zap, assistere ai tuoi allenamenti nel mio soggiorno per perdere 5 chili in 3 giorni è stata un'esperienza esilarante, ma almeno non mi hai fatto fuori 9 lattine di cola, miserabile!

Acknowledgments

Grazie a tutti i partecipanti, schiavi e non, della Lega Is Urigus, dominarvi infrangendo ogni record mi ha aiutato molto durante la mia permanenza all'estero :). Mai stati in B.

Un enorme grazie ai miei genitori e Silvia per avermi sempre incoraggiato e sostenuto, e per le abbuffate di bistecche arrosto che non fanno mai male. A Zio Renzo e Zia Teresa per il tifo sfegatato e troppo imparziale :), questo libercolo esiste anche grazie a voi. Grazie a tutto il resto della famiglia, nonne, zii, zie, cugini e cugine, sarà bello vedersi più spesso.

Un sentito grazie ai Sig. Ignazio e Marina per l'affetto e l'accoglienza che mi hanno sempre dimostrato e per aver messo al mondo la persona più dolce che sia mai esistita.

Brissi, Pippi, Alda-Balda, ed è meglio fermarsi qui. Abbiamo condiviso tantissimo, in questi tre anni che sembravano non finire più. Ma ora ci siamo, e il pensiero di tornare a casa per cominciare una nuova vita con te è la parte più bella di questo cammino. Non so immaginare come sarebbe stato senza di te, guardare indietro è una cosa che non si fa quando si è abbastanza fortunati da non rimpiangere niente. Hai sfidato il freddo, mille voli, pioggia e neve per starmi vicino. Se potessi ti dedicherei ogni pagina, ma devi accontentarti della mia infinita gratititudine per te, e per noi. E della mia felicità al pensiero di come sarà. Ti amo.

I felt lucky to have such an experience, and finally, I would like to thank myself for not thinking too much before making an important decision. So far it turned out to work pretty good.

Cagliari, 30 October 2012